NORTHWESTERN UNIVERSITY

X-ray Structural Analysis of In-Situ Polynucleotide Surface Adsorption and Metal-Phosphonate Multilayer Film Self-Assembly

A DISSERTATION

SUBMITTED TO THE GRADUATE SCHOOL
IN PARTIAL FULLFILLMENT OF THE REQUIREMENTS

for the degree

DOCTOR OF PHILOSOPHY

Field of Materials Science and Engineering

By

Joseph Anthony Libera

EVANSTON, ILLINOIS

JUNE 2005

ABSTRACT

X-ray Structural Analysis of In-Situ Polynucleotide Surface

Adsorption and Metal-Phosphonate Multilayer Film Self-Assembly

Joseph Anthony Libera

The X-ray Standing Wave (XSW) analytical technique was adapted to measure nano-scale structures in the 0.5 – 50 nm length range using large d-spacing layered synthetic microstructure (LSM) X-ray mirrors. This allowed for the first ever use of multiple orders of Bragg reflection in long-period XSW analysis. XSW analysis was combined with X-ray reflectivity (XRR) and X-ray fluorescence (XRF) to analyze layer-by-layer assembly of metal-phosphonate multilayer films as a test case and to measure for the first time the *in-situ* process of adsorption of polynucleotides and counterions to charged planar surfaces. The surface chemistry was built on the outermost silica surfaces of 19-22 nm d-spacing Si/Mo LSMs. XSW experiments were conducted by simultaneously collecting X-ray reflectivity and X-ray fluorescence data in continuous θ-2θ scans from the total external reflection (TER) region through four or five orders of Bragg reflection.

Multilayer metal phosphonate thin films were prepared via a layer-by-layer assembly process using the metallic ions Zr^{4+}, Y^{3+}, Hf^{4+}, and phosphonate molecules 1,12-dodecanediylbis(phosphonic acid) (DDBPA), porphyrin bis(phosphonic acid) (PBPA) and porphyrin square bis(phosphonic acid) (PSBPA). An initial study of PBPA and PSBPA using Y, Hf and Zr led to the optimized design of DDBPA and PSBPA films using Zr and Hf only prepared in 1, 2, 3, 4, 6, and 8 layer series on both Si(001) substrates for XRR and on 18.6 nm period Si/Mo LSMs for XSW.

Positively and negatively charged surfaces were prepared for the *in-situ* study of the adsorption of Zn^{2+} and Hg-poly(U). Hydroxyl-terminated surfaces were used to examine the adsorption of Hg-poly(U) to like charged surfaces using Zn^{2+} counterion-mediated adsorption. The measurements were performed in a liquid-solid interface (LSI) cell using aqueous solutions of Hg-poly(U) and $ZnCl_2$. Using 50 μM $ZnCl_2$ alone, adsorption of Zn^{2+} was observed to the hydroxyl terminated surface. When 25 μM Hg-poly(U) and 50 μM $ZnCl_2$ were used, a time-dependent adsorption was observed with no initial absorption of either Zn or Hg-poly(U) followed by Zn adsorption and then Hg-poly(U) adsorption.

Approved:

_____

Professor Michael J. Bedzyk

Department of Materials Science and Engineering

Northwestern University

Evanston, IL

ACKNOWLEDGEMENTS

Thank you to all those who have helped me during my PhD pursuits. Special thanks to Duane Goodner who showed me how to operate the X15A beamline and to Dr. Kai Zhang for getting me started in polyelectrolyte adsorption experiments. Special thanks to Prof. Monica Olvera and Hao Cheng for their assistance in the preparation in Hg-poly(U) and theoretical interpretation of the XSW adsorption observations. Thanks to my fellow group members Anthony Escuadro, Drs. John Okasinski, Chang-Yong Kim, Don Walko, Zhan Zhang and Hua Jin for their assistance in synchrotron experiments. Special thanks to Dr. Chian Liu for manufacturing the excellent LSM X-ray mirrors. Thanks to Dr. Rich Gurney and Craig Schwartz for their assistance in the preparation of metal phosphonate sample films. Thanks to Drs. Zhong Zhong (BNL), John Quintana and Denis Keane (DND-CAT/APS), and Tien-Lin Lee (ESRF) for there assistance in synchrotron experiments. I would also like to thank Prof. Sonbinh Nguyen and Prof. Joseph Hupp for their collaboration in the metal phosphonate film study. I would like to thank Prof. Kenneth Shull, Prof. Alfonso Mondragon and Professor Monica Olvera de la Cruz for serving on my thesis defense committee.

I owe a great debt of gratitude to Prof. Michael Bedzyk who taught me the very exciting XSW method and showed me how to do good science in general. I am especially grateful for the flexibility and patience he has shown towards me.

Lastly, I would like to thank my father-in-law, Dr. Martin Harrow, for his tireless encouragement and advice and my wife Jean and children Natasha, Daniel and Laura for there support and patience while I asked them to endure extra hardship that allowed me to pursue my doctorate.

TABLE OF CONTENTS

LIST OF TABLES ix

LIST OF FIGURES x

Chapter 1 Introduction 1

Chapter 2 Theory and Modeling Details for Long-Period XSW Analysis 6
2.1 Introduction 6
2.2 Theoretical Treatment 11
2.2.1 Multilayer Recursion Formulation 11
2.2.2 Implementation of the Recursion Formula 14
2.2.3 The SUGOM XSW Data Processing Graphical User Interface 15
2.3 Reflectivity Modeling and E-Field Intensity Computation 16
2.4 Atomic Distribution Modeling 24

Chapter 3 Experimental Details 25
3.1. X-ray Setups 25
3.1.1 NSLS X15A Experimental Setup 25
3.1.2. ESRF ID32 Experimental Setup 27
3.1.3 APS 5BMD Experimental Setup 28
3.1.4. NU X-ray Lab Experimental Setup 29
3.2. Data Collection and Processing 29
3.2.1. SUGOM – Experimental Yield Reduction GUI 29
3.2.2 X-ray Fluorescence Emission Sensitivity Factor Calculation 32
3.3 Liquid-Solid Interface Cell 33
3.4. Sample Preparation 36
3.4.1. LSM Substrate Fabrication 36

Chapter 4 XSW Study of Metal Phosphonate Multilayer Thin Films 39
4.1 Introduction 39
4.1.1 Early Work in Metal-Phosphonate Thin Films 40

4.1.2 Recent Work 43
4.2 Experimental Strategy and Sample Preparation 43
4.2.1 Sample Preparation 48
4.3 Results and Discussion of Metal-Phosphonate Films 49
4.3.1 XRR and XRF Results and Discussion of Samples A-D 50
4.3.2 XSW Results and Discussion of Samples A1 and A8 54
4.3.3 XRR and XRF Measurements F- and H-series 64
4.3.4 XSW Results for G- and I-series 65
4.3.5 Discussion for the F-, G-, H-, and I-series 94
4.3.6 Primer Layer Characterization 99
4.3.7 Metal Phosphonate Coordination Chemistry 101
4.3.8 Performance of the Large d-Spacing LSMs 102
4.4 Conclusions 106

Chapter 5 Hg-poly(U) Adsorption to Charged Surfaces 108
5.1 Introduction 108
5.1.1 DNA Condensation in Bulk Solution 109
5.1.2 Adsorption of Polyelectrolytes to Positively Charged Surfaces 112
5.1.3 Adsorption of Polyelectrolytes to Negatively Charged Surfaces 113
5.1.4 Strategy for In-Situ Measurement of Hg-poly(U) Adsorption 114
5.1.5 Charging Behavior of the Planar SiO_2 Surface 117
5.2 Experimental Details 118
5.2.1 Mercuration of Polyuridylic Acid 118
5.2.2 Sample Preparation 119
5.2.3 Ex-situ XSW Measurements 121
5.2.4 In-situ XSW Measurements 121
5.3 Ex-Situ XSW Hg-poly(U) Adsorption Results 122
5.3.1 Adsorption of Hg-poly(U) to an Amine-Terminated Surface 122
5.3.2 Adsorption of Hg-poly(U) to a Zr-Terminated Surface 125
5.4 In-Situ XSW Zn and Hg-poly(U) Adsorption Results 128
5.4.1 In-situ Adsorption of Zn2+ to an OH Surface 131
5.4.2 Zn^{2+} Adsorption to a PO^3 Surface 134
5.4.3 Hg-poly(U) Adsorption to an OH Surface 136
5.4.4 Miscellaneous Results from other *In-Situ* Experiments 145

5.5 Discussion 147
5.5.1 Zn Adsorption to a PO3 Terminated Surface 147
5.5.2 Zn Adsorption to an OH Terminated Surface 148
5.5.3 Adsorption of Hg-poly(U)/Zn to an OH Terminated Surface 149
5.6 Conclusions 154

Chapter 6 Summary and Future Work 156
6.1 Thesis Summary 156
6.2 Future Work 158

REFERENCES 160

Appendix A Software Documentation for SUGOM XSW Analysis Program 170

LIST OF TABLES

Table 4.1 XRR and XRF results of sample films C and D 52

Table 4.2 Results from XRR and XRF analysis for the F- and H-series 68

Table 4.3 XSW and XRF results for the G- and I-series samples 73

Table 5.1 XSW model parameters for the *in-situ* adsorption 143

Table 5.2 XSW ICP_AES analysis results 145

Table 5.3 Results from miscellaneous additional experiments 146

LIST OF FIGURES

Figure 2.1 Conceptual diagram of the XSW principle 7

Figure 2.2 Comparison of grazing angle XSW methods 9

Figure 2.3 Simple model fit for the 15 layer-pair Si/Mo LSM 17

Figure 2.4 LSM model fit with graded d-spacing 18

Figure 2.5 Final LSM model fit with graded interfaces 19

Figure 2.6 Comparison of the 18.6 and 21.6 nm LSM designs 23

Figure 3.1 Experimental setup at the NSLS X15A beamline 26

Figure 3.2 Screen shot of the SUGOM graphical user interface program 30

Figure 3.3 Liquid-Solid Interface cell 34

Figure 4.1 Effect of incubation time on Zr/phosphonate layer thickness 41

Figure 4.2 Molecular diagrams of phosphonate molecules 44

Figure 4.3 Layer structure of sample film A8 45

Figure 4.4 Structural diagrams of metal-phosphonate films 46

Figure 4.5 XRR results of sample films C and D 51

Figure 4.6 Sample A8 XSW results 55

Figure 4.7 Electron density profile for sample film A8 56

Figure 4.8 Surface plot of the calculated E-field intensity 57

Figure 4.9 Sample A1 XSW results 62

Figure 4.10 Perspective diagram of porphyrin square molecules 63

Figure 4.11 XRR results of F-Series films 66

Figure 4.12 XRR results of H-Series films 67

Figure 4.13 XRR results for F- and H-series films 69

Figure 4.14 XRR of I2 film from XSW scan 71

Figure 4.15 Typical MCA spectrum for I-series films 72
Figure 4.16 XSW results for film G1 74
Figure 4.17 XSW results for film G2 75
Figure 4.18 XSW results for film G3 76
Figure 4.19 XSW results for film G4 77
Figure 4.20 XSW results for film G6 78
Figure 4.21 XSW results for film G8 79
Figure 4.22 G-series XSW Hf results 80
Figure 4.23 G-series XSW Zr results 81
Figure 4.24 XSW results for film I1 83
Figure 4.25 XSW results for film I2 84
Figure 4.26 XSW results for film I3 85
Figure 4.27 XSW results for film I4 86
Figure 4.28 XSW results for film I6 87
Figure 4.29 XSW results for film I8 88
Figure 4.30 I-series XSW Hf results 89
Figure 4.31 I-series XSW Zn/Re results 90
Figure 4.32 I-series XSW Zr results 91
Figure 4.33 Modeled atomic heights for G- and I-series 92
Figure 4.34 Atomic coverage of the F-I series films 93
Figure 4.35 Primer Layer Structure 100
Figure 4.36 Alternate models comparison for film I8 103
Figure 4.37 Sensitivity of model to layered vs single slab 104
Figure 4.38 Sensitivity of LSM to sense layered structure 105
Figure 5.1 Spermine concentrations versus DNA concentration 110

Figure 5.2 Adsorption phase diagram of polyelectrolyte chains 111

Figure 5.3 AFM image of adsorption of DNA to DPDAP 113

Figure 5.4 Schematic diagram of Zn2+ mediated Hg-poly(U) adsorption 115

Figure 5.5: MCA Spectrum for Sample A1b 123

Figure 5.6: XSW Results for Sample A1b 124

Figure 5.7: MCA Spectrum for Sample B1a 126

Figure 5.8 XSW results for sample B1a 127

Figure 5.9 Modeling details of in-situ reflectivity 129

Figure 5.10: MCA Spectrum for Sample JL817BOH_A 132

Figure 5.11: In-situ XSW result for 50 mM ZnCl2 placed in contact with an OH terminated LSM/SiO2 substrate. 133

Figure 5.12: Adsorption of Zn to a PO_3 surface 135

Figure 5.13: MCA Spectrum for Sample JL817OH_A 137

Figure 5.14: Hg-poly(U)/Zn Adsorption Time Sequence 138

Figure 5.15: Results from the XSW scan 53 from sample JL817OH_A 139

Figure 5.16: Results from the XSW scan 54 from sample JL817OH_A 140

Figure 5.17: Results from the XSW scan 55 from sample JL817OH_A 141

Figure 5.18: Condensed layer coverages of Zn and Hg as a function of time 142

Figure 5.19: Calculated adsorption for sample JL817OH_A 151

Figure 5.20: Calculated surface charge for sample JL817OH_A 152

Figure 5.21: Calculated divalent metal ion coverage for sample JL817OH_A 153

Chapter 1: Introduction

Nano-engineering is an emerging area scientifically important to both the electronic and biomolecular industries. In order to understand the behavior of structures as their dimensions approach the nanoscale, better characterization tools are a continuing need for today's scientific and technological communities. While many important characterization tools such as scanning probe microscopy, electron microscopy and numerous spectroscopic methods have been adapted or were already well suited for nano-scale objects, additional tools are always welcome. In this thesis the extension of X-ray Standing Wave (XSW) analysis to nanoscale objects is described. The applicability of XSW analysis to nanoscale objects was improved by the development of large d-spacing layered-synthetic-microstructure (LSM) X-ray mirrors whose long-period XSWs provide a probe well suited for characterizing the structure of 0.5-50 nm sized objects. This new extension of the XSW technique was used to analyze the structure of metal phosphonate layer-by-layer assembled thin films and for the *in-situ* study of the polynucleotide adsorption to charged surfaces.

Layer-by-layer assembled mono- and multi-layer thins films are most commonly assembled onto SiO_2 or Au substrates whose surfaces are not atomically flat[1]. In these films, the surface over-layers are typically not in registry with the crystallographic planes of an underlying single crystal so that conventional single crystal XSW analysis is not applicable. Even if atomic registry was present, the large period of the multilayer films, typically 1-2 nm in this thesis, requires longer period

XSWs to determine their structure. In the structural characterization of thin films, the following properties are of interest: (a) chemical structure, (b) atomic or molecular density, (c) thickness and position of each layer in the film, (d) uniformity and size of lateral domains. Functional properties such as photoluminescence, dielectric behavior, porosity, magnetism, electrochemical, and catalytic behavior are aggregate properties which are often closely related to the structural properties. The commonly used characterization techniques are ellipsometry, scanned probe microscopy, and a variety of spectroscopic techniques [2]. In certain instances sufficient ordering exists to allow scanned probe microscopy to resolve ordered domains and the lateral variation thereof. Other less commonly used techniques are X-ray photoelectron spectroscopy for the determination of chemical bonding states and quantification of atomic coverage and various spectroscopic tools (ATR FTIR, SPR, and Raman) to determine various properties that are related to atomic vibration states or electronic transitions. Small angle X-ray scattering methods such as X-ray reflectivity (XRR) and grazing incidence diffraction (GIXRD) are less frequently used methods that provide structural information in the surface normal and lateral dimensions, respectively.

XSW analysis is a highly specialized technique that permits both the atomic distribution and absolute amount of the atoms or molecules within the distribution to be measured[3]. The atomic positions are determined with respect to the X-ray reflecting planes of the substrate. In the most common variety of XSW analysis, the atomic positions are determined with respect to a perfect single crystal lattice. A limitation of any variation of the XSW technique is that the unknown structures should be of the same length scale as the period of the XSW in order to determine

both the position and width of the distribution. Since the period of the XSW is nominally the crystallographic spacing of the X-ray mirror, a synthetic crystal with a much larger d-spacing can be designed with the appropriate length scale for the problem of interest. These synthetic crystals are called layered synthetic microstructures (LSMs) consisting of alternating layers of high and low electron density materials and have been in common use for many years as X-ray and UV optics components[4-8] and as substrates for XSW analysis[9-13]. Previous XSW work however, has incorporated LSMs with relatively small d-spacing (less than 8 nm) and utilized only 1^{st} order Bragg reflection since the higher orders of Bragg reflection were too weak. In this thesis the range of applicability of LSMs is expanded by making very large d-spacing LSMs (18.6-21.6 nm) which provide many orders of Bragg reflection permitting the simultaneous probing of distributions of medium (~ 0.5 nm) and large (~ 50 nm) length scales. The lower limit of this range is determined at the same time by the attainable degree of perfection of the LSM and by the surface roughness of the LSM onto which sample films are constructed. For example, an LSM that provides a 0.2 nm period XSW is of little use if the over-layer sample structures are superposed onto a high (~0.5 nm) surface roughness topography. The XSW period upper level of 50 nm is achieved in the TER low-angle condition. Samples in this thesis were only up to 20 nm in height. Thicker over-layers present a coupled problem in which the XSW within the sample films depend strongly on the films themselves especially at the lower angles but the coupling can be easily handled using a self-consistent modeling procedure. Experimentally, the efficiency of the XSW technique depends on the emission rate of X-ray fluorescence and the efficiency in which these can be collected. In general, the higher energy X-

ray lines of the higher atomic weight atoms (Z ~ 20 or higher) provide the most efficient XSW measurements.

An excellent thin-film system for study by XSW is metal-phosphonate layer-by-layer assembled thin-film architecture. Metal-phosphonate films are ideally suited for study by XSW because they contain metal atoms in layers parallel to the substrate or LSM surface. In addition, several metals can be used interchangeably, namely Hf, and Zr so that one or the other can be used in a single layer to mark a specific location in a multilayer film. In general, thin films do not necessarily contain the heavy atoms required to provide a strong X-ray fluorescence signal. For such cases similar thin films must be made that incorporate heavy atoms as fluorescent markers.

Many systems of biological relevance can be easily made accessible to XSW techniques by attaching suitable heavy-atom markers, such as Se, Br, or Hg, to the biological objects of interest. Further advantage from the XSW technique is made possible by *in-situ* experimentation which is not available in many other methods. In this thesis the adsorption behavior of Hg-labeled polyuridylic acid (Hg-poly(U)) to a negatively charged surface using Zn^{2+} aqua ions is examined. The simultaneous measurement of the position and concentration of both the counterion and biomolecular polyion has never been attempted before and development of this technique will provide highly sought after data for the verification of theoretical treatment of the adsorption process.

This thesis presents the first use of long-period XSW using multiple orders of Bragg reflections from large d-spacing LSMs. The structural analysis of metal-phosphonate layer-by-layer assembled thin films and *in-situ* biomolecular adsorption

whose structural dimensions are in the 0.5-20 nm length scale is demonstrated. In Chapter 2 the theoretical basis for XSW analysis is summarized with emphasis on the special needs arising from the use of large d-spacing LSM X-ray mirrors. In Chapter 3 the details of the experimental setups are provided. In Chapter 4, an XSW structural analysis of a variety of metal-phosphonate layer-by-layer assembled thin films is presented. These films are based on the metal atoms Zr, Hf, Y, Zn, and Re and the metal phosphonate molecules 1,12-dodecanediylbis(phosphonic acid), porphyrin bis(phosphonic acid) and porphyrin square bis(phosphonic acid). In Chapter 5 the study of the adsorption of Hg-poly(U) and Zn to a hydroxyl terminated SiO_2 surface is presented. The study is performed using a liquid-solid interface (LSI) cell providing *in-situ* analysis of the adsorption of Zn and mercurated long-chain polyuridylic acid (poly(U)) from aqueous solution. The XSW analysis of adsorption from Zn-only aqueous solution to hydroxyl and phosphate terminated surfaces is also presented. In addition, an *ex-situ* XSW analysis of adsorption of Hg-poly(U) to positively charged surfaces is presented. In Chapter 6 a summary of this thesis work is given along with recommendations for future work. Appendix A provides detailed documentation for the MATLAB computer programs developed as part of this thesis.

Chapter 2: Theory and Modeling Details for Long-Period XSW Analysis

2.1 Introduction

X-ray standing wave (XSW) analysis is an established method for determining surface over-layer atom distributions with respect to the substrate diffraction planes. The technique has been successfully applied to a variety of systems ranging from sub-angstrom adsorbate position determination with respect to crystal lattices [14, 15] to locating atomic layers in surface over-layers 100 nm above an x-ray mirror surface using total external reflection x-ray standing waves TER-XSW [16]. The method has also been successfully applied to the study of in-situ ion adsorption to planar substrates from liquids [10, 12, 17, 18]. In all cases the basic principle of standing wave analysis is straightforward. An x-ray standing wave is created when an incoming x-ray plane wave interferes with the outgoing x-ray plane wave after being reflected from an x-ray mirror as shown in Figure 2.1. At any given angle of incidence the XSW field consists of planes of equal electric-field (E-field) intensity perpendicular to the scattering vector, $\vec{q} = \vec{k}_R - \vec{k}_o$. As the angle of incidence (θ) is varied, both the phase and amplitude of the sinusoidal E-field intensity vary to produce a very useful characteristic modulation in the x-ray fluorescence emission from heavy atoms located in layers parallel to planes of equal intensity of the E-field. The various ways of reflecting x-rays lead to variations in the XSW method: (a) total-external reflection (TER) [12, 16, 19] (b) dynamical Bragg diffraction from

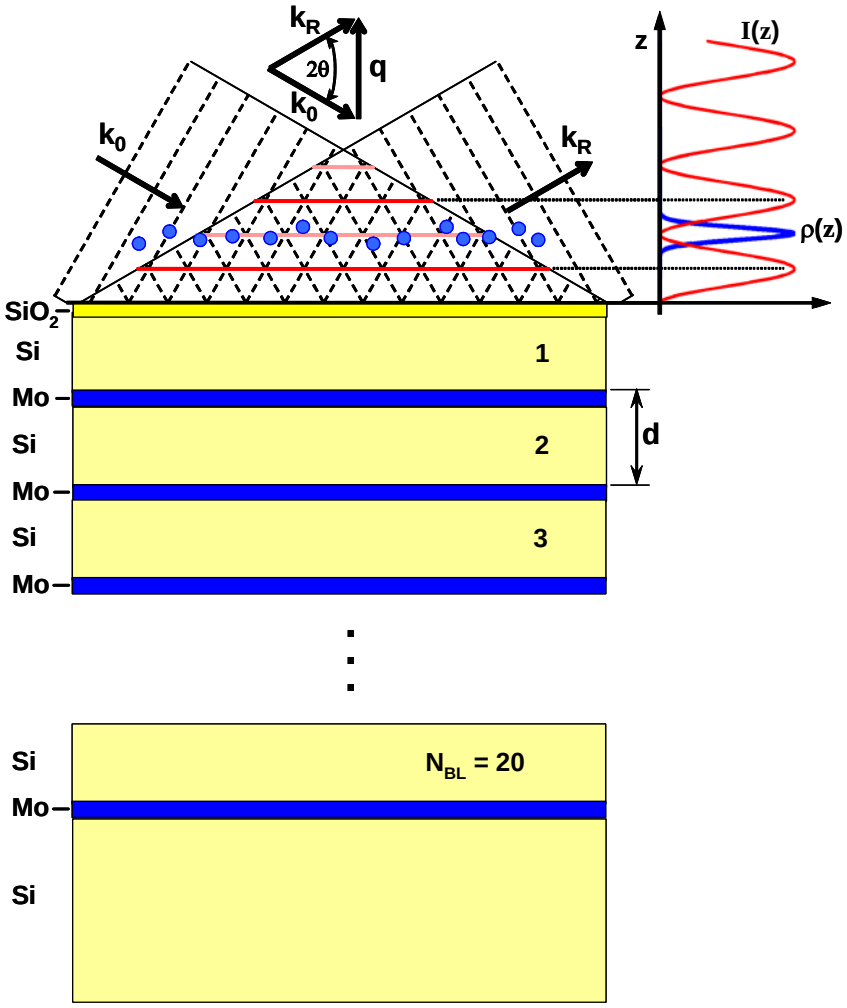

Figure 2.1: Simple model for the N_{BL}=20 layer-pair Si/Mo LSM used in this thesis and a conceptual diagram of the XSW principle. The simplified LSM picture here does not show the graded d-spacing or Nevot-Croce interfacial structure used in the detailed models (see text and Figure 2.5. The inset in the upper right shows the E-field variation (light line) in the **q**-direction for a particular angle theta. The atomic distribution (heavy line) is shown centered on an anti-node position which will produce a minimum XSW fluorescence yield from the atoms

perfect crystal lattices[14, 15, 17, 20, 21] and (c) Bragg diffraction from layered synthetic microstructures (LSMs) [10-13]. The period of the standing wave in a vacuum generated by x-rays of wavelength λ, is $D = \lambda/(2 \sin \theta)$, where 2θ is the angle between the incident ($\vec{k}_o$) and reflected ($\vec{k}_R$) wave vectors. As the incident angle is scanned across a Bragg peak, the phase of the XSW shifts inward by π radians, effectively scanning the XSW nodes in the $-\vec{q}$ direction. When a distribution of atoms $\rho(z)$ is confined to a layer whose thickness is of the same magnitude as the period of the XSW, then a X-ray fluorescence modulation will be produced as the nodal planes pass through the layer. This modulation is a Fourier component of the atomic distribution and contains information about the position and width of the layer.

Recent advances in single crystal XSW have shown that by using many orders of Bragg reflections, a mathematical Fourier inversion technique can be used to reconstruct the 3-dimensional atomic distribution relative to the underlying perfect crystal lattice [22, 23]. In this method each XSW measurement at a Bragg reflection provides a single Fourier component of the unknown atomic distribution. If enough Fourier components can be measured, then Fourier inversion can be performed to obtain a model independent determination of the atomic distribution. For the present case of surface over-layers, the atomic distribution varies in a single dimension only but the process of Fourier inversion is applicable as well.

Previous long-period XSW studies at grazing angles of incidence have only utilized TER [12, 16, 18, 19] or TER plus a single LSM Bragg peak[11,13]. In Figure 2.2 we show for comparison the reflectivity for these previous studies along with the

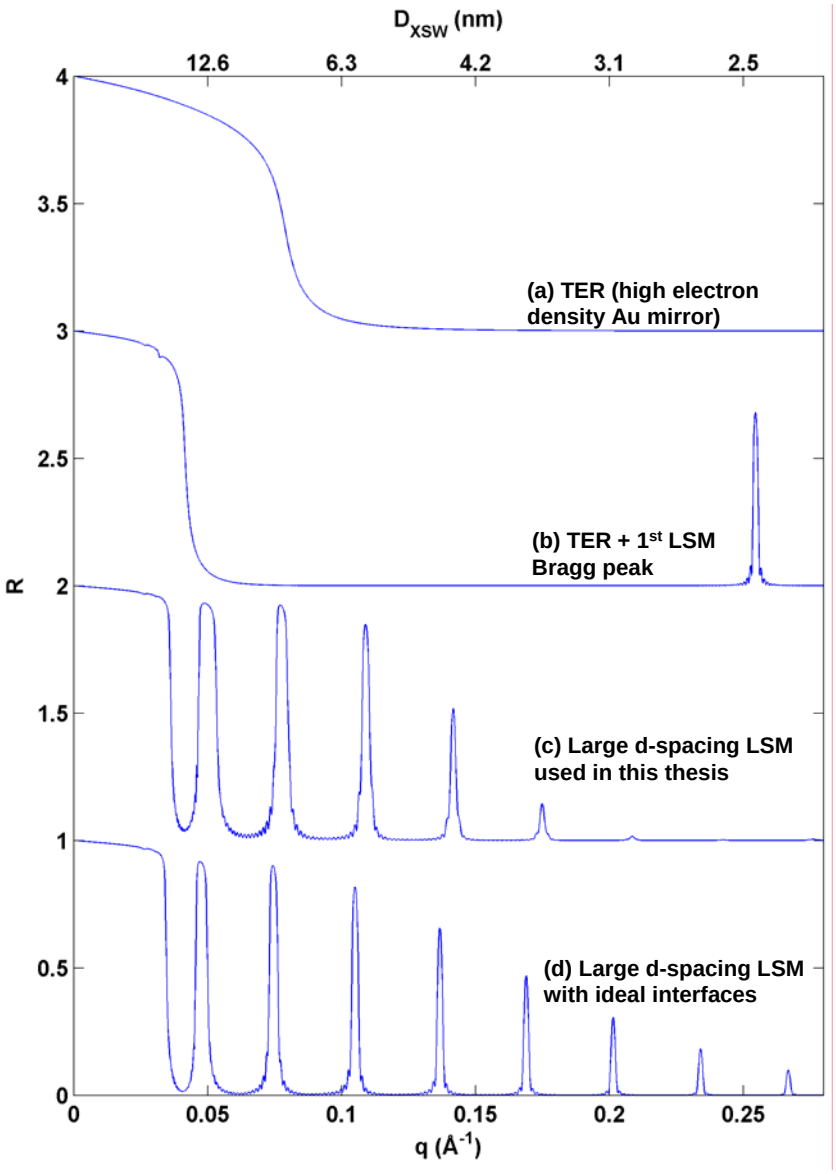

Figure 2.2: Comparison of grazing angle XSW methods. Calculated X-ray specular reflectivity vs. scattering vector magnitude for different X-ray mirror designs. (a) Au mirror (b) 200 layer-pair Si/W LSM with d = 2.5 nm and t_{Si} = 0.75d (c) 20 layer-pair Si/Mo LSM with d = 18.6 nm and t_{Si} = 0.86d (d) same as (c) but with t_{Si} = 0.9d and ideal layers (sharp interfaces and uniform d-spacing)

reflectivity for LSMs from this thesis. In Figure 2.2a we show the reflectivity resulting from a simple Au mirror [16]. The high optical density provides an extended TER region making Au an ideal substrate for studying narrow distributions as high as 100 nm above the Au surface. In Figure 2.2b we show the reflectivity for a 200-layer pair Si/W LSM x-ray mirror with a 2.5 nm LSM period as used in Ref.[11]. For this case both TER and the single Bragg peak were used to probe structure within Langmuir-Blodgett films and where the Bragg peak together with the TER region were able to remove the modulo-d ambiguity that exists if just the TER XSW modulation is used. However, this also requires that the atomic distribution profile be narrow enough to produce a modulation in the 2.5 nm period XSW resulting from the 1^{st} Bragg peak. The LSMs used in this thesis overcome this limitation by using a large d-spacing LSM as shown in Figure 2.2c. The bilayer period d and Si/Mo thickness ratio were adjusted to provide high reflectivity Bragg peaks over as large a range in q as possible. In Figure 2.2c the calculated reflectivity of LSMs used in this thesis is shown which very closely fits the measured reflectivity (see below Fig. 2.5). In Figure 2.2d an ideal Si/Mo LSM is shown which is not realized due to imperfections in the manufacturing process. This calculation demonstrates the potential of large d-spacing LSMs to provide many orders of Bragg reflection over a very large range in q. Improvements in LSM manufacture will be desirable to obtain the many Fourier component needed for a direct-methods Fourier inversion technique. It will also be important to obtain a very high LSM surface quality since high order Bragg reflection with a 2-3 nm d-spacing will only be useful if the surface over-layers are sufficiently parallel and narrow with respect to the XSW period of the highest order Bragg peak. The interfacial roughness inside the LSM, surface roughness and subsequent

parallelism of the surface overlayers each need to be maintained within tolerances dictated by the smallest period XSW under consideration. In this thesis the XSW analysis uses model-dependent determination of atomic distribution profiles in several systems of interest which provides valuable experience for the future use of LSM's for use as direct methods probes.

2.2 Theoretical Treatment

2.2.1 Multilayer Recursion Formulation

The theoretical basis for predicting x-ray standing wave phenomena is based on Parratt's recursion formulation[24] which applies Maxwell's equation to the system described in Figure 2.1 which models an X-ray multilayer mirror by a series of N layers with thickness d_m and indices of refraction $n_m = 1 - \delta_m - i\beta_m$. Detailed and complete derivations have been documented in previous PhD work[25, 26] and journal publications[27, 28].

Below we present a summary derivation for the calculation of the x-ray reflectivity and E-field intensity based on the MS and PhD thesis work of Bommarito[25] which is used for the theoretical prediction of the experimentally measured x-ray reflectivity and x-ray fluorescence yield respectively. The E-field amplitudes of the incident and reflected x-ray plane waves in the m^{th} layer are expressed as:

$$E_m(\vec{r}_m) = E(0)\exp\left[i(\omega t - \vec{k}_m \cdot \vec{r}_m)\right]$$
$$E_m^R(\vec{r}_m) = E(0)\exp\left[i(\omega t - \vec{k}_m^R \cdot \vec{r}_m^R)\right] \qquad (2.1)$$

By applying the interface boundary conditions that require continuity of the tangential components of the electric and magnetic fields and invoking Snell's law the following recursive formulation for predicting the reflectivity from any interface in the layered model system is derived,

$$R_{m-1,m} = \frac{F^{R}_{m-1,m} + R_{m,m+1}\exp\left[-i(2k_1 f_m d_m)\right]}{1 + F^{R}_{m-1,m}\cdot R_{m,m+1}\exp\left[-i(2k_1 f_m d_m)\right]} \qquad (2.2)$$

where

$$F^{R}_{m-1,m} = \frac{f_{m-1} - f_m}{f_{m-1} + f_m} \qquad (2.3)$$

is the Fresnel coefficient and where $f_m = \sqrt{\theta_1^2 - 2\delta_m - 2i\beta_m}$ which follows from Snell's law and uses the small angle approximation $\theta = \sin\theta$. The incident wave vector $k_1 = 2\pi/\lambda$ where λ is the x-ray wavelength in air. In Equation 2.2 and 2.3, the complex quantities $F_{m,m-1}$ and f_m are determined by model parameters (d_m, δ_m, and β_m) and can be easily calculated for each value of the incident angle $\theta = \theta_1$. The recursive calculation begins with the infinitely thick bottom layer (m=N) where there is only a transmitted and no reflected beam; and therefore the reflectivity is zero. Therefore with the substrate as the N^{th} layer we have,

$$R_{N,N+1} = 0 \qquad (2.4)$$

The topmost layer (m = 1) of the system is an air or vacuum layer and the recursive relation Equation 2.2 is repeated until $R_{1,2}$ is found which is the observable x-ray reflectivity of the system. The formulation to this point is all that is needed to compute the reflectivity R experimentally observed in the X-ray Reflectivity (XRR) measurements presented in this thesis.

In order to proceed to x-ray standing wave analysis, we must next compute the E-field in the layers in which the unknown atomic distribution resides. We start with the definition of the reflectivity coefficient,

$$R_{m,m+1} = \frac{E_m^R(d_m)}{E_m(d_m)} \tag{2.5}$$

to obtain the E-field amplitudes at the interface of layer m. For XSW calculations we need the E-field intensity I(q,z), for each angle θ of the experiment and for all interior positions z in the layer m over which the unknown atomic distribution is assumed to reside. After lengthy derivation we obtain,

$$\mathrm{I_m(z_m)} = \left|\mathrm{E_m(0)}\right|^2 \exp(-2\mathrm{k_1 B_m z_m})\left[1+\left|\mathrm{R_{m,m+1}}\right|^2 \exp(-4\mathrm{k_1 B_m z'_m}) + 2\left|\mathrm{R_{m,m+1}}\right|\cos(\phi_m^{\mathrm{R}} - 2\mathrm{k_1 A_m z'_m})\right] \tag{2.6}$$

Where $\mathrm{z'_n = d_n - z_n}$ and $\phi_m^R = \arg(R_{m,m+1})$. In the present nomenclature, $E_m(0)$ and $E_m(d_m)$ refers to the transmitted E-field amplitude at the top and bottom of the m^{th} layer respectively and $E_m(z)$ is thus the E-field amplitude at a location z below the top of the m^{th} layer. $E_m(0)$ is the transmitted E-field amplitude at the m-1,m interface and is computed using a recursion formula for the transmission coefficient similar to Equation 2.2. The terms A_m and B_m were defined as follows:

$$A_m = \frac{1}{\sqrt{2}}\sqrt{(\theta_1^2 - 2\delta_m) + \sqrt{(\theta_1^2 - 2\delta_m)^2 + 4\beta_m^2}} \tag{2.7}$$

$$B_m = \frac{1}{\sqrt{2}}\sqrt{-(\theta_1^2 - 2\delta_m) + \sqrt{(\theta_1^2 - 2\delta_m)^2 + 4\beta_m^2}} \tag{2.8}$$

2.2.2 Implementation of the Recursion Formula.

In order to analyze the XSW data, it was necessary to develop computer algorithms for computing the reflectivity, $R(\theta)$, E-field intensity, $I(\theta,z)$ and X-ray fluorescence yield, $Y(\theta)$. The algorithms were implemented in a number of computing functions written in the MATLAB technical computing environment which are documented in Appendix A. The most important MATLAB function is called xswan2b.m and computes the reflectivity and E-field intensity for a given incident angle θ and position z in layer m. This function is the starting point of the XSW analysis and is based on the Fortran program xswan.f from a previous PhD work[25]. Many new MATLAB functions were developed for the modeling of reflectivity and x-ray fluorescence yield. The most important of these are functions that create layered models from a set of input parameters which was required in order to implement least squares regression analysis.

For the theoretical modeling of reflectivity data, we use the *xswan2b.m* function. We begin with an assumed layered model of the system and adjust the unknown model parameters using least squares regression analysis until a satisfactory prediction of the experimental reflectivity is obtained. Once this is complete, the calculation of the E-field intensity follows by repeatedly invoking *xswan2b.m* over a suitable θ_i, z_i computational grid. Normally we choose θ_i to match the experimental data and for z_i we choose an appropriate grid density that will provide sufficient point density in the geometric scale of the assumed atomic distribution profiles. A typical computational 2D grid had 600 steps in θ and 800 steps in z. In order to permit the calculation of atomic distribution repeatedly for many atomic profiles and several atoms, the E-field intensity, $I(\theta_i,z_i)$, is saved to a

computer file for later retrieval. This is done to avoid repeating the lengthy computation over the 600 x 800 computational grid each time a yield curve is calculated. Once we have computed and stored the E-field intensity $I(\theta,z)$, modeling of the measured fluorescence yield proceeds by assuming a functional form for the unknown atomic distribution. For example, the most common functional form is the Gaussian profile centered at z_0 with Gaussian width σ. The theoretical fluorescence yield is then calculated using the following integral,

$$Yield(\theta) = \int \rho(z) I(\theta, z) e^{-\mu z / \sin\alpha} \, dz \qquad (2.9)$$

where $\rho(z)$ is the unknown atomic distribution. The attenuation factor in the integrand accounts for the attenuation of the outgoing fluorescent X-rays. This is an important factor when the fluorescence originates from within the LSM and the fluorescence detector takeoff angle (α) is small or when Kapton and water films are used. Normally, the attenuation term is taken outside the integral since this term is essentially constant for typical atomic distributions $\rho(z)$. Optimization is done by using a least squares minimization of the parameters of the atomic distribution model $\rho(z)$.

2.2.3 The SUGOM XSW Data Processing Graphical User Interface.

Also written were MATLAB functions and a graphical user interface (GUI) program for computation of normalized fluorescence yield and reflectivity from experimental XSW data. This MATLAB GUI named *SUGOM.m*, is a successor to the Macintosh Fortran programs SUGO and parts of SWAN. The functionality of SUGOM includes (a) parsing of the raw XSW 2D data files (XRF MCA channels and reflectivity

vs. angle θ), (b) peak fitting of the x-ray fluorescence spectra at each angle step to extract the total fluorescence counts from the atoms of interest, (c) automatic normalization for XRF detector dead-time effects and incident photon intensity and (d) calculate the measured normalized specular reflectivity. *SUGOM.m* was an essential requirement due to the very large single scan files (600 steps) that could not be handled easily using the original SUGO program.

2.3 Reflectivity Modeling and E-Field Intensity Computation

In order to precisely model the fluorescence yield, the E-field intensity, $I(\theta,z)$ must be accurately predicted. The validity of the $I(\theta,z)$ prediction is premised on the successful prediction of the observed reflectivity. A layered model was used for the LSM which included a sample film. In this thesis samples are prepared as over-layers on (a) bare Si substrates or (b) N_{BL} = 15 or 20 Si/Mo LSM substrates. A layered model is used to represent both LSM and surface over-layers except where the surface over-layers are monolayers coverages of atoms in which case they are not included. A layered model consists of a list of N layers in which we specify the index of refraction $n_m = 1 - \delta_m - i\beta_m$, the layer thickness d_m and an optional Debye-Waller type interface roughness σ_m. The 1^{st} layer in the model is a vacuum layer and the final or N^{th} layer is the Si substrate whose thickness is set high enough to guarantee the zero-reflectivity premise. In the case of the 15-layer pair Si/Mo LSM, the simplest possible model consists of (a) vacuum layer, (b) 15 pairs of Si/Mo bi-layers and (c) Si substrate layer for a total of 32 layers. In Figures 2.3 to 2.5 a comparison of successive model improvements used to model the LSM portion of the system is

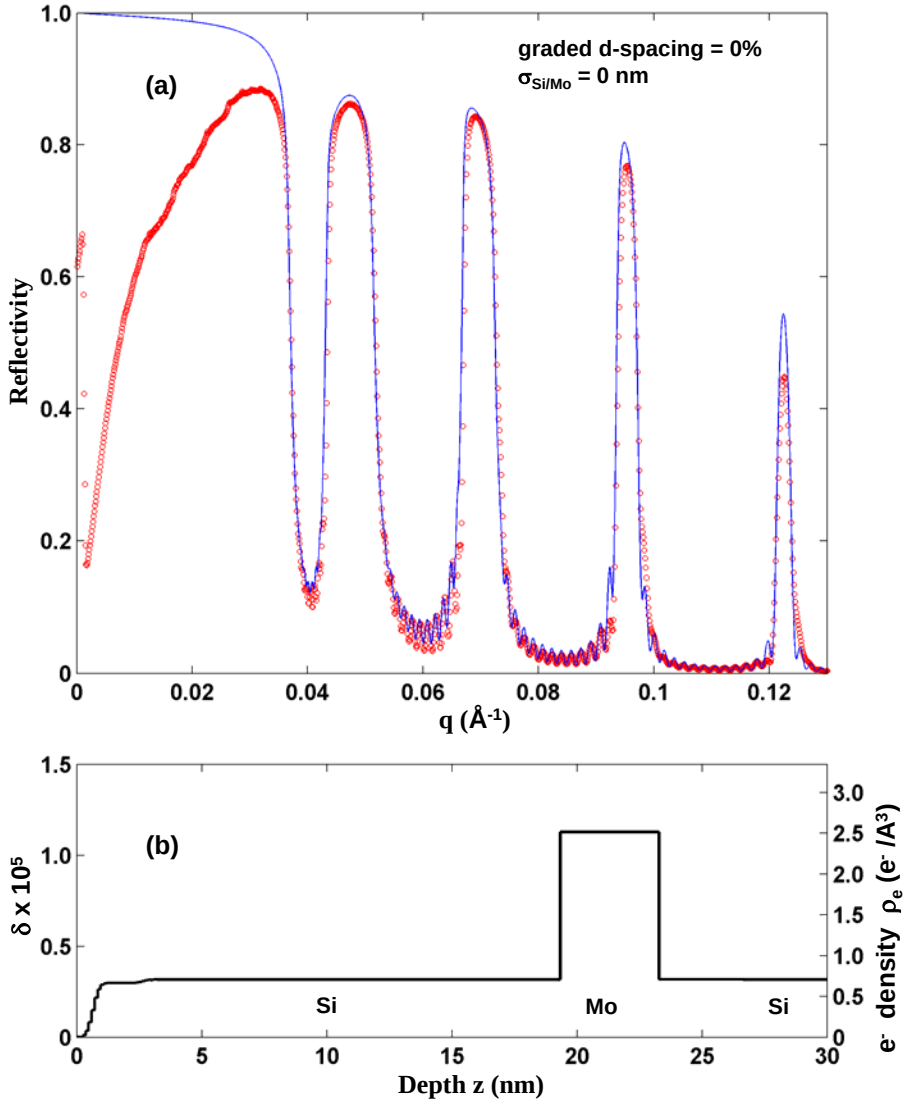

Figure 2.3: Simple model fit for the 15 layer-pair Si/Mo LSM used in the X15A experiments. The model uses ideally sharp interfaces and a uniform d-spacing. (a) Predicted (solid line) and measured (open circles) x-ray reflectivity. (b) electron density profile (graphical equivalent of the layered model). Only the 1st full LSM period is shown. The surface roughness, σ_S, has no noticeable effect on R.

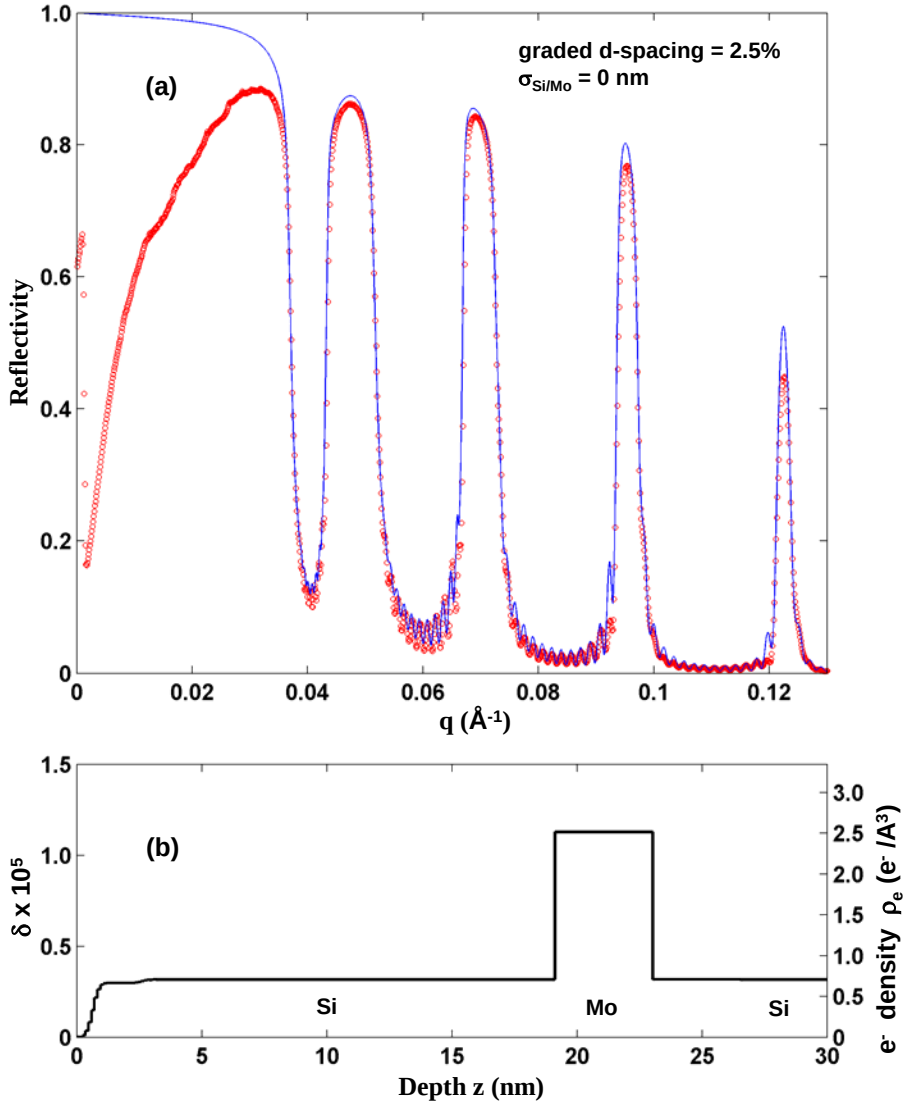

Figure 2.4: LSM model fit for the 15 layer-pair Si/Mo LSM in Figure 2.3 with the addition of a 2.5% graded d-spacing. (a) Predicted (solid line) and measured (open circles) x-ray reflectivity. (b) electron density profile (graphical equivalent of the layered model). Only the 1st full LSM period is shown.

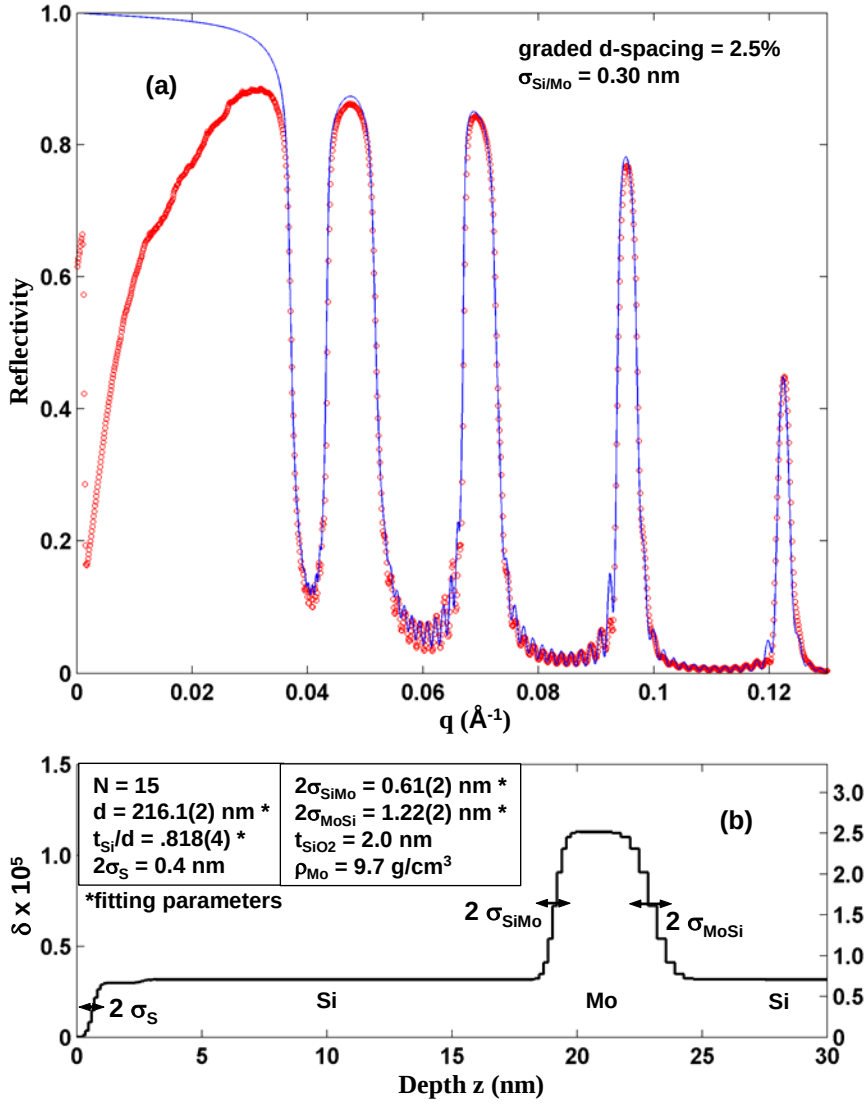

Figure 2.5: Final LSM model fit for the 15 layer-pair Si/Mo LSM in Figure 2.3 with the addition of a 2.5% graded d-spacing and Nevot-Croce interfacial structure. (a) Predicted (solid line) and measured (open circles) x-ray reflectivity. (b) electron density profile (graphical equivalent of the layered model). Only the 1st full LSM period is shown.

presented starting with the simplest model having ideal interfaces and a uniform d-spacing. In Figure 2.3 the best fit to the reflectivity of the N_{BL}=15 LSM using the simplest model is shown along with the electron density profile. It can be seen that the simplest model provides a reasonable fit to the experimental reflectivity. Two additional model features were added to improve the reflectivity fit. In Figures 2.4 and 2.5 the improvement in the predicted reflectivity from the model refinements is shown. In Figure 2.3, the peak reflectivity at the higher Bragg peaks are over-predicted which cannot be corrected by implementing a Debye-Waller type roughness factor without causing a rather poor prediction at the lower order Bragg peaks. The first model refinement is the use of a graded d-spacing correction to account for a small decrease in the sputter deposition rate during the manufacture of the LSMs. A linear decrease of 2.5% from the first layer to the final layer was used. The resulting incremental improvement is shown in Figure 2.4. The main effect in the predicted reflectivity is to cause an angle shift of the Bragg peaks relative to the thickness fringes which primarily is a function of the overall LSM thickness. This shift affects the peak shape as the thickness fringes superpose asymmetrically as compared to the simpler model. The correction is most visible in the right flank of the 3rd Bragg peak in Figures 2.3 and 2.4. Further improvement occurs in the prediction of the peak heights due to the fact that the graded d-spacing results in a less perfect periodicity so the superposition of reflected wave fronts from all the interfaces is lowered. In the second model refinement a Nevot-Croce type treatment [29] is added to account for the inter-diffusion of Si and Mo at the interfaces. Several published reports [30-32] providing TEM micrographs have shown the widths of the interfaces are asymmetric with the Mo on Si interfacial width being about twice the Si

on Mo which is a consequence of sputter deposition properties of the heavier Mo versus Si atoms. The main effect of the Nevot-Croce correction is to reduce the sharpness of the electron density gradient. In implementing the Nevot-Croce interfacial profile which is essentially an error function profile, 10 additional layers were used in the model at each boundary between Si and Mo. Thus the 32 layer model shown in Figure 2.3 and 2.4 increased to a 332 layer model from the additional 20 interface layers added for each bilayer of Si/Mo. Although the published asymmetrical nature of the Mo/Si versus Si/Mo interfaces was implemented here, it was found that the asymmetry could be implemented in the opposite way to give a similar improvement. The main effect of this model refinement was reduction of the electron density gradient. Figure 2.5 show the very good fit resulting from both additional model features.

After implementing the graded d-spacing and Nevot-Croce interfacial structure model refinements, one peculiar deviation remains which is the over-prediction of the height of the first visible thickness fringe on the low-angle flank of the Bragg peaks. This anomaly is most probably due to a more complex variation of electron density over the whole LSM structure and was considered too minor warrant further model refinement. However, throughout this thesis the over-predicted thickness fringe is almost always present and in most cases is carried over to an over-predicted XSW thickness fringe modulation. Some experimentation in model features was attempted and it was found that a simple perturbation of several percent in the thickness of just one layer (perhaps due to an anomaly in sputter deposition conditions) resulted in disruption in the regularity of the thickness fringe

envelope. Although possibly leading to slight further improvements, the model was not further refined.

The discussion demonstrating the LSM model used throughout this thesis referred to 21.6 nm d-spacing LSMs that were used in the first study conducted at the NSLS X15A beamline. Subsequently, the LSM properties were refined to optimize them for XSW purpose. To this end the LSM in Figure 2.2d would have been the best choice but was not attempted because the large interface widths observed in the 21.6 nm LSM suggested that there would have been a complete penetration of Si from both sides of the Mo layers causing a lowering of the peak optical density that is provided by a pure Mo layer. Thus the Mo layer was kept to a minimum thickness of ~2.6 nm to avoid this. The next LSMs were fabricated and the resulting reflectivity compared in Figure 2.6 to the original 21.6 nm LSM. The main improvement is the increase in the peak heights of the higher order Bragg peaks. The primary adjustment parameter is the Si/Mo ratio which affects the Bragg peak at which extinction in Bragg reflectivity occurs. For example, if the d:Mo thickness ratio is 5:1, then the 5^{th} Bragg peak will be extinct. Essentially, by choosing a higher value for the d:Mo ratio, the form-factor envelope that decreases Bragg peak intensity is extended. One can also see why this parameter is important in predicting higher order peak intensity. Fortunately, the position of the critical angle and 1^{st} Bragg peak width are very sensitive to the Si/Mo ratio and so that the conflict in predicting high order peak reflectivity among the interfacial width, Si/Mo ratio and Mo density is avoided.

The preceding discussion of LSM modeling has focused primarily on the Si/Mo layer structure and composition. Consideration of the effects of the oxide of the top

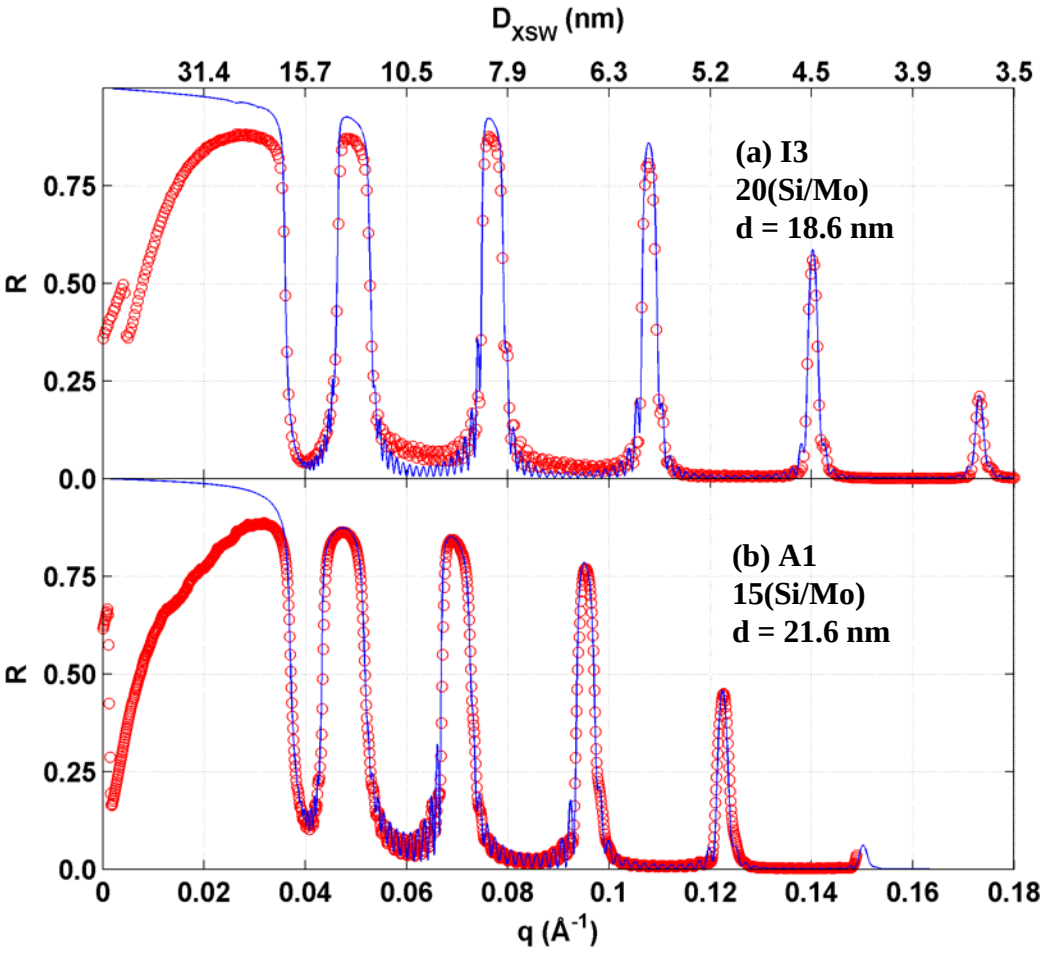

Figure 2.6: Comparison of the (a) 20 layer-pair Si/Mo LSM used in ESRF ID32 experiments with (b) 15 layer-pair Si/Mo LSM used in NSLS X15A experiments. The LSM in (a) was an adjusted design following experience gained from using the LSM in (b). The XSW period, $D_{XSW} = 2\pi/q$, in vacuum or air is shown on the secondary axis on the top.

Si layer and the sample film over-layers must also be given. The main effect of the Si oxide layer is to add uncertainty to the absolute position of the top surface of the LSM with respect to the LSM. The exact value of the oxide layer thickness and subsequently the total thickness of the oxide plus the remainder of the top Si layer is very difficult to determine from the specular reflectivity measurements. The oxide is expected to consume some fraction of the sputter deposited top layer of Si. A value of 2.0 nm was chosen for the oxide thickness, 1.0 nm of which was subtracted from the thickness of the top Si so that the final thickness of the top SiO_2/Si layer was 1.0 nm thicker. Several samples having monolayer coverage of a heavy atom at the SiO_2 surface were consistent with this assumption.

2.4 Atomic Distribution Modeling.

The E-field intensity, $I(\theta,z)$, is calculated for a discrete set of values z_i and θ_j, where i = 1…M and j = 1…N. The values of M and N depend on the measured angular range and predicted range in z of the unknown atomic distribution $\rho(z)$ as well as the minimum Δz_i to properly discretize $\rho(z)$. The integral in Equation 2.7 is performed numerically using the trapezoid rule:

$$Yield = \sum_{i=1}^{N-1}\left[\left(EFI(\theta_j, z_i)\rho(z_i) + EFI(\theta_j, z_{i+1})\rho(z_{i+1})\right)/2\right]\left(z_{i+1} - z_i\right) \qquad (2.8)$$

The choice of Δz is made when $I(\theta,z)$ is computed. Typically Δz = 0.05 nm or greater. Details of the MATLAB computer implementation are provided in Appendix A.

Chapter 3: Experimental Details

3.1 X-ray Setups

XSW experiments were performed at the X15A beamline of the National Synchrotron Light Source (NSLS), Brookhaven National Laboratory and at the ID32 beamline of the European Synchrotron Radiation Facility (ESRF) in Grenoble, France. XRR experiments were performed at the Northwestern University X-ray Facility using the 18-kW rotating anode reflectometer. XRF measurements were performed during XSW measurements and additionally at the 5BMD beamline of the Advanced Photon Source (APS), Argonne National Laboratory.

3.1.1 NSLS X15A Experimental Setup

A schematic diagram of the X15A experimental setup is shown in Figure 3.1a. An unconditioned white beam enters the hutch directly from the synchrotron bending magnet where it is conditioned by a Ge(111) double-crystal monochromator followed by a 0.05-mm -high by 2-mm-wide slit. Ion chambers before and after the incident beam defining slit record the full and reduced size beam intensities. The incident beam flux was 4.0×10^8 p/s/mm^2 at 12.4 keV and 2.0×10^9 p/s/mm^2 at 18.3 keV. The sample was mounted on a specially designed vertical translation stage shown in Figure 3.1b which was mounted to a horizontally configured Huber 2-circle diffractometer. The reflected x-ray intensity was recorded by an ion chamber or photodiode mounted on the 2θ arm which also had guard and detector slits for

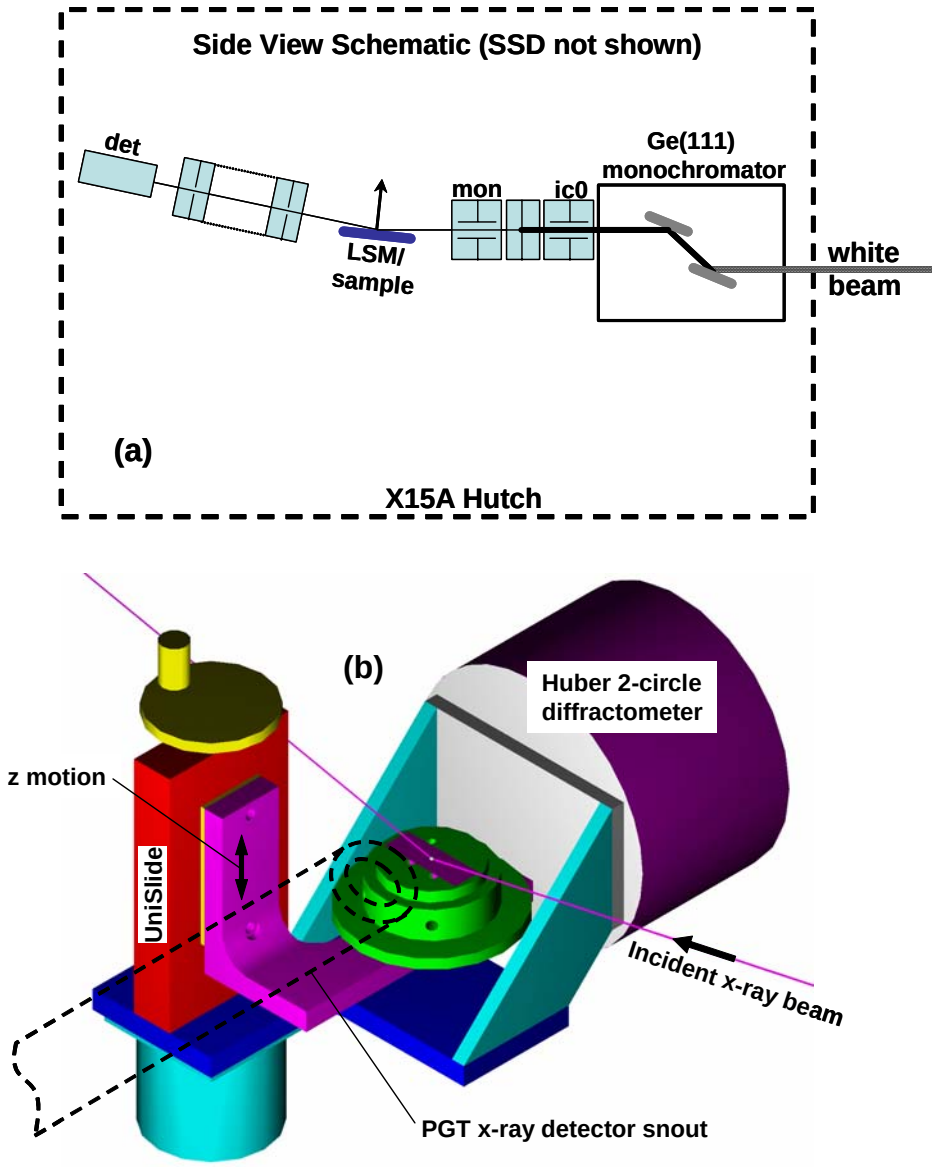

Figure 3.1: Experimental setup at NSLS X15A beamline. (a) beamline layout showing white radiation entering the experiemental hutch from right. (b) custom stage for providing vertical positioning of sample with respect to the center of rotation or beam. Shown with a liquid-solid interface cell.

shielding stray radiation. An PGT energy dispersive Si(Li) solid-state detector was used with a Tennelec TC244 spectroscopic amplifier and an Oxford PCA3 computer board multi-channel-analyzer (MCA) to collect x-ray fluorescence spectra at each angle step of the scan. A Berkely Nucleonics random pulse generator of constant average input pulse frequency was used for dead-time correction. A Sr implanted standard having an RBS calibrated coverage of 10.0 Sr/nm^2 was used to determine the absolute coverages of Hf, Zr, Zn, Re and Hg. At E_γ = 18.3 keV the atomic x-ray fluorescence sensitivity factors [33] for Zn Kα, Y Kα, Zr Kα, Hf Lα and Re Lα relative to Sr Kα are 0.330, 1.11, 1.23, 0.352 and 0.497, respectively. A nitrogen gas purged polypropylene chamber was used to protect the samples from air exposure during all measurements.

3.1.2. ESRF ID32 Experimental Setup

The ID32 beamline at ESRF has a 0.77 x 0.05 mm^2 (HxV) FWHM source size with a divergence of 0.028 x 0.004 mrad^2 (HxV) FWHM with two undulators available for the production of a high flux ($7x10^{14}$ ph s^{-1} mm^{-2}) beam. The incident beam was conditioned by a double-crystal Si(111) monochromator which has a cryogenically cooled first crystal. The second crystal has the ability to focus horizontally but this feature was not used so the beam size at the diffractometer was V x H = 400x800 μm^2 which was reduced in size by a 20-μm -high by 1.0-mm-wide slit so that the full beam width was used at all times and was reduced in the vertical direction only. Knife edge scans measured the actual vertical size FWHM to be 15 μm. The incident flux on the sample was $1.5x10^{11}$ p/s at 14.3 keV and $1.8x10^{11}$ p/s at 12.4 keV. Vertical and horizontal positioning of the sample was done by a Huber tower which

also provided the θ motion using the phi arc of the Huber tower. The reflectivity and fluorescence data was simultaneously collected in a θ-2θ (chi-gamma at the ID32 beamline) scan covering the range of TER through the first four Bragg peaks of the LSM mirrors used in each sample (theta (chi) = 0.0 to 0.6 deg). MCA x-ray fluorescence spectra were collected at each angle step of the scan using a Canberra 8715ADC multi channel analyzer with a high count-rate RONTEC Si-drift diode solid-state detector with a 5 mm^2 area. The x-ray detector dead-time was measured using a hardware counter from the Canberra MCA for the input count-rate and using the totalized MCA spectrum counts for the output count-rate. The dead-time correction method was verified by taking two scans on the same sample with a small and large incident beam. A nitrogen gas purged polypropylene chamber was used to protect the sample from air exposure during all measurements. An As implanted with an RBS calibrated coverage of 10.4 As/nm^2 was used determine atomic coverage of Hf, Zr, Zn, Re, and Hg. The absolute coverage calculation also required an additional correction for the fluorescence detector whose detector element is only 300 μm thick so that the detector efficiency for Zr Kα x-rays is 0.44 compared to 0.99 for Hf Lα for example.

3.1.3 APS 5BMD Experimental Setup

XRF measurements were performed at the 5BMD bending magnet beamline of the Advanced Photon Source, Argonne National Laboratory. Incident x-rays of 18.5 keV energy were provided by a Si(111) monochromator. X-ray fluorescence from the samples was collected using an Ortec IGLET Ge fluorescence detector and an XIA DXP digital signal processing system which also provides all the necessary data

channels for dead-time correction. An ion chamber after the defining slits was used as the incident x-ray flux monitor. Samples were placed at a glancing angle of θ = 0.5^{o} and fluorescence was collected for 6 minutes. The long counting time was required due to the relatively low flux of a bending magnet beamline. An As implanted standard that had an RBS calibrated coverage of 32 As/nm^{2} was used in the same geometry to provide a reference atomic coverage. Atomic coverages of the unknown atoms was determine by referring to the As coverages using calculated fluorescence emission sensitivity factors[33].

3.1.4. NU X-ray Lab Experimental Setup

Northwestern University X-ray Facility using Cu Kα (8.04 keV) X-rays from a rotating anode vertical line source coupled to an OSMIC parabolic, graded d-spacing, collimating, multilayer mirror, followed by a 2-circle diffractometer. The beam size was 0.10-mm-wide by 10-mm-high. The incident flux was 1x10^{8} p/s. The instrumental resolution was Δq = 5x10^{-3} Å^{-1}. The XRR data from the NaI detector was dead-time corrected and background subtracted.

3.2 Data Collection and Processing

3.2.1. SUGOM – Experimental Yield Reduction GUI

A special requirement created by the use of the large d-spacing LSMs is a way to handle the very large scan size which was as high as 600 angle steps, each step having a 512-2048 channel MCA spectrum and as well as all the normal motor angle and counter data. The predecessor programs which performed the XSW data analysis

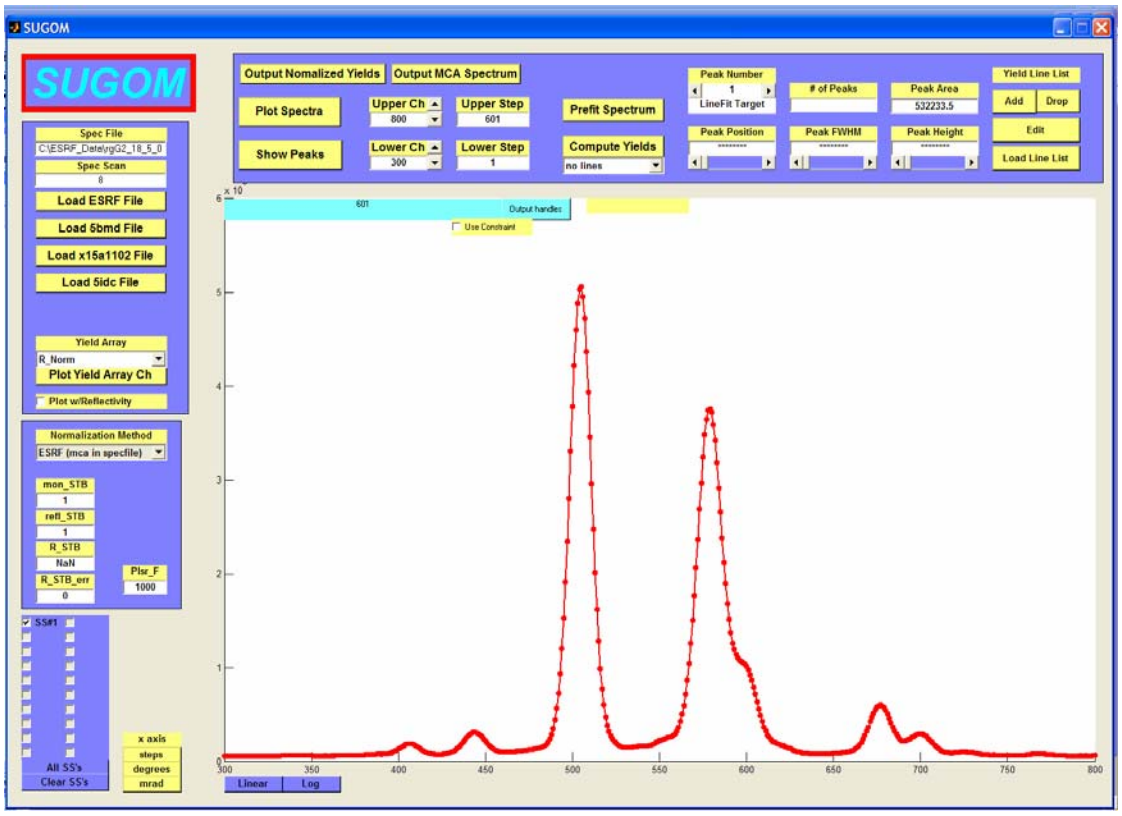

Figure 3.2: Screen shot of the SUGOM graphical user interface program for analyzing XSW data. The program is written in the MATLAB computing environment.

were the Macintosh Fortran programs SUGO and SWAN. The SUGO program was used to parse the XSW data files and perform peak fitting of x-ray peaks in the MCA files and produced individual output files for the net counts in each XRF peak or counter channel as a function of angle. The SWAN program is used to performed file arithmetic to calculate the normalized fluorescent yield. It was found to be advantageous to write an updated data reduction program to handle the larger number of steps and to integrate the functions of the SUGO and SWAN programs in a

single program. *SUGOM.m* was written in the MATLAB computing environment for this purpose. This program can take arbitrarily large 2D files (600 angle steps x 2048 MCA channel scans was the largest used in this thesis) and automatically perform all normalization operations including error reporting. Atomic yield curves from as many as ten x-ray lines can be fit and stored during one fitting operation. The SUGOM features a graphical user interface to perform file loading, peak fitting and normalized fluorescence yield output reporting. A screen shot of the SUGOM graphical interface is shown in Figure 3.3. The main features of the SUGOM program are:

- A parser to convert SPEC data files into a standard fixed internal data structure called *yield_array*. Beamline specific differences in SPEC macro preferences and detector configurations are written in the parser functions. The X15A, ESRF, and 5BMD each required a modified parser. At ESRF, the parser was written in about 4 hours so the task is not too bad after some practice.
- A file loading program allows the user to navigate to the desired files for input. The file loader finishes by calling the standard display routines which display the angle integrated spectrum for all channels collected.
- The peak fitting interface is a user friendly graphical fitting program that allows initial peak estimates to be made by mouse-clicking on the display and adjusting the appropriate slider controls. A predefined file of x-ray line labels is used to associate x-ray peaks with specific atomic lines. A “Prefit Spectrum” button invokes a free-parameter fit of the initial user guess. The “Calculate Yields” button invokes the fitting routine for each step in the selected step

range after fixing the position and widths of the peaks. Special functions are built in to SUGOM which allow the user to program special fitting constraints. For example, the Zn Kβ position, width and height can be specified to be a function of the Zn Kα peak parameters.

- Once fitting is complete, the "Output Normalized Yields" button writes an output text file that contains all of the input columns from the parser along with the computed live-time-fraction, reflectivity, raw and normalized fluorescence yield. Each output variable is reported along with its error. The x-ray reflectivity requires user input of the straight through beam detector and monitor counts input in the SUGOM graphical interface. Another output feature allows the user to output the current MCA spectrum as a text file.

Several features still not implemented in SUGOM which would be very useful are (a) the ability to select arbitrary baseline ranges (b) the ability to input channel to energy calibration values and thus display the x-ray spectrum on an energy axis.

3.2.2 X-ray Fluorescence Emission Sensitivity Factor Calculation. Initially, the NRLXRF program was used to calculate the relative fluorescent x-ray emission rates or sensitivity factors. However, it was discovered that this program contains an error in the calculation of L lines of the heavier elements. For example, Hf Lα is over-predicted by a factor of 2. Subsequently, the work of Puri et. al. [33] found and used to compute the sensitivity factors. This recent work provides an updated set of tabulated x-ray fluorescence cross sections taking into account the most recent experimental and theoretical developments as of 1995. The tabulated values provide x-ray fluorescence cross sections for the K_i (i= α,β) for z = 13 to 92 and L_k (k = *l*, α,

β and γ) for z = 35 to 92. The L x-ray cross sections are only tabulated above the L1 edge. The Lα cross sections result from the L_1-$M_{4,5}$ transitions so that the tabulated values are for the sum of $L\alpha_1$ and $L\alpha_2$. The Lβ cross sections result from the L_1-$M_{2,3,}$ L_2-M_4, L_3-$N_{1,4,5}$, $O_{1,4,5}$ and P_1 transitions so that Lβ is the sum of $L\beta_1$ and $L\beta_2$. Tables are provided which are essentially lookup tables for the x-ray cross sections as a function of energy. A logarithmic interpolation procedure is provided for obtaining intermediate values. In order to calculate the x-ray cross section, σ_i (i = Kα, Kβ, L*l*, Lα, and Lγ), at intermediate energies, the following interpolation formula is provided,

$$\sigma_i(E) = \sigma_i(E_2)(E/E_2)^b$$

where

$$b = \frac{\log(\sigma_i(E_2)) - \log(\sigma_i(E_1))}{\log(E_2) - \log(E_1)}$$

The process is a simple one of looking up the values of the cross-section for two values of E spanning the desired energy and using the above interpolation formula.

3.3. Liquid-Solid Interface Cell

Experiments of ion and bio-molecular adsorption require the use a Liquid-Solid Interface cell to maintain a liquid contact to the sample surface and at the same time allow XSW measurement. The design of the LSI cell for experiments in this thesis was adapted from previous designs made by Dr. Z. Zhang and others before him. A photograph of the LSI as used in the ESRF ID32 in-situ experiments is shown in Figure 3.3a and a description of the operation of the cell follows below. The primary modification of the present cell design is the addition of an o-ring on the rounded corner of the top face of the cell as the sealing O-ring with the lower o-ring

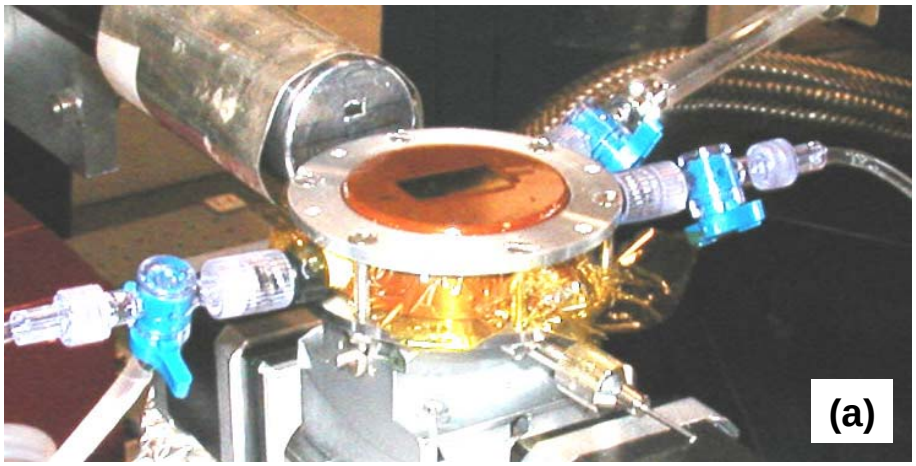

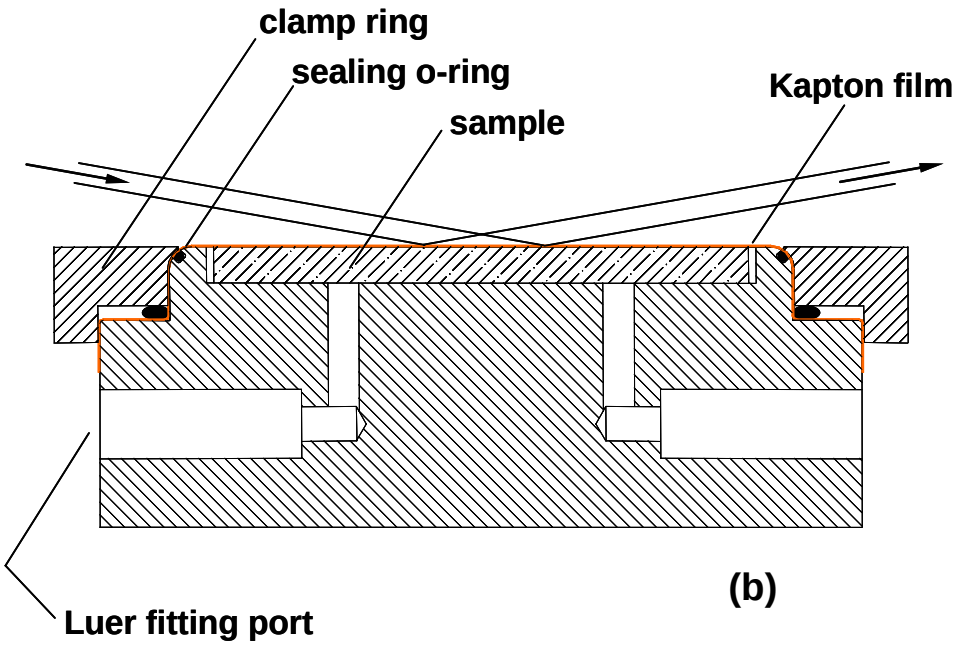

Figure 3.3: Liquid-Solid Interface (LSI) cell setup at the ESRF ID32 beamline.(a) photo showing the LSI cell with Rontec fluorescence detector in the background.(b) CAD drawing showing the sealing detail of the modified cell design.

serving to stretch the Kapton downward as the Al clamping ring is drawn down by screws and presses the Kapton to the upper sealing o-ring. The cross-sectional CAD drawing in Figure 3.3b shows this detail.

Figure 3.3a is a photograph of the liquid-solid interface cell used for the in-situ XSW measurements. The shell is machined from Vespel™(a polyimide), the x-ray window on top of the cell is a 7 μm Kapton ™ film sealed by Viton™ o-rings. Three fluidic ports are used for the injection and withdrawal of test solutions. A N_2 filled purge chamber (not shown) with polypropylene windows surrounded the top of the cell to prevent transport of unwanted CO_2 through the slightly permeable Kapton. The procedure for operating the LSI cell is described below for sample JL817OH_A which used a solution that was 50μM $ZnCl_2$ and 25 μM Hg-poly(U). The LSI cell is assembled with a freshly hydroxylated substrate and flushed using 50 ml of Millipore water that was injected into port A and withdrawn from ports B and C leaving a small residual volume (~ 0.2 ml). Next, 50 ml of $ZnCl_2$ solution was flushed back and forth using ports A and B and ejecting a few ml through C. The excess $ZnCl_2$ solution was withdrawn (leaving ~ 0.2 ml) and valves A, B and C were closed. Next 2-3 ml of Hg-poly(U)/$ZnCl_2$ solution was injected through port C and a small amount was used to purge the previous solution past valves A and B. When injected into the LSI cell the test solution inflates the Kapton film to form a 2 ml reservoir of solution over the sample surface. The surface was allowed to incubate in this configuration for 60 min. The solution was then withdrawn back thru Port C and stored for future analysis. Finally a negative pressure was applied and maintained by withdrawing solution thru Port A using the 50 μM $ZnCl_2$ syringe. Upon withdrawing the test solution and applying a negative pressure it took several minutes for the Kapton film to pull down

to the sample surface and thus trap a very thin film of test solution (2-3 μm) above the sample surface. During this process visible light interference fringes could be seen on the sample surface as the film approached its final thickness, indicating that the water thickness varied by less than 0.5 μm across the cm lateral extent of the sample surface. Measurement by XSW followed in the usual way with the X-ray beam passing through the Kapton and water films establishing the X-ray standing wave in the test solution above the substrate surface. The water and Kapton layers refract and partially absorb the incoming and outgoing X-ray beams. This becomes an increasingly significant effect at small angles.

3.4. Sample Preparation

3.4.1. LSM Substrate Fabrication

Metal/phosphonate mono- and multi-layer films were deposited onto polished Si (001) wafers or onto specially prepared Si/Mo multilayer x-ray mirrors having SiO_2 top surfaces. The Si/Mo x-ray mirror multilayers were prepared by the Optics Group of the Advanced Photon Source at Argonne National laboratory. The fabrication was performed using dc magnetron sputtering in a vacuum system pumped by a turbomolecular pump with a base pressure of low 10^{-7} Torr. Two 3-in. diameter sputter guns, 50 cm apart, were deployed facing upward at the bottom side of the chamber, with uniformity-control masks placed on top of the shield cans. Substrates were loaded facing downward on a substrate holder on a transport stage. The transport system is computer controlled and can be synchronized with the sputter gun power suppliers. The substrates moved linearly over each sputter gun during deposition, with the gun turned on and off for each layer growth. The thickness of

each layer of Mo and Si was controlled by the moving speed and the number of passes of the substrates over each gun. The sputter guns were set at a constant current mode, 0.2 A for Mo and 0.5 A for Si, corresponding to a power of ~50 W for Mo and ~205 W for Si during deposition. The depositions were carried out at ambient temperatures and at an Ar pressure of 2.3 mTorr.

Si (001) substrates of 2.5 mm x 12.5 mm x 37.5 mm pieces were cut from pre-polished wafers obtained from Umicore Semiconductor Processing Corp. The surface roughness of the pre-polished wafers was 0.2-0.5 nm rms. They were cleaned by piranha etch (2:1 H_2SO_4:H_2O_2) at 90^oC for 30 minutes followed by copious rinsing in Millipore water. Fifteen Si/Mo bilayers were deposited on to these substrates as described above. The bilayer thickness was d=21.6 nm and the thickness ratio d_{Mo}/d was 0.17. The terminating surface of the sputter deposition was a 17.9 nm thick Si layer which oxidizes in air to provide an SiO_2 surface on which surface functionalization and subsequent metal/phosphonate multilayer growth or adsorption was done. The final thickness of the top Si/SiO2 layer is different in general from the Si thickness in any bilayer due to an increase in thickness due to the oxidation layer.

Due to the small substrate size, the LSM x-ray mirrors produced for this thesis suffered one major drawback due to the use of clamps to hold the small samples in the sputter deposition chamber. Each LSM has a visible 1-2 mm margin along the long edge which shows where the clamps were. Not as obvious is the lateral gradient in the d-spacing caused by a reflection effect of the clamps causing an increase in general of the d-spacing near the clamped edges as compared to the center. The original intent of the small substrates was to minimize the operations to

the LSM substrates after deposition. For example, cutting the LSM substrates from a larger single slab would expose Mo from within the LSMs at the substrate side surfaces. There was concern that the Piranha etch technique used for the over-layer depositions would cause severe attack of the Mo. The final coating in the LSM is Si which provides some protection for the Mo. The lateral gradient was troublesome when movement of the x-ray beam on the sample was required since different Bragg peak pattern would be observed requiring refitting of the LSM substrate model parameters. At the edges of the LSMs close to the clamping stripes, the Bragg patterns could not be modeled as well as in the center. Most experiments were performed in the center of the substrates where we consistently observed Bragg peak patterns that could be fit well with the LSM model described in Chapter 2.3.

Chapter 4: XSW Study of Metal Phosphonate Multilayer Thin Films

4.1 Introduction

The design and evaluation of layer-by-layer assembled thin films critically depends on knowledge of the as-deposited structural properties of the films. In this chapter the use of long period XSW techniques for measuring the structural properties of several varieties of metal-phosphonate thin films by probing the atomic distributions of several different metal atoms simultaneously is described. The long-period X-ray standing waves (XSWs) generated by total external reflection and Bragg diffraction from large d-spacing Si/Mo LSM's provide the ability to simultaneously examine the heavy-atom profiles over length scales varying from 0.5 to 20 nm. The electron density profiles of these films are measured by XRR.

Metal-phosphonate thin-film architectures owe their popularity to the ease of fabrication and the versatility in choice of both the metallic and phosphonate components. The layer-by-layer assembly process relies on the coordination chemistry of phosphonate-terminated molecules and the various transition metal ions. Early efforts focused primarily on the use of Zr metal and alkane bisphosphonic-acids as the phosphonate component and Zr remains the favorite choice for the metal component.

4.1.1 Early Work in Metal-Phosphonate Thin Films

The first report of a metal-phosphonate multilayer film was given by Lee et al [34], where 1,10-decanediylbis(phosphonic acid) and Zr were used to make 1 through 8 layer samples. The crystallographic layer spacing of the solid state compound was reported as 1.73 nm [35]. Ellipsometry was used to measure the layer thickness for samples with 2-8 layers prepared on Si for which an average thickness per layer of 1.70 nm was found. Putvinsky et. al. [36] prepared multilayers using 1,12-dodecanediylbis(phosphonic acid) for which a layer spacing of 1.95 nm/layer was predicted assuming a 35^{o} cant angle while they measured 1.5 nm/layer.

Schilling et al [37] prepared monolayers of various alkane phosphonates. Ellipsometric thickness measurements were found to be consistent with expectation when the organophosphate step was allowed to incubate for approximately 1-3 days. In particular a monolayer of 1,12-dodecanediylbis(phosphonic acid) monolayer gave a thickness of 1.3 nm when a 2 hour incubation time was used but gave 2.1 nm when a 1 day incubation was used. This is very consistent with the previous two studies cited above and suggests that longer incubation times are required for high quality films. Metal-phosphonate multilayers were prepared by Yang et. al. using Zn and Cu divalent species in place of the tetravalent Zr ion[38]. Ellipsometric data from Ref. [38] are shown in Figure 4.1 for the formation of 1,8-octanediylbis(phosphonic acid) (C_8BP)/Zr multilayers for 40 min and 4 hour immersion times for the C_8BP step. The 4 hour immersion time results in 1.34 nm/layer versus 1.358 nm/layer for the bulk solid whereas the 40 min immersion time results in a substantially lower per layer thickness which improves only up to

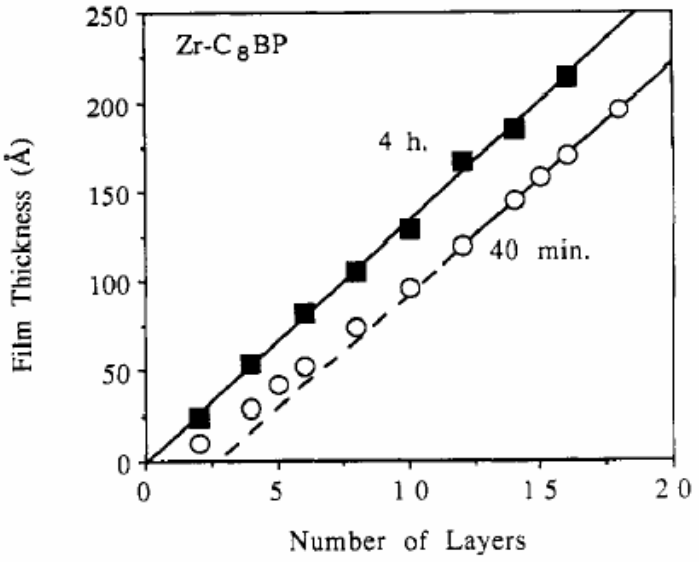

Figure 4.1: Effect of incubation time on Zr/phosphonate layer thickness. This figure shows a typical example of the requirement of longer immersion times to form full dense layers with layer thicknesses close to bulk solid crystallographic spacing. The films were grown on Si wafers and the film thickness was measured elliposometrically. Figure taken from reference [38]

1.28 nm/layer after a induction period of about 10 layers. In sharp contrast, multilayers based on Zn and Cu require only short immersion times of 10 min to ensure fully packed layers. The reason given for the difference in formation times is the lower solubility of Zr vs Zn or Cu phosphonates which allows greater ease of surface ordering of the more soluble Cu and Zn phosphonates. It is suggested that non-aqueous solvents and higher temperatures be used for applying the phosphonate layers in order to promote the growth of crystalline domains by Ostwald ripening.

Zeppenfeld et al [39] prepared multilayers of Zr/1,10-decanediyl-(bisphosphonic acid) (DBPA) on Hf primed substrates. The Hf primer layer preparative conditions were varied as well as the deposition times for the DBPA which was at least 4 hours. Ellipsometric thickness of the average per-layer thickness was found to vary from 1.48 to 2.07 nm while the spacing in the bulk ZrDPA solid was reported to be 1.69 nm. This large range was attributed to the condition of the initial Hf primer step which establishes an initial conformation that depends on the initial surface density of Hf groups which carries forward to all subsequent layers.

In all the above examples of metal-phosphonate films, the assembly involved metal-phosphonate chemical bonding at every step except for the primer step which was some form of covalent attachment. While good ordering in the films using these methods is difficult to achieve, the use of Langmuir-Blodgett (LB) techniques in combination with metal-phosphonate self assembly has been show to produce very well ordered films [40-42] for which Bragg peaks from the films are routinely obtained as a measure of their well-ordered nature. In these examples, the LB technique is used to apply a very well ordered “template” film of phosphonate molecules and then apply the metal layers from aqueous solution in the normal way. In this way, the phosphonate ordering is decoupled from the substrate surface condition. The drawback of this method, however, is that LB films are inherently less robust because the attachment of layers in the LB process is by physisorption.

It is apparent from this brief literature review that the layer thickness and packing density of metal-phosphonate thin films can vary greatly depending on the primer processing conditions, choice of metal and complexity of the phosphonate

molecule and that obtaining high packing densities and crystalline layers is exceptional.

4.1.2 Recent Work

Thin-films based on mono- and multi-layer metal-phosphonate chemistry continue to receive developmental effort primarily by modification of the molecular structure of the phosphonate component [43, 44]. Multifunctional, microporous thin-films with uniform thicknesses and a well-defined porous structure are desirable from a functionalized nano-materials perspective. Microporous thin-film materials could function as molecular sieves,[45-47] frameworks for size-selective heterogeneous catalysis,[48] chemical sensors,[49, 50] and in liquid-junction solar cells,[51] when an appropriate chromophoric molecular framework is chosen. Pillared organic microporous films containing pores that are in the 10-20 Å range were formed[52] by crosslinking zirconium phosphate-like layers with several types of diphosphonic acids. Direct assembly of tetrameric porphyrin arrays has been studied by drop casting from toluene solutions of porphyrin square molecules based on Pt and Pd[53].

4.2 Experimental Strategy and Sample Preparation

In this study, 1,12-dodecandiylbis(phosphonic acid) (DDBPA), porphyrin bis(phosphonic acid) (PBPA) and porphyrin square bis(phosphonic acid) (PSBPA) were used as the phosphonate components, The molecular structures are shown in Figure 4.2. The metals Hf, Zr, and Y were used as the metal component while Zn and Re were present in PSBPA as a chemically inactive metals atoms. Figure 4.3 provides

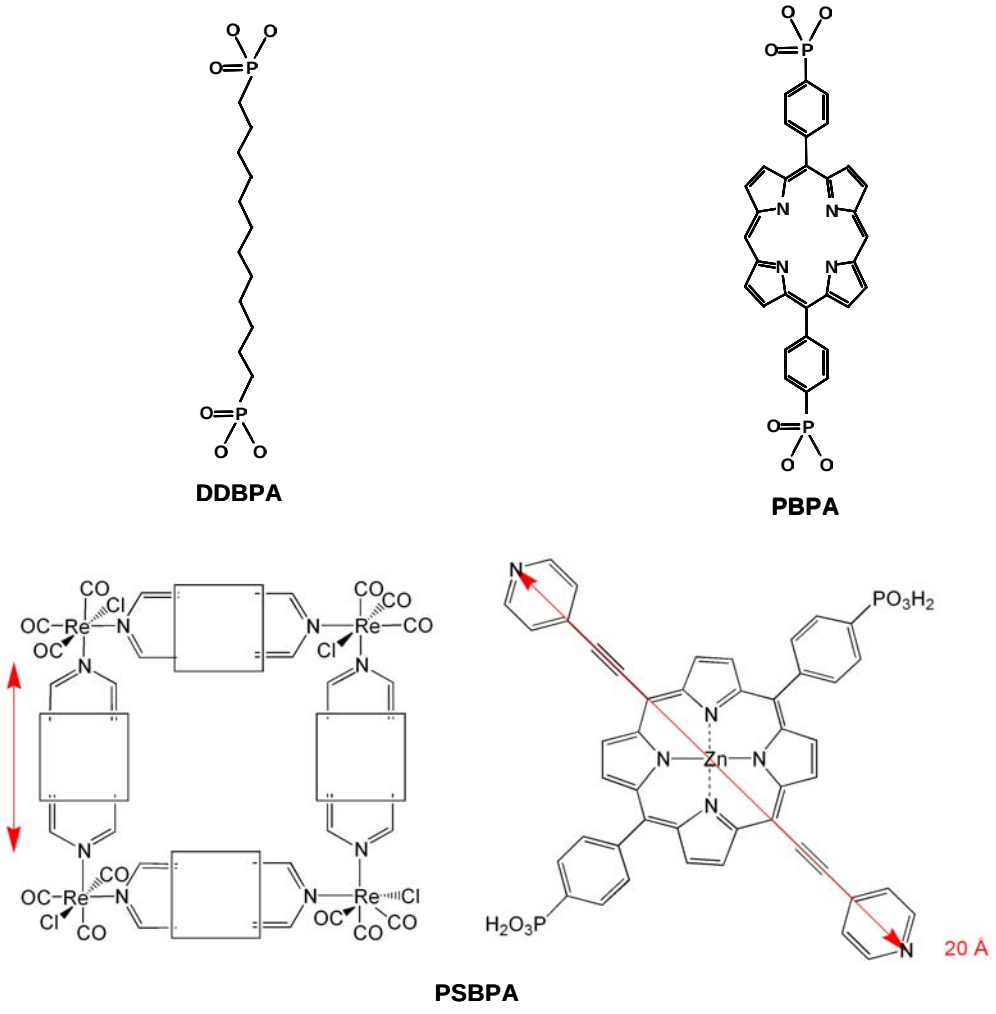

Figure 4.2: Phosphonate molecules. Molecular diagrams of 1,12-dodecandiylbis(phosphonic acid) (DDBPA), porphyrin bis(phosphonic acid) (PBPA) and porphyrin square bis(phosphonic acid) (PSBPA). In the PSBPA molecule, the Zn and Re atoms form a plane that is expected to lie parallel to the sample surface. The four porphyrin constituents are expected to assemble in the films with the PO_3-PO_3 axes lying perpendicular to the plane of the Re atoms and thus perpendicular to the sample surface.

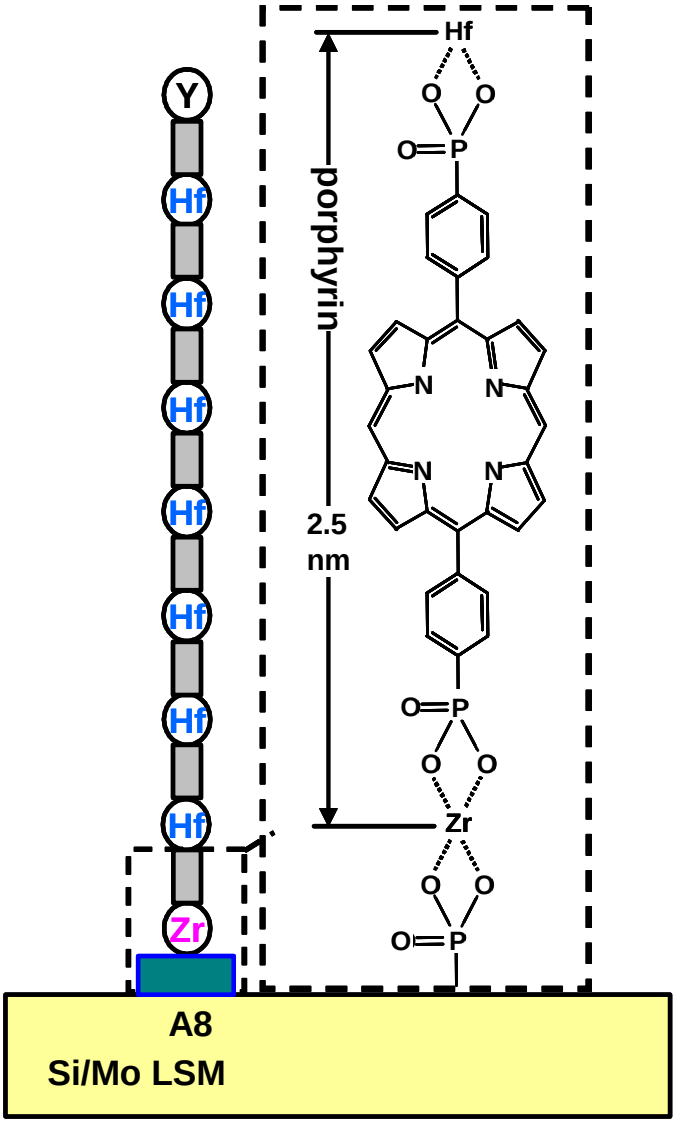

Figure 4.3: Layer structure of sample film A8. This example shows the expected arrangement of metal and phosphonate molecules in the films of this chapter. The diagram show a portion of the assembly chain for films incorporating porphyrin bis(phosphonic acid). The metal-phosphonate linkage is probably more complex but probably no longer than shown. The details of the primer are omitted for simplicity.

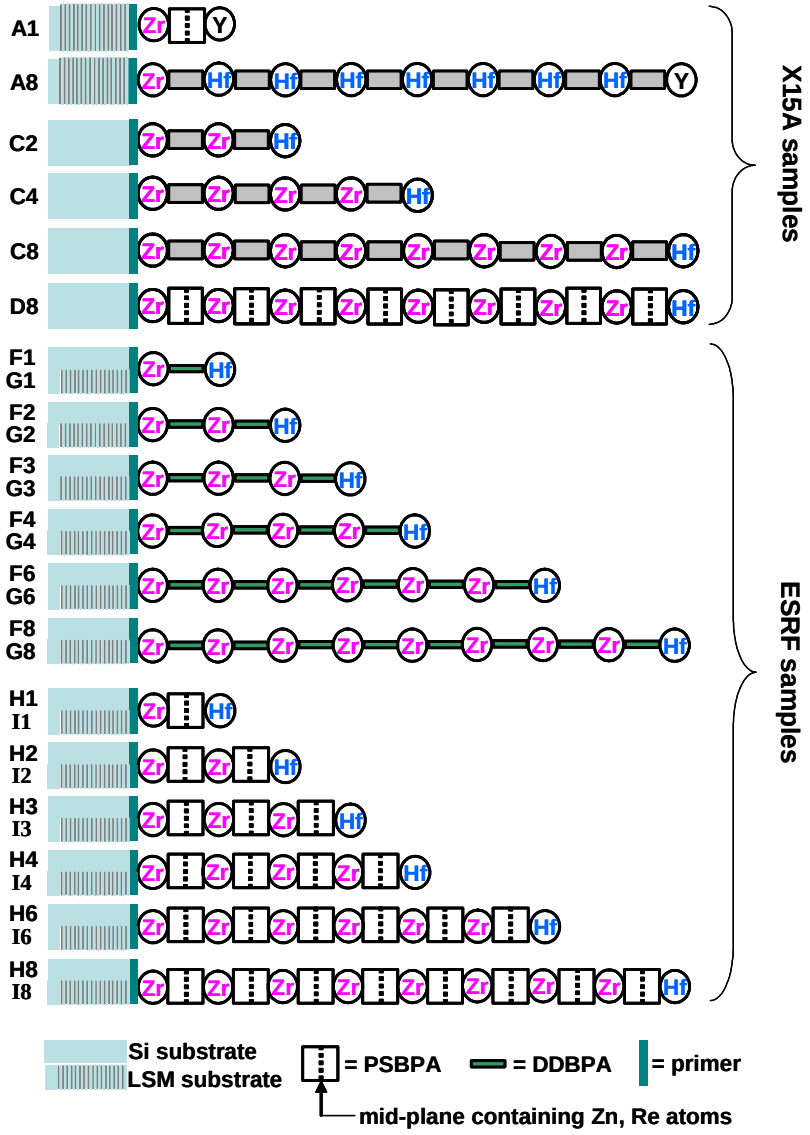

Figure 4.4: Structural diagrams of metal-phosphonate films: Each circle, rectangle, or square represents a layer assembly step by immersion of an LSM or plain Si substrate in a solution of the indicated atom or phosphonate molecule. The primer indicated by the narrow vertical rectangle is a separate sequence of steps.

an idealized picture of the chemical structure of a typical layered sample in this study showing a simple bonding between metal and phosphonate components based on charge balance only. All of the samples in this study are shown schematically in Figure 4.4. In selecting the configuration of the metal-phosphonate multilayer films we use the interchangeability of the different metal atoms to selectively mark strategic locations in the films by substituting a different metal at any given step in the assembly process. The cations Zr^{4+}, Hf^{4+} and Y^{3+} were chosen and assumed to be chemically interchangeable.

In this study the Zn fills the center of the porphyrin squares and Re binds the four “walls” of the square together at the corners (see Figure 4.2 and 4.10). The Zn and Re provide convenient metal markers of the phosphonate component and permit the measurement of both the structure and coverage of the phosphonate component which has never before been done for these types of thin films. This is an especially valuable opportunity to check the assumed ratio between the metal and phosphonate groups.

An initial set of samples (A-D) using PBPA and PSBPA were prepared to evaluate the large d-spacing LSMs which were never used before and to find the optimum metal atom marker scheme. The initial strategy was to use a 3-color scheme, one metal type as the base or primer, a second metal for intermediate layers and a third metal for the final capping metal layer. For all samples Zr was chosen for the primer metal layer. Samples films A1 and A8 were prepared on 21.6 nm d-spacing LSMs. Sample film A1 was prepared using a single layer of PSBPA (containing Zn and Re) followed by an Y capping layer. Sample film A8 used PBPA in an 8-layer sample where Hf was used for all intermediate layers with a final Y

capping layer. The C-series films and sample film D8 were made on bare Si(001) substrates for XRR study where Zr was chosen for all of the metal layers except the final capping layer for which Hf was used. The first XSW experiments were performed at the NSLS/X15A beamline where it was found that Y tended to bind indiscriminately throughout the films while Zr and Hf were found in their expected layer positions. Following the results of the first XSW study which is detailed below, a more extensive study was undertaken using the PSBPA molecule and the much simpler DDBPA molecule using Zr for all metal layers except the last for which Hf was used. The DDBPA alkane phosphonate molecule provided the opportunity to compare an XSW analysis result to previously published structural information. Thus the F-, G-, H-, and I- film series were prepared where the F- and G-series were identical series using DDBPA prepared on Si(001) (XRR) and Si/Mo LSM (XSW) substrates respectively. The H- and I-series were identical series using PSBPA prepared on Si(001) (XRR) and Si/Mo LSM (XSW) substrates respectively. All samples are shown schematically in Figure 4.4.

4.2.1 Sample Preparation

All substrates in this study received an identical primer treatment prior to subsequent layer deposition. The primer chemistry was based on the work of Horne et al.,[54] with slight modifications. In the first step, the substrates were placed in piranha solution (2:1, sulfuric acid: hydrogen peroxide) to remove organic contaminants from the surface and then rinsed with Millipore water (18.2 megohms) and dried under a stream of N_2. **(Caution! This solution can react violently with organics.)** Immediately afterwards, the substrates were immersed in 2 M HCl for 5

min, rinsed with ultrapure-water, dried under a stream of dry N_2, and oven-dried at 80 ^oC for 15 min. The substrates were placed in an 80^oC solution of anhydrous octanol and 3-aminopropyl-trimethoxysilane (APTMS) (100:1 v:v) for 10 min; followed by rinsing with hexanes and ultrapure-water, drying under a stream of dry N_2, and drying in an oven at 80^oC for 30 min. Phosphorylation followed by placing into a mixture of 0.1 M $POCl_3$ and 0.1 M 2,4,6-collidine in anhydrous acetonitrile (ACN), for 1 h. The samples were then heated in warm, dry ACN for 15 min; followed by rinses with ACN and ultrapure-water. The samples were then dried under a stream of dry N_2 and then placed in an aqueous solution of 5 mM $ZrOCl_2 \bullet 8H_2O$ for 2 h, rinsed with ultrapure-water, and dried under a stream of dry N_2. In Figure 4.4 each circle or rectangle represents a single immersion step into an appropriate solution as described below: (1) Porphyrin: 1 mM solution of diphosphonic acid porphyrin in dimethyl sulfoxide (DMSO) for 2 h. (2) Porphyrin Square: 0.0125 mM solution of porphyrin square in DMSO for 2 h. (3) Dodecanediylbis(phosphonic acid): 1 mM in 60% ethanolic solution for 2 hours. (4) Zr: 5 mM $ZrOCl_2 \bullet 8\ H_2O$ for 30 min. (5) Hf: 5 mM $HfOCl_2 \bullet 8\ H_2O$ for 30 min. (6) Y: 5 mM aqueous solution of $Y(NO_3)_3$ for 30 min. Full details of the synthesis and characterization of the porphyrin and porphyrin square molecule are given elsewhere[55].

4.3 Results and Discussion of Metal-Phosphonate Films

XSW and XRF measurements of samples A-D were performed at the NSLS X15A beamline using E_γ = 18.3 keV (λ = 0.674 Å) incident X-rays to excite Zr K, Y K, Zn K, Re L, and Hf L fluorescence. A Sr-implanted standard was used to measure the

atomic coverage. XSW measurements of the G- and I-series films were performed at the ESRF ID32 beamline using E_γ= 18.5 keV (λ = 0.670 Å) incident x-rays to Zr K, Zn K, Re L, and Hf L fluorescence x-ray fluorescence and an As-implanted standard was used to measure the atomic coverage. In addition, XRF coverage measurement of the F-, G- and H-series films was performed at the APS 5BMD beamline using 18.5 keV x-rays to excite Hf, Zn, Re and Zr fluorescence. XRR on sample films C, D, F and H was performed at the Northwestern University X-ray Facility using Cu Kα (8.04 keV) X-rays from the rotating reflectometer. Complete details for all of the experimental setups are provided in Chapter 3.

4.3.1 XRR and XRF Results and Discussion of Samples A-D

Sample films A-D were prepared from either PBPA (films A8, C2, C4, and C8) or PSBPA (films A1 and D8) molecules which share the same porphyrinic phosphonate constituent. If the tilt angle of the porphyrinic constituent is the same in all samples then equal layer thickness will be observed. However, differences in film structure are expected due to the different surface density and tilt angles that the two molecules will adopt. The experimental and calculated reflectivity (XRR) for samples C2, C4, C8 and D8 and are shown in Figure 4.5 with the fit determined parameters listed in Table 4.1. The graded interface modeling procedure, as described in Chapter 3, was used for fitting the observed reflectivity. The layered model consisted of a Si substrate, a 2.0-nm SiO_2 layer for the native oxide, and a single layer for the film. The inset in Figure 4.5 shows the model for film D8. The free fitting parameters were the σ widths of the error function interface profile, σ_{VF} for the air/film interface, σ_{FS} for the film/native oxide interface, t_F for the film

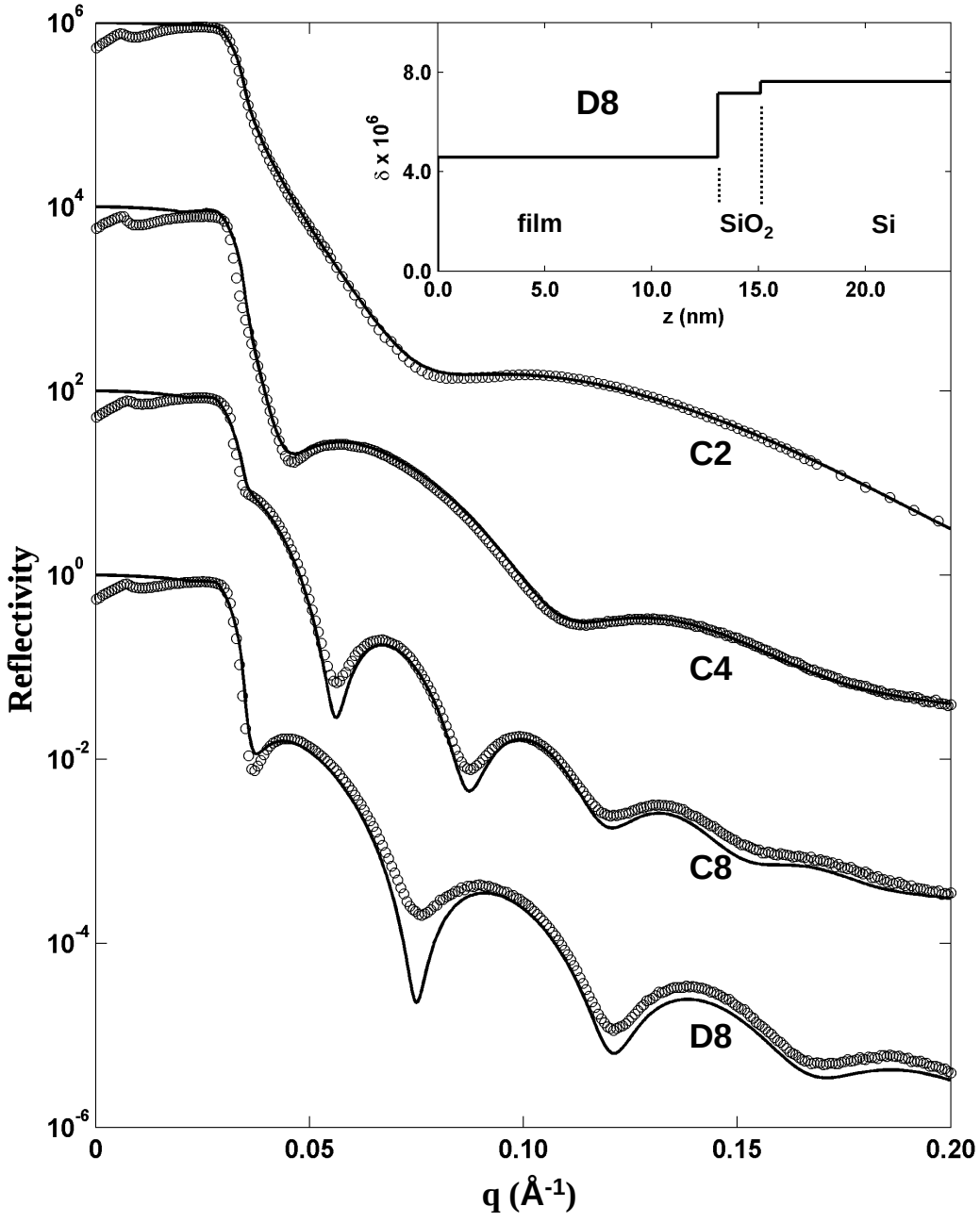

Figure 4.5: XRR results of sample films C and D. Measured (open circles) and calculated (solid line) XRR of the C-series films and film D8. The inset show a layered model of the electron density for sample D8 as an example.

Film	N	ρ_F / ρ_{Si}	$t_{F,e}$ nm	t_F nm	σ_{FS} nm	σ_{VF} nm	Θ_{Zr} nm^{-2}	Θ_{Hf} nm^{-2}	Θ_Y nm^{-2}	$\Theta_{Zn}=\Theta_{Re}$ nm^{-2}
C2	2	0.38(2)	5.5	4.2(1)	0.45(5)	0.8(3)	4.3(2)	3.1(2)	--	--
C4	4	0.50(2)	10.5	8.5(1)	0.25(5)	1.4(3)	9.9(5)	9.8(5)	--	--
C8	8	0.58(2)	20.5	18.6(1)	0.25(5)	1.6(3)	24.6(9)	3.3(2)	--	--
D8	8	0.60(2)	20.5	13.1(1)	0.20(5)	1.3(3)	13.3(7)	3.1(2)	--	2.6(3)
A1	1	--	3.0	--	--	--	1.32(7)	--	0.50(3)	0.05(2)
A8	8	--	20.5	19.0(2)	--	--	1.07(7)	17.7(9)	14.0(8)	--

Table 4.1: XRR and XRF results of sample films C and D. The electron density of the film relative to the Si substrate, ρ_F/ρ_{Si} , the film thickness, t_F , and the Gaussian widths of the film-substrate interface, σ_{FS} , and film-air interface, σ_{VF} , were measured by XRR. The expected film thickness, $t_{F,e}$, is based on a 2.5 nm metal atom-to-metal atom spacing plus 0.5 nm for the primer layer. The measured depth-integrated atomic coverages, Θ_{Zr}, Θ_{Hf} , Θ_Y, Θ_{Zn} and Θ_{Re} , were determined by XRF.

thickness and ρ_F/ρ_{Si} for the ratio of the film to Si electron density. (Where ρ_{Si} = 699 e/nm^3.) The expected film thickness ($t_{F,e}$) is based on the approximation of 0.5 nm for the primer layer plus 2.5 nm per layer based on the fully extended molecular configuration. (See Table 4.1.) For the N = 2, 4 and 8 layer porphyrin films we measure thicknesses (t_F) that are slightly less than the expected (average layer thicknesses of 1.85, 2.0, and 2.26 nm, respectively, versus 2.5 nm), but agree well with an average layer thickness of 2.1 nm obtained previously by a lower precision approach (atomic force microscopy) using micro patterned films.[56] If the smaller

than expected layer thicknesses are indicative solely of tilting of the phosphonate-porphyrin-phosphonate axis away from surface normality (90^o), the average angles would be ca. 48^o, 53^o, and 66^o,respectively.

XRF coverage measurements give Zr atomic densities of 4.3, 9.9 and 24.6 Zr/nm^2 for samples C2, C4 and C8, respectively. Assuming coverages similar to the initial Zr surface density found for samples A1 and A8, we expected maximum Zr/nm^2 coverages of 3.4, 6.8 and 13.6, respectively for samples C2, C4 and C8. This indicates that the Zr excess is increasing with each additional layer. Samples C2, C4, C8, and D8 were terminated by a Hf metal layer in order to evaluate the use of Hf as a metal marker atom. The observed Hf atom coverages of 3.1, 3.3 and 3.1 Hf /nm^2 for samples C2, C8 and D8 are nearly triple the Zr surface densities of the films grown with a single Zr layer. The value of 9.8 Hf/nm^2 obtained for sample C4 is abnormally high and is attributed to free particles containing Hf and not associated with the film. Since XSW analysis is not possible on these non-LSM samples, the partitioning of the 9.8 nm^{-2} observed coverage into film and contaminant particle contributions was not determined.

Sample D8 was prepared to be similar to C8 but using a different phosphonate layer. The porphyrin square molecule used for D8 has an identical PO_3-to-PO_3 axis but is different in that four such porphyrin molecules are assembled into the square configuration (Figure 4.3). Nominally, film D8 is expected to have the same 2.26-nm per layer thickness as C8. However, the measured average layer thickness was found to be 1.61 nm implying a more tilted structure. Again, there is good agreement with atomic force microscopy measurements which yield 1.9$\pm$0.4 nm per layer.[57]

The XRR measured average electron densities expressed as ρ_F/ρ_{Si} for samples C2, C4 and C8 were found to be 0.38, 0.50, and 0.58, respectively. The porphyrin square macromolecule shown in Figure 4.3 has Z = 2284 electrons and as described above for sample D8 takes up a footprint of 12 nm^2 and has a layer thickness of 1.61 nm. This corresponds to a partial electron density of 2284/12/1.6 = 119 e/nm^3. Based on the XRF coverage, the partial film-averaged electron density for Zr is 40•13.3/8/1.6 = 42 e/nm^3 and for Hf is 72•3.1/8/1.6 = 17 e/nm^3. This would lead to 178 e/nm^3 for the average electron density of the D8 film as depicted in Figure 4.5. The reason that this is only 42% of the XRR measured electron density is due to unaccounted for low-Z containing molecules, such as DMSO solvent molecules, that fill in the large open spaces of this microporous film. Since the C-series of films with porphyrin molecules (see Figure 4.4) did not contain a Zn (or Re), a similar XRF deduction cannot be made concerning the lateral packing of the porphyrin molecules as was made for the porphyrin square molecules. However a lower limit of 0.45 nm^2 for molecular footprint for C8 can be computed, assuming there is no residue (e.g., no solvent) in the film. This is based on Z = 342 for the PO_3-R-PO_3 molecule, the XRR measured ρ = 405 e/nm^3 and layer thickness of 2.26 nm, and the XRF measured Zr and Hf coverages.

4.3.2 XSW Results and Discussion of Samples A1 and A8

The XSW measurements of samples A1 and A8 were performed at 18.3 keV to provide excitation of the highest-energy X-ray fluorescence line of interest, namely Zr Kα. Prior to collecting a long count-time XSW data set, a relatively quick reflectivity scan was taken, which is shown in Figure 4.6d for sample A8. The dip in

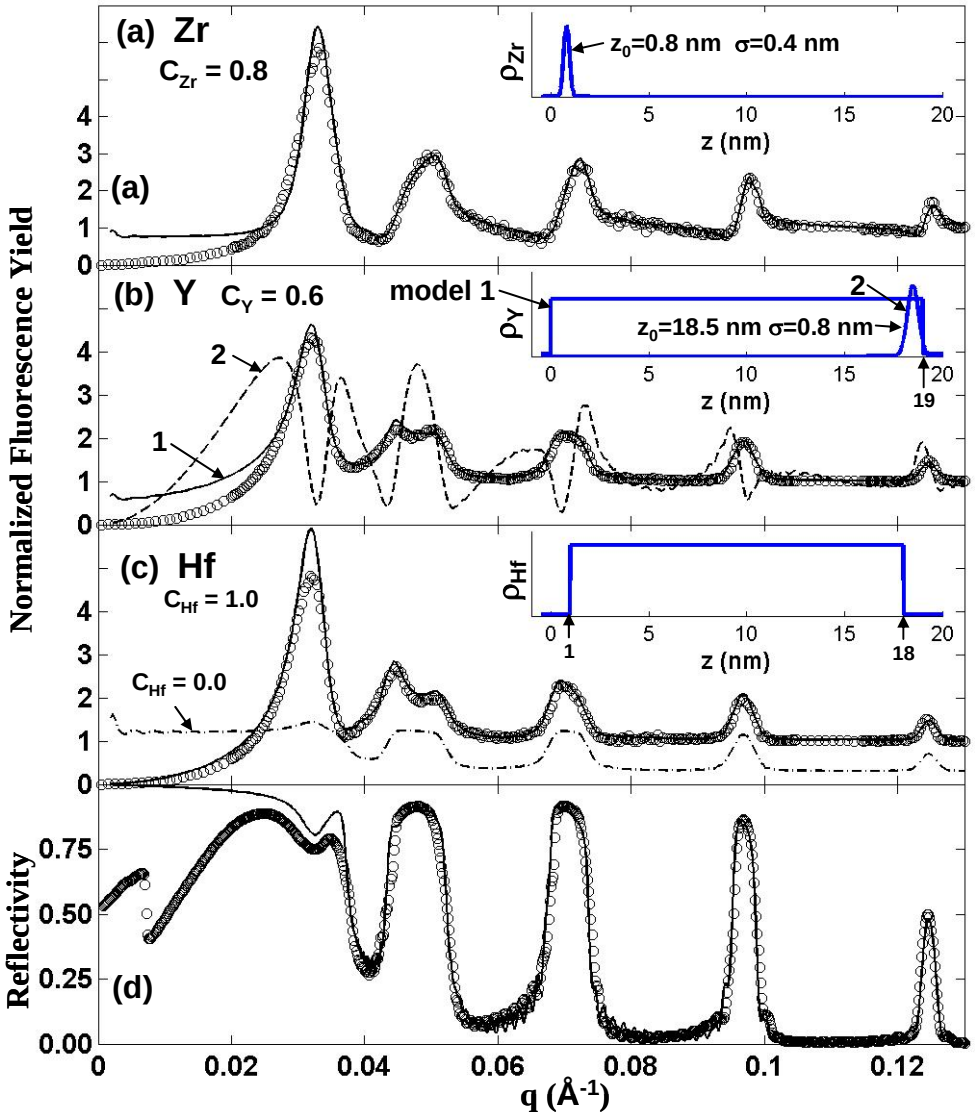

Figure 4.6: Sample A8 XSW results: (a-d) Simultaneously measured(open circles) and calculated (solid lines) reflectivity and Zr Kα, Y Kα, and Hf Lα X-ray fluorescence yield. (c) theoretical simulation (dash-dot line offset vertically for clarity) for a 100% extended uniform distribution. The insets show the atom distribution ρ(z) models that were used for the fluorescence yield fits (a-c).

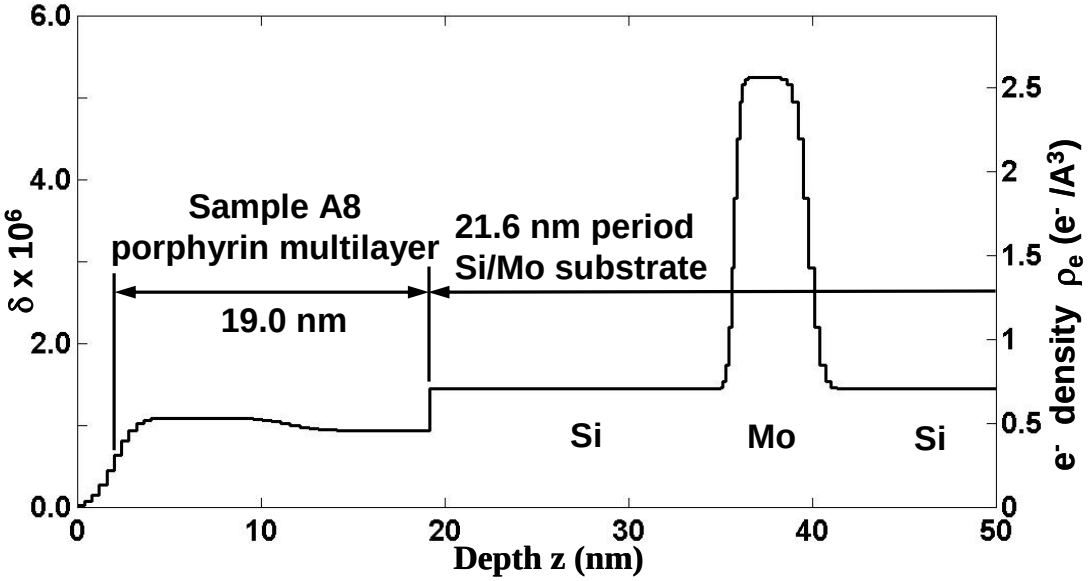

Figure 4.7: Electron density profile for sample film A8: The layered model of the electron density used to model sample film A8 (see Figure 4.6d). Only the topmost Si/Mo bilayer is shown.

the reflectivity in the TER plateau at q = 0.032 $Å^{-1}$ is the only obvious deviation from a bare substrate reflectivity curve (see Figure 2.5) and is due to a resonant cavity (or wave-guide) effect within the film.[58] Using the simplest possible model for the film, namely a single slab model, a resonant cavity effect was predicted but resulted in a poor fit to the observed reflectivity. After various trials, the more complex model shown in Figure 4.7, which has a slight build-up of electron density in the top half of the film, was found to yield a reasonable simulation of the reflectivity and was subsequently found to give very reasonable fits for the X-ray fluorescent yields. Following the computational scheme detailed in Chapter 2, the E-field intensity was

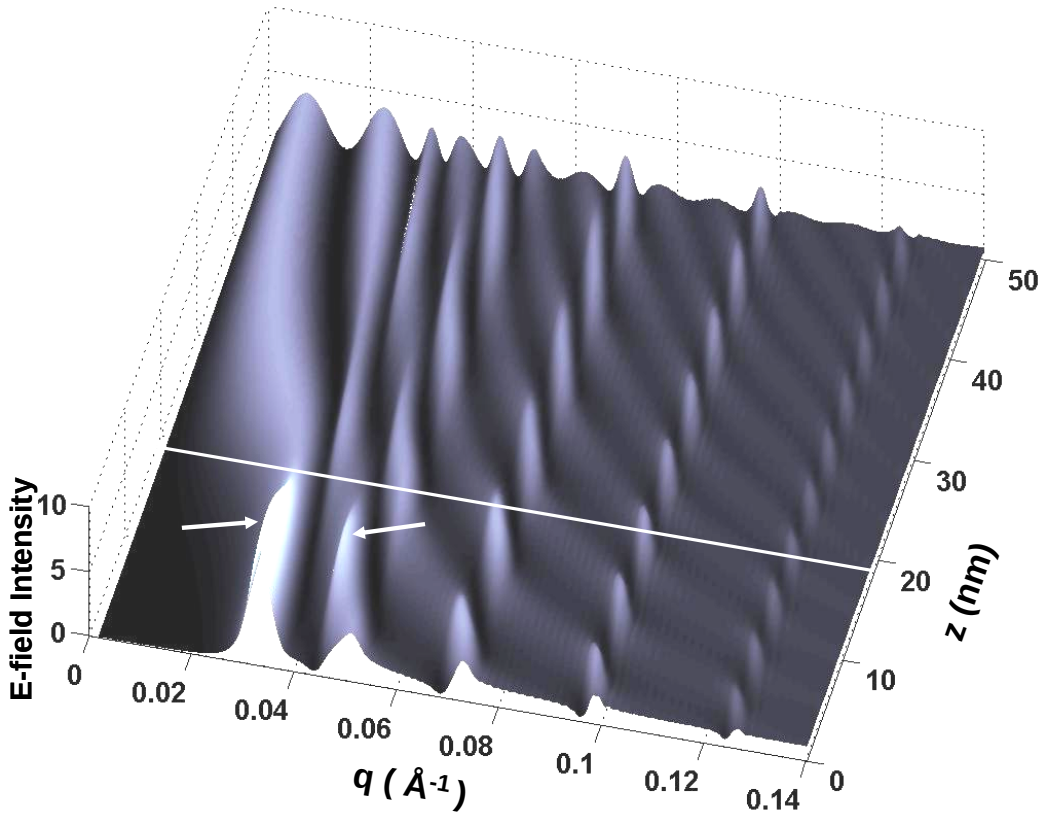

Figure 4.8: Surface plot of the calculated E-field intensity as a function of scattering-vector, q , and position, z, above the substrate surface for sample A8. The white line indicates the film/air interface of the sample. The arrows indicate the first two modes of a resonant cavity or waveguide effect in the sample film that gives rise to the dip in the XRR (Figure 4.6d) and large yield peaks (Figures 4.6a-c) at the same value of q.

computed and is plotted in Figure 4.8 as a surface in θ-z space in order to highlight the features of the resonant cavity. The first and second modes of the resonant cavity effect (indicated with arrows) show a normalized E-field intensity value in

excess of 4, which is the maximum value in the vacuum region above the film. At higher angles, the effect of the film on the E-field intensity dramatically diminishes and can be ignored.

The X-ray fluorescent yield data and simulations for Zr Kα, Y Kα and Hf Lα of sample A8 are shown in Figure 4.6a-c. XRF coverage measurement results are shown in Table 4.1. All the data shown in Figure 4.6 were collected simultaneously. Note that each element has a distinct fluorescence yield curve with the most pronounced differences occurring in the first two Bragg peaks. Referring to the schematic diagram of sample A8 shown in Figure 4.4, the Zr and Y were expected to occupy thin layers at the bottom and top of the film, respectively, while Hf would be found throughout the film, except at the very bottom and top. From Figure 4.8 note that the first mode of the resonant cavity will strongly affect all atoms inside the film while atoms at the top of the film will show no affect, since the resonance creates an E-field intensity node at the film-air interface. X-ray fluorescence peaks coinciding with the position of the dip in the reflectivity data for all three elements are clearly visible indicating that Zr, Hf and Y are present inside the film. Figure 4.6 also shows simulations of X-ray fluorescence yields. For the Zr Kα fluorescence yield (Figure 4.6a), the Zr distribution, $\rho(z)$, was partitioned into two parts: 1) a fraction C_{Zr} of the total Zr is contained within a Gaussian and 2) the remainder $(1-C_{Zr})$ for Zr atoms not contained in distributions that are proportional to 1+R. These latter Zr atoms are modeled by an extended uniform distribution from z = 0 to z = 219 nm, the upper limit being chosen to be several times larger than the longest XSW period generated by the LSM at the low q end of the scan range. The best fit for this model has C_{Zr} = 0.8 with the Zr Gaussian distribution centered at z = 0.8 nm from the top of the

substrate surface and having a width of σ = 0.4 nm. The Hf Lα XSW yield (Figure 4.6c) was best fit by a model that used a uniform slab from z = 1.0 to 18.0 nm which bounds the expected Hf position based on Figure 4.4. Hf coverage modeled by an extended uniform distribution did not improve the fit to the data. The XSW determined Zr and Hf distributions are in very reasonable agreement with the model for film A8 depicted in Figure 4.4. However, Y, which was intended to serve as a marker atom for the terminal phosphonate position failed to do so and apparently diffused inward uniformly throughout the film. The best simple model for Y Kα fluorescence was found to be a rectangle profile uniformly distributed throughout the film plus an extended uniform distribution with C_Y = 0.6, where C_Y is the fraction contained in the rectangular profile. Apparently, Y did not selectively bind to the terminal phosphonate positions of the 8th porphyrin layer as desired, but instead was able to diffuse into the film and bind at other locations. XRF measurements support the XSW finding with the Y coverage measured to be 14.0 nm^{-2}, well in excess of the coverage of ~1.3 or ~3.1 nm^{-2} that was found for the single layers of Zr and Hf, respectively.

Figure 4.6 also presents some alternate model simulations as a comparison to the best-fit simulations. Figure 4.6b shows what the fluorescence yield resulting from the expected position for Y which was modeled to be a Gaussian distribution centered at z = 18.5 nm from the top of the substrate surface and having a width of σ = 0.4 nm. The predicted Y fluorescence yield is unique and complex proving that Y certainly is not confined to the expected terminal location. Such dramatic modulations are observed in the G- and I-series samples (see below) when Hf was used to mark the terminal phosphonate position instead of Y. Figure 4.6c shows the

yield simulation that would result for C_{Hf} = 0 (100% of the Hf contained in an extended uniform distribution). We see that for Hf, the extended uniform distribution model does not simulate the observed fluorescence at low angle but does so reasonably well for the 3rd and 4th order Bragg reflections. Figure 4.8 shows that atoms distributed uniformly throughout the film will overlap nearly a whole period of the XSW for the 3rd Bragg reflection and nearly two whole periods for the 4th Bragg reflection. The Hf distribution in sample A8 appears to be uniformly distributed when examined by the 3rd and 4th order Bragg XSW yields and is thus modeled equivalently by both the slab shown in the inset in Figure 4.6c or by the much larger slab used for the extended uniform distribution model. The true nature of the Hf distribution only becomes known by examining the fluorescence yield from the longer period XSW generated by the 1st and 2nd order Bragg reflections. This illustrates why it is useful to examine the atomic distributions with several different XSW periods to appropriately match the length scale of the unknown atomic distribution.

Sample A1 uses a complex molecule with rotational freedom of the constituent porphyrins about the Re-Re axes, which form the sides of the “porphyrin square”. This rotational freedom of the porphyrin square molecule is shown in Figure 4.10 in 3-d perspective for both a fully extended perpendicular conformation and with a tilt angle of 60° away from the surface normal. For sample A1 consider two limiting conformations of the porphyrin square molecule. In conformation A, the porphyrin PO_3-PO_3 axes are perpendicular to the plane of the square and in conformation B, the porphyrin constituents rotate about the Re-Re axes and lie approximately flat in the plane of the square. (Note, however, that a completely flat conformation is sterically prohibited.) For conformation A, the formation of a

monolayer takes the place of the four PO_3 positions on one side of the square to the Zr terminated surface with the PO_3-PO_3 axes standing normal to the surface. In the capping step, Y atoms bind to the terminal PO_3 positions. In this configuration, if Zr are assigned to be located at z_0, then the Zn/Re would be at (z_0 + 1.25) nm and Y at (z_0 + 2.5) nm. For conformation B, all heavy atoms would be approximately at the same location. Data from sample D8, which is based on the same molecule, suggests an average layer thickness of 13.0 / 8 = 1.63 nm/layer. For comparison, AFM measurements of square films yield (with somewhat less precision and on inherently rougher surfaces) an average layer thickness of ca. 1.9 nm, i.e. in good agreement with the x-ray result.[57] Comparing 1.63 nm/layer with 2.5 nm per layer for a square having the limiting perpendicular conformation, A, an average porphyrin wall angle of 40^o, roughly midway between the two limiting conformations, is implied.

XSW results of sample A1 are presented in Figure 4.9. In Figure 4.9a, 4.9b, and 4.9c we show the measured X-ray fluorescence yields for Zr Kα, Zn Kα + Re Lα and Y Kα, respectively. (The Zn K and Re L peaks were inseparable due to overlap in the fluorescence spectra. However, this is not overly detrimental to the analysis, since Zn and Re atoms are expected to be located at the same height as illustrated in Figure 4.2.) The three elements show very similar distributions. In Figure 4.9a, the Zr distribution is modeled with a Gaussian profile, C_{Zr} = 0.8 centered at 0.5 nm with σ = 0.4 nm. In Figure 4.9b, Zn/Re is modeled in a Gaussian profile, $C_{Zn/Re}$ = 1.0, centered at 0.5 nm with σ = 0.4 nm. In Figure 4.9c, Y is modeled in a Gaussian profile, C_Y = 0.6, centered at 0.5 nm with σ = 0.4 nm. The Zr, Zn/Re, and Y are all well modeled by very narrow distributions centered at z = 0.5 nm from the substrate

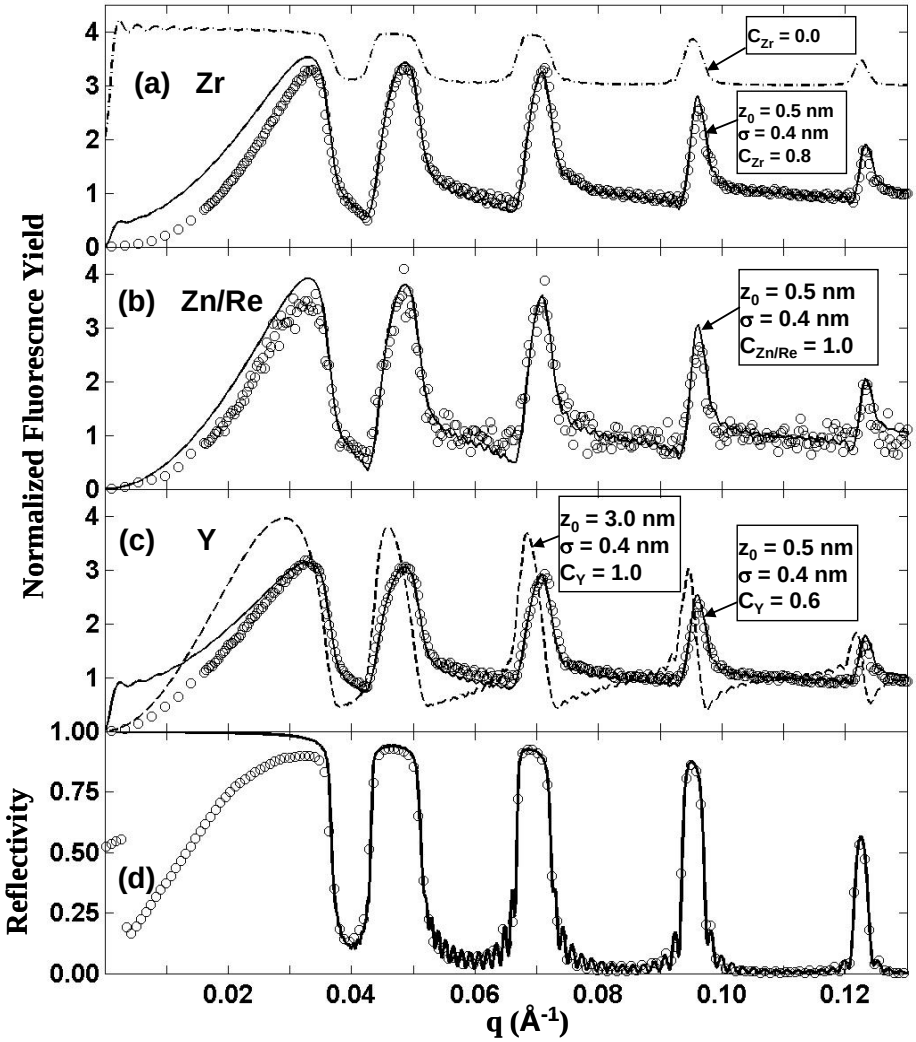

Figure 4.9: Sample A1 XSW results: (a-c) Simultaneously measured X-ray fluorescence yields for Zr Kα, Zn Kα + Re Lα, and Y Kα (open circles) and best theoretical fits (solid lines). A theoretical simulation for Y (dashed line) using a Gaussian model for Y centered at z = 3.0 nm is shown in (c). A theoretical simulation (dash-dot line offset vertically by 2 for clarity) in (a) is shown for a 100% extended uniform distribution model. (d) Measured (open circles) and theoretical fit (solid line) of X-ray reflectivity.

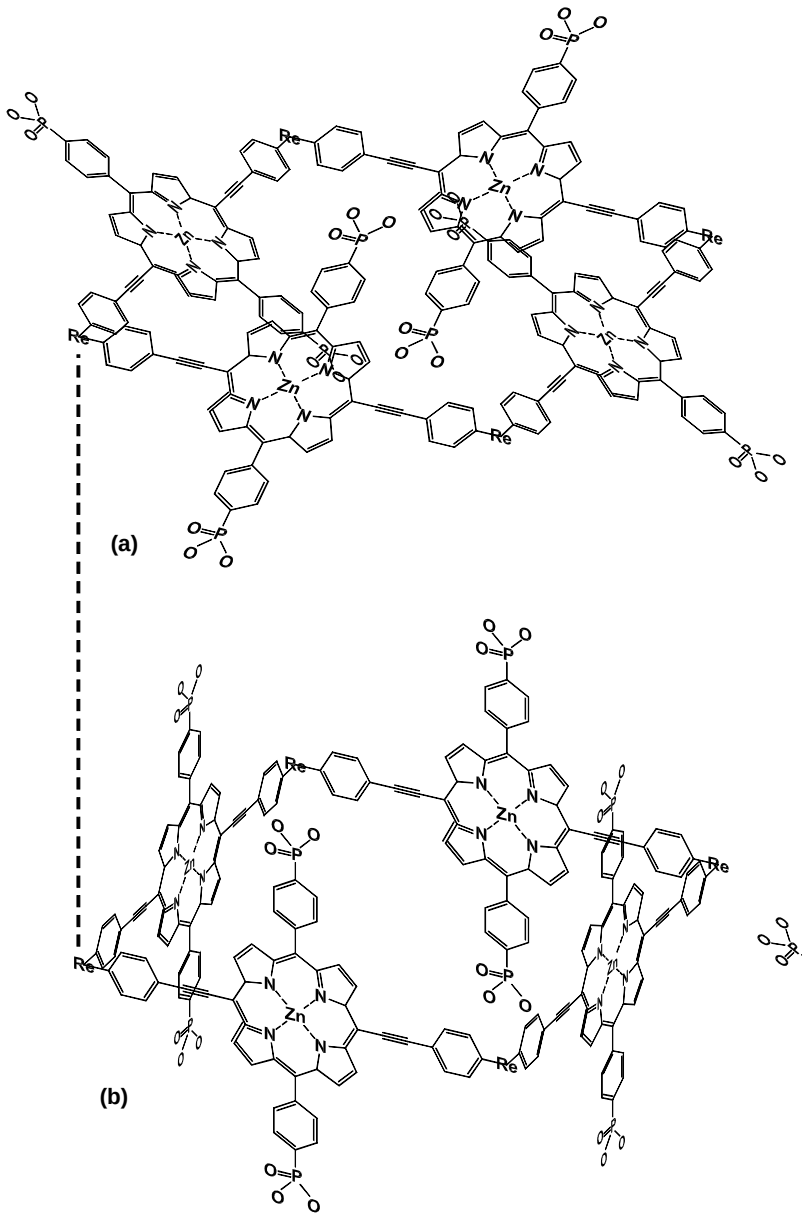

Figure 4.10: Perspective diagram of porphyrin square molecules: A single porphyrin square molecule is shown in a perpendicular (a) and tilted (b) conformation. The tilt angle of the walls of the porphyrin square in (b) is 60^{o}.

surface. It is very interesting that Zr and Y, which were delivered from aqueous solutions, require considerable fractions to be modeled by extended uniform distributions, while the Zn/Re pair was best fit by assuming 100% in the surface layer modeled by a Gaussian distribution. This suggests that the porphyrin square molecule dispersed well and had no tendency to agglomerate or otherwise crystallize into non-monolayer conformations. For comparison, Figure 4.9c shows the theoretical yield for Y if it had been in the fully extended terminal phosphonate position at z = 3 nm. In addition, we show an extended uniform distribution in Figure 4.9a for comparison with the measured Zr yield. For this particular single monolayer sample the XSW data strongly suggest that the 1-layer porphyrin square film of sample A1 is in a collapsed configuration. The previously discussed low Zn/Re coverage for A1 further substantiates this finding. This again demonstrates the strength of this combined XRF, XSW, and XRR approach.

4.3.3 XRR and XRF Measurements F- and H-series

The F- and H-series films were prepared identically to the G- and I-series films respectively but on Si(001) substrates in order to provide suitable samples for XRR measurement. The experimental XRR data were measured at the Northwestern University X-ray Facility using a rotating anode reflectometer as described in Chapter 3 and simulated by using the same dynamical scattering theory based on Parratt's recursive formulation [22] as was used for modeling the LSMs of this study. A Nevot-Croce treatment of the interfaces was required for these films due to the very large roughness of the film surfaces. The layered model consisted of layers for the Si substrate, SiO_2 surface oxide, and sample film with 10 additional layers to

approximate the error function profile of the Nevot-Croce treatment of the interfaces. The sample film was treated as a single layer of uniform electron density. The fit parameters were the electron density of the film, film thickness, and surface and interface roughness. Figure 4.11 shows the measured and calculated x-ray reflectivity for F-series samples with the inset showing the electron density profile for sample F8. Figure 4.12 shows the measured and calculated x-ray reflectivity for H-series samples. The XRR thicknesses, electron density and interface roughness are listed in Table 4.2 along with the Hf, Zr and Zn+Re coverage. In Figure 4.13 the XRR determined thicknesses with χ^2 fits are plotted for the F- and H-series as well as the Hf mean position, $z_{0,Hf}$, for the companion G- and I-series.

4.3.4 XSW Results for G- and I-series

The XSW measurement of the G- and I-series samples was performed at the ID32 beamline at ESRF using 18.5 keV incident x-rays. The high photon flux ($3x10^{10}$ p/s) at the ID32 beamline permitted fast scans to be taken (1 hour at ID32 compared to 12 hours at x15a) as well as permitting the use of a very small beam (0.015 mm x 1 mm compared to 0.05 mm x 5 mm.) The data were taken in 600 steps from q = -.0033 to 0.1915 A^{-1} (Δq = 0.000327 A^{-1}) with a 5 sec counting time. The sample reflectivity was modeled from reflectivity data collected simultaneously during the XSW scan. The small step size revealed thickness fringes from the LSM which were sometimes visible as fluorescence modulations in the XSW yield data. A single slab was used to model the metal-phosphonate film on top of the LSM substrate whose thickness t_F was determined by iteration from the XSW yield results of the Hf position marking the top of the film. The fitting of the reflectivity was

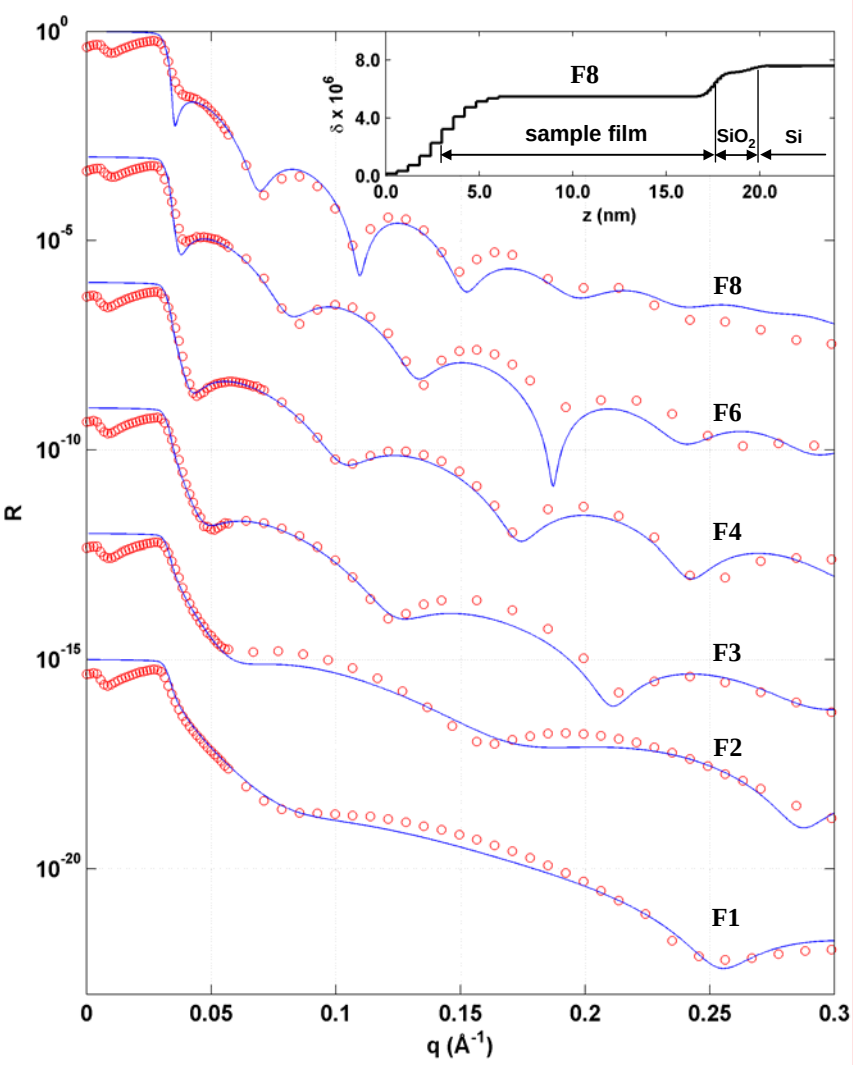

Figure 4.11: XRR results of F-Series films: The measured (open circles) and calculated (solid lines) X-ray reflectivity of the F-series sample films. The inset shows the electron density (shown as the index of refraction) model used to calculate the reflectivity for film F8 as an example. The graded interface approach (Nevot-Croce) was necessary due to the high surface roughness in the films of this series.

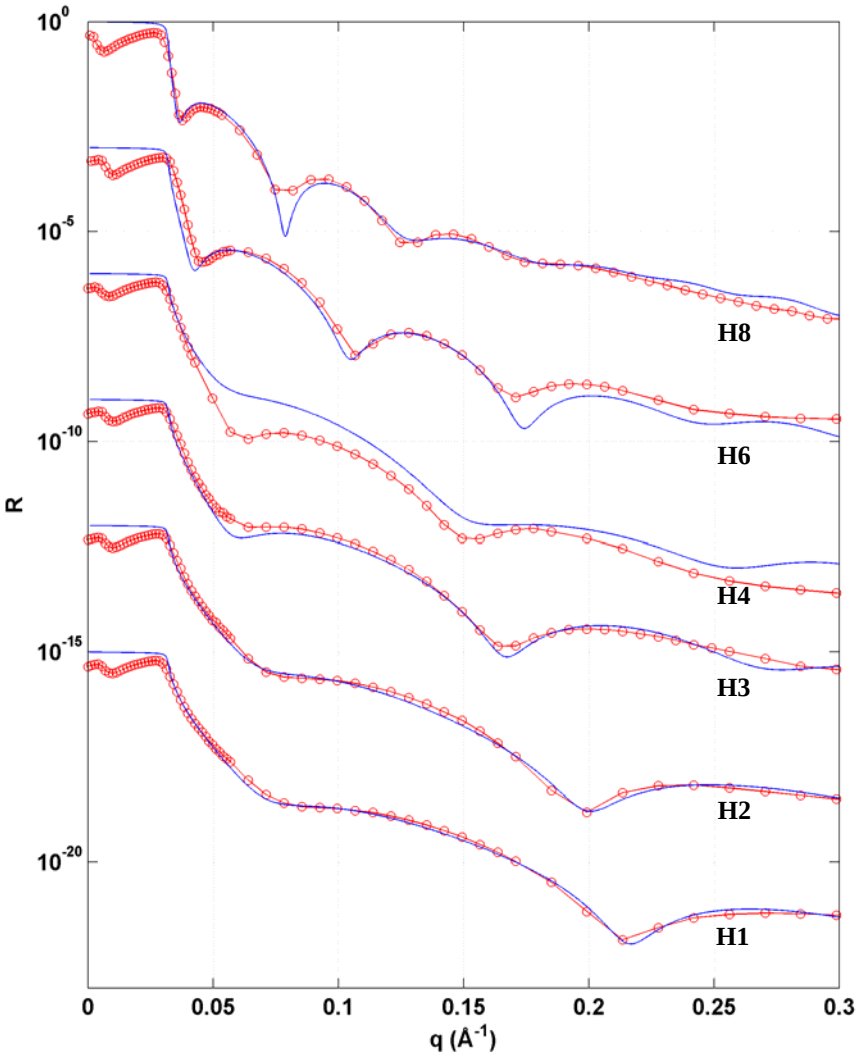

Figure 4.12: XRR results of H-Series films: The measured (open circles) and calculated (solid lines) X-ray reflectivity of the H-series sample films. The graded interface approach (Nevot-Croce) was necessary due to the high surface roughness in the films of this series.

	t_F	$(\rho_F/\rho_{Si})_{meas}$	σ_{int}	σ_{surf}	Θ_{Hf}	Θ_{Re}	Θ_{Zr}	$(\rho/\rho_{Si})_{calc}$
	nm		nm	nm	nm^{-2}	nm^{-2}	nm^{-2}	
F1	3.74(4)	0.75(2)	0.28(5)	0.77(3)	5.1(5)	-	3.9(4)	-
F2	5.6(1)	0.72(3)	0.34(1)	0.49(3)	4.6(5)	-	8.3(8)	-
F3	7.6(2)	0.72(3)	0.45(4)	0.97(6)	4.3(5)	-	11(1)	-
F4	9.2(1)	0.71(1)	0.40(4)	0.86(2)	5.9(6)	-	15(2)	-
F6	11.9(2)	0.74(1)	0.40(4)	1.02(4)	4.6(5)	-	21(2)	-
F8	14.6(2)	0.72(1)	0.40(4)	1.4(1)	4.7(5)	-	30(3)	-
F1	4.39(3)	0.72(1)	0.1(1)	0.83(2)	4.2(5)	0.12(2)	4.0(4)	0.24
H2	4.7(1)	0.75(1)	0.05(5)	0.98(2)	3.3(4)	0.39(7)	7.6(8)	0.43
H3	5.8(1)	0.68(3)	0.12(8)	0.78(1)	3.4(4)	0.18(3)	10(1)	0.26
H4	6.1(1)	0.71(4)	0.3(1)	1.1(1)	3.3(4)	0.24(4)	10(1)	0.28
H6	9.1(1)	0.70(1)	0.4(1)	1.1(4)	3.8(4)	0.34(6)	18(2)	0.28
H8	12.3(2)	0.61(3)	0.5(1)	1.6(2)	4.4(5)	0.48(9)	24(2)	0.28

Table 4.2. Results from XRR and XRF analysis for the F- and H-series. (See Figure 4.2.) The film thickness, t_F, measured electron density of the film relative to the Si substrate, ρ_F/ρ_{Si}, and the Nevot-Croce widths of the film-substrate interface, σ_{int}, and film-air interface, σ_{surf}, were measured by XRR. The calculated electron density of the film relative to the Si substrate, $(\rho_F/\rho_{Si})_{calc}$, is based on the measured depth-integrated atomic coverages, Θ_{Zr}, Θ_{Hf}, and Θ_{Re}, determined by XRF.

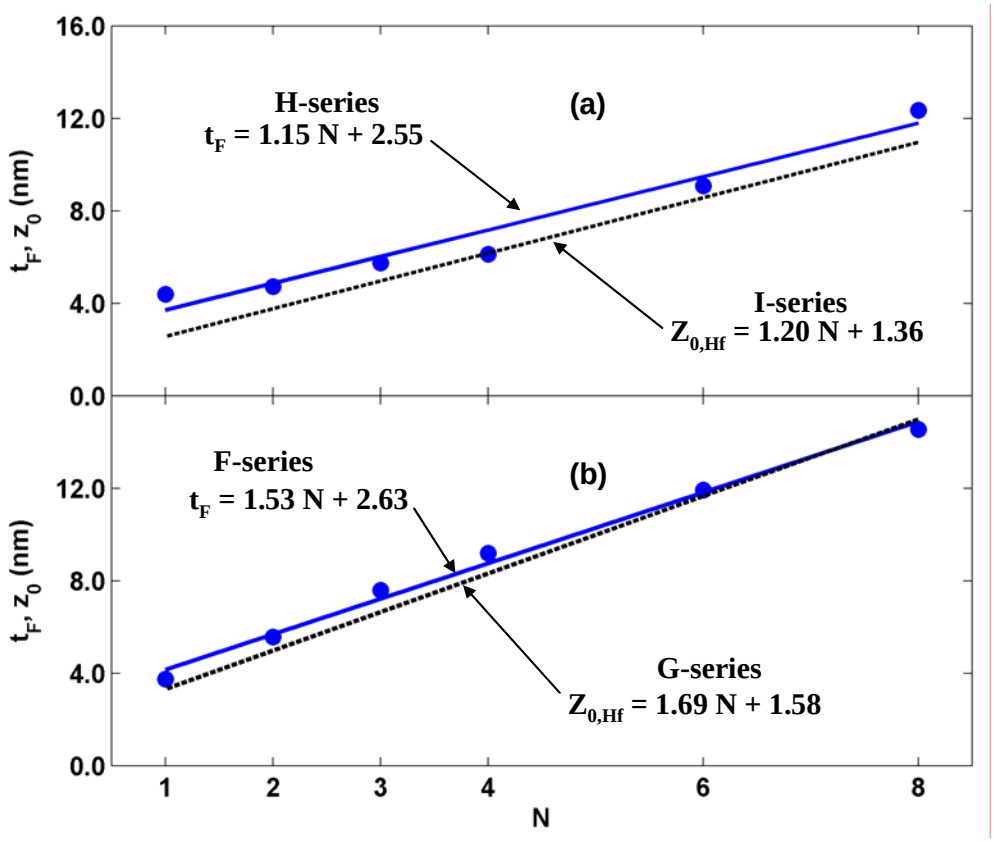

Figure 4.13: XRR results for F- and H-series films. Film thickness (closed circles), tF, and χ2 fits (solid lines). Also shown for comparison are the χ2 fits (dashed line) of the Hf mean position z_0 from the companion G- and I-series films.

mostly insensitive to the film thickness except at lower angles for the thickest films. The free fitting parameters for the reflectivity model were the Si/Mo bilayer period and the ratio of the Si to Mo layer thicknesses. Due to the variations in deposition conditions within the sputter deposition chamber the d-spacing of the LSM was found to vary from substrate to substrate. In addition, clamps used to hold the Si substrates caused a shadowing near the clamps resulting in a lateral gradient of the d-spacing. This latter problem was not significant for XSW analysis in this Chapter

since a small beam confined to the center of the sample was used. Thus, each sample required a fit to the reflectivity data. A typical fit to the reflectivity is shown in Figure 4.14a for sample film I2. The corresponding layered model is shown in Figure 4.14b for the first two periods of the LSM. A typical X-ray fluorescence emission spectrum of an I-series sample is shown in Figure 4.15 for sample I8. The displayed spectrum is the angle integrated spectrum (summation of 601 individual X-ray spectra) from the XSW scan. With the exception of the Fe Kα and Fe Kβ, all labeled X-ray lines could be integrated to provide a characteristic XSW signature originating from the substrate. Since the main points of interest here are the structural properties of the metal-phosphonate films, the yield data for those metals found in the films, namely, Hf, Zn, Re, and Zr were analyzed. The X-ray spectra for samples in the G-series are similar to those for the I-series after the Zn and Re lines are removed.

The G-series samples are multilayer metal-phosphonate films using Zr for the metal layers and 1,12-dodecanediylbis(phosphonic acid) for the phosphonate layers as shown in Figure 4.4. For each film, Hf was substituted for Zr in the final metal layer to provide a distinct marker for the phosphonate sites at the top of the film. The measured and calculated Hf and Zr fluorescence yields are shown for each XSW scan in the G-series in Figures 4.16 to 4.21. The models for the χ^2 fits used a Gaussian profile $\rho_G(z)$ for the Hf and a rectangular profile $\rho_R(z)$ for the Zr. The free fitting parameters for the Hf distribution were the mean position z_0 and width σ of the Gaussian distribution. The free fitting parameters for the Zr distribution were the mid-height z_0 and width Δz of the rectangular distribution. Also included in each

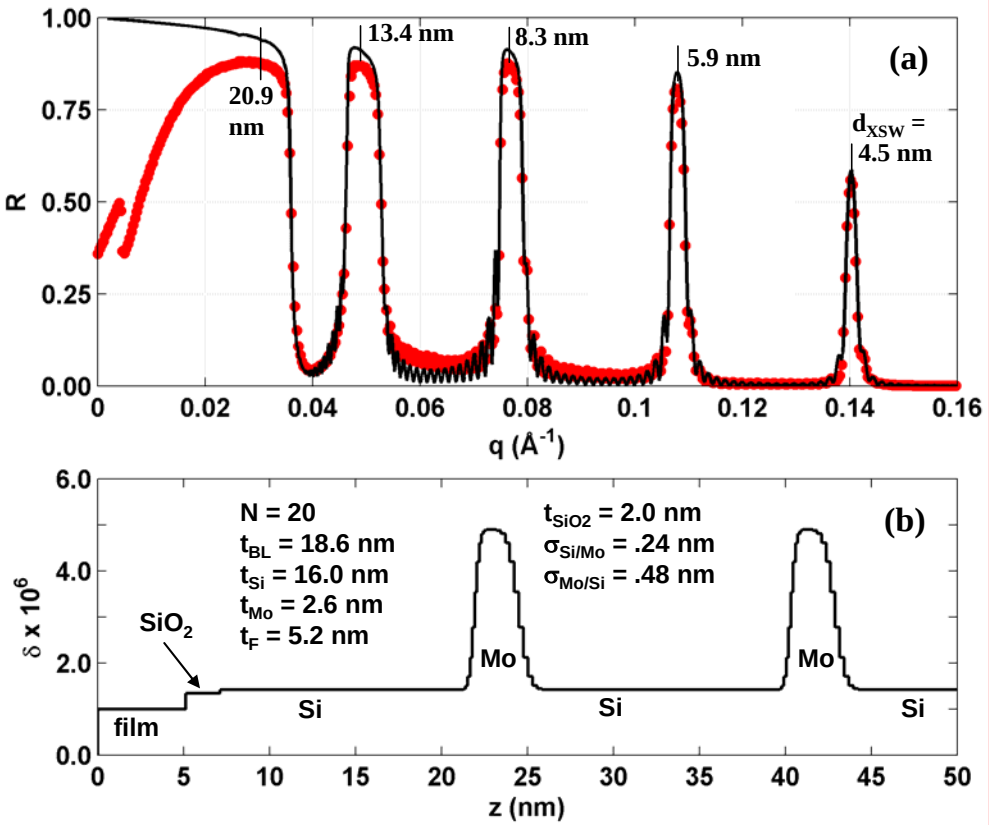

Figure 4.14: XRR of I2 film from XSW scan. (a)Typical measured (filled circles) and calculated (solid line) XRR results taken simultaneously during the XSW of sample film I2. (b) the electron density profile used to model the LSM + film shown by plotting the real part of the index of refraction, δ. Only the first 2 of 20 LSM Si/Mo bilayers are shown. The period of the XSW is shown above each Bragg reflection.

model was an extended uniform distribution, $\rho_E(z)$ to account for atoms not contained in the assumed profiles. The final distribution was $\rho(z) = C\ \rho_M(z) + (1\text{-}C)\ \rho_E(z)$, where C is the partition fraction and $\rho_M(z)$ is either the Gaussian or rectangular profile. A fixed value of C = 0.85 was used for all of the distributions in the G- and

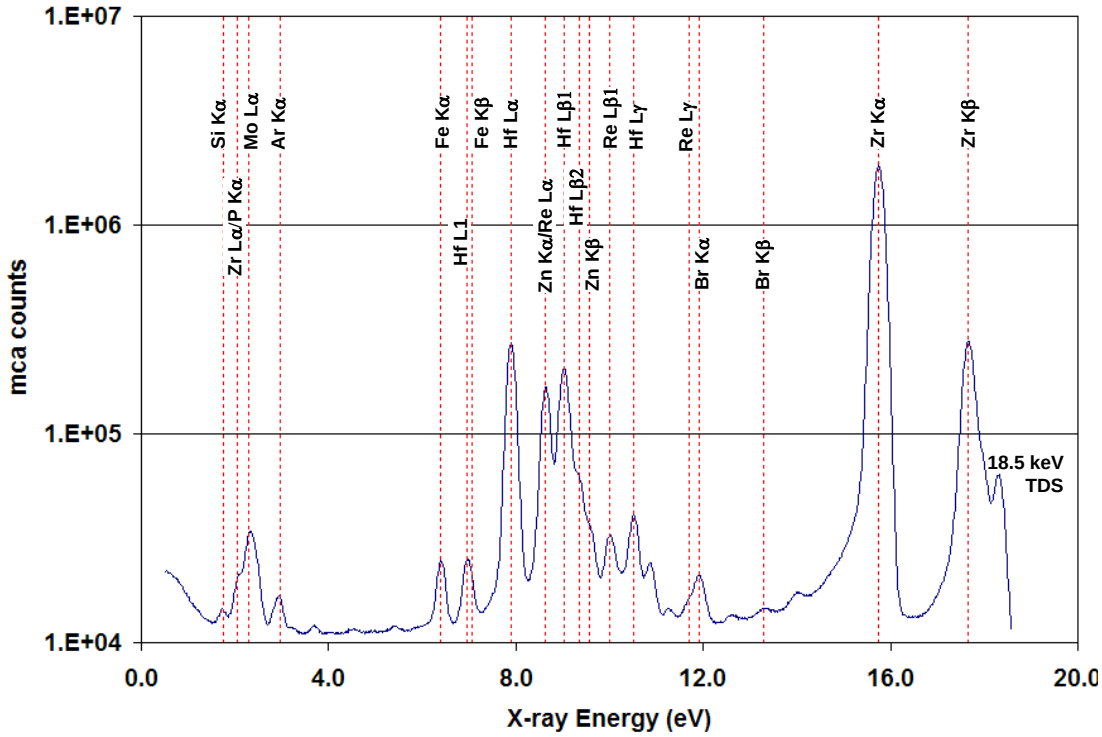

Figure 4.15: Typical MCA spectrum for I-series films. Typical I-series x-ray fluorescence spectrum showing the angle-integrated spectrum from the XSW scan of sample I8. All labeled lines (except Fe and Br lines) give characteristic XSW fluorescence yield curves. The G-series samples give similar spectra with the Zn and Re lines absent.

I-series. The effect of assuming an extended uniform distribution is to allow for a component of fluorescence yield that is proportional to 1+R. The Hf and Zr fluorescence yields of the G-series are shown as a layer sequence in Figures 4.22 and 4.23, respectively. In Figure 4.22 the changing characteristic yield profile of the Hf can be followed as it occupies a higher and higher position with respect to the LSM.

	Hf			Zr			Zn, Re		
	z_0	σ	Θ	z_0	Δz	Θ	z_0	Δz	Θ
Film	**nm**	**nm**	**nm^{-2}**	**nm**	**nm**	**nm^{-2}**	**nm**	**nm**	**nm^{-2}**
G1	2.76(3)	1.05(4)	5.7(6)	2.20(2)	1.50(1)	4.3(4)	-	-	-
G2	5.81(3)	1.42(2)	7.7 (12)	3.66(3)	4.16(5)	14(2)	-	-	-
G3	6.63(2)	1.07(2)	6.1(6)	3.80(4)	5.3(1)	13(1)	-	-	-
G4	8.30(4)	1.30(4)	4.9(5)	4.78(5)	6.9(1)	19(2)	-	-	-
G6	11.1(1)	1.27(4)	5.1(5)	6.41(9)	9.2(1)	23(2	-	-	-
G8	15.2(1)	2.30(4)	5.3(5)	8.68(2)	14.1(1)	33(3)	-	-	-
I1	2.72(2)	0.88(3)	2.3(2)	1.72(3)	1.5	2.9(3)	2.04(3)	1.5	0.37(3)
I2	3.68(2)	1.16(2)	2.1(2)	2.08(2)	2.4	4.9(5)	2.66(2)	2.4	0.43(4)
I3	4.70(3)	1.04(3)	2.5(3)	2.65(1)	3.4	7.8(8)	3.08(2)	3.4	0.66(5)
I4	6.23(2)	1.25(2)	2.5(3)	3.25(3)	4.9	10(1)	3.94(4)	4.9	0.93(6)
I6	8.79(2)	1.42(2)	3.1(3)	4.69(3)	7.5	16(1)	5.23(4)	7.5	1.48(9)
I8	10.9(1)	1.88(4)	2.8(3)	5.47(6)	9.3	20(2)	6.49(4)	9.3	1.62(9)

Table 4.3. Results from XSW and XRF analysis for the G- and I-series samples. (See Figure 4.4.) The mean position, z_0, and width, σ, were determined from Gaussian model profiles for the Hf atomic distribution. The mid-height, z_0, and width, Δz, were determined from rectangular model profiles for the Zr and Zn+Re atomic distributions. . The depth-integrated atomic coverage, Θ_T, were determined by XRF.

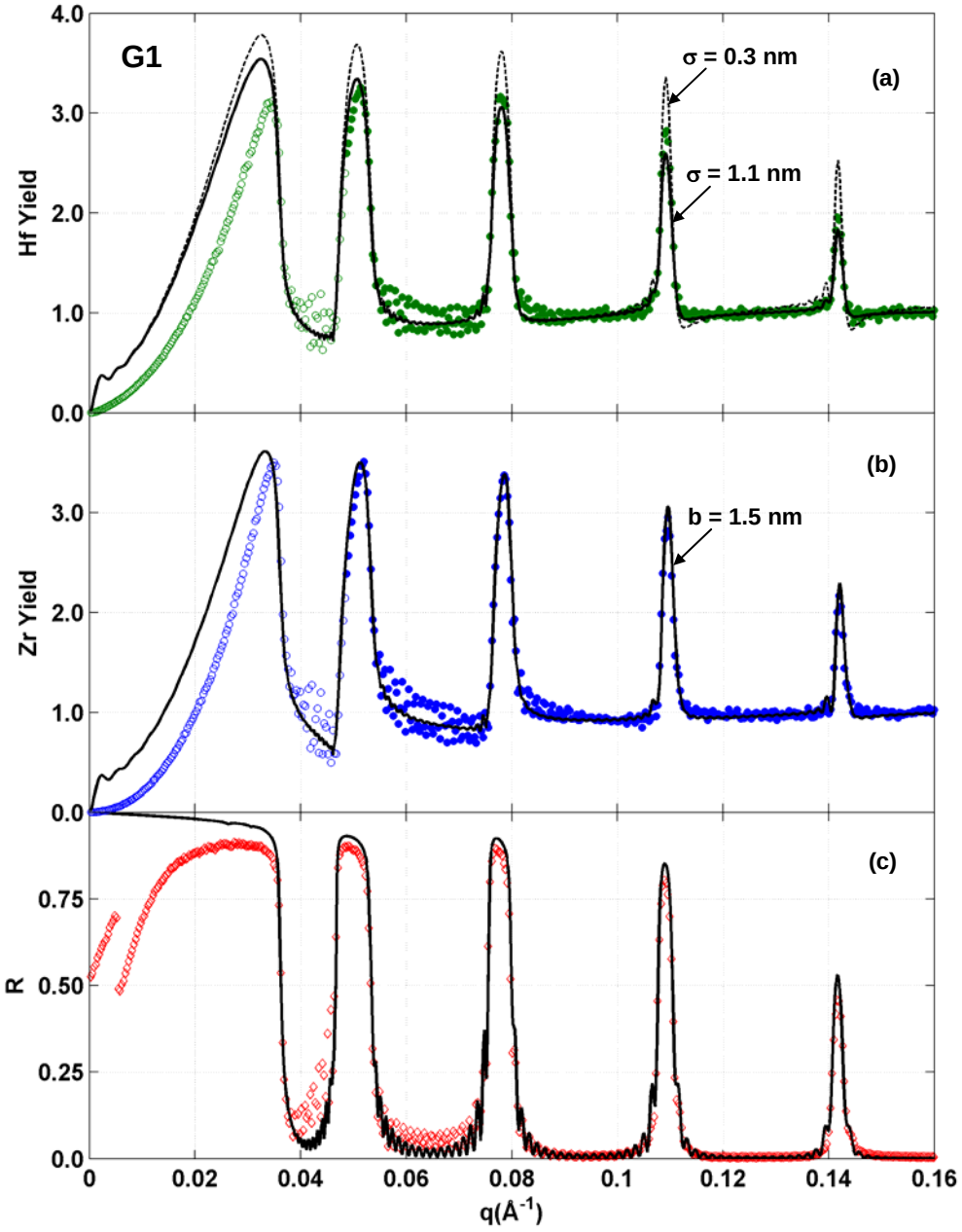

Figure 4.16: XSW results for film G1. Measured (open circles) and calculated (solid lines) for (a) Hf yield, (b) Zr yield and (c) XRR. In (a) the calculated result for a narrower distribution (σ=0.3 nm) is shown for comparison. All data were collected simultaneously during a single XSW scan

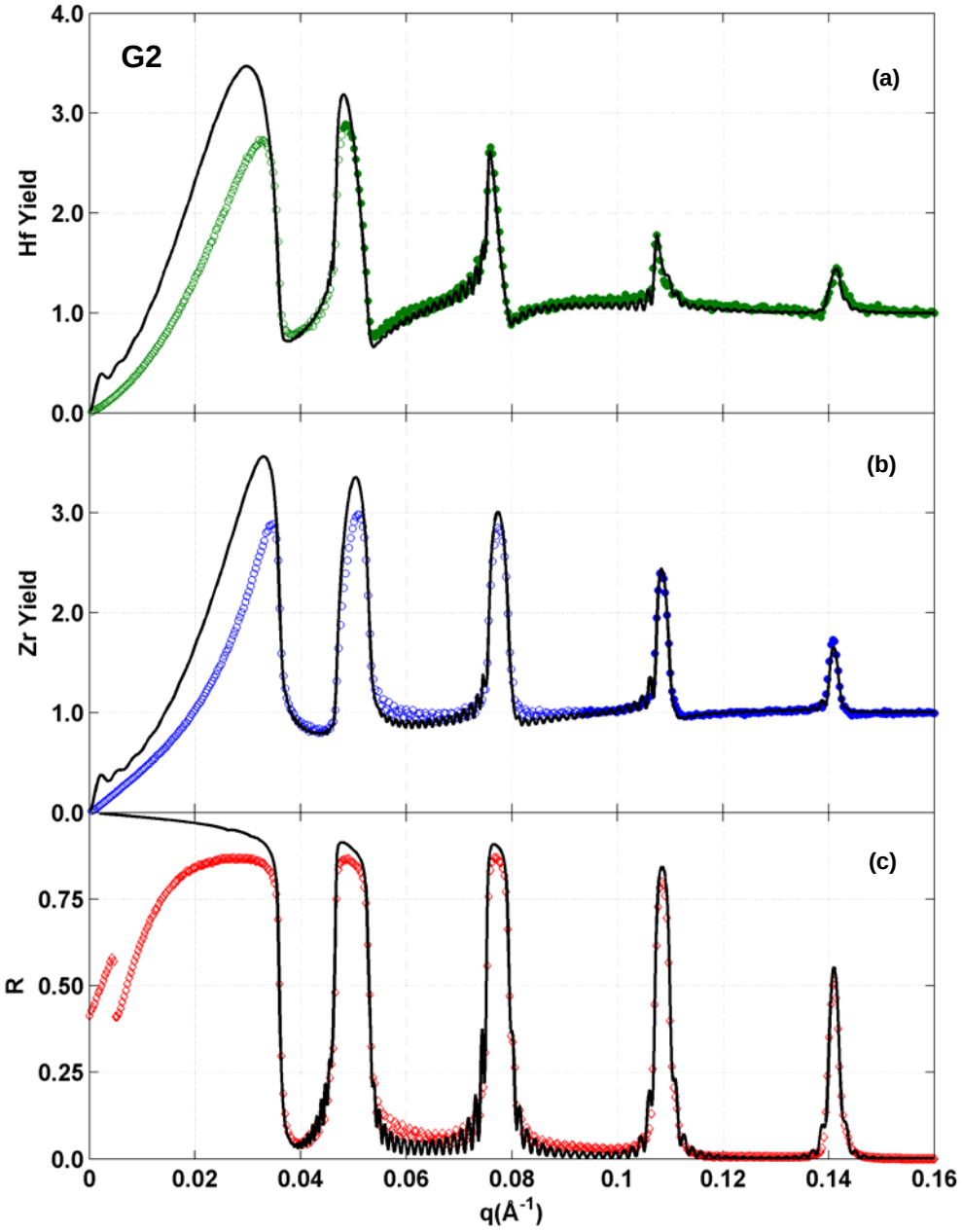

Figure 4.17: XSW results for film G2. Measured (open circles) and calculated (solid lines) for (a) Hf yield, (b) Zr yield and (c) XRR. All data were collected simultaneously during a single XSW scan

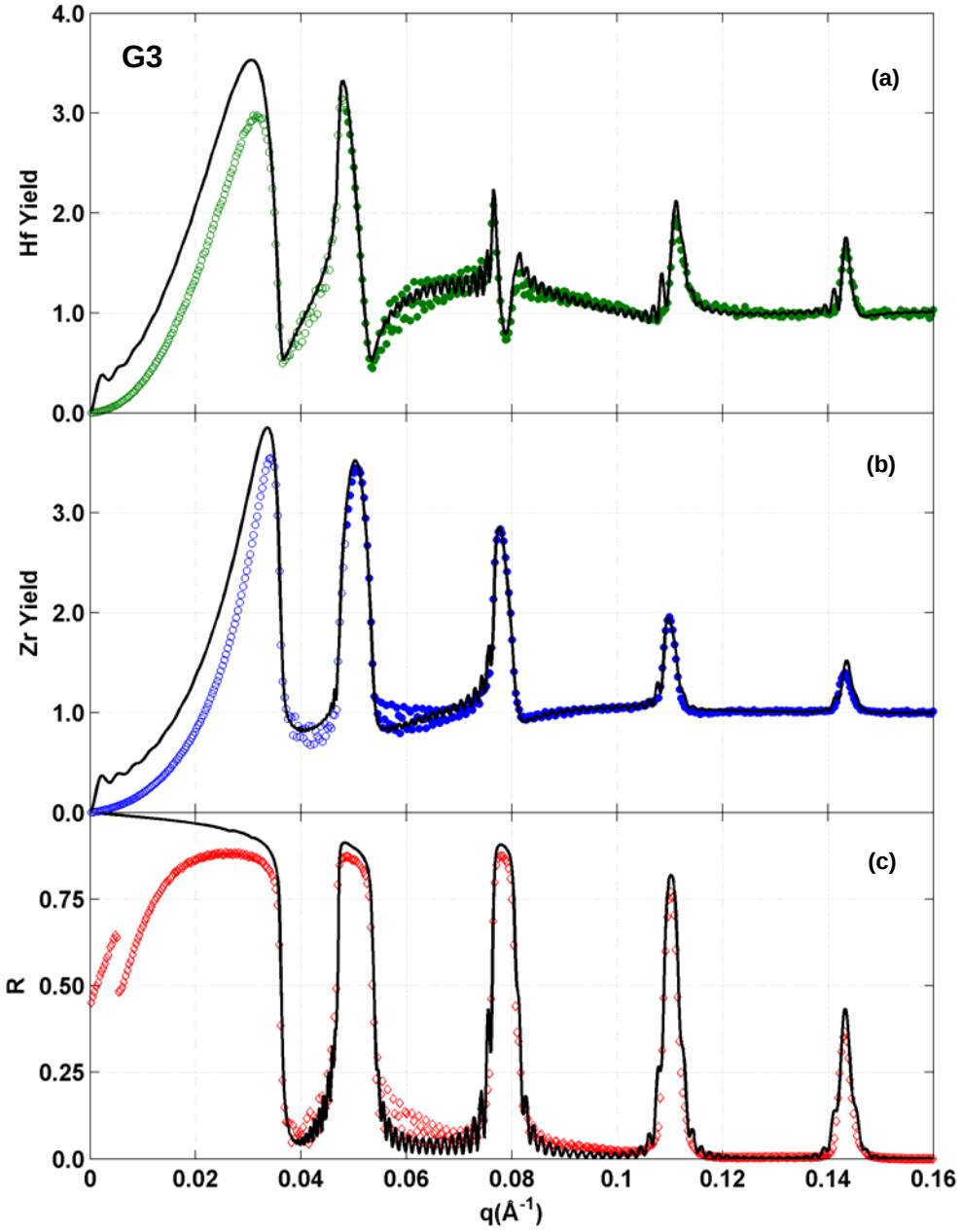

Figure 4.18: XSW results for film G3. Measured (open circles) and calculated (solid lines) for (a) Hf yield, (b) Zr yield and (c) XRR. All data were collected simultaneously during a single XSW scan

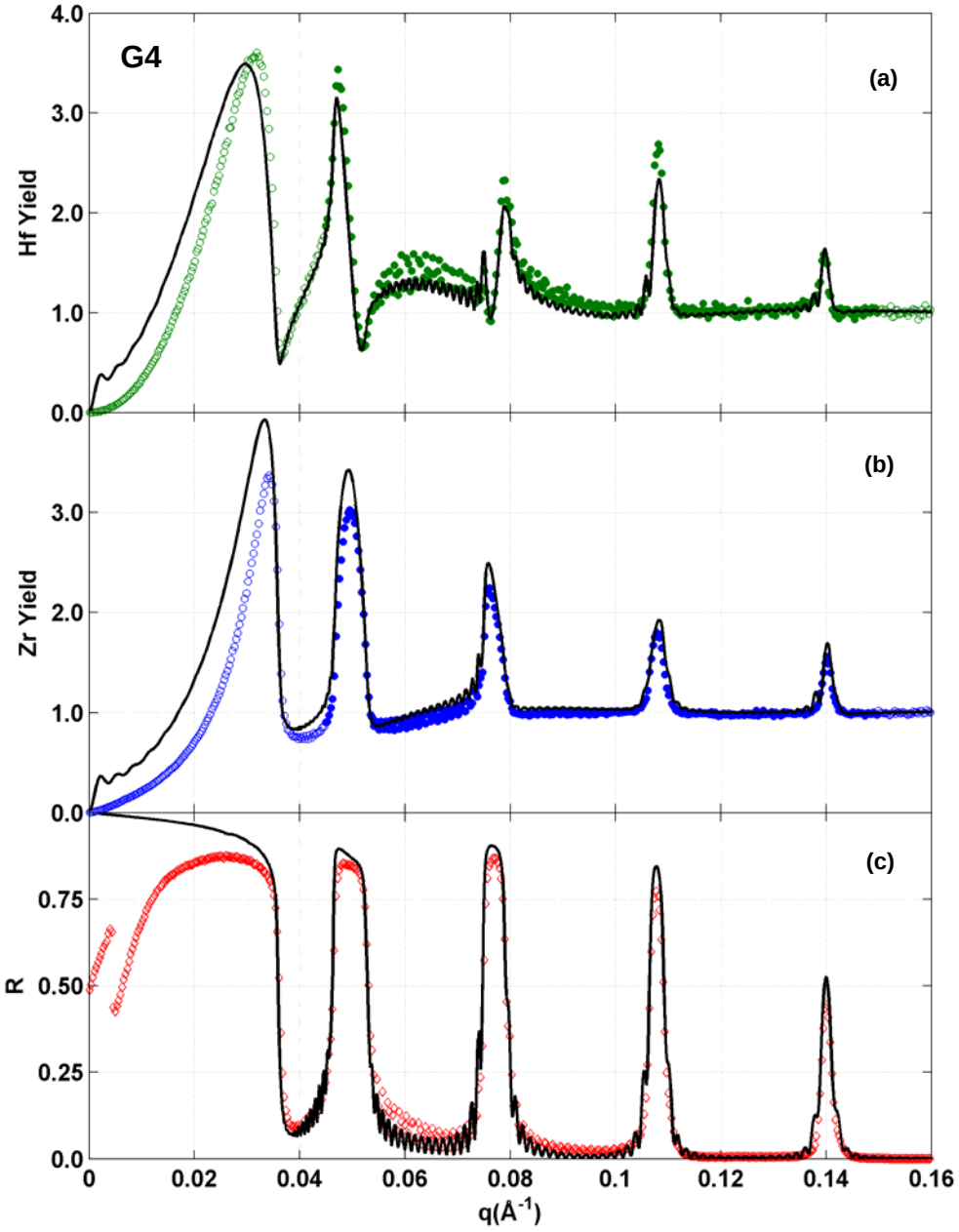

Figure 4.19: XSW results for film G4. Measured (open circles) and calculated (solid lines) for (a) Hf yield, (b) Zr yield and (c) XRR. All data were collected simultaneously during a single XSW scan

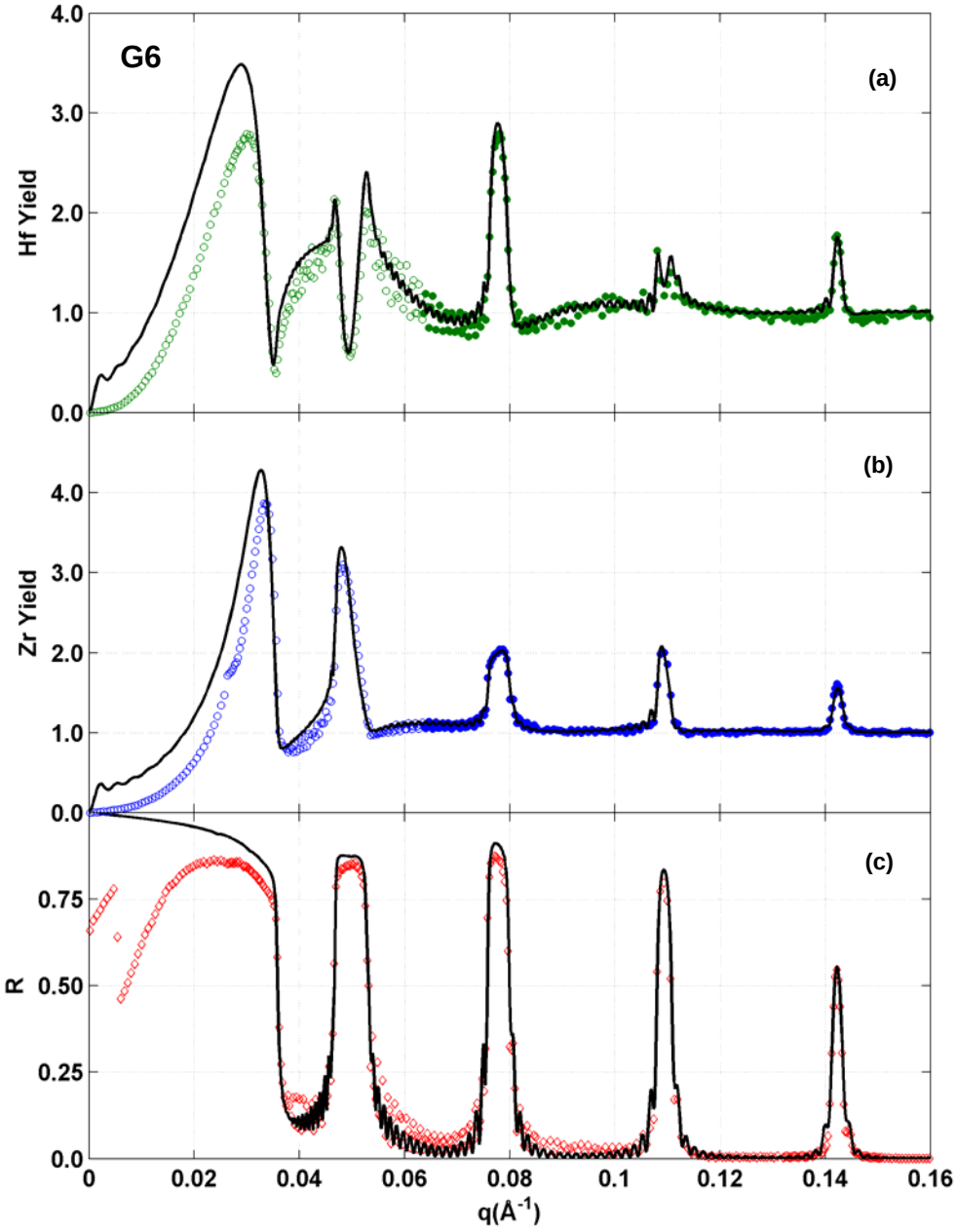

Figure 4.20: XSW results for film G6. Measured (open circles) and calculated (solid lines) for (a) Hf yield, (b) Zr yield and (c) XRR. All data were collected simultaneously during a single XSW scan

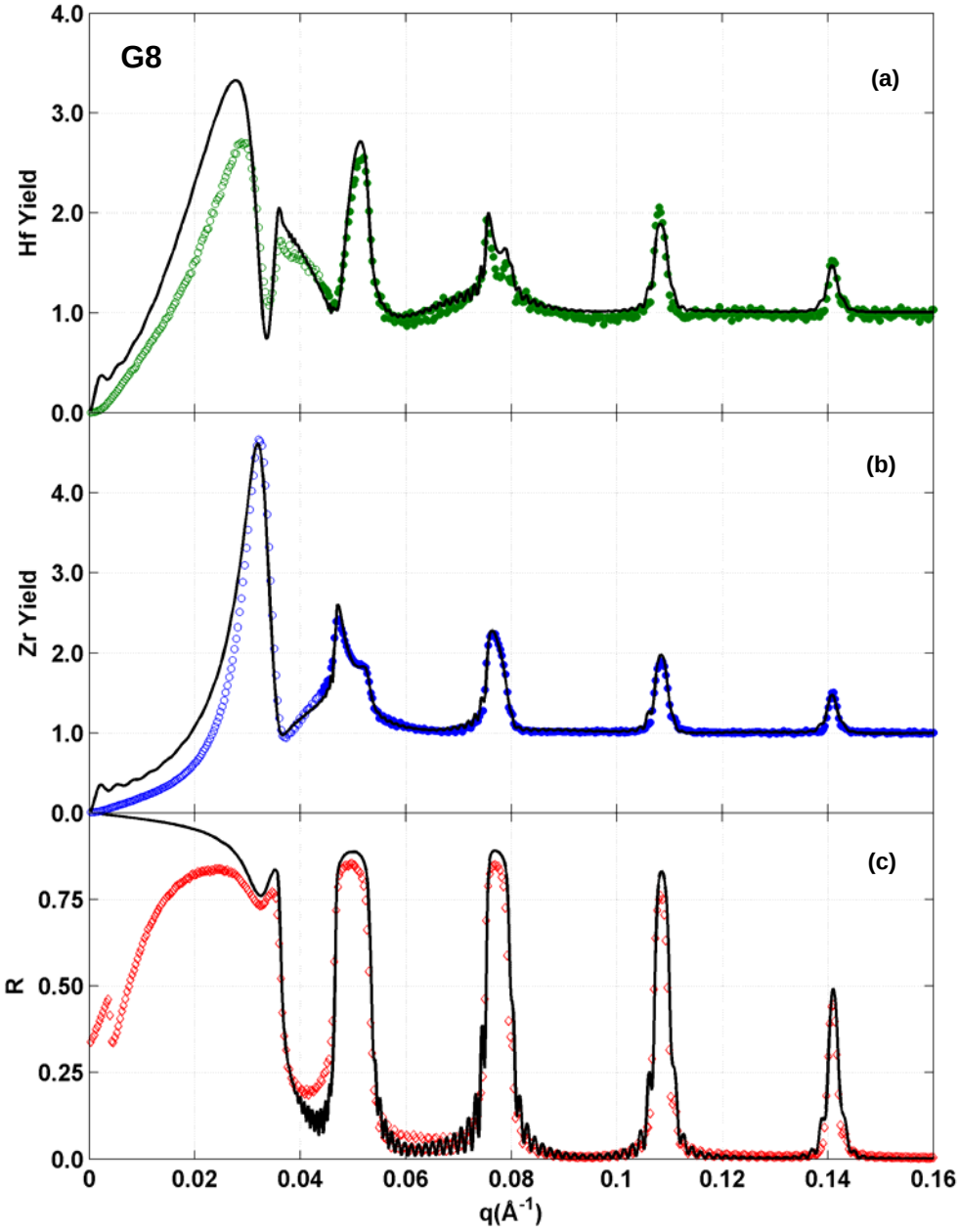

Figure 4.21: XSW results for film G8. Measured (open circles) and calculated (solid lines) for (a) Hf yield, (b) Zr yield and (c) XRR. All data were collected simultaneously during a single XSW scan

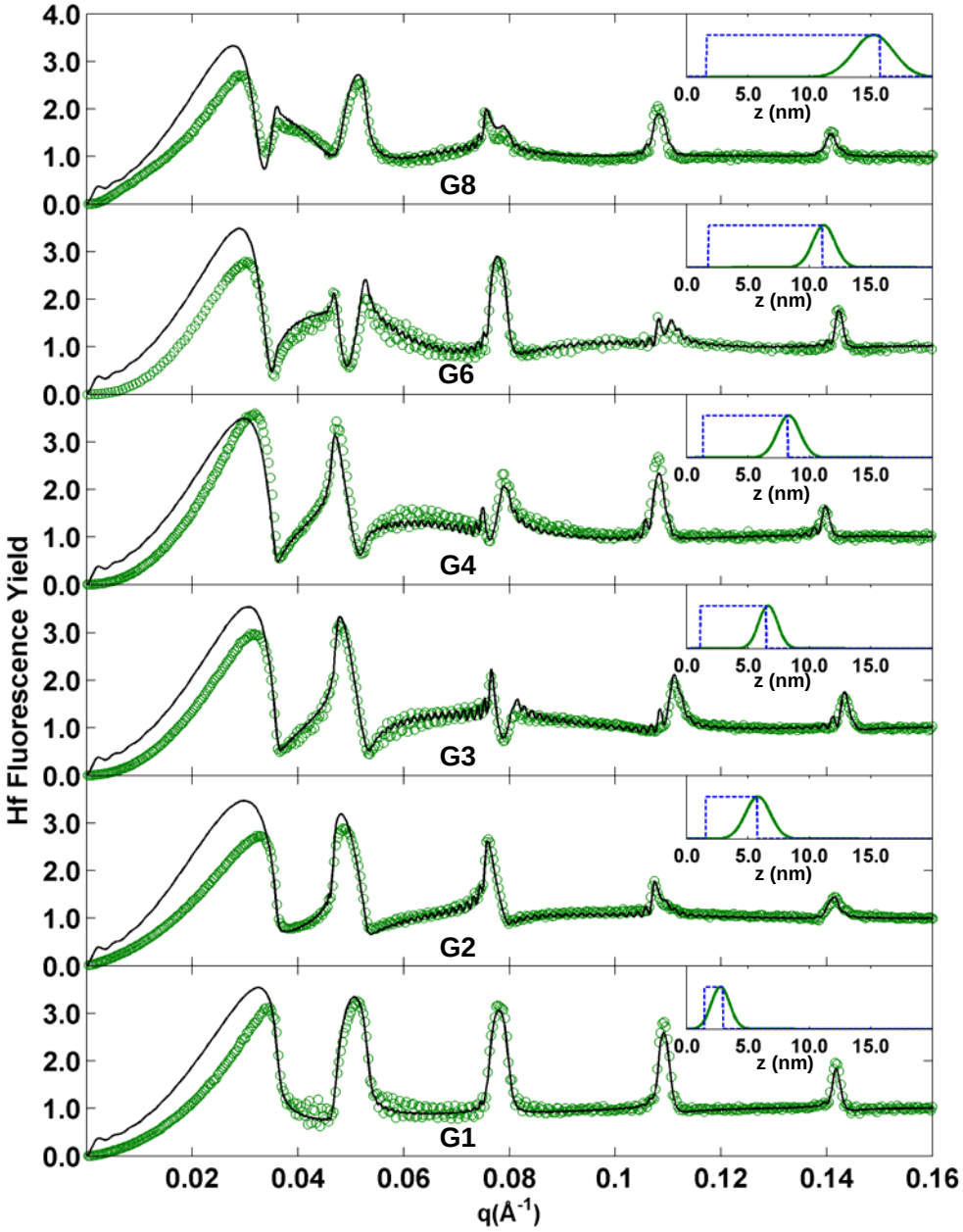

Figure 4.22: G-series XSW Hf results. Measured (open circles) and calculated(solid lines) Hf fluorescence yield of the G-series films. The atomic distributions are scaled vertically for clarity and are not proportional to the atomic coverages

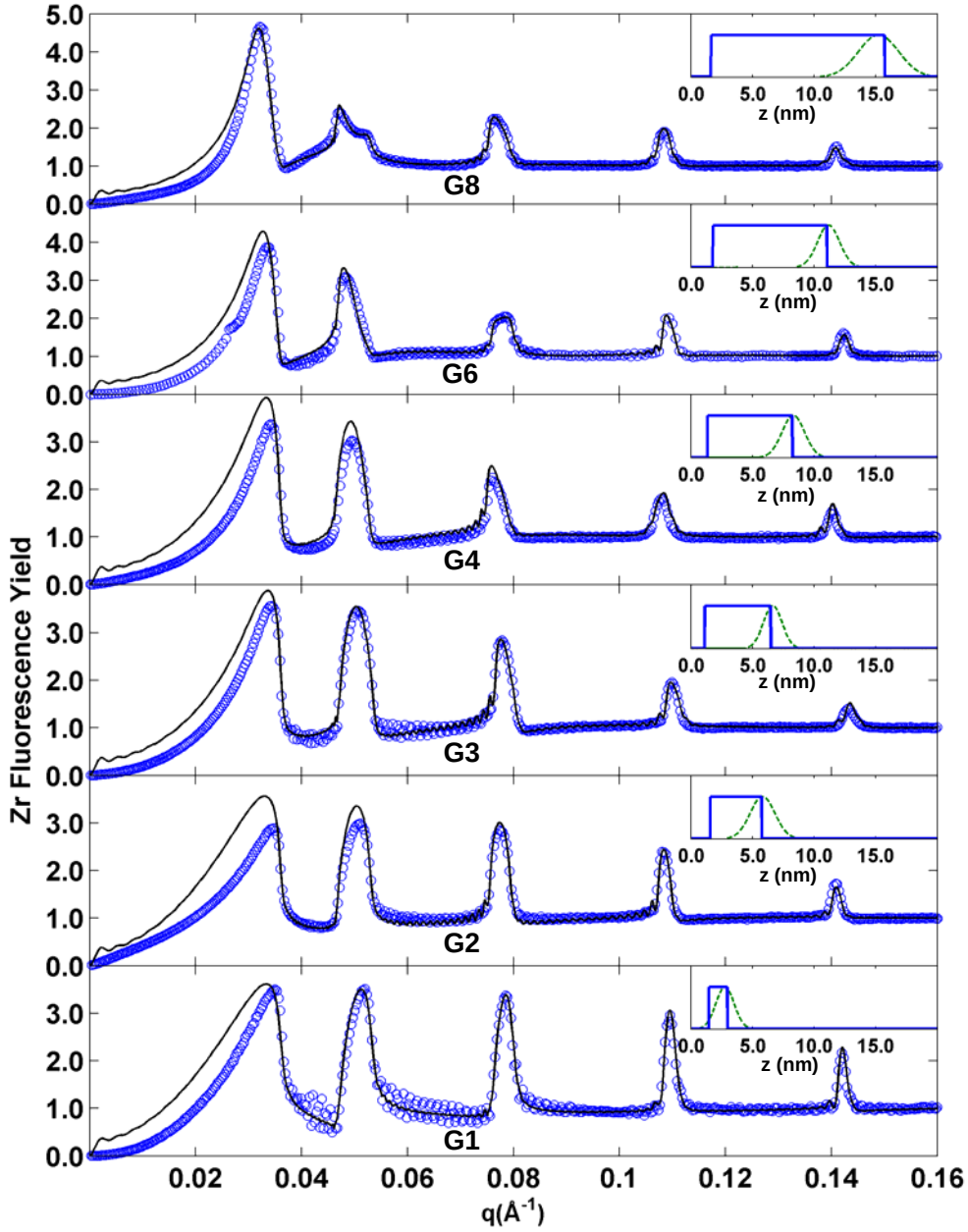

Figure 4.23: G-series XSW Zr results. Measured (open circles) and calculated(solid lines) Zr fluorescence yield of the G-series films. The atomic distributions are scaled vertically for clarity and are not proportional to the atomic coverages

The I-series samples are very similar to the G-series except that a porphyrin square bis(phosphonic acid) is used instead of 1,12-dodecanediylbis(phosphonic acid) for the phosphonate layers as shown in Figure 4.4. Consequently, the same structure is expected, but with the addition of Zn and Re which are expected to be located at the mid-plane of the ideally configured porphyrin square molecule or equidistant from adjacent Zr or Hf metal atom layers. The strong fluorescence lines from Zn and Re are the Zn Kα and Re Lα x-ray lines which are only 20 eV apart and thus were analyzed together as a single fluorescence. Although it is also possible to see Zn Kβ and Re Lβ in the x-ray spectra, these peaks were too weak to be analyzed over the full angle range. The measured and calculated Hf, Zn/Re and Zr yield are shown for each XSW scan in the I-series in Figures 4.24 to 4.29. The χ^2 fits were obtained using an identical procedure as for Hf in the G-series using a Gaussian distribution for Hf and rectangular distributions for Zn+Re and Zr. However, for the rectangular distributions for Zn/Re and Zr, a coupling between the mid-height z_0 and width Δz was observed in several of the I-series samples that was not observed in the G- series. Better results were obtained by fixing the width Δz of the profile using a constraint based on the Hf fit result. For each sample in the series, the width Δz of the rectangular distribution for both the Zr and Zn/Re was set to $\Delta z = z_{0,Hf} - 1.3$ nm. This value was chosen from an average of values observed when Δz was left to be a free fitting parameter from those samples in the I-series that did not show the coupling between parameters. All of the model parameters for the atomic distributions of Hf, Zn+Re and Zr are summarized in Table 4.3. The Hf, Zn/Re and Zr yield results are plotted as a vertical sequence in Figures 4.30, 4.31, and 4.32, respectively. In Figure 4.33 plots are given for the Hf mean position of the Gaussian

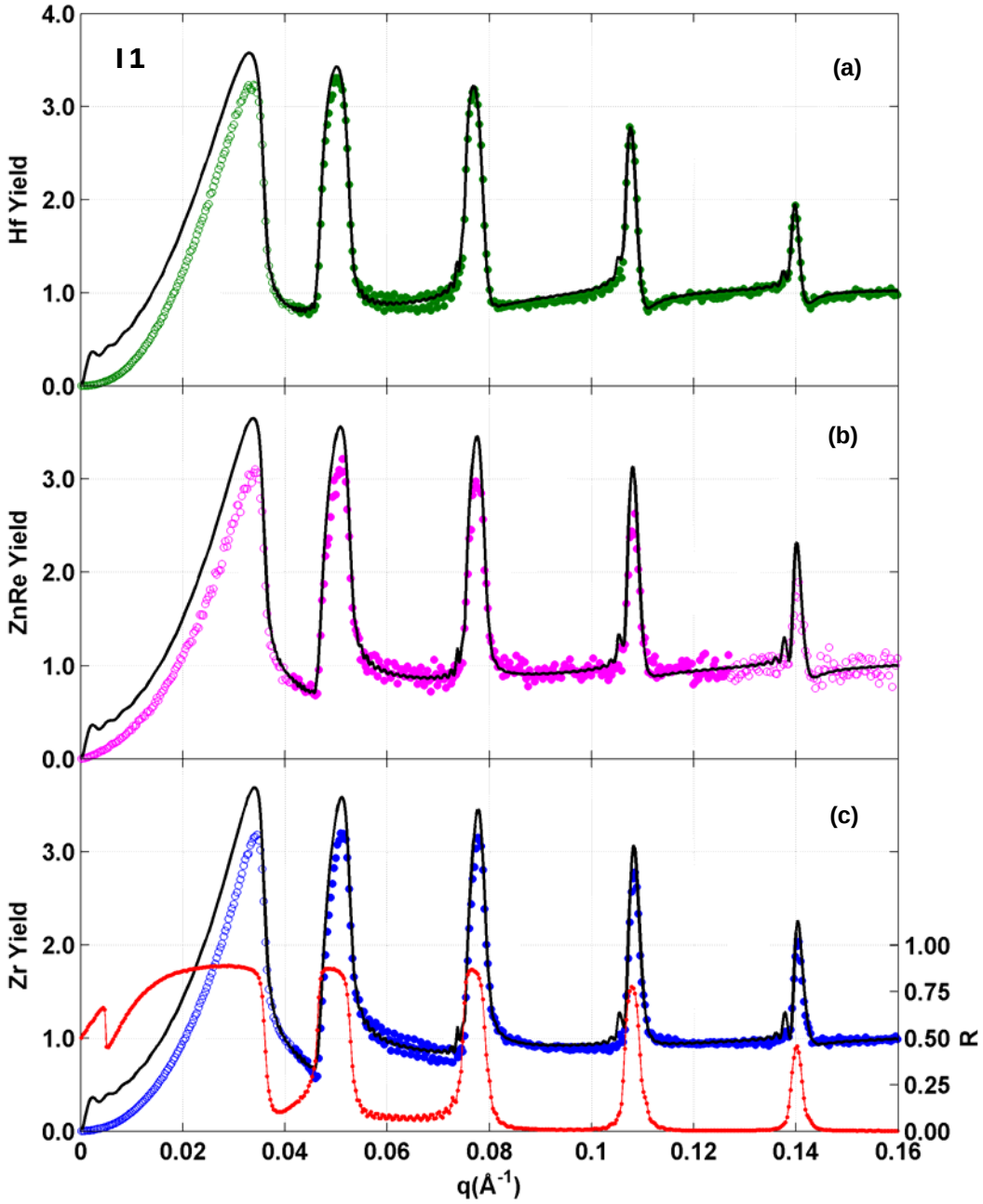

Figure 4.24 XSW results for film I1: Measured (open circles) and calculated (solid lines) for (a) Hf yield, (b) Zr yield and (c) Zr yield and XRR. All data were collected simultaneously during a single XSW scan

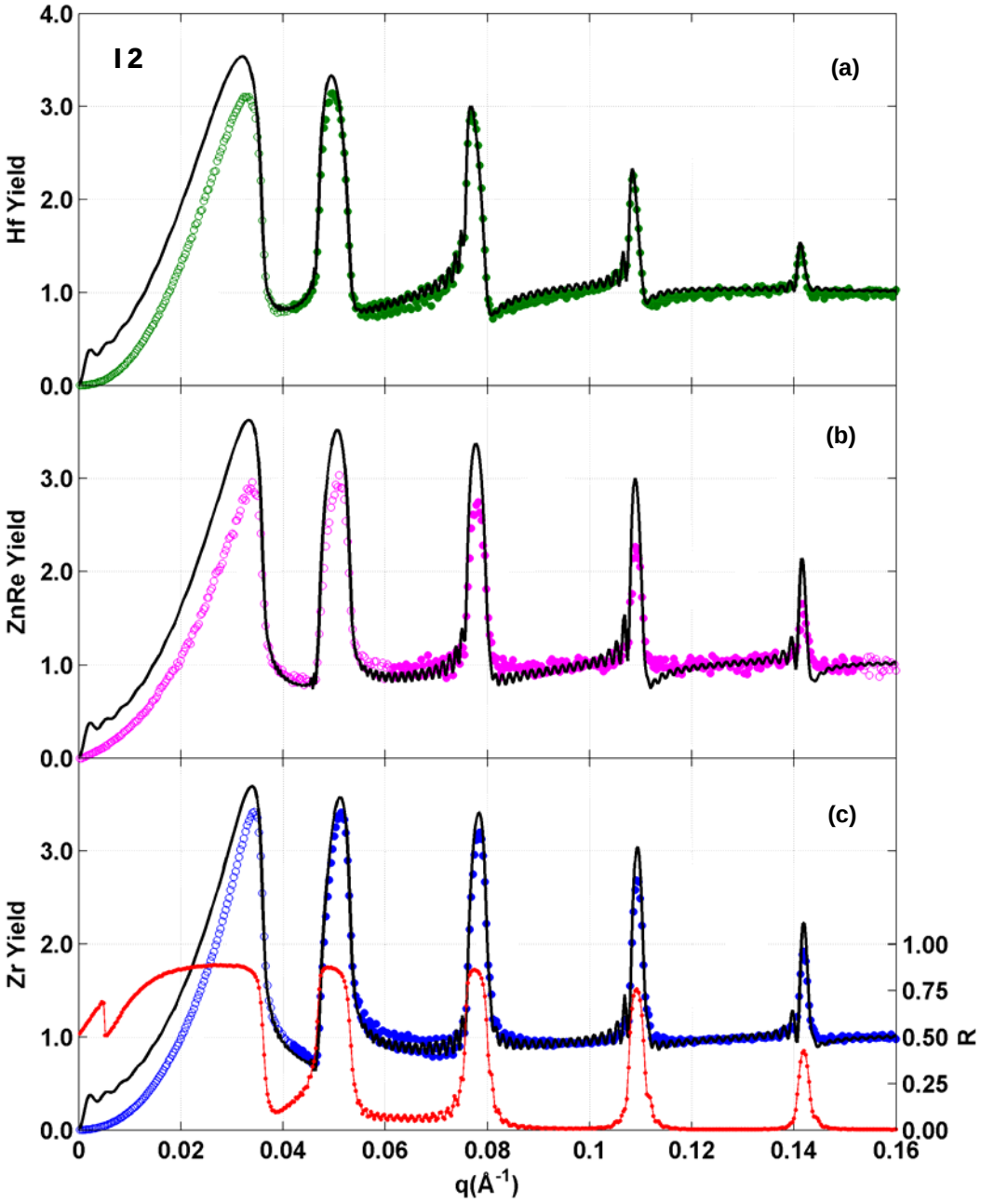

Figure 4.25 XSW results for film I2: Measured (open circles) and calculated (solid lines) for (a) Hf yield, (b) Zr yield and (c) Zr yield and XRR. All data were collected simultaneously during a single XSW scan

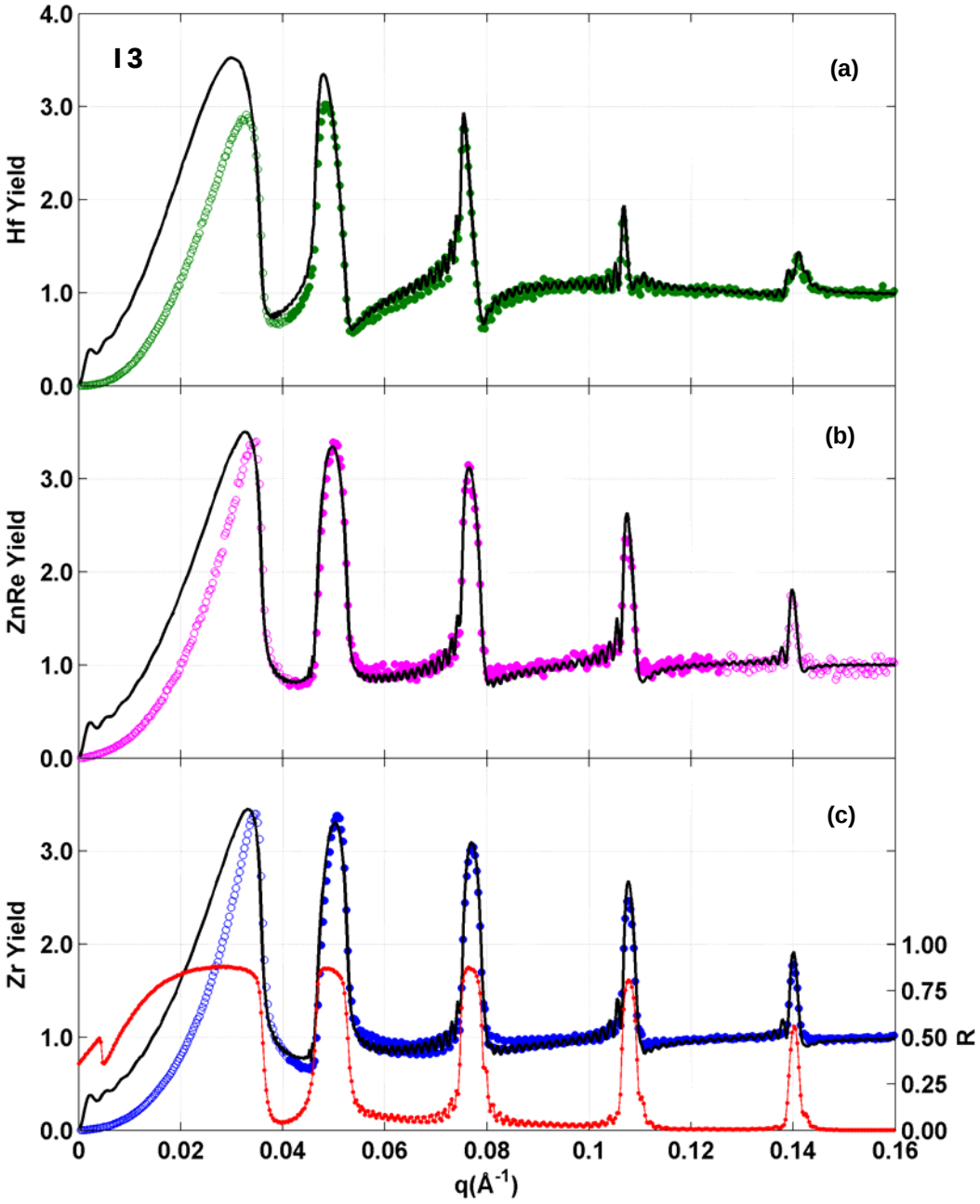

Figure 4.26 XSW results for film I3 Measured (open circles) and calculated (solid lines) for (a) Hf yield, (b) Zr yield and (c) Zr yield and XRR. All data were collected simultaneously during a single XSW scan

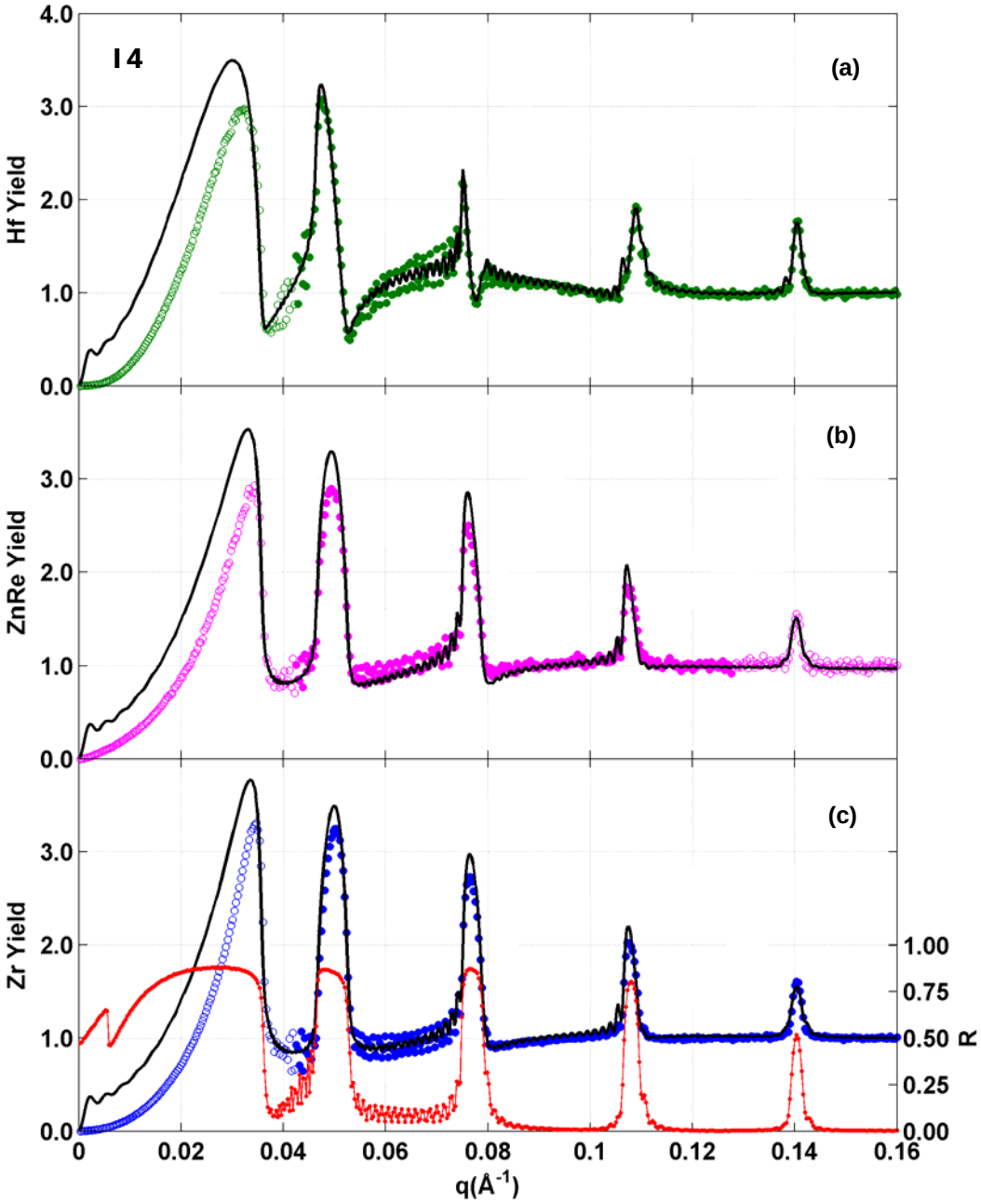

Figure 4.27 XSW results for film I4 Measured (open circles) and calculated (solid lines) for (a) Hf yield, (b) Zr yield and (c) Zr yield and XRR. All data were collected simultaneously during a single XSW scan

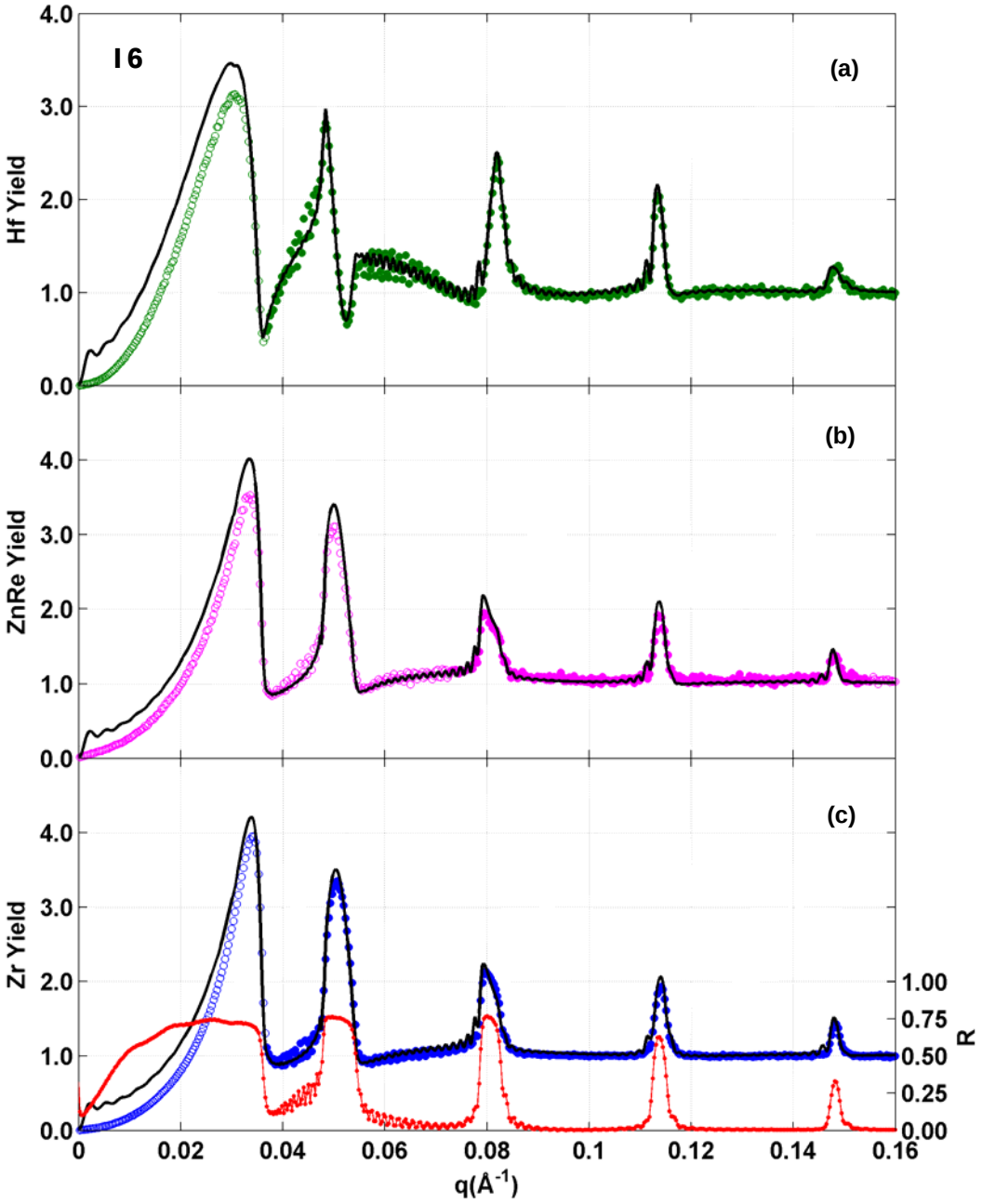

Figure 4.28 XSW results for film I6 Measured (open circles) and calculated (solid lines) for (a) Hf yield, (b) Zr yield and (c) Zr yield and XRR. All data were collected simultaneously during a single XSW scan

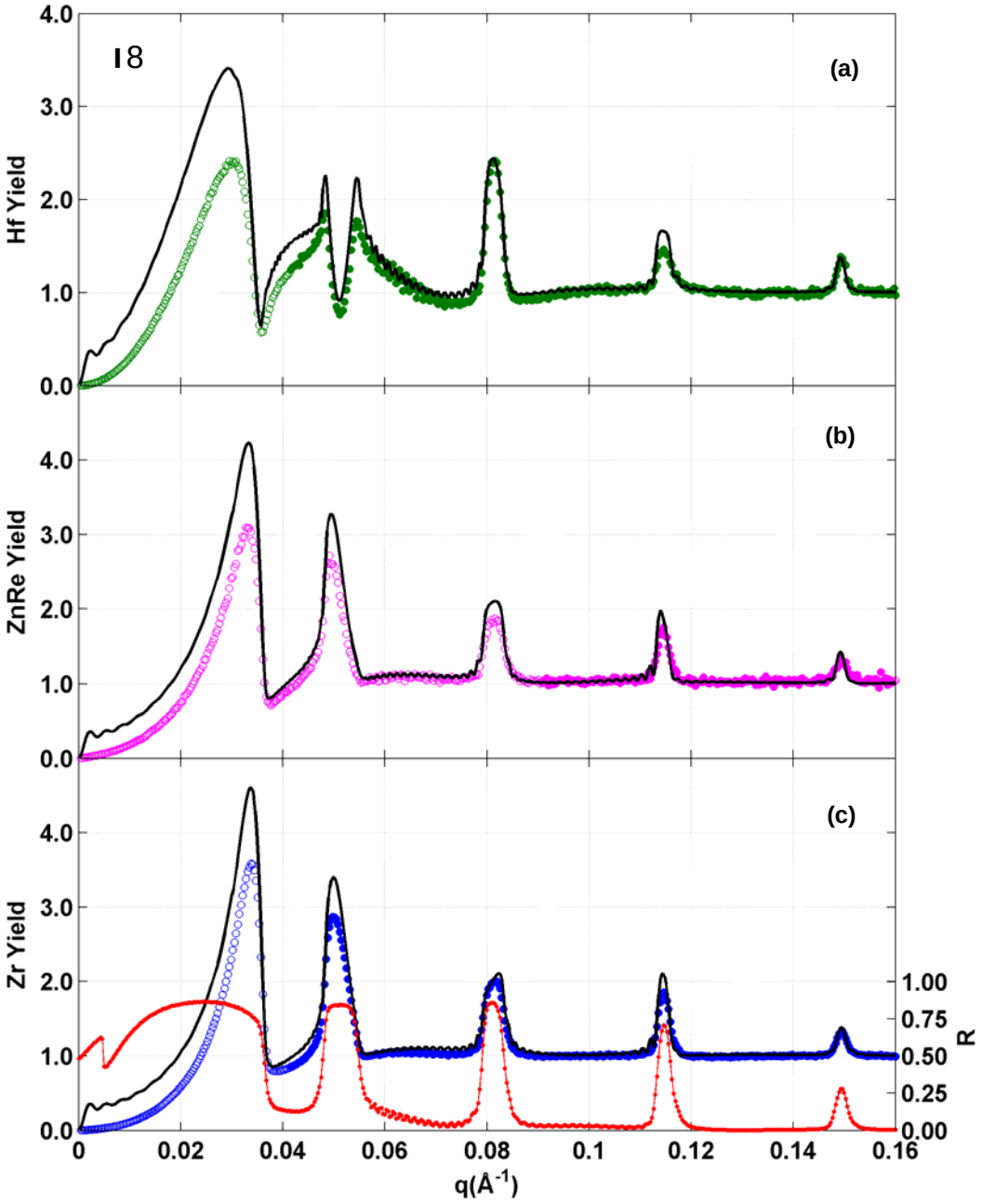

Figure 4.29 XSW results for film I8 Measured (open circles) and calculated (solid lines) for (a) Hf yield, (b) Zr yield and (c) Zr yield and XRR. All data were collected simultaneously during a single XSW scan

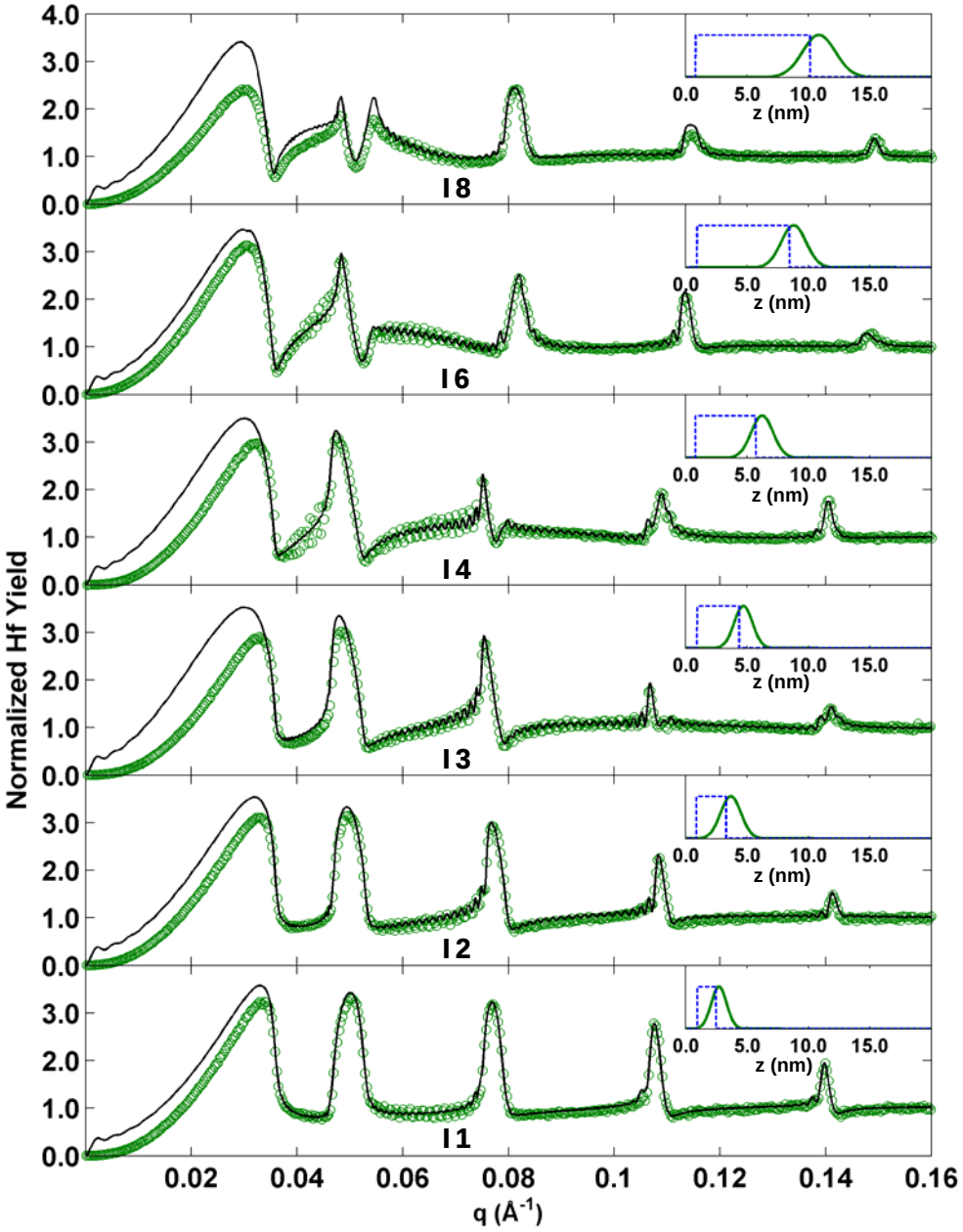

Figure 4.30: I-series XSW Hf results. Measured (open circles) and calculated (solid lines) Hf fluorescence yield of the I-series films. The atomic distributions are scaled vertically for clarity and are not proportional to the atomic coverages

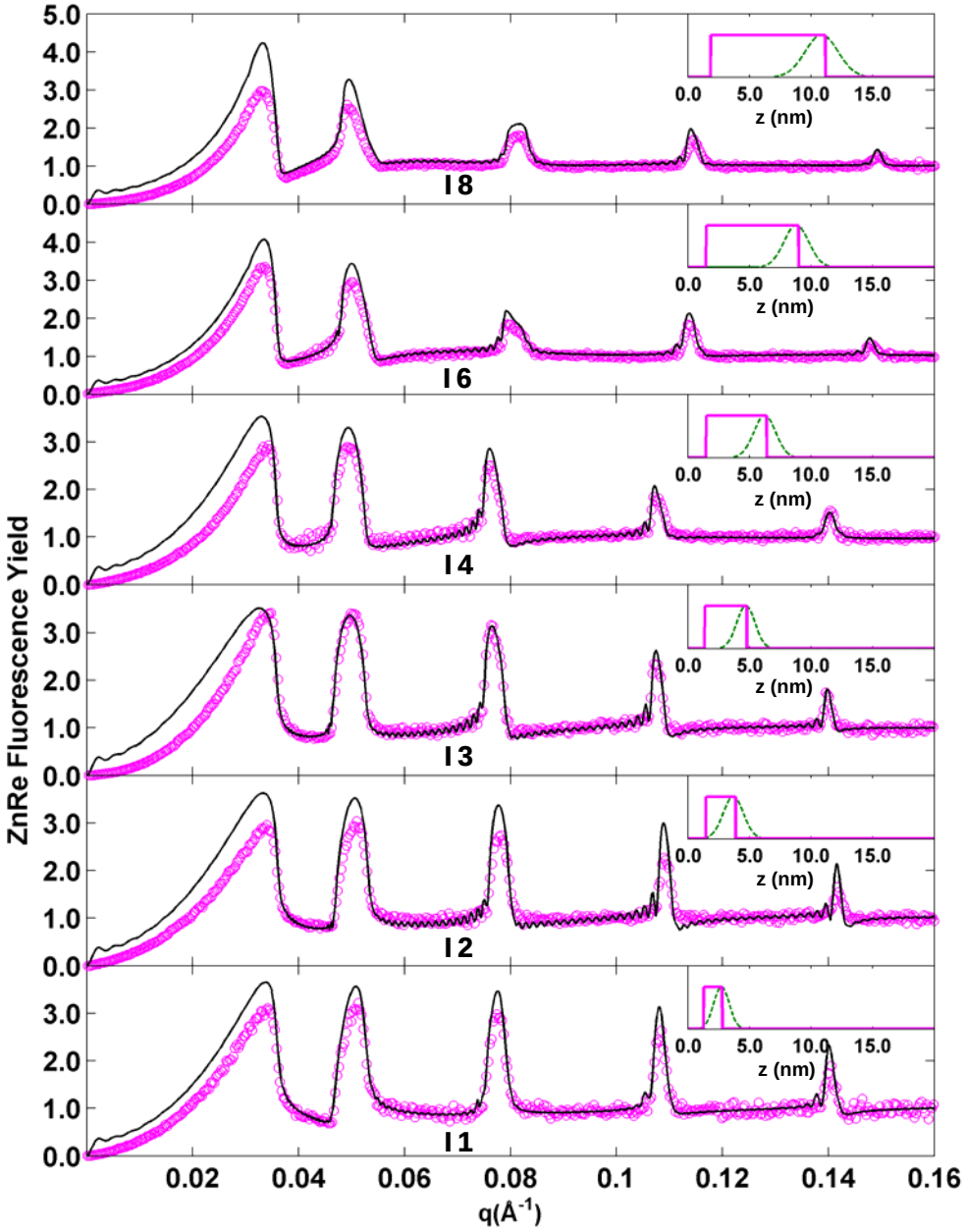

Figure 4.31: I-series XSW Zn/Re results. Measured (open circles) and calculated (solid lines) Zn/Re fluorescence yield of the I-series films. The atomic distributions are scaled vertically for clarity and are not proportional to the atomic coverages

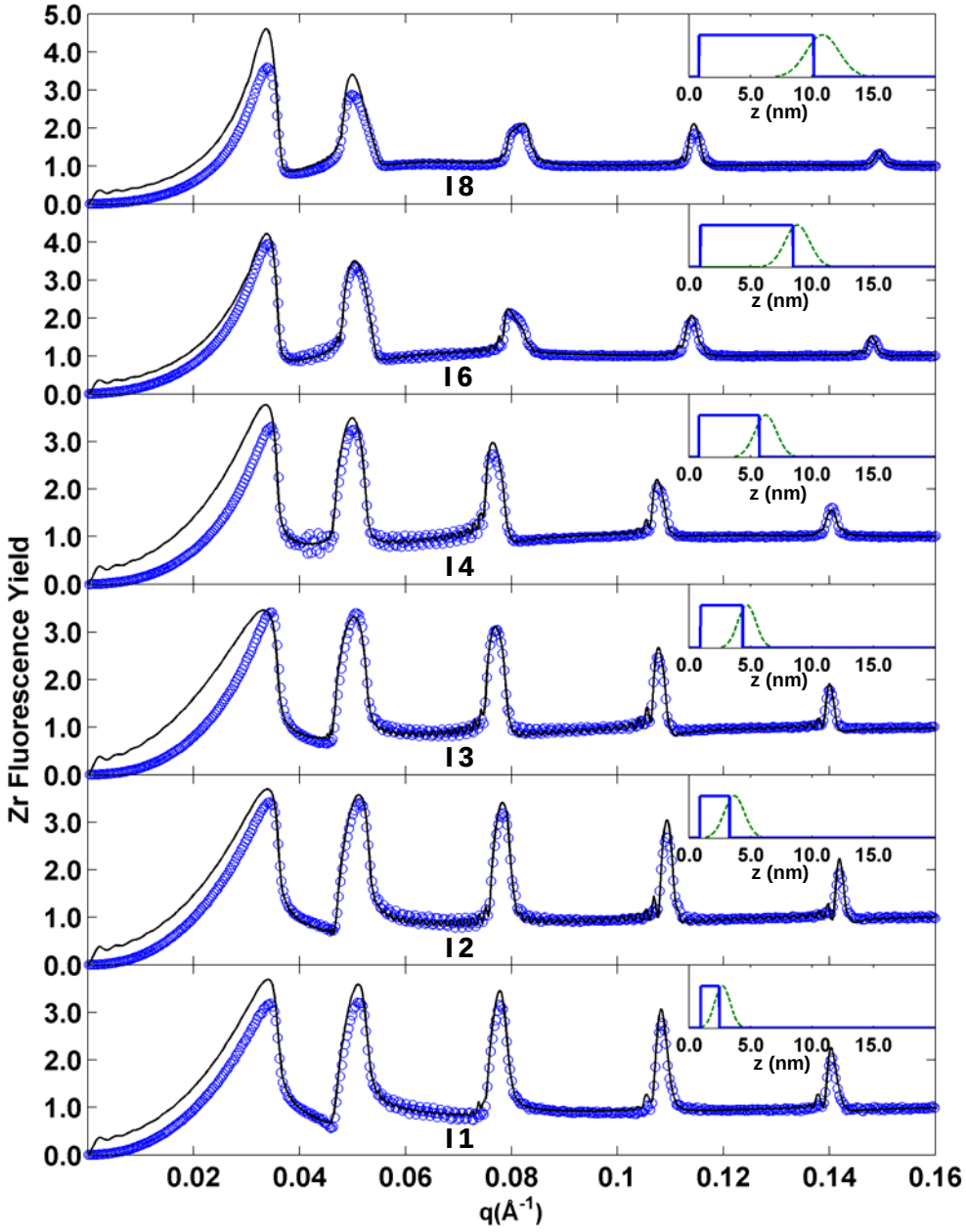

Figure 4.32: I-series XSW Zr results. Measured (open circles) and calculated (solid lines) Zr fluorescence yield of the I-series films. The atomic distributions are scaled vertically for clarity and are not proportional to the atomic coverages

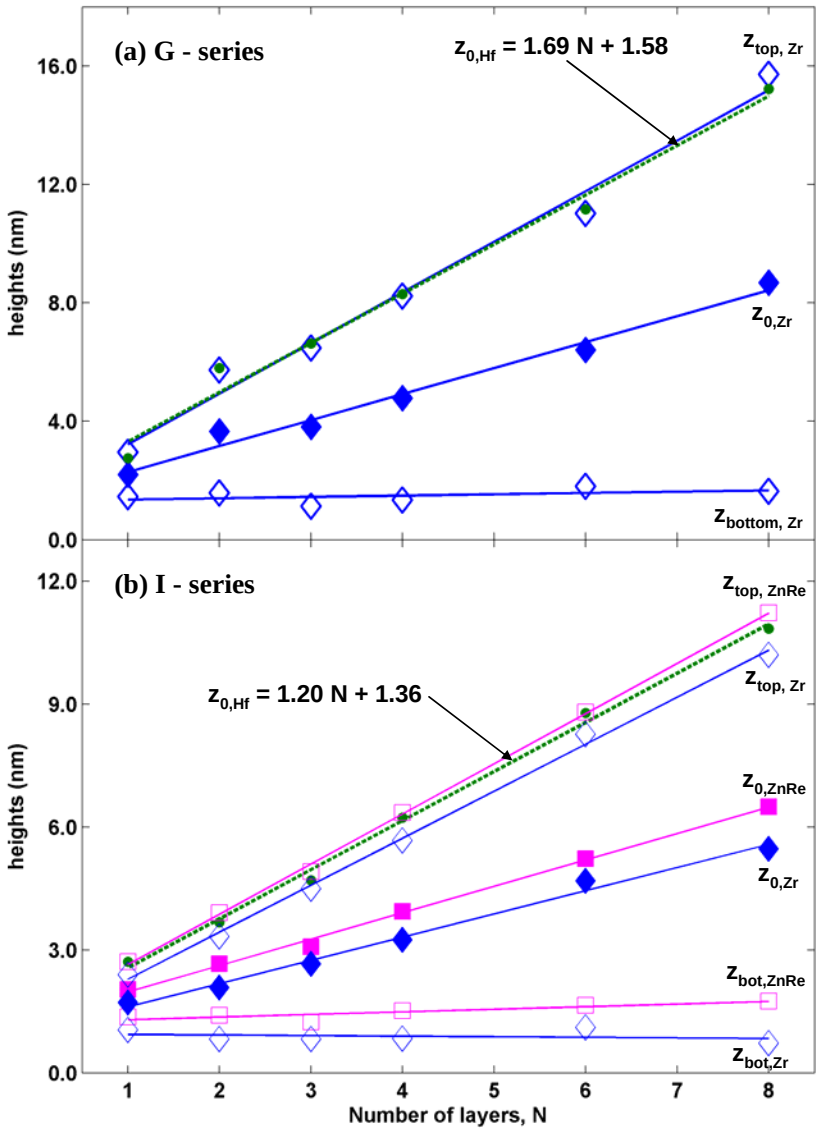

Figure 4.33: Modeled atomic heights for G- and I-series. The rectangular profiles for Zr and Zn/Re are shown by plotting the mid-height (filled diamonds for Zr, filled squares for ZnRe), top and bottom (open diamonds for Zr and open squares for ZnRe). The mean position z0, of the gaussian profiles for the Hf (closed circles).

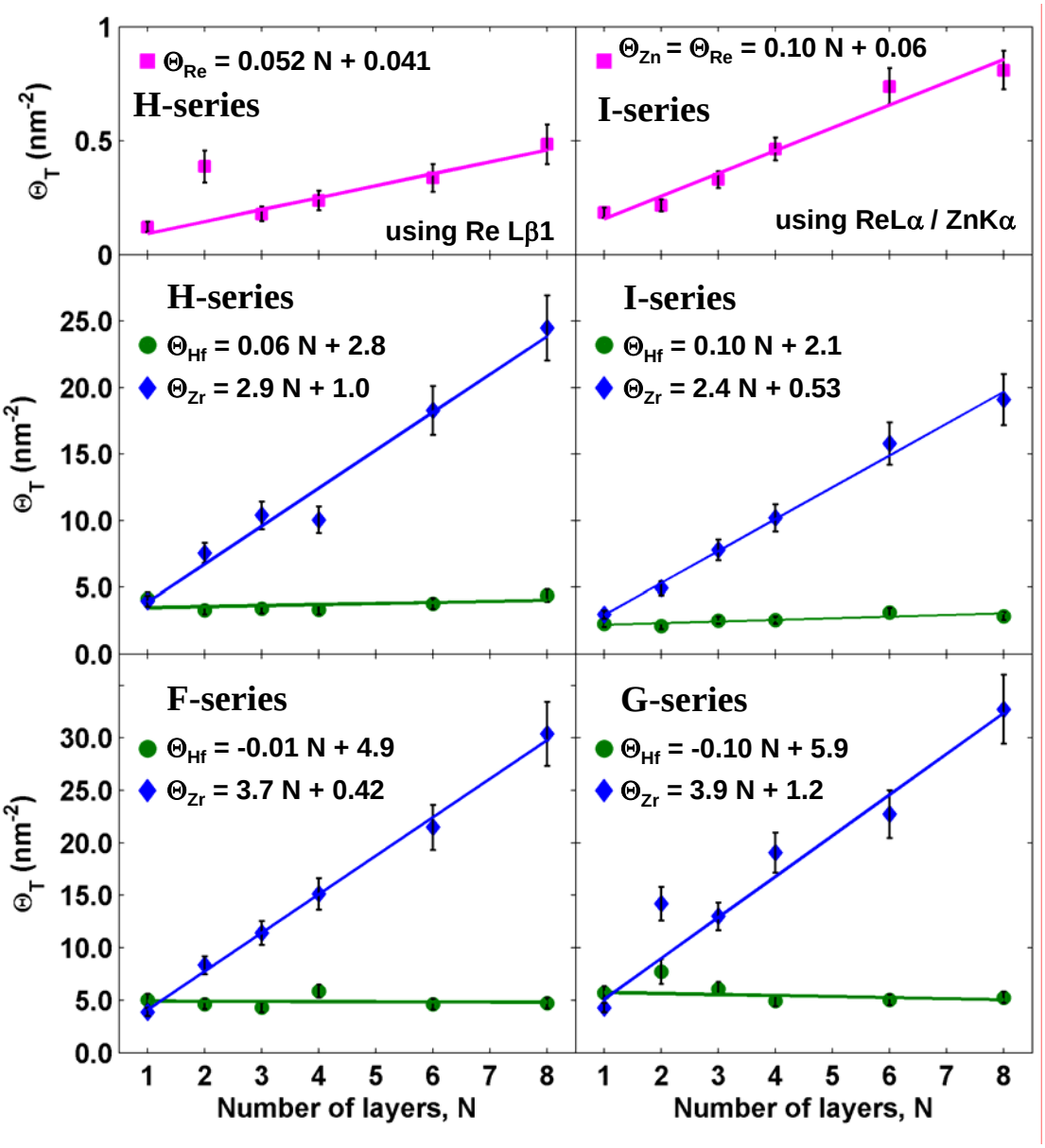

Figure 4.34: Atomic coverage of the F-I series films: XRF measured atomic coverages for Hf (filled circles), Zr (filled diamonds) and Zn or Re (filled squares) and χ^2 fits (solid lines).

profile and the bottom, mid-height and top of the rectangular profiles for Zr and Zn+Re where the top and bottom are calculated from the mid-height and width. For the G- and I-series XSW scans an As-implanted standard was used to calibrate the coverages based on off-Bragg fluorescence emission at q = 0.162 A^{-1}. The coverage results for the G and I series samples are also given in Table 4.3.

4.3.5 Discussion for the F-, G-, H-, and I-series

The 1,12-dodecanediylbis(phosphonic acid) layer series (F- and G-series) were chosen to provide a comparison of XSW analysis with previous published structure data. The XSW determined structural properties of the G-series are given in Figure 4.33a, where the Hf mean position, $z_{0,Hf}$ together with the position of the top ($z_{top} = z_0 + \Delta z/2$), middle ($z_0$) and bottom ($z_{bot} = z_0 - \Delta z/2$) of the rectangular profiles used to model the Zr are plotted. Also shown are χ^2 fits of each parameter. The χ^2 fit of the Hf mean position gives $z_{0,\ Hf}$ = 1.69 N + 1.58 (nm). The per-layer increase in thickness of 1.69 nm is in good agreement with previously published values for this same system [37]. The offset value of 1.58 represents the expected Hf mean position if it were used in place of Zr at the primer step. This value is higher than expected based on the length of a single APTMS/phosphonate/Zr moiety that was deposited as the primer layer and may be due to polymerization of the APTMS. The larger than expected offset is present in all of the samples in the F-, G-, H-, and I-series which were prepared together. For each sample in the G-series, the top of the Zr atomic distribution is found to be very close to the Hf mean position. The deviations of the Hf mean position from the linear trend are closely followed by the top of the Zr rectangular profile. This is compelling evidence that these deviations

represent true variation in sample structure. The average value of the bottom of the Zr atomic profiles is 1.49 nm which is close to the offset value of 1.58 nm of the Hf mean position.

While the overall trends indicated by the Hf mean position and Zr rectangular profile parameters are in excellent agreement with the expected layer structure, individual samples in the series exhibit significant variation from the trends. For example, consider the simplest case of the one layer sample, G1. From Table 4.3 note that the mean position of the Hf layer is z_0 = 2.8 nm compared to z_0 = 2.1 nm for the middle of the Zr distribution giving a separation between the Hf and Zr layers of 0.7 nm which is less than half of the per-layer thickness of 1.69 nm. The largest deviation from the trend is sample G2 whose Hf mean position is 5.81 nm. From this value a per-layer thickness of (5.81-1.58)/2=2.12 nm can be calculated which suggests that the 1,12-dodecanediylbis(phosphonic acid) molecules are nearly perpendicular to the surface. This in turn implies a higher packing density in sample G2 which is supported by the higher than average Zr and Hf atomic coverage for this sample (see Table 4.3 and Figure 4.34). The general observation is that while the overall trends suggested by both the Hf and Zr atomic profiles are in excellent agreement with the expected structure, there is significant variation of structure in individual samples.

The I-series is based on the porphyrin square molecule whose PO_3-to-PO_3 axial length allows a maximum metal-to-metal layer spacing of 2.5 nm as compared to 2.1 nm for the 1,12-dodecanediylbis(phosphonic acid) in the G-series. In Figure 4.33b the Hf mean position along with the top, middle and bottom of the rectangular profiles for both the Zr and Zn+Re atoms are plotted. The χ^2 fit of the Hf mean

position gives $z_{0,Hf}$ = 1.20 N + 1.36 (nm). The 1.20 nm per-layer value is considerably lower than the maximum value of 2.5 nm permitted by the porphyrin square in a perpendicular conformation. This is also lower than the XRR measured per-layer thickness of 1.61 nm from the identical sample D8. The deviation of the Hf mean position for any given sample in the I-series is considerably less than in the G-series indicating that this seems to be a preferred conformation for the porphyrin square. In Figure 4.33b the mid-height of the Zr and Zn+Re is given by the filled diamonds and filled squares, respectively. The Zn+Re mid-height is vertically offset from the Zr mid-height by an average value of 0.59 nm which is half of the per layer spacing of 1.2 nm. The analysis shows that XSW analysis can measure the offset between the rectangular distributions of Zr and Zn+Re in each sample in the series. This is a powerful confirmation that the ordering of Zr, Zn+Re and Hf in the I-series is precisely as we expect and is an excellent demonstration of the XSW method.

In Figure 4.34 the measured atomic coverage for the all of the samples in this study is plotted. The Hf coverage is essentially constant in any given series and is very close to the Zr coverage in the one layer samples. The average value of the Hf coverage in the G- and I-series is 4.9 and 5.4 nm^{-2}, respectively while in the F- and H-series it is 3.7 and 2.6 nm^{-2}, respectively. The greater capacity of the DDBPA based films compared to PSBPA films is expected since the larger molecular footprint of the PSBPA will have a much lower PO_3 surface density than the DDBPA. Since there are both Zn and Re atoms on the PSBPA molecules, the Zn or Re coverage provides a measure of the coverage of the PSBPA. In Figure 4.34 the slope of the χ^2 fit of the measured coverage shows that the per-layer coverage of PSBPA is 0.1 nm^{-2}/layer which in turn gives an average area per porphyrin square molecule of 40 nm^2

(given 4 Zn or Re per square). Each molecule would thus occupy a 6.3 x 6.3 nm area. From the measured per layer thickness of 1.2 nm a tilt angle of 60^o from vertical can be calculated assuming a 2.5 nm for the Zr-to-Zr distance based on Figure 4.2. The projected width of the tilted porphyrin square molecule would then be a $2.4 + 2.5\sin(60^o) = 4.6$ nm assuming 2.4 nm is the distance between opposing zinc centers (i.e. neglecting any inward or outward bowing of the pyridyl(ethynyl)porphyrins and neglecting the van der Waals thicknesses of the porphyrin planes) (see Figure 4.2). Thus the measured coverage agrees reasonably well with the footprint implied by the measured per-layer thickness. Table 4.3 shows that the Zr or Hf coverage is nearly 30 times greater than the Zn or Re coverage implying that there must be alternate modes of incorporation in these films. One possible mode is an extended 2-d sheet of ZrO_2 or HfO_2 where a fraction of the O atoms are from the phosphonate groups and the remainder comes from the water in the solution used for the deposition of the Hf or Zr. Since there is no heavy atom in the DDBPA molecule, we were not able to measure the coverage of this molecule with our present methods.

The results of the XRR analysis of the F- and H-series samples are given in Table 4.2. Figure 4.13 shows plots of the XRR measured and χ^2 fit film thickness along with the χ^2 fit of the Hf mean position for the XSW series. The XRR determined film thickness is larger than the Hf mean position. This is to be expected since the Hf mean position does not measure the maximum in the electron density gradient as does the XRR method. The location of the maximum of the electron density gradient can be estimated from the Hf atomic profile to be at $z_0+\sigma$ which falls close to the XRR measured film height. The per-layer increase in film thickness indicated by the

slopes of the Hf mean position and XRR determined film heights are in general agreement but it is important to note that the measurements come from separate sample series using different initial surfaces, i.e., sputter deposited Si for the XSW substrates versus single crystal Si for the XRR series. The XRR determined surface roughness in Table 4.2 follows the same trend as the width of the Gaussian profiles for the Hf, whereas the interface roughness is consistently in the 0.2-0.5 nm range for the initial substrate roughness. For both the XRR and XSW series, the very rapid roughening of the surface implies a large variability in tilt conformation of the phosphonate components.

The final information from the XRR analysis is the overall electron density of films which is given in Table 4.2. The average electron density is $0.73\rho_{Si}$ and $0.69\rho_{Si}$ for the DDnR and PSnR series, respectively. The slightly lower electron density for the PSnR series is consistent with the more porous structure expected for these sample but far higher than expected based on the measured atomic coverage of Zr, Hf and Zn+Re in the PSnX series. In Table 3.2 the electron density is calculated according to $(\rho/\rho_{Si})_{calc} = (\Theta_{Hf} \times 72 + \Theta_{Zr} \times 40 + \Theta_{PS} \times 2284)/699/t_F$ (72, 40 and 2284 are the number of electrons in the Hf, Zr and porphyrin square components, respectively and 699 is the electron density of Si). The value of the electron density based on the measured atomic coverage is only one third of that measured by XRR. This is consistent with the previous finding[59] that there must be additional material such as solvent molecules present in these films. A similar conclusion about an excess electron density in the case of the DDBPA series cannot be made since there are no heavy atom markers with which to measure the coverage.

4.3.6 Primer Layer Characterization

An important question regarding metal-phosphonate films is whether the metal atom density in each metal layer depends on the PO_3 density. To answer this question the Zr coverage on the PO_3 primed surface can be compared to the Hf coverage which involves PO_3 groups from the phosphonate molecules only. The primer layer preparative steps are shown schematically in Figure 4.35. All samples in this study were prepared using this substrate priming procedure. Due to a weak P X-ray fluorescence signal, our XRF was not able to directly measure the coverage of P in the primer layer. Samples A1, A2, F1, G1, H1, and I1 from this chapter (See Figure 4.4.), as well as sample B1a from Chapter 5 contained Zr only in the primer layer. From these samples, the surface density of PO_3 functional groups can be estimated by measuring the Zr atom coverage and assuming one Zr for each PO_3 group. XRF measured coverages for these seven samples were in the range of 1.0 to 4.3 Zr atoms/nm^2. It is well known that the fully hydroxylated SiO_2 surface has 5 OH groups per nm^2 [60]. Each APTMS molecule can potentially occupy one to three OH sites to imply a coverage range of APTMS/PO_3/Zr moieties from 1.7 - 5 Zr/nm^2 if all OH groups are bound to APTMS molecules. The observed Zr coverage result suggests that the primer APTMS/PO_3 coverage varies somewhat but falls within the limits suggested above. In Figure 4.35b we show the XSW results for the position of the Zr atoms from all of the samples where the Zr is present in only a primer layer. Samples B1a, (A1 & A8) and (G1 & I1) were prepared on separate occasions but using essentially identical procedures in air-free glassware. Apparently, subtle differences in preparative details are likely responsible for the variation in the coverage and thus position of the Zr atoms in the primer layer.

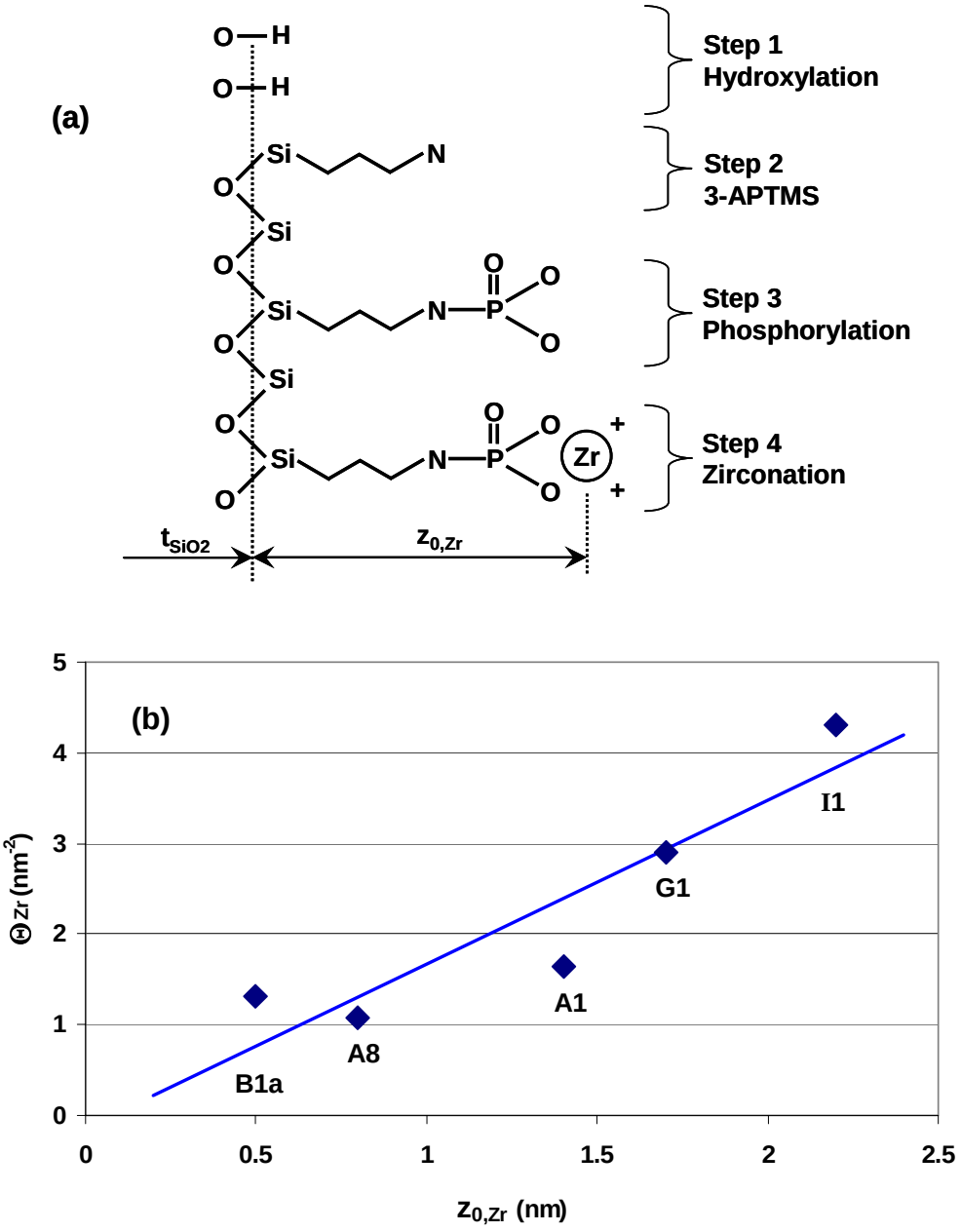

Figure 4.35: Primer Layer Structure. The preparative steps in the primer layer are shown in (a) with the details given in the text. In (b) the XSW measured and χ^2 fit (solid line)of Zr mean position z_0 is shown.

4.3.7 Metal Phosphonate Coordination Chemistry

The exact bonding structure between the PO_3 groups and the metal atoms is not known. Consider the assumption of one Zr/PO_3 group as the chemical stoichiometric ratio. (See Tables 4.1 to 4.3 for a list of XRF measured heavy atom coverages.) For sample D8 with N = 8 layers, the Re (or Zn) measured atomic coverage can be converted to a pe-layer coverage of 0.33 Re /nm^2, which corresponds to a macromolecular footprint of 12 nm^2. (Here 4 Re (or 4 Zn) per macromolecular square is assumed as shown in Figure 4.2) This footprint would correspond to a 3.5 x 3.5 nm^2 square, which is a reasonable random packing density, given an approximate length of 3.2 nm for the OC-Re-porph-Re-CO shown in Figure 4.2. The complexation, at the end-groups of the diphosphonic acid porphyrin molecule in Figures 4.2 and 4.3(right-hand-side), is shown schematically as one metal ion per PO_3/PO_3 junction. This is based solely on charge balance (at least for zirconium(IV) and hafnium(IV)). If metal ions retain charged halo, oxo, or hydroxo ligands, however, the metal:phosphonate ratio would likely be higher. In layered Zr/phosphonate compounds featuring sterically undemanding alkane spacers, continuous 2-D Zr/phosphonate layers, rather than discrete junctions, are formed.[61] In these layers, each oxygen atom of a given phosphonate binds to a different zirconium ion, i.e. the chelation motif simplistically sketched in Figure 4.4 is absent. If chelation is likewise unused here, and if Zr ions retain an oxo ligand, an alternative stoichiometry, more closely structurally resembling the known 2-D layers, would be two zirconium ions per PO_3/PO_3 junction.

Based solely on this expected complexation (two metal ions per junction) and the molecular footprint, the Zr, Hf or Y atomic coverage per layer, in for example

sample D8, should be 0.65 atoms/nm^2. The measured Zr and Hf coverages per layer in sample D8 are respectively 2.5 and 4.8 times higher. This excess and similar Zr, Hf or Y excesses in the other samples, indicates that these metal ions have additional modes of incorporation in these films.

4.3.8 Performance of the Large d-Spacing LSMs

In this thesis the use or large d-spacing LSMs is reported for the first time. It is strongly desirable to be able to use the multiple Fourier components obtained in the XSW scans to apply a direct methods determination of atomic distributions. In this section the performance of the LSMs for this purpose will be considered. In the G- and I-series films (see Figures 4.16 to 4.32, XSW scans covering 4 Bragg reflections were presented. A 5th Bragg peak was measured but provided no additional information and was not shown. In the earlier XSW work using samples A1 and A8, characteristic XSW modulations were observed through the 4th Bragg peak. In the G-series and I-series, the roughness and general imperfection of the films did no require more than the 3rd Bragg peaks. To evaluate the sensitivity of the LSM as a probe of structure, several hypothetical atom distributions were constructed and the yield was computed. In Figure 4.36 alternate models for the Zr distribution of sample film I8 were considered. In particular the Zr distribution shown in Figure 4.36 was constructed by summing the Gaussian distributions measured for Hf in samples I1, I2, I3, I4, I6, and I8. The positions for the 5th and 7th layers were interpolated from the I4, I6 and I8 films. The summed distributions were then shifted down by one half of the layer thickness or 0.6 nm. The calculated yield for the distribution thus

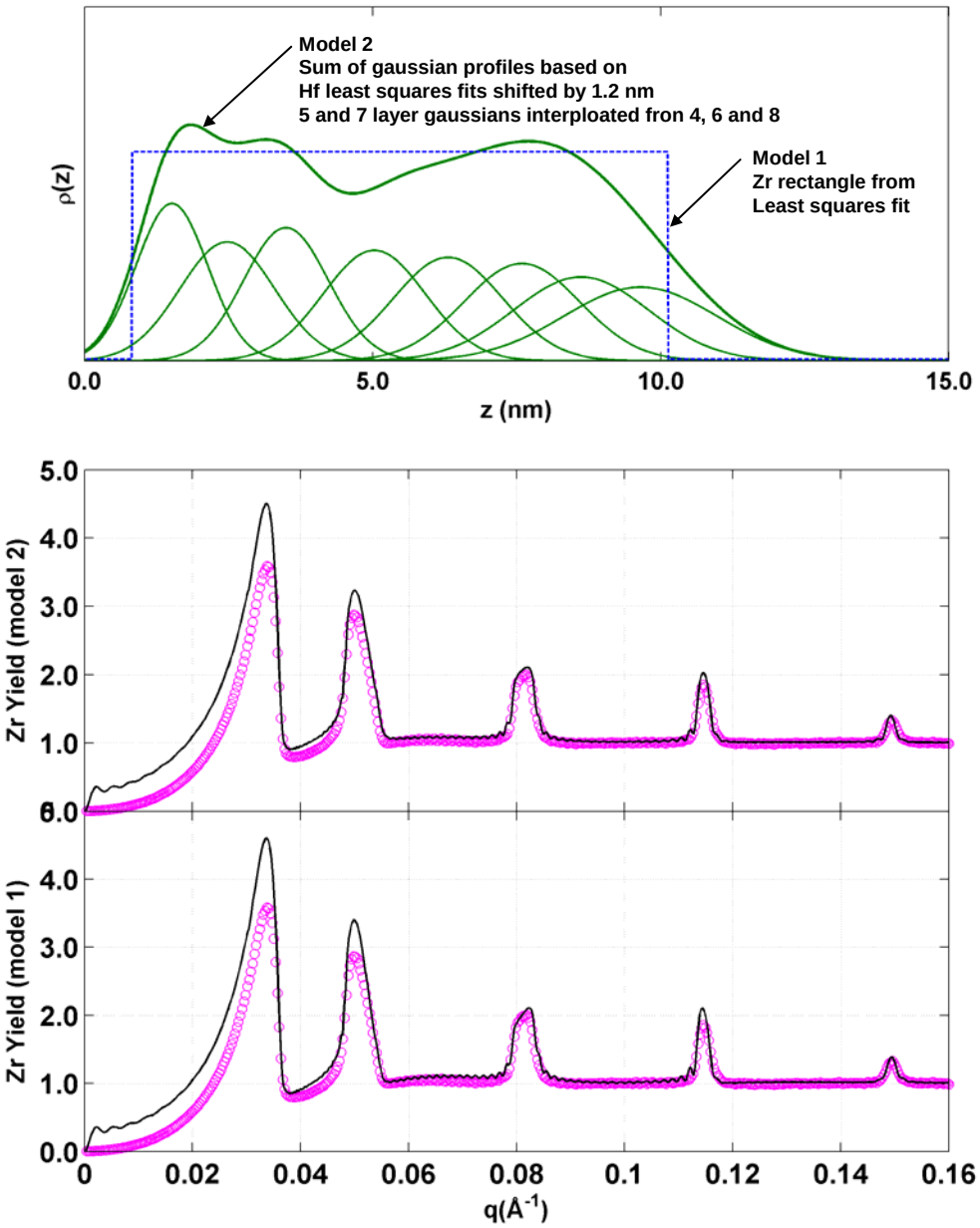

Figure 4.36: Alternate models comparison for film I8: XSW calculated yield comparison of film I8 for a simple rectangular distribution (dashed line) versus a model constructed from Hf position data. The calculated yield for the two models shows a nearly identical result.

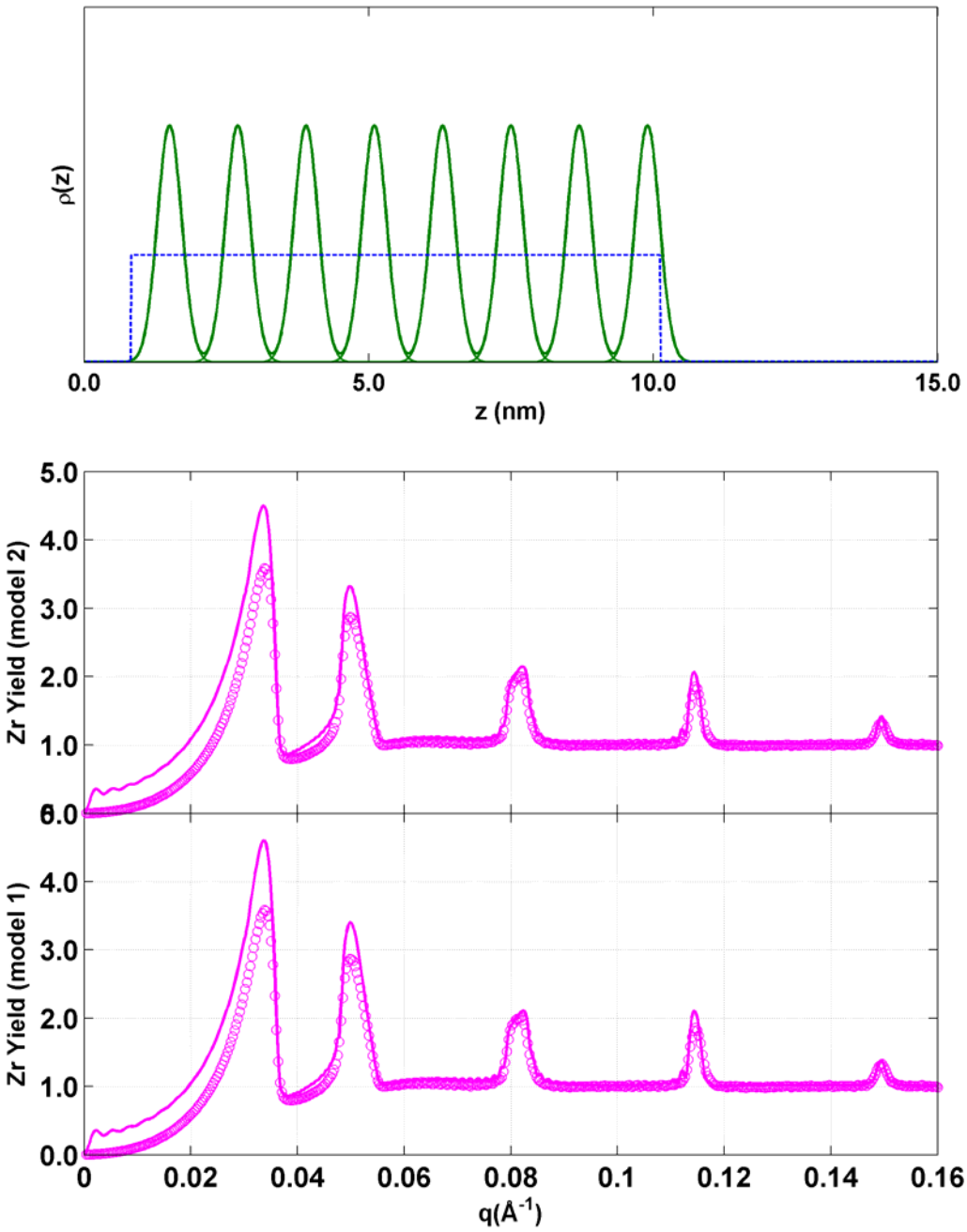

Figure 4.37: Sensitivity of model to layered vs single slab models. XSW calculated yield comparison of film I8 for a simple rectangular distribution (dashed line) versus a model constructed from the expected layered Zr structure.

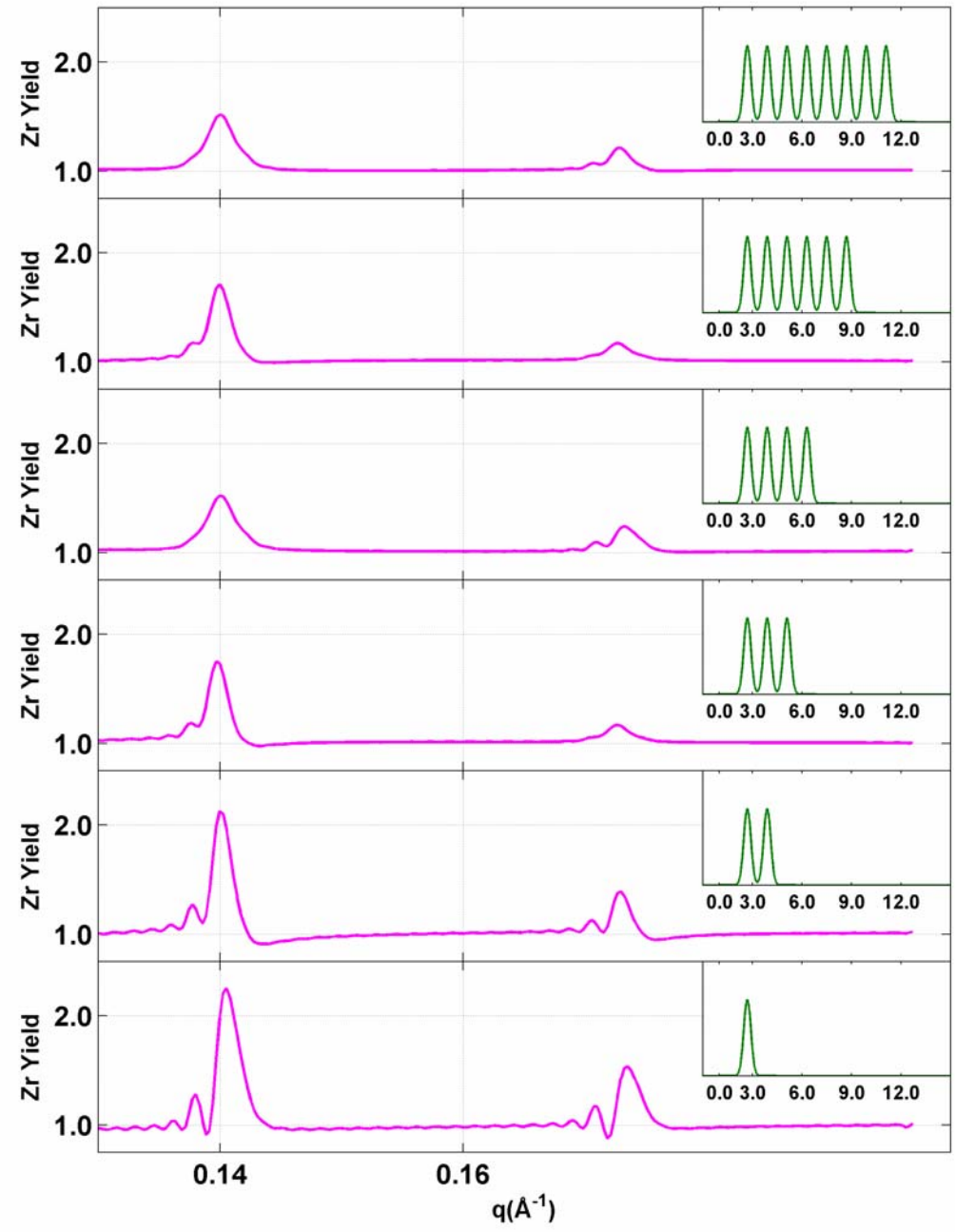

Figure 4.38: Sensitivity of LSM to sense layered structure. XSW calculated yield comparison a sequence of layered films based on the I-series. The calculation is shown for the 4th and 5th Bragg peaks.

constructed is compared in Figure 4.36 to the simple rectangular model used earlier shows very little difference in the two results. In Figure 4.37 a distribution was constructed for the Zr based solely on the $\chi 2$ fit of the Zr mean position $z_{0,Zr}$ (see Figure 4.33b). Once again very little difference between the rectangular and constructed models is visible. In Figure 4.38 we show the calculated yields for a series of Zr atomic distribution constructed as in Figure 4.37 but shown for the 4^{th} and 5^{th} order Bragg reflections. There is apparently some contrast visible in the series of yields suggesting it may be possible to resolve this level of detail using long period LSMs.

4.4 Conclusions

In this chapter it was shown that long-period XSW is a very useful probe of the structure of layer-by-layer assembled metal phosphonate films, providing a simultaneous measurement from multiple atomic distribution profiles of various shapes and sizes over length scales of 1 to 20 nm. When combined with XRF and XRR, the ability to directly evaluate important assumptions about film chemistry and quality is made possible. In the layer series based on 1,12-dodecanediylbis-(phosphonic acid) the per-layer thickness was found to agree with previously published values and metal layer atom densities of about 5 nm^{-2} were observed. The Hf metal atom distributions showed that the surface roughness increases rapidly with layer number and individual samples showed large variations from the general trends but stayed within the constraints imposed by molecule length or maximum layer spacing. In the porphyrin square I-series a 1.2 nm per layer spacing indicating a 60^{o} tilt angle of the walls of the porphyrin square away from the surface normal

which differed from the 1.69 nm per layer observed in sample D8. However, in both cases, the tilt implied by the per-layer thickness agreed reasonably well with the footprint implied by the measured atomic coverage emphasizing why it is so important to be able to measure both the atomic distribution and coverage. The layer density of Hf and Zr in the porphyrin square layer series was ~30 times higher than the PO_3 group density so that the primary mode of incorporation of the metals Hf and Zr is one other than attachment to the PO_3 groups and is probably a 2-d sheet incorporating the O atoms of the PO_3 groups as anchor points. The XRR measured film thickness was found to be consistent with the XSW determined film thickness but the XRR measured electron density indicated the presence of additional components in the films not accounted for by the deposited metal or organophosphate components. The large *d*-spacing LSM X-ray mirrors used in this study have been shown to be excellent probes of nano-scale structure.

Chapter 5: Hg-poly(U) Adsorption to Charged Surfaces

5.1 Introduction

The adsorption of poly-electrolytes to charged surfaces is a classical topic in physics that requires an understanding of the complex balance of electrostatic and entropic forces. Interest in this topic has been driven by applications in biophysics and colloid science but more recently advances made in nano-scale engineering have placed more importance on these processes as nano-architectures involving DNA molecules are developed[62-64]. Poly-electrolytes are most commonly handled and assembled in aqueous solution in which the pH and ionic composition are used to control the behavior of the polyelectrolyte. Strongly charged chains, including single and double stranded DNA, are usually water soluble in monovalent salt solutions. While condensation of counterions along the backbone of the chains reduces their effective and electrostatic repulsion, the chains retain an overall charge and therefore remain water-soluble. In the presence of multivalent cations of valence $z \geq 3+$, however, the chains condense (precipitate) into dense neutral cation-polyelectrolyte aggregates within some range of multivalent cation concentration[65]. The reversibility of multivalent cation-induced polyelectrolyte condensation by controlling the ionic strength of the solution makes the process useful for DNA delivery applications. Reversible adsorption of strong negatively charged chains to negatively charged surfaces via multivalent cations is a powerful technique to manipulate polynucleotides that is not well understood.

Experimental studies of the adsorption of polyelectrolytes are almost exclusively done using atomic force microscopy (AFM) which can be performed *in-situ*. An inherent limitation of the AFM technique is the requirement for a robust attachment of the polyelectrolyte molecules; otherwise, the imaging fails because mobile or loosely attached molecules create image defects. Neither can AFM provide any information about the counterions that may be involved in the adsorption process. The verification of many predicted regimes of DNA adsorption that involve partial attachment, loose attachment, or ball and chain conformations are great challenges for AFM techniques. An analytical determination of the distribution along the surface normal for both the DNA and counterions is a highly desirable result for the verification of theoretical predictions. For this purpose, the XSW technique presents a good opportunity to compliment AFM studies. In this Chapter, the conditions and physical reasons for polyelectrolyte adsorption onto like-charged surfaces via cations are determined by following the polynucleotide adsorption process in-situ with X-ray standing waves and by theoretically analyzing the process.

5.1.1 DNA Condensation in Bulk Solutions

It has been shown that in bulk solution polyelectrolyte molecules can be reversibly condensed by multivalent counterions. The condensation of DNA by spermine (3^+) [65] and polystyrene sulfonate by multivalent salts [66] reveals that the condensation only occurs when the counterion and polyelectrolyte concentrations lie within certain bounds. An example of the bulk condensation behavior of DNA [65] is provided in the phase diagram shown in Figure 5.1 for the DNA + spermine + monovalent-salt system. Condensation of DNA by spermine was observed in the

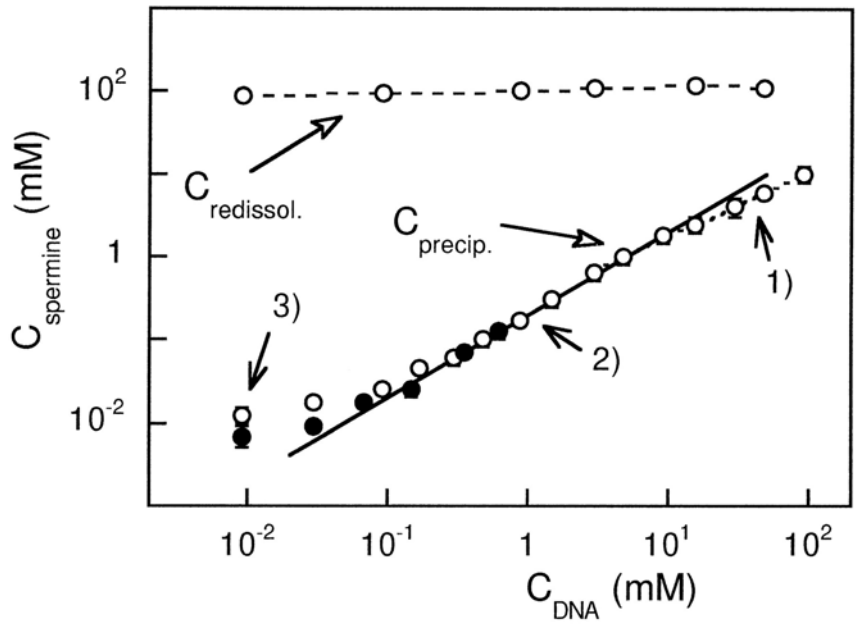

Figure 5.1: Spermine concentrations $C_{precip.}$ and $C_{redissol.}$ versus DNA concentration. Precipitation and re-dissolution conditions were obtained for solutions of 150-bp fragments diluted in TE buffer and precipitation conditions for DNA solutions. The lines indicate three different fits: solid line, constant ratio $C_{precip.}/C_{DNA}$ = 0.20 ± 0.02; dashed line for the precipitation, a power law $C_{precip.}$ C_{DNA}0.77 ± 0.03; dashed line for the re-dissolution of the 150-bp fragments, a constant $C_{redissol.}$ = 105 ± 10 mM. Figure taken from reference [65].

region between the upper and lower lines. In general, the addition of spermine to a solution with DNA caused precipitation when $C_{spermine} \geq 0.20(2)\ C_{DNA}$ with re-dissolution occurring upon further addition of spermine when $C_{spermine} \geq 105(10)$ mM. The observed condensation behavior was explained by an electrostatic “ion-bridging” model and is controlled by the density of adsorbed positively charged counterions (spermine) along the negatively charged DNA backbone. The details of condensing

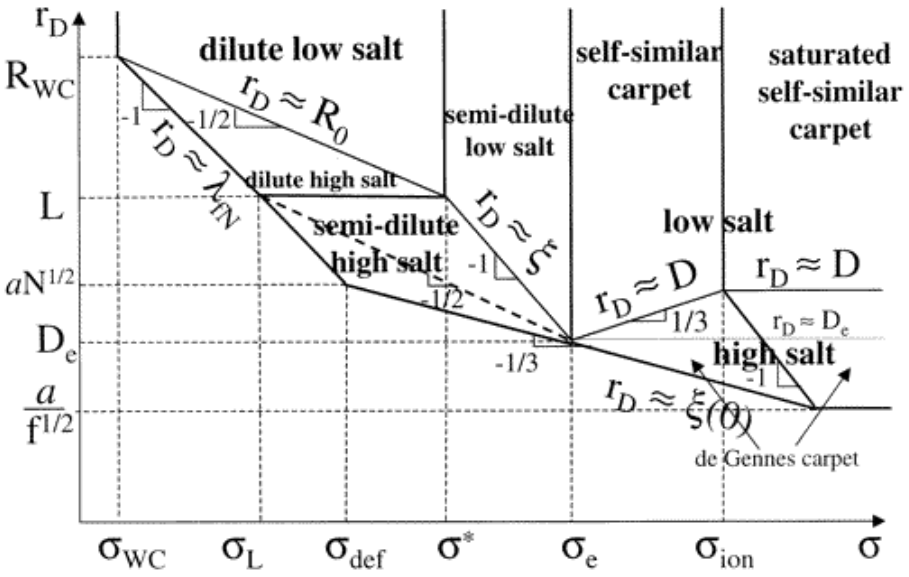

Figure 5.2: Adsorption diagram of polyelectrolyte chains in a salt solution as a function of surface charge density and Debye radius r_D. Figure taken from reference [69].

behavior depend on the charge of the polyelectrolyte and counterion and the probability of adsorption of the counterion to a monomer of the polyelectrolyte. Adding a monovalent salt to the system such as NaCl introduces a competition for adsorption sites narrowing the limits within which condensation can take place. By analogy to the observed bulk solution behavior, condensation of a polyelectrolyte to a charged surface is expected to follow a similar behavior but where we need to consider separately both positively and negatively charged surfaces. The adsorption of polyelectrolytes to an oppositely charged surface has been treated theoretically[67-69] with the prediction of a very complex phase diagram as shown in Figure 5.2. Here multiple regimes are predicted which depend on the length scale of charges along the polyelectrolyte, monovalent salt concentration and surface

charge density. Two-dimensional as well as three-dimensional conformations with the adsorbed polyelectrolytes extending above the surface are predicted.

5.1.2 Adsorption of Polyelectrolytes to Positively Charged Surfaces

Polyelectrolyte adsorption to oppositely charged surfaces has been extensively studied both theoretically[67-69] and experimentally[70-73]. The adsorption, controlled by the surface charge density and the ionic strength of the solution, is due to the entropy gained by the release of the surface and polyelectrolyte condensed counterions and by the strong ionic correlations formed in the dense surface-polyelectrolyte layer. The adsorption of DNA to a positively charged surface of dipalmitoyldimethyl ammonium propane (DPDAP) results in very high adsorption densities [70, 72] as shown in the AFM image in Figure 5.3 where the reported surface charge density was $4x10^{-5}$ C/cm^2 = 2.5 nm^{-2}. The effect of monovalent salt concentration did not have significant effects on the density of condensed DNA but did affect AFM image quality and lowered the incubation times required to achieve fully packed DNA on the surfaces. The bright spots in the AFM image in Figure 5.3 are imaging defects attributed to free ends of the DNA molecules extending above the condensed layer. The concentration of DNA adsorbed to the surface also does not depend on the free solution concentration of DNA or monovalent salt and similar images were reported in de-ionized water. Cationic surfaces, prepared by functionalization with amine-terminated species have also been used to adsorb DNA[71]. However, in this case the surface density of adsorbed DNA was much lower than on the DPDAP surface due mainly to the much lower surface charge density.

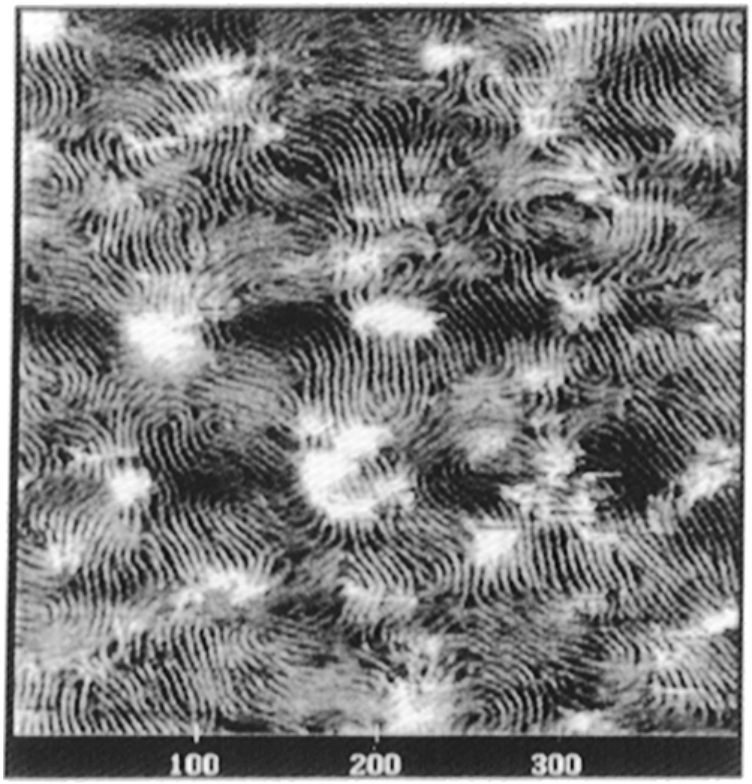

Figure 5.3: Adsorption of DNA to DPDAP. AFM image of closely packed Col E1 plasmid DNA molecules on DPDAP in 20 mM NaCl. The bright spots on the image are loose ends of the DNA molecules that create scanning image defects. Figure taken from reference [70].

5.1.3 Adsorption of Polyelectrolytes to Negatively Charged Surfaces

Condensation of DNA to negatively charged surfaces has been studied in great detail on the mica surface using the counterions Ni(II), Co(II), Zn(II), Ca(II), Mg(II), La(III) and Zr(IV) (see Ref. [74] and references therein). The binding strength of DNA is assessed by the ability to get AFM images. It was found that the cationic radius is important in the degree and strength of adsorption by relating the

ability to image DNA. The counterions Ni(II), Zn(II) and Co(II) were found to be the most effective while Ca(II) and Mg(II) were less effective. A maximum DNA adsorption density is observed when the concentrations of Ni, Zn and Co are near 1 mM. A recent theoretical and experimental study was reported in this system using $MgCl_2$ [75]. In this study, the adsorption of DNA was explained by attractive forces due to the correlation of shared counterion clouds. This mechanism required that the mica and DNA possess similar surface charge densities which is true for DNA and mica. Pretreatment of mica by the divalent ion, Ni^{2+}, enhances the adsorption by reducing the mica surface charge density. In all the above cited studies, there is no measurement of the adsorption density of the counterions. Studies demonstrating the adsorption of DNA to a negatively charged surface prepared by the hydroxylation of a silica surface have not been found.

5.1.4 Strategy for In-Situ Measurement of Hg-poly(U) Adsorption

In this chapter we seek to understand the adsorption of Hg-poly(U) to an anionic hydroxyl-terminated SiO_x surface using Zn^{2+} counterion mediated attraction. The choice of using Hg-poly(U) was motivated by the fact that the mercuration of bases is 100% so that in the XSW measurements, the number of Hg atoms is equated with the number charges on the poly(U) molecules. A schematic diagram of the adsorption scheme is shown in Figure 5.4. The distribution of the Zn and Hg atoms normal to the adsorbing surface will reveal the structure of the adsorbed conformation, which by analogy with the observed self-condensation behavior of polyelectrolytes described above, is only expected to occur within relatively narrow limits of relative concentration of Zn and Hg-poly(U). In Figure 5.4 we show the Hg

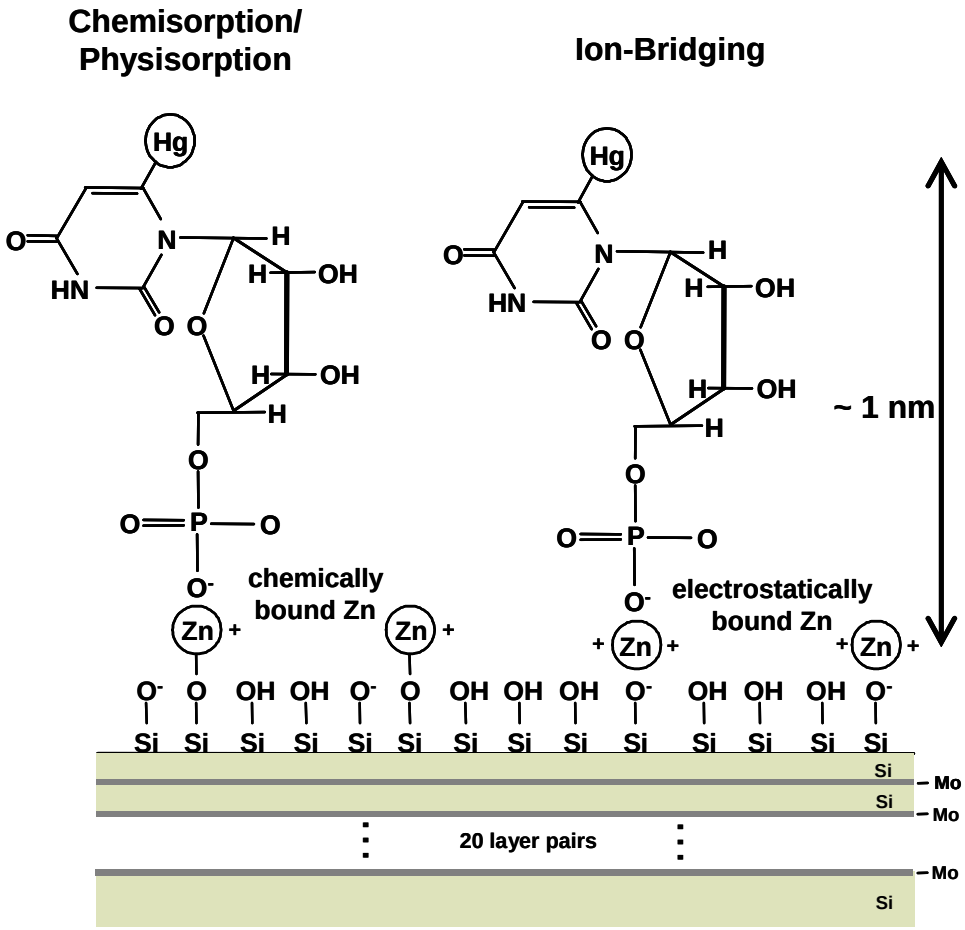

Figure 5.4: Schematic diagram of Zn^{2+} mediated Hg-poly(U) adsorption to an O-(H+) surface. Surface hydroxyl groups can be either un-dissociated (OH), dissociated (O^-) or Zn reacted (ZnO^+). Two models of adsorption are shown. In (a) the Zn is chemically bound. In (b) the Zn remains a +2 aqueous ion and the adsorption is by an "ion-bridging" mechanism. The diagram also shows the position of Hg attachment onto the RNA and the expected physical separation from the adsorbed Zn ions.

atoms approximately one-half of a width of the RNA molecule away from the surface, or Zn atom. This distance is less ~1.0 nm and could be less depending on the actual atomic arrangement of the base and overall tilt of the adsorbed monomer with respect to the substrate.

Surface hydroxyl atoms can be either un-dissociated (uncharged) or dissociated (charged). Zn can also react (chemisorption) with the surface hydroxyl groups, effectively inverting the charge from (-) to (+). The adsorption of Hg-poly(U) via Zn is postulated to occur by one or both of the mechanisms indicated in Figure 5.4. An aqueous solution of Hg-poly(U) and $ZnCl_2$ are placed in contact with the hydroxylated SiO_2 surface. The available experimental ranges of concentration of Zn and Hg is limited by the need to maintain sensitivity of adsorbed atoms with respect to bulk atoms. For example, given an adsorbed Zn coverage of 0.1 atoms per nm^2, the value of the bulk concentration which contains an equal amount of Zn in 5 μm of bulk solution is 33 μM. In other words, 0.1 atoms per nm^2 on the surface will project to a bulk concentration of 33 μM in 5 μm of solution above. Greater sensitivity to the adsorbed Zn will be achieved if the solution thickness is smaller, the surface concentration is higher, or if the bulk concentration lower and so forth. We can see that if the surface coverage of Zn does not exceed 0.1 nm^{-2}, then observing adsorption from 330 μM $ZnCl_2$, for example, will be very difficult because only 10% of the fluorescent Zn X-rays will originate from the adsorbed layer atoms. The Zn coverage given in the preceding discussion is typical of adsorption onto hydroxylated SiO_x surface so for this reason, the range of Zn bulk concentration is confined to a range of about 5-200 μM. In addition to measuring the adsorption behavior of the

combined Hg-poly(U) + Zn system, we also need to measure the adsorption behavior of Zn in the absence of the poly(U) to understand how or even if Zn might pre-adsorb to the substrate.

While the primary objective of this study was to measure the adsorption behavior in the Zn/Hg-poly(U) system, some simpler but related experiments were performed using the Hg-poly(U) and/or Zn alone. Hg-poly(U) was adsorbed to positively charged surfaces formed by functionalizing with (a) amine or (b) Zr^{4+}. Zn was adsorbed to a negatively charge surface formed by functionalizing with a PO_3 terminated surface. These alternate systems provide additional measurements with results that compliment and strengthen the in-situ Zn/Hg-poly(U) studies.

5.1.5 Charging Behavior of the Planar SiO_2 Surface

While the surface density of silanol groups is well known to be in the 5-8 nm^{-2} range for all forms of silica[76], the surface charge density or degree of dissociation depends on the bulk solution chemistry and can be altered by the presence of macro ions in the vicinity of the surface. The hydroxylated silica surface acquires a charge by the following reaction,

$$SiOH \longrightarrow SiO^- + H^+ \qquad (5.1)$$

A planar surface has a very low specific area so that the concentration of H+ is controlled by the bulk solution ionic strength and pH. The surface charge density is described by the mass action law,

$$\frac{[H^+]_0 \Gamma_{SiO^-}}{\Gamma_{SiOH}} = 10^{-pK} \qquad (5.2)$$

where $[H^+]_0$ is the hydronium ion concentration the surface which depends on the surface potential, Γ_{SiO^-} is the surface density of dissociated sites and Γ_{SiOH} is the surface density of chargeable sites which varies between 5-8 nm^{-2} and pK = 7.5 [77]. From Ref. [76] an estimate of the effective charge for the silanol surfaces used in this study assuming a pH = 7 and ionic strength ~ 10^{-4} is Γ_{SiO^-} = 0.01 nm^{-2}. The effective charge increases with pH and ionic strength.

5.2 Experimental Details

All substrates used in the XSW measurements of Zn and poly(U) adsorption were Si/Mo LSM x-ray mirrors whose top surface was the oxide of the final sputter deposited Si layer. This top surface was modified by chemical treatment to provide various charged surfaces for Hg-poly(U) adsorption studies. LSM substrates with a d-spacing of 21.6 nm were used for ex-situ experiments performed at the NSLS X15A. In-situ experiments were performed at ESRF using ID32 using 18.6 nm d-spacing substrates and the LSI cell both described in Chapter 3. All other experimental details are described below.

5.2.1 Mercuration of Polyuridylic Acid

Polyuridylic acid poly(U) can be 100% mercurated[78]. Polyuridylic Acid(5') potassium salt (2380-2900 units) was obtained from Sigma Chemical Co. (St. Louis, MO) and was dialyzed in sodium acetate solution (5 mM CH_3COONa, pH 6.0) to remove low molecular weight material prior to use. Dialysis was continued for 24 h with buffer changes every 8 h. After dialysis, 0.6 mM mercuric acetate was added to

4mM poly(U) and kept at 50^{o}C for 5 h. Quench buffer (10 mM Tris-HCl (pH 7.5)-0.1 M EDTA-1.0 M NaCl) is added to the solution at the end of the mercuration reaction. The product was dialyzed at 4^{o}C against TNE buffer (10 mM Tris-HCl (pH 7.5)- 1 mM EDTA- 20 mM NaCl) for 48 h with buffer changes every 12 h. Finally, dialysis was performed against DI water for 72 hours to reduce NaCl. Compared with the UV spectra of Poly(U), the maximum absorption peak of Hg-Poly(U) has a 5 nm red shift. The unit weight of Hg-poly(U) is 563 Da. After extensively dialysis, we assume all the Hg atoms in solution are covalent bonded on poly(U). The preceding preparation was taken from Dale et al [78]. These authors also provide extensive evidence that Hg-poly(U) retains its biological function despite the Hg attachment. Two points of concern are that (a) some catalysts can rapidly demercurate the Hg-poly(U) and (b) Hg-poly(U) is thermolabile so that prolonged exposure at elevated temperature leads to demercuration. For example, 24 hours at 37^{o}C leads to about 15% demercuration.

5.2.2 Sample Preparation

In sample A1b, Hg-poly(U) was adsorbed to a 21.6 nm d-spacing LSM substrate functionalized to an amine-terminated (NH_3^+) surface. The functionalization of the LSM substrate to an amine surface was performed as follows: the surface was cleaned in piranha solution (2:1, sulfuric acid: hydrogen peroxide) to remove organic contaminants from the surface, rinsed with ultrapure Millipore water and dried under a stream of N_2 gas. Immediately afterwards, the substrate was placed in 2 M HCl for 5 min, rinsed with ultrapure-water, dried under a stream of N_2 gas, and oven-dried at 80 ^{o}C for 15 min. The substrate was then placed in an 80^{o}C solution of anhydrous

octanol and 3-aminopropyl-trimethoxysilane (APTMS) (100:1 v:v) for 10 min, rinsed with hexanes and ultrapure-water, dried under a stream of N_2 gas, and dried in an oven at 80^{o}C for 30 min. Adsorption of the Hg-Poly(U) was done placing 120 μL of 165 μM Hg-poly(U) directly onto the NH_3 terminated substrate surface for 10 minutes. The solution was rapidly blown off with a stream of N_2 gas taking care not to leave drops which would evaporate leaving large agglomerates particles of Hg-poly(U). XSW measurement was performed on the sample in a N_2 purged environment.

Sample B1a was prepared by adsorbing Hg-poly(U) to a Zr-functionalized 21.6 nm d-spacing LSM surface. The substrate surface was prepared identically to sample A1b with the following additional steps: Phosphorylation of the amine-terminated surface was done by immersion in a mixture of 0.1 M $POCl_3$ and 0.1 M 2,4,6-collidine in anhydrous acetonitrile (ACN) for 1 h followed by heating in warm, dry ACN for 15 min, followed by rinses with ACN and Millipore water and then dried under a stream of dry N_2. Zirconation was done by immersion in an aqueous solution of 5 mM $ZrOCl_2 \cdot 8H_2O$ for 2 h, rinsed with Millipore water, and dried under a stream of dry N_2 to yield a Zr surface. Adsorption of the Hg-Poly(U) followed by placing 200 mL of 137 μM Hg-poly(U) directly onto the Zr-funtionalized surface and let incubate at room temperature for 10 min. The liquid was then rapidly blown off with a stream of N2 gas.

Sample JL_C1 was prepared for in-situ observation of Zn^{2+} adsorption to a PO_3-functionalized 18.6 nm d-spacing LSM surface. The substrate surface was prepared identically to sample B1a with the following additional steps: A monolayer of 1,12-dodecanediylbis(phosphonic acid) (DDBPA) was deposited after the Zr-

functionalization step by immersion in 5 mM DDBPA in 60% ethanolic solution overnight.

Samples JL817OH_A and JL817BOH_A were prepared for in-situ observation of Zn^{2+} adsorption or Zn-mediated adsorption of Hg-poly(U) to negatively charged surfaces prepared by hydroxylation of LSM substrates. Fresh LSM substrates (SiO_x top surface) were cleaned in piranha solution (2:1, sulfuric acid: hydrogen peroxide) to remove organic contaminants from the surface and then rinsed with Millipore water and dried under a stream of N_2. Immediately afterwards, the substrate was hydroxylated by immersion in 2M HCl for 5 min, rinsed with Millipore water and dried under a stream of dry N_2. Fully hydroxylated surfaces have a surface hydroxyl group density of 5 nm^{-2} [79]. The substrates were then used in the solid-liquid interface-cell described in Chapter 3 for in-situ studies of the adsorption of Hg-poly(U) using various aqueous mixtures of Hg-poly(U) and $ZnCl_2$.

5.2.3 Ex-Situ XSW Measurements

XSW measurement of samples A1b and B1a was performed in the dry state after adsorption of the Hg-poly(U) at the NSLS X15A using E_γ= 12.4 keV (λ = 1.00 Å) incident x-rays to excite Hg L fluorescence for sample A1b and E_γ= 18.3 keV (λ = 0.674 Å) incident x-rays to excite Hg L and Zr K fluorescence for sample B1a.

5.2.4 In-situ XSW Measurements

In-situ XSW measurements using the LSI cell for samples JL817BOH_A, JL_C1, and JL817OH_A were performed at the ESRF ID32 beamline as described in Chapter 2. Incident X-rays with E_γ= 14.3 keV (λ = 0.867 Å) were used for sample

JL817BOH_A to excite Zn Kα, Hg Lα, and Hg Lβ fluorescence. Incident X-rays with E_γ= 12.4 keV (λ = 1.0 Å) were used for samples JL_C1 and JL817OH_A to excite Zn Kα and Hg Lα fluorescence.

5.3 Ex-Situ XSW Hg-poly(U) Adsorption Results

5.3.1 Adsorption of Hg-poly(U) to an Amine-Terminated Surface

The measurement of polynucleotide adsorption to a positively charged surface was motivated primarily by the desire to test the XSW measurement scheme for a simpler configuration. By doing so we verify that the Hg atoms are attached to the poly(U) as expected. In sample A1b, we measure the adsorption of Hg-poly(U) to an amine (NH^{3+}) terminated surface and in sample B1a we measure the adsorption of Hg-poly(U) to a Zr surface. XSW measurement of A1b was taken by scanning over θ = 0.08° to 0.6°. Figure 5.5 shows angle-integrated X-ray spectra for the angle range of θ = 0.12° to 0.36°. We see Si Kα, Mo Lα, Ar Kα, W Lα and W $L\beta_1$ which originate for the LSM substrate with W being an impurity in the Mo layers and Ar being an impurity in the Si layers. Cu Kα and Zn Kα are present as environmental impurities and Hg Lα is present from the adsorbed Hg-poly(U) and is the only signal originating from the surface of the sample. The proximity of W Lβ1 and Hg Lα in the X-ray spectrum requires careful fitting especially since the W exhibits strong modulations across the Bragg peaks. This difficulty becomes worse at higher angles where the penetration of incident X-rays into the substrate is higher and thus W fluorescence

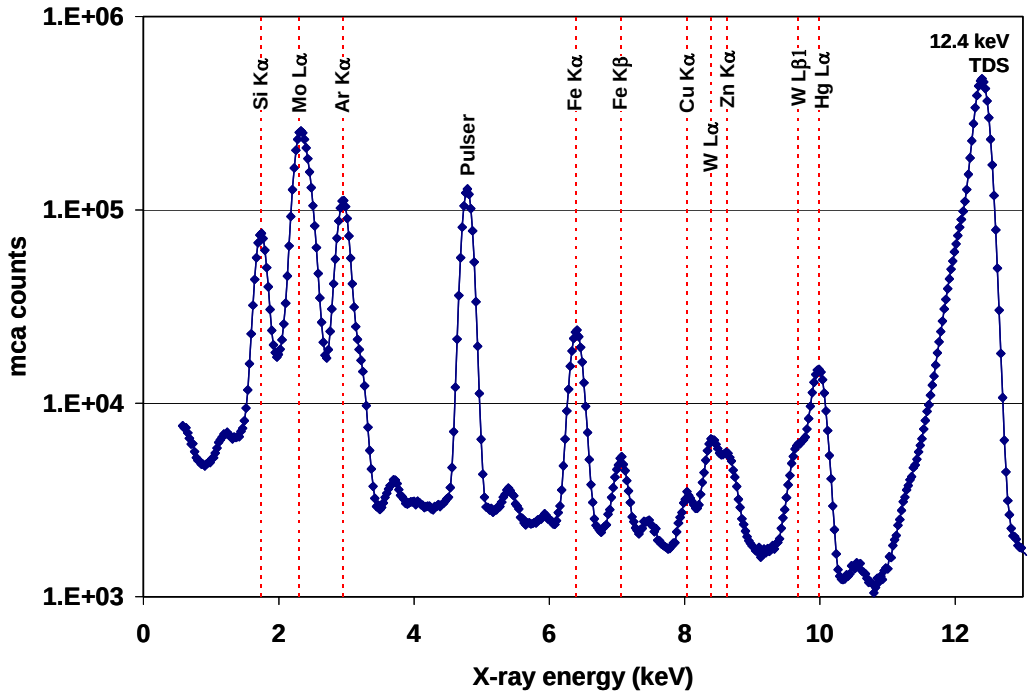

Figure 5.5: MCA Spectrum for sample A1b. The angle integrated X-ray spectrum from the XSW measurement of sample A1b taken at Eγ = 12.40 keV.

becomes stronger relative to Hg. Prior to taking the XSW scans, a fast reflectivity scan was taken and used for the modeling of the substrate reflectivity properties. In Figure 5.6a the reflectivity from the fast scan is shown with excellent agreement between the measured and theoretical reflectivity. In Figure 5.6b we show the measured and theoretical Hg fluorescence yield. The functional form used to model the Hg, $\rho_{Hg}(z)$, was: (i) A Gaussian model characterized by a mean position z_0 and spread σ, and (ii) an extended uniform distribution (rectangular profile from z = 0 to $z = t_F + 200$ nm) representing a disordered fraction. The Hg was thus modeled as $\rho_{Hg}(z) = C_{Hg}$ x (i) + $(1-C_{Hg})$ x (ii). The best fit yielded z_0 = 1.0 nm, σ = 0.5 nm and

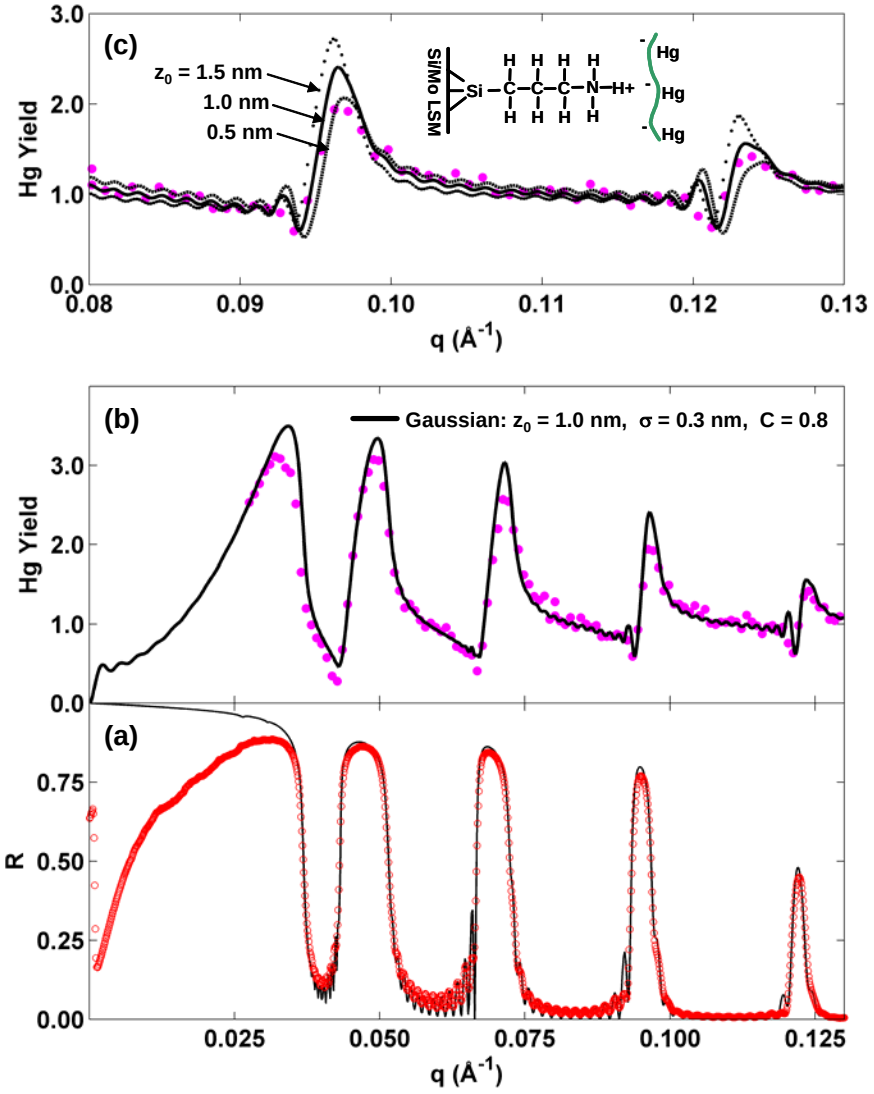

Figure 5.6: XSW Results for sample A1b. Hg-poly(U) adsorption to an amine-terminated Si/Mo LSM; (a) measured (filled circles) and calculated (solid line) reflectivity, (b) measured (filled circles) and calculated (solid line) Hg yield and (c) measured (filled circles) and calculated (solid lines) Hg yield for the 3rd and 4th Bragg peaks for various values of the mean position, z_0. The inset in (c) shows the surface functionalization by 3-aminopropyl(trimethoxy) silane and scheme for Hg-poly(U) attachment.

C_{Hg} = 0.8 which indicates that the Hg atoms are very close to SiO2 surface. The mean position determined to be 1.0 nm is consistent with the expected primer layer and RNA molecule dimensions. In Figure 5.6c theoretical yield curves for several alternate values of the mean position, z_0 = 0.5, 1.0 and 1.5 nm are shown to indicate the sensitivity to this parameter.

5.3.2 Adsorption of Hg-poly(U) to a Zr-Terminated Surface

Hg-poly(U) was adsorbed to a Zr terminated surface in Sample B1a as described above. XSW measurement of B1a was taken at 18.20 keV in order to excite X-ray fluorescence from both Zr and Hg atoms. The angle integrated X-ray fluorescence spectrum is shown in Figure 5.7. The same X-ray lines appear as in sample A1b with the addition of Zr Kα and Hg Lβ. Sample B1a was also analyzed with XSW using 12.40 keV incident X-rays and the X-ray fluorescence spectrum was identical to that shown in Figure 5.5 for sample A1b. The experimental XSW fluorescence yields for both measurements are shown in Figure 5.8. Due to the low photon flux at 18.50 keV at the X15A beamline, a large 10 mm wide X-ray beam was required for this measurement. Unfortunately, this large beam averaged the large lateral variation of the d-spacing of LSM substrate resulting in reflectivity data could not be modeled well using our standard modeling techniques. For this reason the XSW analysis gave poor fits to the reflectivity and fluorescence yield but qualitative interpretation was still possible. Previous experience with various XSW yield profiles indicates that the Hg and Zr are contained in narrow distributions close to the substrate surface. The sharp kinks in Figure 5.8b indicate that the atomic distribution is very narrow. The asymmetry towards the high side of the Bragg peaks indicates

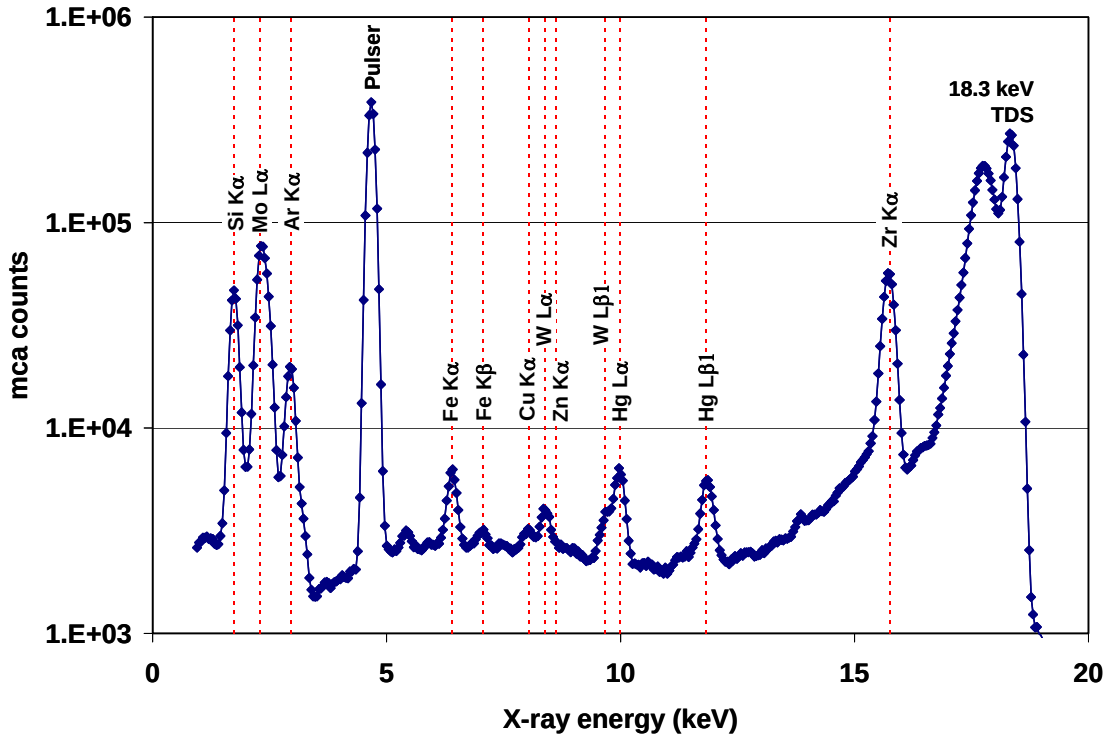

Figure 5.7: MCA Spectrum for sample B1a. The angle integrated X-ray spectrum from the XSW measurement of sample B1a taken at Eγ = 18.30 keV.

that the center of the distribution is very near the surface. The similarity of the Hg fluorescence yield profile taken at 12.4 keV in samples B1a(Figure 5.8a,b) and A1b (Figure 5.6b) suggest that the Hg atomic yield for profiles are very similar for both samples although the sharper kinks in the Hg sample B1a suggest that the distribution may be narrower than in sample A1b. The fluorescence yield data taken at 18.3 keV for sample B1a shown in Figure 5.8c indicate that the Zr and Hg atoms appear to be in very nearly the same location because their fluorescence yield profiles are nearly identical. Apparently, the Hg and Zr atoms are narrowly confined to the surface of the substrate. The positions of the Hg and Zr atoms are likely to be

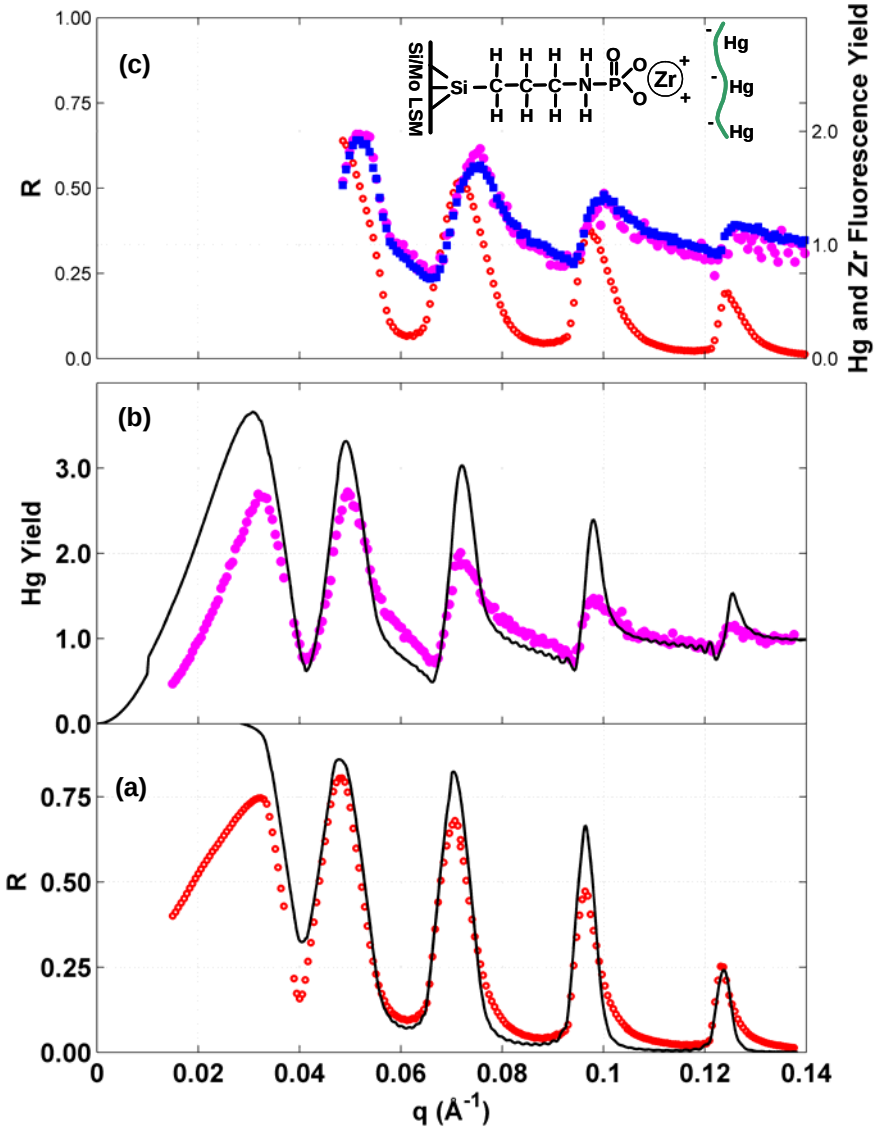

Figure 5.8 XSW results for sample B1a. Hg-poly(U) adsorption onto a Zr-terminated surface; (a) experimental (open circles) and calculated (solid line) reflectivity taken at 12.40 keV, (b) measured (open circles) and calculated (solid line) Hg yield taken at 12.40 keV and (c) measured (open circles) reflectivity, Hg yield (filled circles) and Zr (filled squares) fluorescence yield taken at 18.50 keV.

within 0.5 nm of each other. An examination of the simulations at the 4th Bragg peak in Figure 5.6c show that a 0.5 nm separation would give a noticeable difference in fluorescent yield profiles and the similarity of the Hg and Zr profiles in Figure 5.8c leads us to this conclusion. Coverage measurements performed on sample B1a revealed a Zr atomic coverage of 1.6 nm^{-2} and an Hg atomic coverage of 0.019 nm^{-2}.

5.4 In-Situ XSW Zn and Hg-poly(U) Adsorption Results

XSW measurement of the absorption of Hg-poly(U) to a negatively charged surface using Zn counterion mediated attraction was performed *in-situ* using the liquid-solid interface (LSI) cell described in Chapter 3. The concentrations [Zn^{2+}] = 50 μM and [Hg-poly(U)] = 25 μM were chosen based on experimental and theoretical considerations as discussed above. The modeling of the X-ray reflectivity from measurements using the *in-situ* LSI cell is accomplished by simply adding one water and one Kapton layer to the LSM model. The thickness of the water is unknown while the thickness of the Kapton is 7 μm. In Figure 5.9 the measured reflectivity for a typical in-situ sample with water and Kapton layers is shown along with several intermediate steps of prediction to demonstrate the details of the modeling procedure. The inset in Figure 5.9b shows the LSM model with the added water and Kapton layers. The remainder of the layered model is just the typical LSM model refined from *ex-situ* studies presented throughout this thesis. The $ZnCl_2$ (and Hg-poly(U)) are taken to have a negligible effect on the scattering properties of the water layer. When very large thickness layers are present, the dynamical scattering theory predicts high frequency oscillations. For example, for a single 12 μm layer,

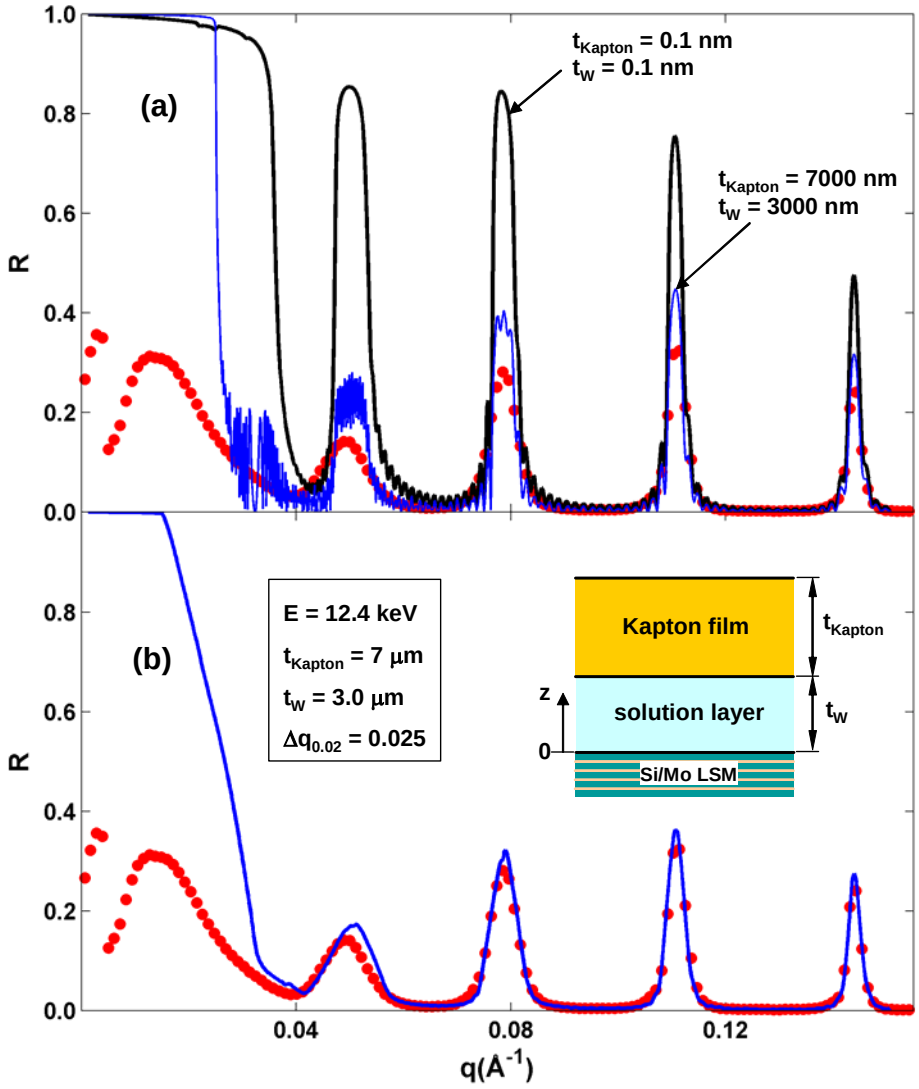

Figure 5.9: Modeling details of in-situ reflectivity. (a) Measured (filled circles) and calculated (solid lines) reflectivity from the *in-situ* LSI cell. The heavy solid line in (a) is the calculation without Kapton and water for comparison. The thin solid line in (a) adds the Kapton and water and shows high frequency oscillations due to the very large thickness of these layers. In (b) the calculated (solid line) reflectivity after applying a footprint related angle averaging.

thickness fringes of period 1/d = 8e-6 $Å^{-1}$ are predicted but are never observed experimentally because of the high waviness of the Kapton surface. Smoothing is used to eliminate the high frequency oscillations predicted by the model which simulates the effect of the waviness of the Kapton surface. However, for the in-situ measurements reported here, we also observe an apparent foot-print related angle-averaging which may be due to warping of the substrate due to the force of the Kapton film on the sample edges. This angle-averaging exceeds in general the angle-averaging necessary to smooth the high frequency oscillations. To account for the apparent substrate warping, a boxcar angle-averaging proportional to 1/q is implemented as follows:

$$R_{smeared}(q_i) = \sum_{j=i-n/2}^{j=i+n/2} R(q_j)/(n+1)$$

where n includes a range of points spanning Δq_i which is computed at each point according to,

$$\Delta q_i = \frac{0.02(\Delta q_{0.02} - \Delta q_{min})}{q_i} + \Delta q_{min}$$

where $\Delta q_{0.02}$ is a Δq_i at q = 0.02 $Å^{-1}$ and Δq_{min} is an asymptotic value to account for angle-averaging due to roughness at high angle where the footprint related angle-averaging dies off. We apply this angle-averaging to the calculated reflectivity. Figure 5.9a shows the calculated reflectivity for the LSM alone with and without the water and Kapton layers and without applying any angle-averaging calculation. Note that the critical angle in this case corresponds to the effective δ of the Si/Mo LSM. When the water and Kapton layers are added but no angle averaging applied, the thickness oscillations can be seen. In Figure 5.9b the final theoretical reflectivity is

shown in which a footprint related angle-averaging has been applied using $\Delta q_{0.02}$ = 0.025 Å^{-1} (corresponding to an approximate radius of curvature of 7m) and Δq_{min} = 0.001 Å^{-1}. The fitting of the water layer thickness was done after the determination of the smoothing parameters.

5.4.1 In-situ Adsorption of Zn^{2+} to an OH Surface

The adsorption of Zn^{2+} in the absence of poly(U) constitutes a baseline measurement. In sample JL817BOH_A Zn^{2+} was exposed to an OH^- terminated SiO_2/LSM surface using 50 μM $ZnCl_2$ solution. XSW measurements were made using 14.3 keV X-rays. Figure 5.10 shows the angle integrated MCA spectrum and Figure 5.11 shows the XSW results which are also tabulated in Table 5.1.

The measured and calculated Zn fluorescence yield is shown in Figure 5.11b which clearly shows a condensed Zn layer. The reflectivity was modeled as described above and gave a water layer thickness, t_W = 2.41 μm. The E-field intensity is computed in the normal fashion using the LSM model determined from the reflectivity fit shown in Figure 5.11a. The E-field intensity was computed in the water layer at the following z positions; z = 0-20 nm with Δz = 0.1 nm and z = 20 -3000 nm with Δz = 10.0 nm. Prior to performing the Zn atom distribution model calculations, the same angle averaging that was determined from the reflectivity fit was applied to the E-field intensity. The Zn atom distribution was modeled using a rectangular distribution, $\rho_S(z)$, with one edge fixed at z=0 and the other edge defined by $z=t_{Zn}$ left as a free fitting parameter. The mean position, $z_{0,Zn}$, of the Zn is just the center of the rectangular distribution. The bulk Zn atoms were modeled

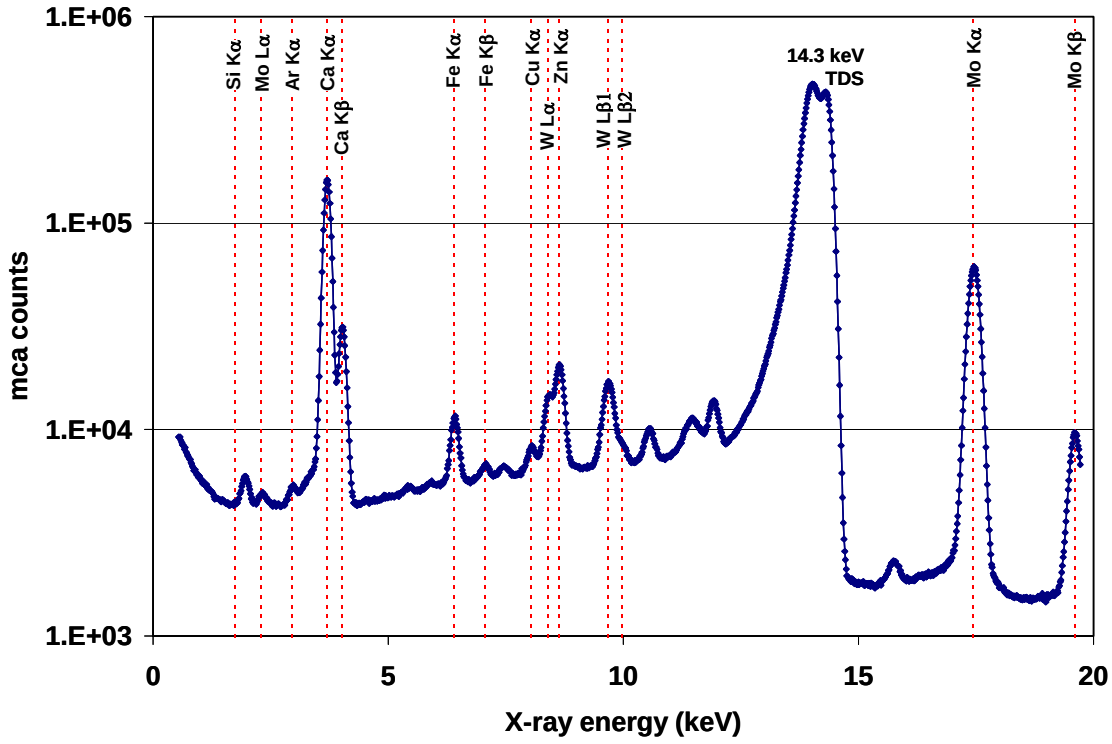

Figure 5.10: MCA Spectrum for sample JL817BOH_A. The angle integrated X-ray spectrum from the XSW measurement of sample JL817BOH_A taken at Eγ = 14.30 keV.

using a uniform distribution, $\rho_B(z)$ over the entire water layer. The total Zn yield was $\rho_{Zn}(z) = C_{Zn}\,\rho_S(z) + (1-C_{Zn})\,\rho_B(z)$, where C_{Zn} is the fraction in the surface condensed layer modeled by $\rho_S(z)$. When there is no surface condensed layer then we have $C_{Zn} = 0$. The attenuation of the incident beam by the Kapton and water was accounted for by using the XSW calculated yield at the off-Bragg position which takes into account the model distribution of the Zn. The attenuation of exiting fluorescence was

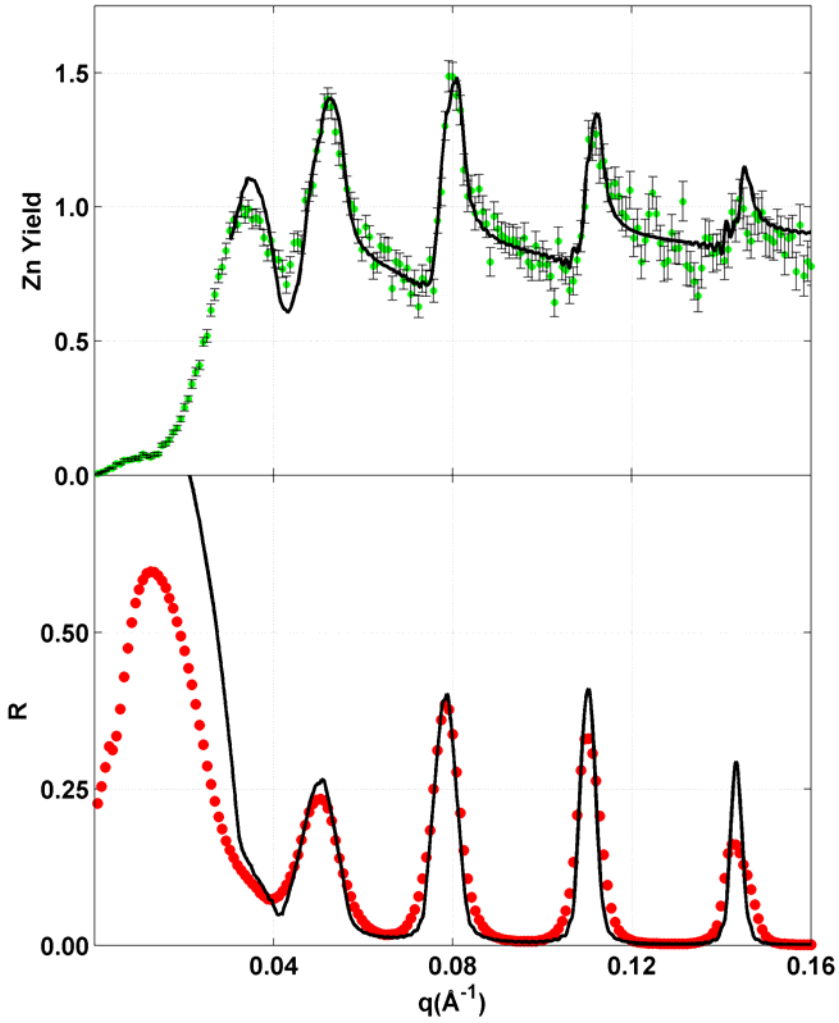

Figure 5.11: In-situ XSW result for 50 µM ZnCl2 placed in contact with an OH terminated LSM/SiO2 substrate. (a) Model atomic distribution (b) Measured (filled circles) and theoretical Zn yield for various values of the coherent fraction C_{Zn}. The line for C_{Zn} = 0.0 is equivalent to the case where all Zn in contained in the bulk solution only and for C_{Zn} = 1.0 all Zn is condensed on the surface. (c) Measured (closed circles) and calculated (solid line) in-situ reflectivity. The dashed line shows the calculated reflectivity with no Kapton or water.

accounted for by using the attenuation properties of Kapton and water at the fluorescence X-ray energy using a 2^o fluorescence detector takeoff angle. Using the above described model and experimental corrections, the χ^2 fit gave a condensed Zn layer thickness t_{Zn}=1.1(1) nm ($z_{0,Zn}$ = 0.55(7) nm) and C_{Zn} = 0.59(4). The absolute coverage of Zn in the adsorbed layer was found to be Θ_{Zn} = 0.037(4) Zn/nm^2.

5.4.2 Zn^{2+} Adsorption to a PO_3 Surface

In addition to experiments performed using a negatively charged surface provided by the hydroxylated SiO_2 surface, a negatively charged surface was prepared by functionalizing to PO_3 using an identical procedure as was used for the metal/phosphonate samples in Chapter 4. An LSM substrate was prepared identically to sample G1 from Chapter 4 but without the final Hf metal layer so that the final preparation step was the addition of a monolayer of 1,12-dodecanediylbis(phosphonic acid) which provides a terminal PO_3 group. Sample JL_C1 was prepared in this way and used in an in-situ XSW measurement using a 50 μM Zn acetate solution. The Zn acetate was used in place of $ZnCl_2$ in order to evaluate the effect of the salt counterion on the frequently observed Zn accumulation phenomenon in Zn X-ray experiments. XSW measurements were made at 12.4 keV with the results shown in Figure 5.12. The modeling of the Zn was performed identically as for sample JL817BOH_A above and yielded a mean position t_{Zn} = 4.5(2) nm ($z_{0,Zn}$ = 2.3(2) nm) and C_{Zn} = 0.75(8). The absolute coverage of Zn in the adsorbed layer was found to be Θ_{Zn} = 0.28(4) Zn/nm^2.

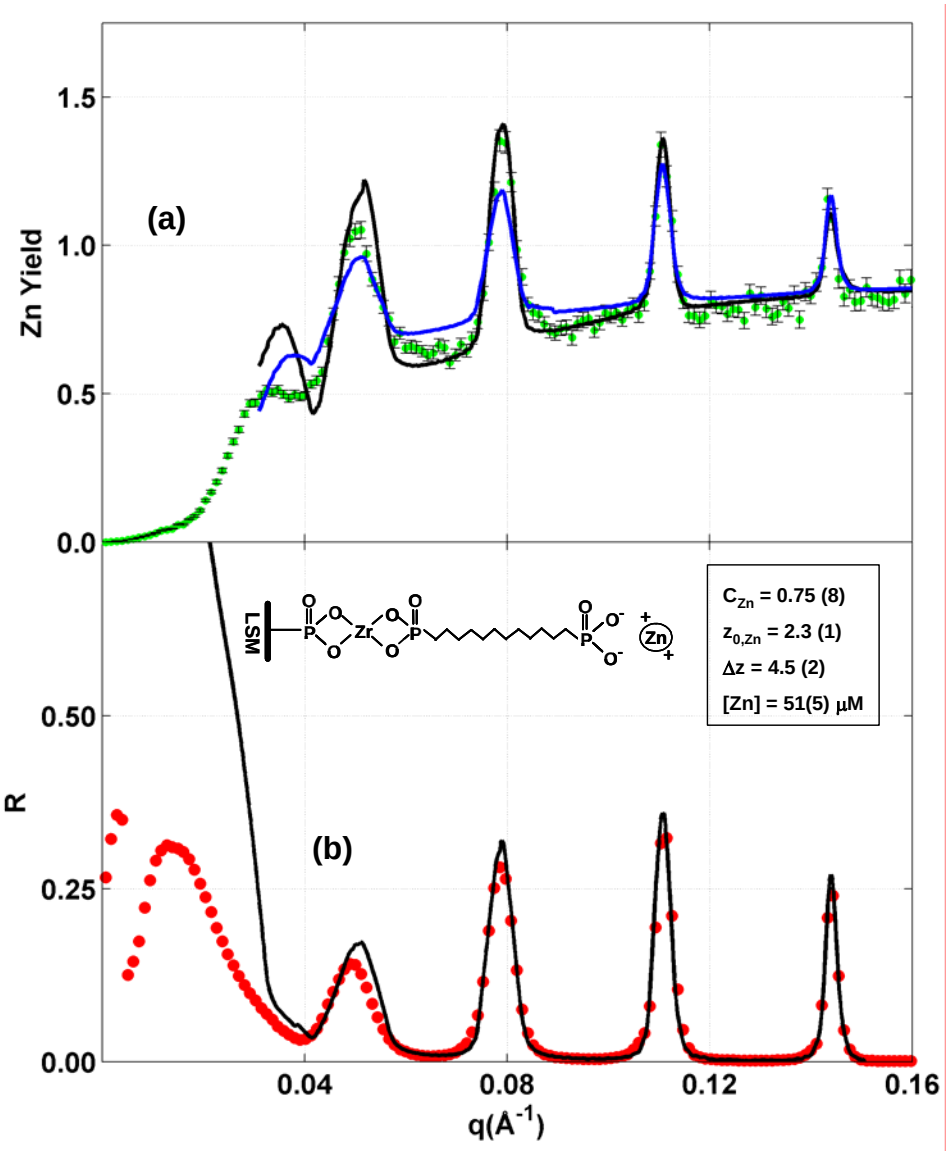

Figure 5.12: Adsorption of Zn to a PO_3 surface. In-situ XSW results for adsorption of Zn from 50 mM Zn acetate placed in contact with an PO_3^{2-} terminated LSM substrate. (a) Measured (closed circles) and calculated Zn yield for C_{Zn}=0 (solid blue line) and C_{Zn}=0.75 (solid black line) (b) Measured (filled circles) and calculated (solid red line) X-ray reflectivity. The inset show the schematic structure of the surface preparation and expected configuration for Zn adsorption.

5.4.3 Hg-poly(U) Adsorption to an OH Surface

The adsorption of Hg-poly(U) was examined by XSW measurement of sample JL817OH_A using a solution with 50 μm $ZnCl_2$ and 25 μM Hg-poly(U). The solution was let incubate for 1 hour prior to the first XSW scan. Six scans of 30 min duration each were taken, two each at lateral positions x = 0.0, 1.5, and 3.0 mm. The total time between the start of the 1st scan and end of the 6th was 180 minutes The initial plan was to measure the Zn and Hg atom distribution twice at several locations to check for consistency both spatially and in time. Instead we observed a time dependent phenomenon as equilibrium had not been established after a 1-hour incubation period. An angle integrated X-ray spectrum is shown in Figure 5.13. We see Zn Kα with an adjacent W Lα line and Hg Lα with an adjacent W Lβ line. We also see Ca Kα which comes from the top surface of the Kapton film. Ca is important because it provides us with a marker for a random distribution from which comparisons to the Zn and Hg yield curves can provide immediate qualitative evidence of bulk versus condensed distributions. The yields for both Zn and Hg for the full sequence of XSW measurements is shown in Figure 5.14 which shows the position as well as the times for each scan with the first scan on the bottom and progressing upward. For scans 51-53 the comparison to Ca indicates that the Zn and Hg atomic distributions appear to be bulk-like with no evidence of condensed layers. While we expect that initially Zn might be present as a condensed layer, we do not observe one. Scan 54 shows a dramatic change over scan 53 taken at the same position. Apparently Zn changed from being completely bulk-like to being partially condensed on the surface while the Hg showed a small fraction in the condensed state which is not obvious by visual inspection but is revealed in the modeling. Scan

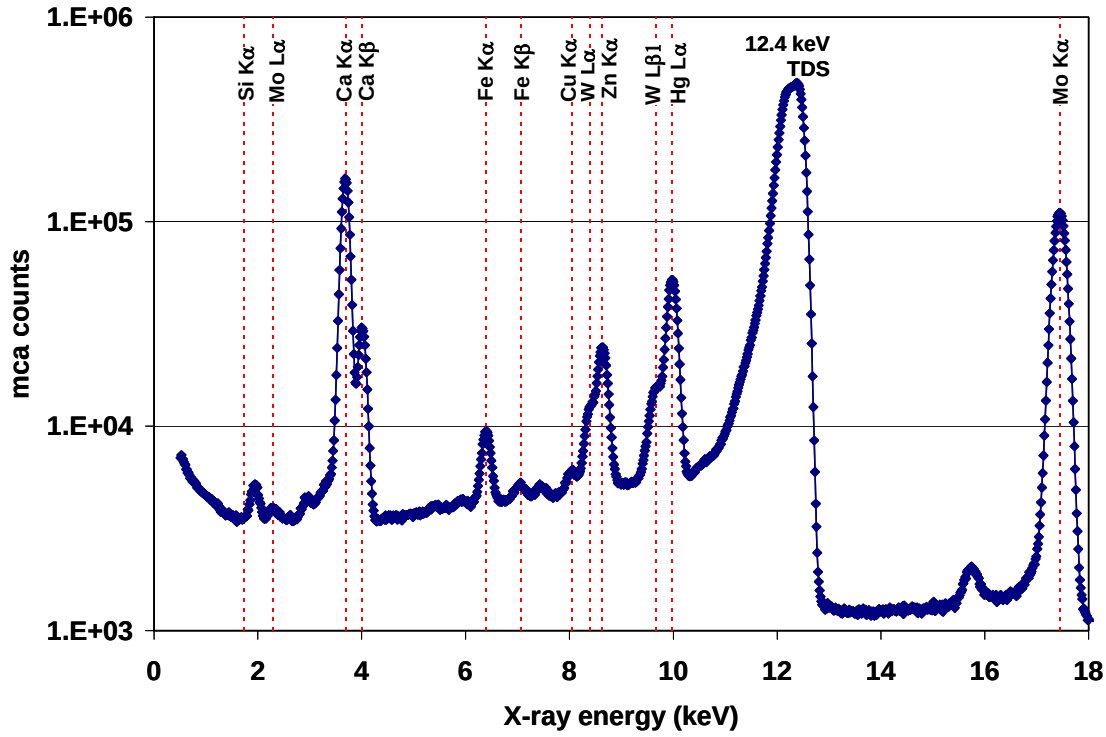

Figure 5.13: MCA Spectrum for Sample JL817OH_A. The angle integrated X-ray spectrum from the XSW measurement of sample JL817BOH_A taken at Eγ = 12.40 keV.

55 was taken next at x=3.0 mm and showed condensed Hg-poly(U) and Zn layers. No change was observed from scan 55 to 56. In brief, a qualitative examination indicates that adsorption of Hg-poly(U) is first preceded by Zn adsorption alone followed by adsorption of the Hg-poly(U).

The same modeling treatment made for the 50 μM $ZnCl_2$ in sample JL817BOH_A above was performed the Zn and Hg yields. The results are shown for scans 53-55 in Figures 5.15 to 5.17 omitting scans 51-52 and 56 since they appear nearly identical to scans 53 and 55 respectively. The model fit parameters and

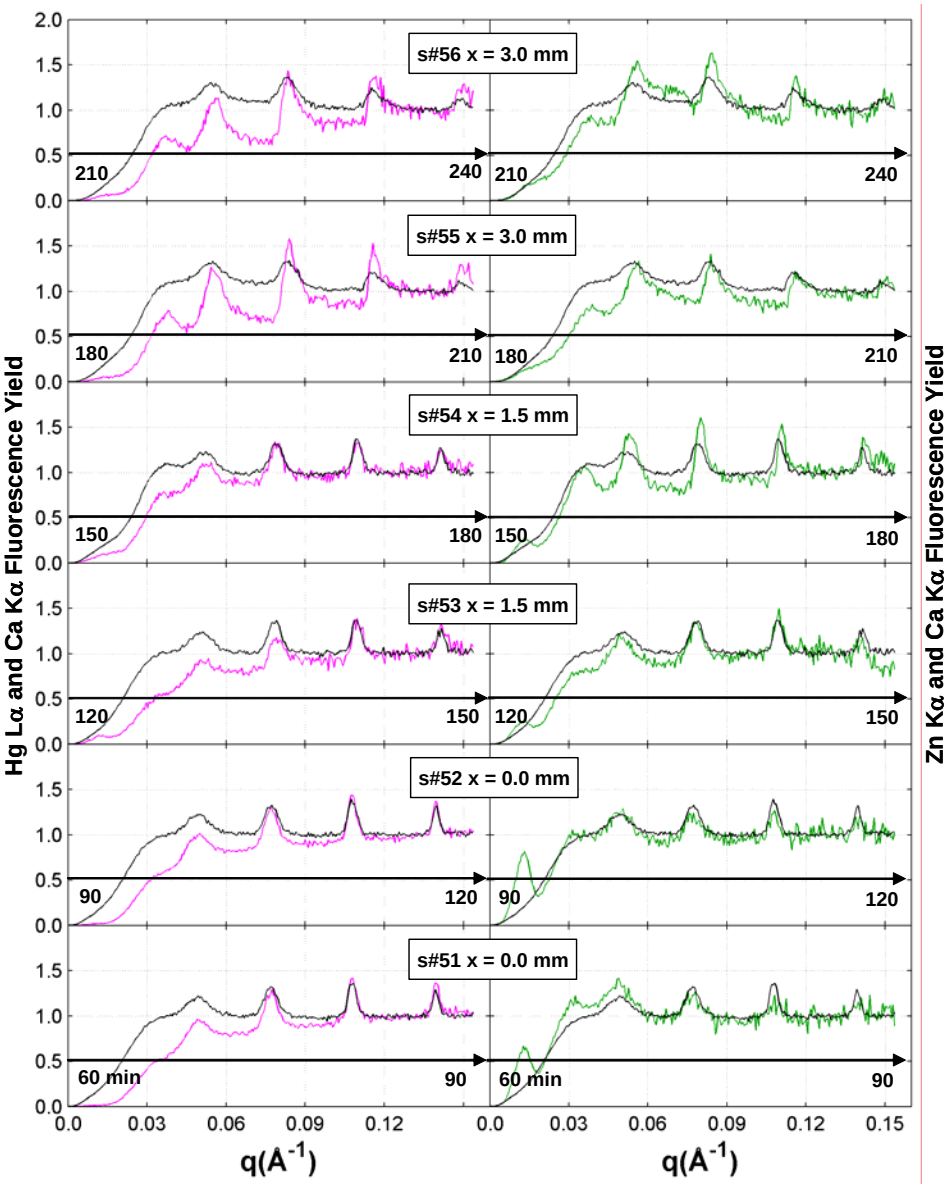

Figure 5.14: Hg-poly(U)/Zn Adsorption Time Sequence. A series a six consecutive XSW scans showing the time sequence of events started with no Hg or Zn adsorption (scans 51-53) followed by Zn-only adsorption (scan 54) followed by Hg along with Zn adsorption (scans 55-56). The Ca yield (black solid line) is shown for random distribution XSW yield reference.

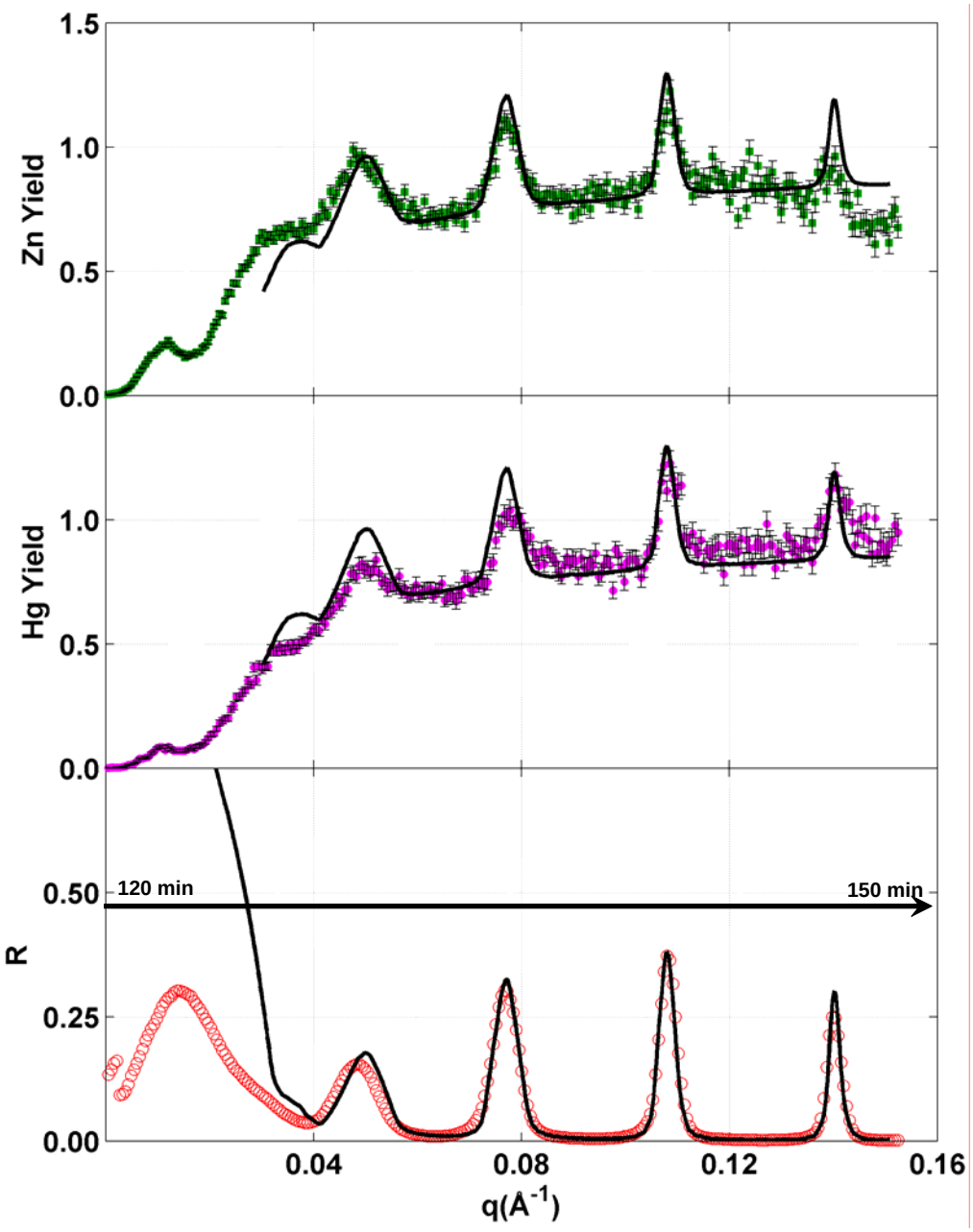

Figure 5.15: Results from the XSW scan 53 from sample JL817OH_A. (a) Measured (open circles and calculated (solid line) reflectivity, (b) measured (filled circles) and calculated Hg yield and (c) measured (filled squares) and calculated (solid line) Zn yield.

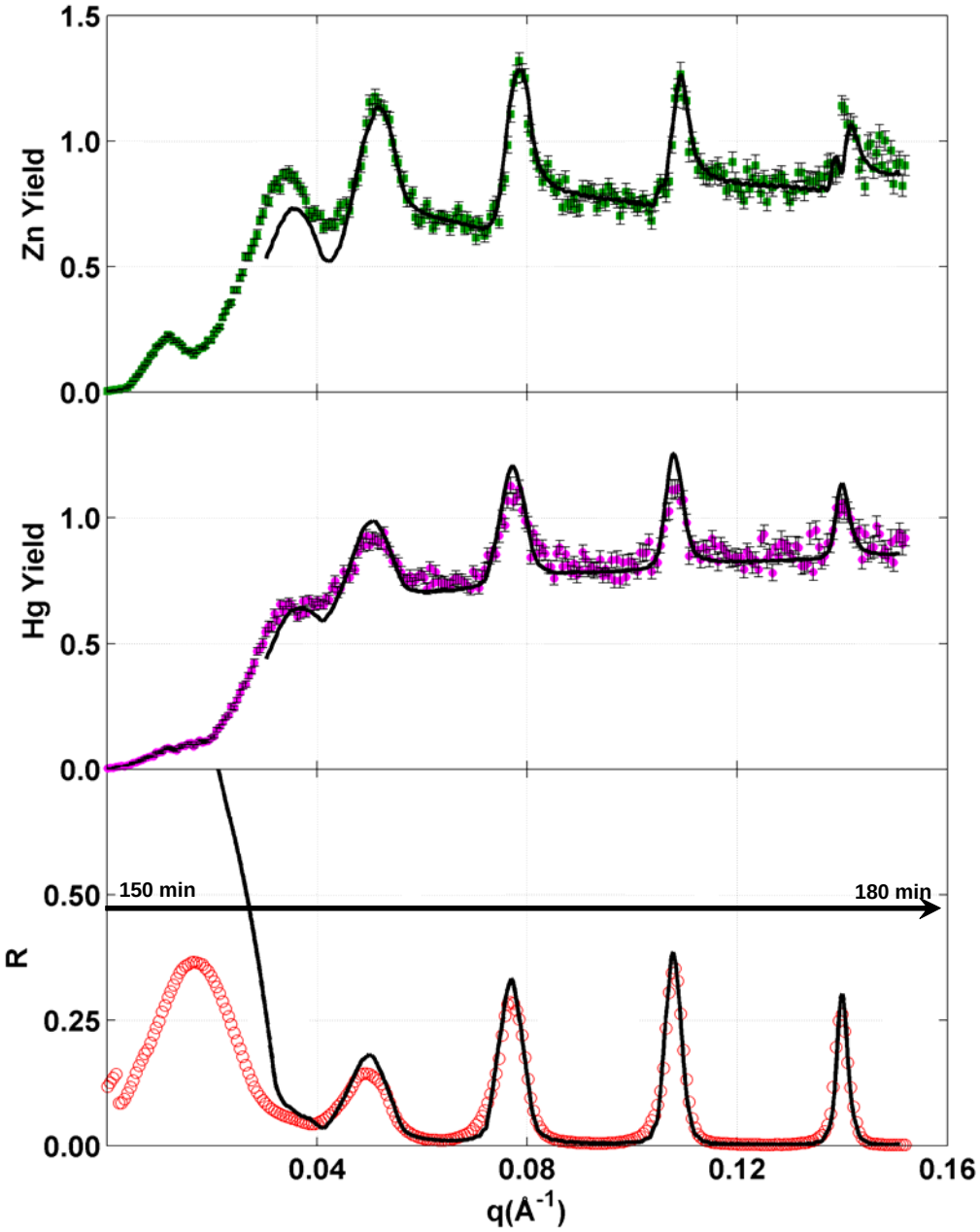

Figure 5.16: Results from the XSW scan 54 from sample JL817OH_A. (a) Measured (open circles and calculated (solid line) reflectivity, (b) measured (filled circles) and calculated Hg yield and (c) measured (filled squares) and calculated (solid line) Zn yield.

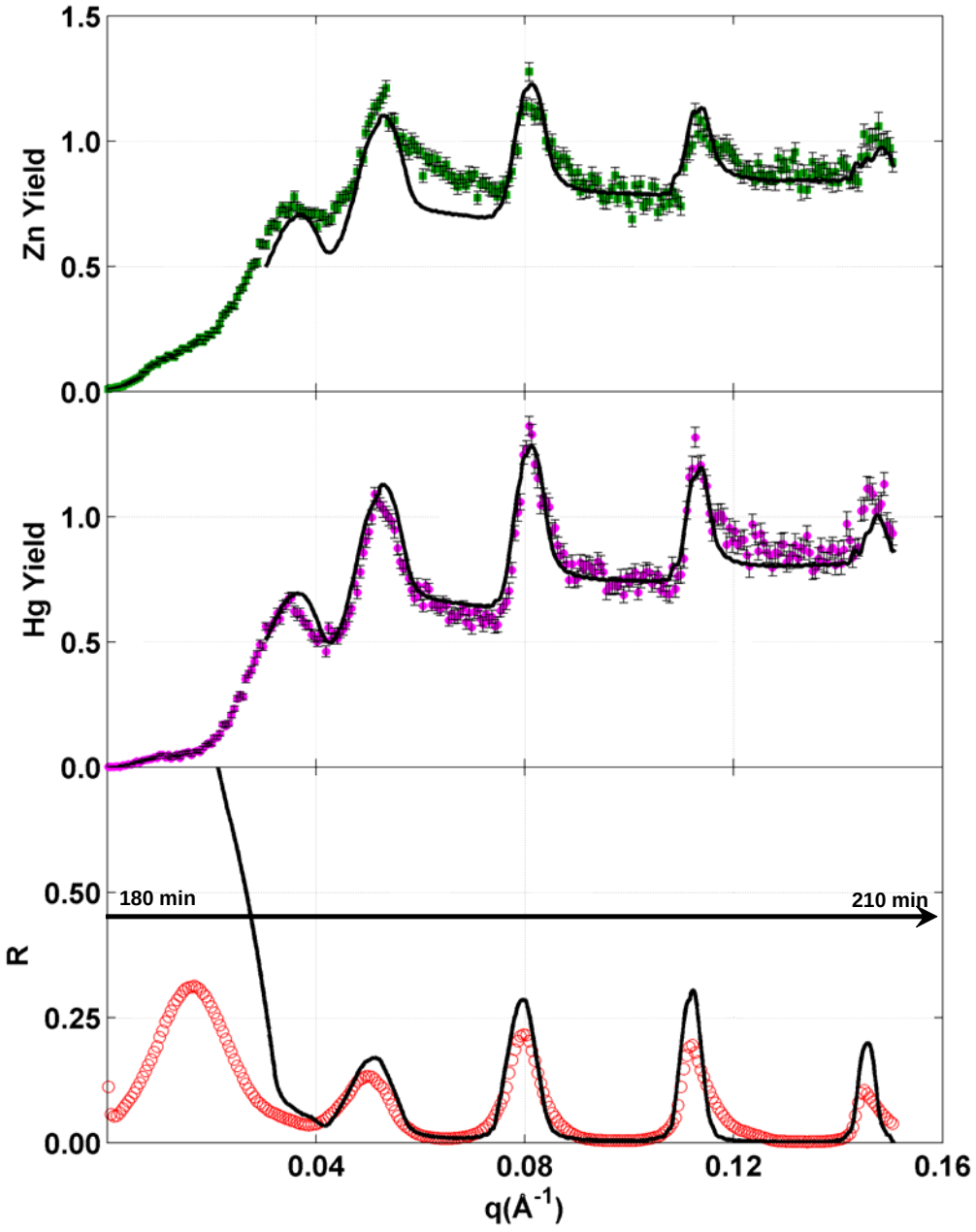

Figure 5.17: Results from the XSW scan 55 from sample JL817OH_A. (a) Measured (open circles and calculated (solid line) reflectivity, (b) measured (filled circles) and calculated Hg yield and (c) measured (filled squares) and calculated (solid line) Zn yield.

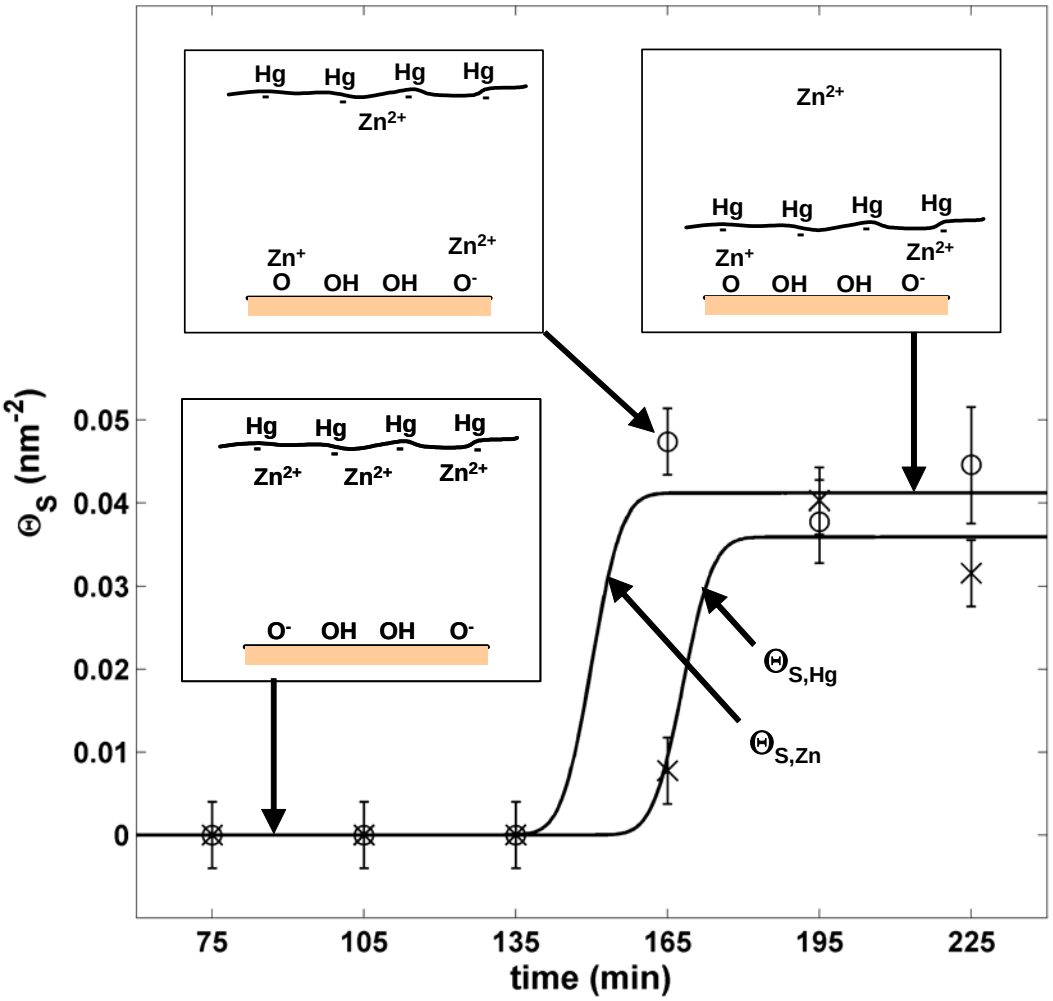

Figure 5.18: Plot of the condensed layer coverages of Zn and Hg as a function of time for the adsorption of Zn and poly(U) to an OH surface. The insets are a graphical representation of the adsorption process implied by the XSW analysis. The first two times (75 and 105 min) were taken at lateral position x=0 mm, the next two times (135 and 165 min) were taken at x=1.5 mm and the last two times (195 and 225 min) were taken at x=3.0 mm.

Sample	time min	t_W μm		C	Θ_T nm^{-2}	t nm	Θ_S nm^{-2}	[Bulk] μM
JL817BOH_A $ZnCl_2$/OH	75	2.4(2)	Zn	0.59(4)	0.063(5)	1.1 (2)	0.037(4)	17(2)
JL817BOH_A $ZnCl_2$/OH	165	2.4(2)	Zn	0.44(3)	0.061(5)	0.9(2)	0.027(3)	25(3)
JL817OH_A Zn/poly(U) /OH	75	2.8(1)	Zn	0	0.082(6)	-	0	48(4)
			Hg	0	0.186(10)	-	0	110(7)
JL817OH_A poly(U)/Zn/OH	105	3.0(1)	Zn	0	0.091(7)	-	0	49(4)
			Hg	0	0.218(12)	-	0	119(8)
JL817OH_A poly(U)/Zn/OH	135	3.1(2)	Zn	0	0.120(8)	-	0	64(5)
			Hg	0	0.071(5)	-	0	38(3)
JL817OH_A poly(U)/Zn/OH	165	2.5(2)	Zn	0.46(2)	0.104(8)	1.08(9)	0.047(4)	38(4)
			Hg	0.10(2	0.077(5)	2.0(8)	0.008(2)	47(11)
JL817OH_A poly(U)/Zn/OH	195	3.0(2)	Zn	0.35(4)	0.109(8)	0.90(3)	0.038(5)	40(6)
			Hg	0.49(3)	0.083(6)	1.9(1)	0.040(4)	24(3)
JL817OH_A poly(U)/Zn/OH	225	3.0(2)	Zn	0.39(6)	0.114(8)	0.99(5)	0.045(7)	38(7)
			Hg	0.39(4)	0.082(6)	1.6(1)	0.032(4)	28(4)
JL_C1 $ZnAc/PO_3$		2.4	Zn	0.75(8)	0.37(3)	4.5(2)	0.28(4)	51(4)

Table 5.1: XSW model parameters for the *in-situ* measurement of adsorption Zn and poly(U). The model used in all cases is a rectangular distribution (from z=0 to t) with fraction C plus a uniform bulk component (from z=0 to t_W) with fraction (1-C). The water layer thickness t_W was determined from XRR analysis of the reflectivity taken simultaneously with the X-ray fluorescence. Θ_T was determined by XRF analysis and Θ_S calculated by $\Theta_S = C\,\Theta_T$. The bulk solution concentration was calculated from [Bulk] = $(1\text{-}C)\,\Theta_T / t_W/N_a$.

coverages are given in Table 5.1. The Zn and Hg condensed layer coverage are plotted as a function of time in Figure 5.18. The insets in Figures 5.18 graphical depict what the adsorption process that is implied by the XSW results.

Chemical analysis was performed for a selection of test solutions from the ESRF experiments using inductively-coupled plasma atomic emission spectroscopy (ICP-AES). The analysis was performed for Zn, Hg, P, Na, K and Ca and are listed in Table 5.2. Unfortunately, the period between the collection of the samples in ESRF and the ICP measurement was too long (13 months) and the Hg most likely detached from the poly(U) and was adsorbed into the polyethylene walls of the centrifuge tubes used to store the samples. Discussions with Dr. D. Graczyk of Argonne National Laboratory who performed the ICP analysis led to this conclusion. His experience with Hg in any form stored in plastic containers is that it “disappears” after 3 months or so. This raises concerns over the freshness of Hg-poly(U) used in the experiments. In the ESRF experiments, the Hg-poly(U) was prepared 2-3 weeks prior to its use at ESRF. This is probably a safe margin although based on the results of the ICP analysis, a recommended future procedure is to (a) perform and ICP measurement immediately after preparation, (b) limit the use of the Hg-poly(U) solution to 1 month after preparation and (c) conduct post-run ICP immediately after the experiments. These precaution are primarily to acknowledge the instability of Hg on the poly(U) while the other elements do not have this problem. The biggest surprise from the ICP analysis was the presence of significant quantities of Na. The analysis was performed for three additional samples for which no adsorption was observed in XSW experiments. These samples are desribed below in section 5.4.4.

	Concentration in micromole/L (+/- 10% error)					
Sample	Zn	Hg	P	Na	K	Ca
JL817OH_A 50 μM $ZnCl_2$ 25 μM Hg-poly(U)	38.3	5.93	22.7	160	61.5	20.5
JL817DOH_A 100 μM $ZnCl_2$ 25 μM Hg-poly(U)	80.0	7.50	28.6	215	13.7	14.0
JL817EOH_A 25 μM $ZnCl_2$ 25 μM Hg-poly(U)	19.2	6.91	17.2	107	18.9	10.1
JL817FOH_A 100 μM $ZnCl_2$ 25 μM Hg-poly(U)	36.6	3.87	34.8	130	8.5	10.9

Table 5.2: ICP-AES chemical analysis results for a selection of samples used at the ESRF synchrotron experiments. The analysis was performed by the Analytical Chemistry Laboratory at Argonne National Laboratory.

5.4.4 Miscellaneous Results from other *In-Situ* Experiments

So far in this chapter, results have been presented for those cases when adsorption was clearly observed and could be modeled well. Many other XSW in-situ experiments where performed in which experimental difficulties rendered the data unusable or for which no adsorption was observed. It was learned from sample JL817OH_A that the timescale of the adsorption process could be considerably longer than originally expected. Table 5.2 lists the experiments and results for these cases.

Sample	Description
JL_A8_18_5_01 DI water on 21.6 LSM/APTMS/PO3/Zr/DDBPA	$E\gamma$ = 18.5 keV. In this sample, the objective was to see signature of Zr (a monolayer very close to surface such as sample G1) in the LSI cell.
JL_A8_18_5_01 50 μM $ZnCl_2$ on 21.6 LSM/APTMS/PO3/Zr/DDBPA	$E\gamma$ = 18.5 keV. In this sample, Zn was added to measure offset between Zr and Zn adsorbed to PO_3 of DDBPA
JL_C1_12_4_02 25 μM Hg-polyU + 50 μM $ZnCl_2$ 21.6 LSM/APTMS/PO3/Zr/DDBPA	$E\gamma$ = 12.4 keV. This run was a follow up to Sample JL_C1 in this chapter that measured Zn adsorption. In this run Zn was adsorbed as in Zn-only but Hg yield was unclear
JL817BOH_C 25 μM Hg-polyU/A + 50 μM $ZnCl_2$ 21.6 LSM/OH	$E\gamma$ = 14.3 keV. This run followed the Zn on OH adsorption observed in this chapter (JL_B1). Both Hg and Zn appeared random for a long time and at several x-locations.
JL817COH_A 200 μM $ZnCl_2$ 21.6 LSM/OH	$E\gamma$ = 14.3 keV. Zn appeared random.
JL817COH_B 25 μM Hg-polyU + 200 μM $ZnCl_2$ 21.6 LSM/OH	$E\gamma$ = 14.3 keV. Both Hg and Zn appeared random.
JL817DOH_A 100 μM $ZnCl_2$ 21.6 LSM/OH	$E\gamma$ = 14.3 keV. Zn appeared random.
JL817EOH_B 25 μM Hg-polyU + 200 μM $ZnCl_2$ 21.6 LSM/OH	$E\gamma$ = 14.3 keV. Both Hg and Zn appeared random.
JL817EOH_B 25 μM Hg-polyU + 25 μM $ZnCl_2$ 21.6 LSM/OH	$E\gamma$ = 14.3 keV. Both Hg and Zn appeared random.

Table 5.3: Listing of additional XSW experiments performed at ESRF in July, 2003 but for which only bulk solution signatures were observed in the XSW analysis or for which experimental difficulties rendered the XSW analysis unusable.

5.5 Discussion

5.5.1 Zn Adsorption to a PO_3 Terminated Surface

Zn was adsorbed to a PO_3 terminated surface which was prepared identically to the metal-phosphonate thin film sample G1 in Chapter 4 (see Figure 4.16) but without the final Hf metal layer. This sample can be considered a substitution of Zn for Hf where the measurement was made *in-situ*. From the measurements of sample G1 of Chapter 4 (see Figure 4.16 and Table 4.3), we can estimate the upper limit of the PO_3 surface density to be equal to the Hf coverage of sample rgG1 which was 5.7 nm^{-2}. However, from Chapter 4 we also know the the Zr and Hf coverage in these samples likely exceed the PO_3 coverage which is not directly measurable. We would thus expect that the Zn coverage could be similar to the Hf coverage.

As shown in Figure 5.12 The XSW measurement of Zn adsorption to the PO_3 surface gave a Zn condensed layer Δz=4.5 nm, $z_{0,Zn}$=2.3 nm and Θ=0.37 nm^{-2}. This measured Zn coverage is ten times lower than the Hf coverage of sample G1. Further, a very large width of the Zn distribution was observed that cannot be explained by a model of Zn adsorption to the PO_3 surface groups plus a diffuse solution layer since we expect the PO_3 surface groups to be located at 2.3 nm from the result of sample G1. If all the Zn were adsorbed to just the PO_3 surface groups then a similar distribution to the Hf obtained in Sample G1 is expected but the XSW observation gave a much wider distribution for the Zn. One possible explanation of the wide Zn layer is that Zn has permeated into the surface film and adsorbed to the primer layer of PO_3 as well the surface PO_3 layer. A similar behavior was observed for Y atoms in sample A8 from Chapter 4 (see Figs. 4.4 and 4.6). In sample A8, the Y

was applied as the final step in the multilayer film for the purpose of marking the terminal PO_3 groups in that film. Instead the Y atoms were found uniformly distributed throughout the film, presumably finding additional adsorption sites at internal PO_3 layers. Thus, it is likely that the observed condensed layer coverage Θ=0.37 nm^{-2} is distributed among Zn adsorbed to the surface and internal PO_3 layers and a diffuse solution layer.

5.5.2 Zn adsorption to an OH Terminated Surface

The XSW measurement of sample JL817BOH_A provided the best example of an *in-situ* XSW measurement for which the yield could be very convincingly modeled as can be seen in Figure 5.11. In this sample, the OH-terminated surface is simply prepared by exposing an SiOx surface to a strong acid or base with hydrolyzes the surface O atoms to make surface Si-O-H terminations. In aqueous solution the $(O^-)(H^+)$ groups can dissociate as described above (see Section 5.1.5). The degree of dissociation is related to pH and other ionic species that may be present. In general the degree of dissociation of OH groups can be predicted based solely on the solution ionic strength and pH of the solution [76] from which the estimated surface charge density for the present case is 0.01 nm^{-2}. Sample JL817BOH_A measured the adsorption of 50 μM $ZnCl_2$ exposed to an OH terminated surface for which the condensed layer coverage of Zn from two separate scans was found to be 0.037(4) and 0.027(3) nm^{-2}. These values are within a factor of 3 of the estimated charge density of the OH surface. The Zn was found in a narrow distribution centered at z = 0.5 nm suggesting that the Debye layer would be at a considerably lower concentration than the surface or otherwise the center of the distribution would be

found at a higher z location. While the discussion here is based simplistically on the surface charge density expected from literature sources, a first principles theoretical treatment of this system below show very good agreement as well.

5.5.3 Adsorption of Hg-poly(U)/Zn to an OH Terminated Surface

The observation of a time-dependent adsorption from the Zn/Hg-poly(U) system was surprising since equilibrium had been assumed for many other XSW measurement attempts in this system prior to this measurement. While the kinetic nature of this observation would be very difficult to explain due to an insufficient detail of the complete chemical environment of the *in-situ* cell, the observed equilibrium state after 195 minutes was predicted theoretically by the theory group of Prof. Olvera.

A theoretical model was developed for the adsorption process that self consistently determined the density of chains and of cations in the bulk and at the surface and the number of ionized surface charges. Poly-anion adsorption to anionic surfaces via divalent cations can be explained if the charge of the surface is inverted by the adsorption of cations. But as shown here, the density of adsorbed cations is not sufficiently high to invert the charge of the surface, nor is the density of charges on the surface large enough to drive adsorption by correlations. A new model was developed for low-adsorption that involves the determination of the degree of surface silanol group ionization was developed

$$SiOH + H_2O \Leftrightarrow SiO^- + H_3O^+ \qquad (5.3)$$

with an equilibrium constant, K_a given by $-\log K_a = 7.2$ [80]. This value of the enthalpy per kBT can generate sufficient surface charge density for adsorption of Zn^{2+} or metallic ions M^{2+}. The adsorbed M^{2+} can react with the silanol groups via

$$SiOH + M^{2+} + H_2O \Leftrightarrow SiOM^{+} + H_3O^{+} \qquad (5.4)$$

The equilibrium constants of Equation 5.4 vary with different kinds of divalent metal ion: -log K ranges from 8.1 for Mg^{2+} to 5.1 for Pb^{2+} [80].

The number of reacted groups, O^- and M^+, as well as the number of unreacted M^{2+} at the surface is determined self consistently from a thermodynamic model that incorporates non-linear electrostatic effects. For Zn^{2+} we expect –log K to be slightly greater than the value 5.5 found for Cu^{2+} [80]. This reasonably matches the degree of adsorption observed in sample JL817BOH_A as shown in Figure 5.19. Next the polyelectrolyte and the NaCl were included in the solution and the adsorption of Zn and poly(U) at the surface in equilibrium with the bulk solution was determined. The values predicted are in close agreement with the experiments for sample JL817OH_A, also shown in Figure 5.19. A large fraction of the zinc on the surface reacts with the silanol group via Eq. 2 as shown in Figure 5.20.

The in situ XSW observed adsorption of Zn and poly(U) is due to the strong binding of Zn^{2+} to silica to form Zn^+ groups at the surface. The condensed Zn^{2+} along the poly(U) chain, upon adsorption promotes the reaction in Eq. 2 to form Zn^+ due to high Zn^{2+} concentration at the surface. In samples JL817BOH_A and JL817OH_A the adsorbed Zn coverages are comparable due to the presence of NaCl in sample JL817OH_A and due to the different values of the free Zn concentration in the bulk given that a fraction of the measured bulk Zn^{2+} is condensed on the poly(U) in the bulk solution. When the degree of adsorption of Zn in a hypothetical sample C is

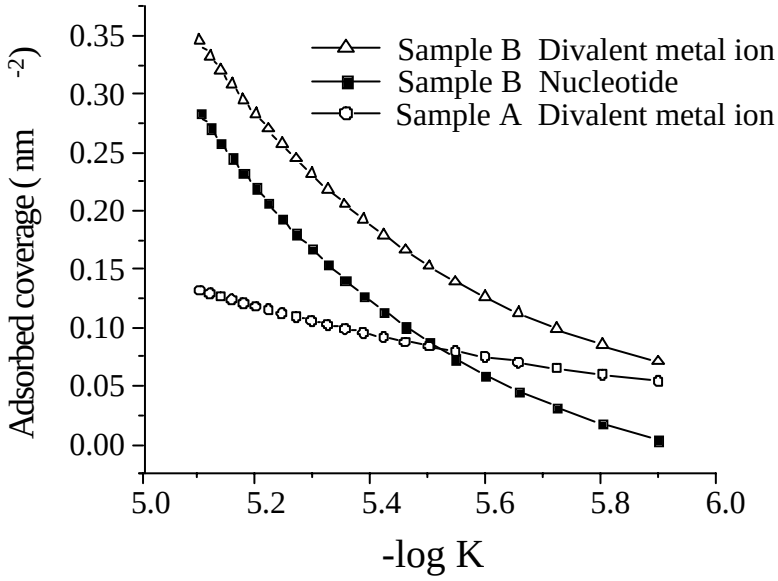

Figure 5.19: The calculated variation of nucleotide and divalent metal ion adsorption onto silica surface as a function of the equilibrium constant of the reaction in Eq. 2 using the following experimental parameters: For sample A (JL817BOH_A) the parameters are: [ZnCl2] = 17 μM, pH = 7, a 0.45 nm hydrated ion radius, 1 nm Zinc layer thickness, -log K_a = 7.2, 5 nm^{-2} silanol group surface density. For sample B (JL817OH_A) the additional parameters are: [ZnCl2] = 40 μM, [NaCl]= 150 μM, 25 μM nucleotide concentration, the distance between neighboring charged nucleotides is 0.45 nm, the diameter of polynucleotide is 1 nm, the polymerization degree of polynucleotide is 2500.

compared with the same conditions as JL817OH_A but without adsorbed poly(U), there is much less Zn adsorption as shown in Figure 5.21; NaCl leads to less overall adsorption of both poly(U) and Zn. The presence of Na and the competition of Zn for the surface and chains may explain the slow adsorption kinetics. The degree of

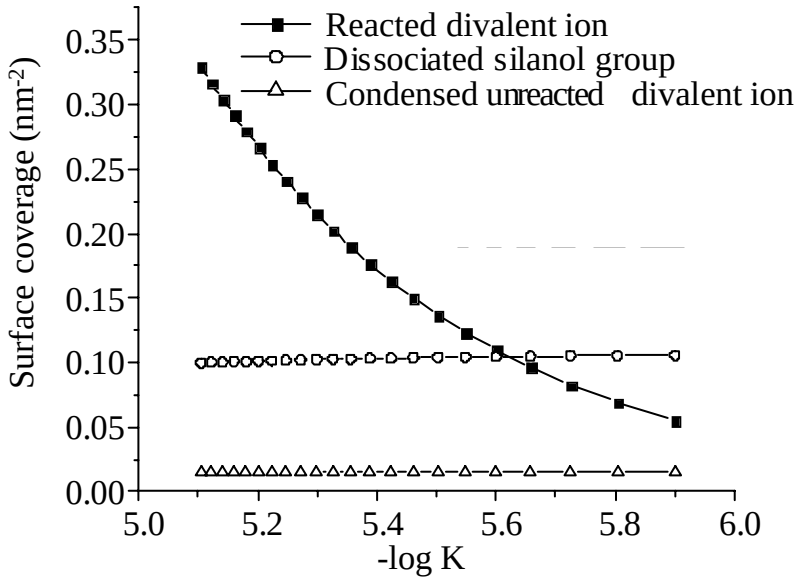

Figure 5.20: The calculated variation of dissociated silanol groups, reacted and un-reacted condensed divalent metal ion at the silica surface as a function of the equilibrium constant of the reaction in Equation 5.3 using the parameters for sample B (JL817OH_A)which are listed in the caption of Figure 5.19

adsorption for various surfaces and/or divalent ions is predicted as a function of the equilibrium constant K. There is a critical K value, $K_c = -Ac_H + BK_a$, where A > 0 and B > 0 depend only on the salt concentration, below which no adsorption occurs. When the pH increases since c^{H+} decreases, Kc increases, and when Ka increases such that the acid group is more likely to be ionized, Kc rises.

Both the experimental observations and theoretical model have shown that polynucleotide adsorption to like charge surface via divalent ions is possible, and does not require the bridging mechanism of the Zn^{2+} to both the surface and the nucleotide. The experimental results and theory generate a revised model for the

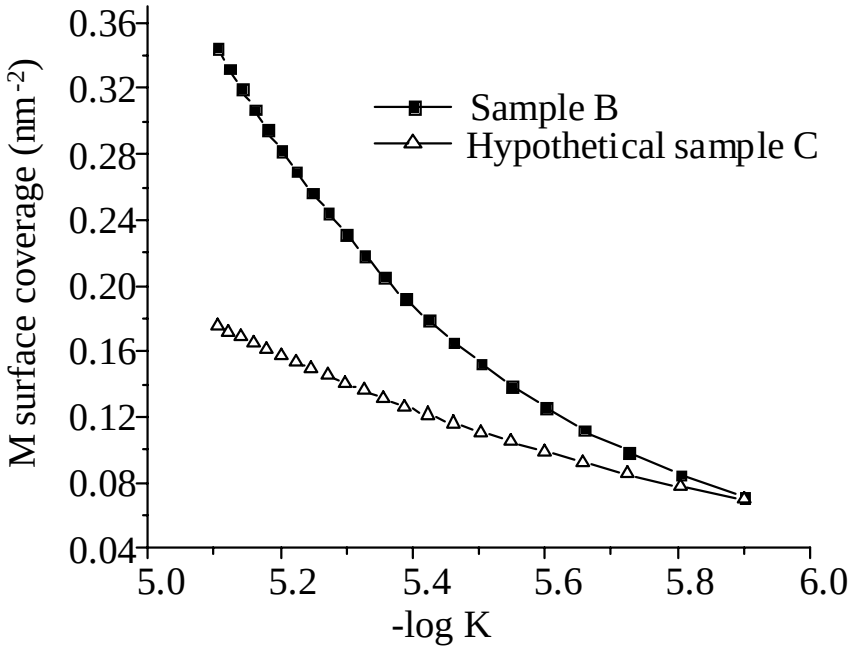

Figure 5.21: Theoretical comparison of total divalent metal ion (M) surface coverage for solutions with and without poly(U). Hypothetical sample **C** has the same amount of free divalent ions and sodium ions in the bulk solution as sample B (JL817OH_A), but without poly(U) in solution. More divalent ions adsorb onto the surface to cancel the charge of adsorbed poly(U). For the condition of larger –logK, less poly(U) is adsorbed. Therefore, the difference of M surface coverage between sample B and hypothetical sample **C** in this limit decreases.

adsorption mechanism. The experimental method, which can simultaneously follow the counterion and polyion distribution profiles during the adsorption process, represents a unique capability that can be applied to study the kinetics and equilibrium structure for a wide range of phenomena related to biomolecular adsorption, including DNA and other types of polyions in aqueous solution.

5.6 Conclusion

In this chapter, the adsorption of Hg-poly(U) and Zn from aqueous solution to the charged surfaces of specially prepared LSM substrates was demonstrated. The suitability of the large d-spacing LSMs for both in-situ and ex-situ XSW measurements in this application was found. Positively charged surfaces prepared by functionalizing to amine or Zr were able to adsorb Hg-poly(U) at low surface coverage. The result of the XSW measurement of the Hg-poly(U) adsorption to a Zr-terminated surface showed that the Hg and Zr atoms were located in narrow layers within several angstroms of each other suggesting that the dry conformation of single stranded RNA is for the base arms to lay flat along the substrate, perhaps attracted by hydrogen bonding to the OH surface. For the amine terminated surface, the attachment was shown to be of an electrostatic nature since rinsing with DI water removed all Hg-poly(U) from the substrate.

In-situ measurements of the adsorption of Hg-poly(U) provided an observation of a time-dependent process in which initial Zn adsorption was apparently inhibited by the Hg-poly(U) and/or NaCl present in the mixture followed by the adsorption of Zn alone after several hours which was then followed immediately by Hg-poly(U) adsorption. When Zn was presented to the same surface alone, adsorption was immediate and found to be of a similar concentration as observed in the Zn/Hg-poly(U) observed adsorption which was of the same magnitude as the expected surface charge of the OH surface. A theoretical treatment of the adsorption of Zn/Hg-poly(U) was able to predict the observed adsorption amounts and provided an explanation of the process, finding that chemisorption of

Zn to the OH surface groups (Equation 5.4) was the dominant process and that binding via an electrostatic bridging mechanism was not.

Chapter 6: Summary and Future Work

6.1 Thesis Summary

The principle accomplishment of this thesis has been the first demonstration of large d-spacing LSM X-ray mirrors for long-period XSW analysis. Their use has been successfully demonstrated for the *ex-situ* XSW analysis of a multilayer films based on metal-phosphonate architecture and for the *in-situ* XSW analysis of adsorption of metal-tagged biomolecules and counterions. These analyses were shown to be capable of measuring multiple atomic distributions in the 0.5 to 5.0 nm length scale. The effectiveness of the large d-spacing was best demonstrated by the results of the porphyrin square metal-phosphonate film series where in each sample, the expected offset of one-half of a layer thickness between the Zr and Zn/Re metal layers was measured by XSW. Previously, such information could only have been obtained by preparing similar films on several different LSMs. This work should provide a strong basis for the use of large d-spacing LSMs for nano structured films.

In this thesis the utility of the large d-spacing LSMs for the *in-situ* study of biomolecular adsorption has been demonstrated. The presence of many orders of Bragg reflection close to the TER region substantially reduces the considerable experimental uncertainty in using TER alone for measuring *in-situ* atomic distributions. This together with the possibility to measure over a range of adsorbate distribution length scales makes the large d-spacing LSMs well suited for *in-situ* studies. The XSW analysis of the adsorption of Zn and Hg-poly(U) demonstrated that

both the biomolecular and counterion components could be measured simultaneously. Very good XSW yield predictions were obtained using the 1st, 2nd and 3rd Bragg reflections. More importantly, the ability to reliably measure the partition between bulk and adsorbed distributions was possible and thus an absolute measure of adsorbed amounts of Zn and Hg-poly(U) that agreed well with theoretical predictions was possible.

6.2 Future Work

There are numerous opportunities for continuing the work in this thesis:

1. The in-situ XSW methodology should be applied to provide experimental verification of ionic distributions near interfaces. To better utilize the present method, surfaces with higher charge density should be studied and attempts to measure the double layer structure using measurable cation and anion components. For example, solutions containing Br or I anions and along with Zn or other cations (Sr, Ni, Co) can be studied.

2. Continuation of the Hg-poly(U)/Zn scheme introduced in this thesis should be pursued. However, the problem of Zn accumulation needs to be solved. As it is suspected that the Zn accumulation is due to the precipitation of $Zn(OH)_2$, it is recommended that $SrCl_2$ be substituted for Zn since the pK for the hydroxide reaction for the Sr^{2+} cation is 13.1 compared to 9.5 for Zn. In this way a higher pH can be used and thus a higher surface charge of the hydroxylated SiOH surface can be realized.

3. The metal-phosponate systems studied in this thesis are a small subset of the numerous examples using this architecture which can be studied using the same technique. Since the experimental difficulties are fewer in *ex-situ* measurements, such systems should be used for the first attempts to apply Fourier inversion direct-methods to the XSW yield from large d-spacing LSMs.

In order to maximize the chance for success, the LSM quality should be improved. In particular, the interfacial widths must be improved and final surface roughness lowered. Another recommendation is to adopt the methods of Professor Talhams group in the University of Florida which can produce well defined metal-phosphonate multilayer films which would be excellent candidates for proving the direct-methods techniques. Such an effort should precede attempts to use direct methods on *in-situ* data.

While the LSM used in this thesis performed very well and produced very useful measurements of phenomena occurring on the nanometer length scale, significant improvements could be made by improving the sharpness of the interfaces in the LSMs and thus create several more usable orders of Bragg reflection as suggested in Figure 2.2. The parameters of the Si/Mo deposition could be optimized and perhaps the addition diffusion barriers could significantly reduce the interfacial widths. Other combinations of high and low electron density materials cold be considered. For example, Pt/C, Rh/Si are potential candidates.

REFERENCES

1. Ulman, A., *An introduction to ultrathin organic films : from Langmuir-Blodgett to self-assembly*. 1991, Boston: Academic Press.

2. Ulman, A., *Characterization of organic thin films*. 1995, Boston: Butterworth-Heinemann.

3. Bedzyk, M.J., *Scattering: X-ray Standing Wave Techniques*, in *Encyclopedia of Condensed Matter Physics*, G. Bassani, G. Liedl, and P. Wyder, Editors. 2005, Elsevier Academic Press.

4. Bilderback, D.H., B.M. Larson, T.W. Barbee, G.E. Ice, and C.J. Sparks, *Design of Doubly Focusing, Thunable (5-30 keV), Wide Bandpass Optics made from Layered Synthetic Micrstructures.* Nucl. Instrum. Meth., 1983. **208**: p. 251-261.

5. Barbee, T.W. *Sputtered Layered Synthetic Microstructure (LSM) Dispersion Elements*. in *AIP Conf. Proc. No. 75 on Low energy X-ray diagnostics*. 1981.

6. Spiller, E., *Reflecting Multilayer Coatings for the Far UV Region.* Appl. Opt., 1976. **15**: p. 2333-2338.

7. Andreev, S.S., M.S. Bibishkin, N.I. Chkhalo, E.B. Kluenkov, K.A. Prokhorov, N.N. Salashchenko, M.V. Zorina, F. Schafers, and L.A. Shmaenok, *Short-period multilayer X-ray mirrors.* Journal of Synchrotron Radiation, 2003. **10**: p. 358-360.

8. Bajt, S.A., H.N. Chapman, N. Nguyen, J. Alameda, J.C. Robinson, M. Malinowski, E. Gullikson, A. Aquila, C. Tarrio, and S. Grantham, *Design and performance of capping layers for extreme-ultraviolet multilayer mirrors.* Applied Optics, 2003. **42**(28): p. 5750-5758.

9. Barbee, T.W. and W.K. Warburton, *X-ray evanescent- and standing-wave fluorescence studies using a layered synthetic microstructure.* Materials Letters, 1984. **3**(12): p. 17-23.

10. Bedzyk, M.J., D. Bilderback, J. White, H.D. Abruna, and M.G. Bommarito, *Probing Electrochemical Interfaces with X-Ray Standing Waves.* Journal of Physical Chemistry, 1986. **90**(21): p. 4926-4928.

11. Bedzyk, M.J., D.H. Bilderback, G.M. Bommarito, M. Caffrey, and J.S. Schildkraut, *X-Ray Standing Waves - a Molecular Yardstick for Biological-Membranes.* Science, 1988. **241**(4874): p. 1788-1791.

12. Bedzyk, M.J., M.G. Bommarito, M. Caffrey, and T.L. Penner, *Diffuse-double layer at a membrane-aqueous interace measured with x-ray standing waves.* Science, 1990. **248**: p. 52-56.

13. Lin, W.B., T.L. Lee, P.F. Lyman, J.J. Lee, M.J. Bedzyk, and T.J. Marks, *Atomic resolution X-ray standing wave microstructural characterization of NLO-active self-assembled chromophoric superlattices.* Journal of the American Chemical Society, 1997. **119**(9): p. 2205-2211.

14. Cowan, P.L., J.A. Golovchenko, and M.F. Robbins, *X-Ray Standing Waves at Crystal Surfaces.* Phys. Rev. Lett., 1980. **44**: p. 1680–1683.

15. Golovchenko, J.A., J.R. Patel, D.R. Kaplan, P.L. Cowan, and M.J. Bedzyk, *Solution to the Surface Registration Problem Using X-Ray Standing Waves.* Physical Review Letters, 1982. **49**(8): p. 560-563.

16. Wang, J., M.J. Bedzyk, T.L. Penner, and M. Caffrey, *Structural Studies of Membranes and Surface-Layers up to 1,000 a Thick Using X-Ray Standing Waves.* Nature, 1991. **354**(6352): p. 377-380.

17. Fenter, P., L. Cheng, S. Rihs, M. Machesky, M.J. Bedzyk, and N.C. Sturchio, *Electrical double-layer structure at the rutile-water interface as observed in situ with small-period X-ray standing waves.* Journal of Colloid and Interface Science, 2000. **225**(1): p. 154-165.

18. Wang, J., M. Caffrey, M.J. Bedzyk, and T.L. Penner, *Direct profiling and reversibility of ion distribution at a charged membrane/aqueous interface: An x-ray standing wave study*. Langmuir, 2001. **17**: p. 3671-3681.

19. Bedzyk, M.J., G.M. Bommarito, and J.S. Schildkraut, *X-Ray Standing Waves at a Reflecting Mirror Surface.* Physical Review Letters, 1989. **62**(12): p. 1376-1379.

20. Batterman, B.W., *Effect of Dynamical Diffraction in X-Ray Fluorescence Scattering.* Physical Review, 1964. **133**(3A): p. A759-A764.

21. Bedzyk, M. and G. Materlik, *X-Ray Standing Wave Analysis for Bromine Chemisorbed on Germanium.* Surface Science, 1985. **152**(APR): p. 10-16.

22. Cheng, L., P. Fenter, M.J. Bedzyk, and N.C. Sturchio, *Fourier-expansion solution of atom distributions in a crystal using x-ray standing waves.* Physical Review Letters, 2003. **90**(25).

23. Zhang, Z., P. Fenter, L. Cheng, N.C. Sturchio, M.J. Bedzyk, M.L. Machesky, and D.J. Wesolowski, *Model-independent X-ray imaging of adsorbed cations at the crystal-water interface.* Surface Science, 2004. **554**(2-3): p. L95-L100.

24. Parratt, L.G., *Surface Studies of Solids by Total Reflection of X-rays.* Physical Review, 1954. **95**(2): p. 359-369.

25. Bommarito, G.M., *In Situ Studies of Electrochemical Interfaces Using X-Ray Standing Waves*, in *Graduate School*. 1992, Cornell University. p. 1-378.

26. Wang, J., *X-ray standing waves and their use in characterizing biologically relevant thin film systems.*, in *Chemical Physics*. 1994, The Ohio State University.

27. Dev, B.N., A.K. Das, S. Dev, D.W. Schubert, M. Stamm, and G. Materlik, *Resonance enhancement of x rays in layered materials: Application to surface enrichment in polymer blends.* Physical Review B, 2000. **61**(12): p. 8462-8468.

28. Ghose, S.K. and B.N. Dev, *X-ray standing wave and reflectometric characterization of multilayer structures.* Physical Review B, 2001. **6324**(24).

29. Nevot, L. and P. Croce, Revue. Phys. Appl., 1980. **15**: p. 761.

30. Petford-Long, A.K., *High-Resolution Electron-Microscopy Study of X-Ray Multilayer.* Journal of Applied Physics, 1987. **61**(4): p. 1422-1428.

31. Holloway, K., *Interfacial Reactions on Annealing Molybdenum-Silicon.* Journal of Applied Physics, 1989. **65**(2): p. 474-480.

32. Stearns, D.G., *Fabrication of High-Reflectance Mo-Si Multilayer Mirrors By.* Journal of Vacuum Science & Technology a-Vacuum Surfaces And, 1991. **9**(5): p. 2662-2669.

33. Puri, S., B. Chand, D. Mehta, M.L. Garg, N. Singh, and P.N. Trehan, *K and L shell X-ray fluorescence cross sections.* Atomic Data and Nuclear Data Tables, 1995. **61**(2): p. 289-311.

34. Lee, H., L.J. Kepley, H.G. Hong, S. Akhter, and T.E. Mallouk, *Adsorption of Ordered Zirconium Phosphonate Multilayer Films on Silicon and Gold Surfaces.* Journal of Physical Chemistry, 1988. **92**(9): p. 2597-2601.

35. Dines, M.B. and P. DiGiacomo, in *Inorganic Chemistry*. 1981. p. 92.

36. Putvinski, T.M., M.L. Schilling, H.E. Katz, C.E.D. Chidsey, A.M. Mujsce, and A.B. Emerson, *Self-Assembly of Organic Multilayers with Polar Order Using Zirconium-Phosphate Bonding between Layers.* Langmuir, 1990. **6**(10): p. 1567-1571.

37. Schilling, M.L., H.E. Katz, S.M. Stein, S.F. Shane, W.L. Wilson, S. Buratto, S.B. Ungashe, G.N. Taylor, T.M. Putvinski, and C.E.D. Chidsey, *Structural Studies of Zirconium Alkylphosphonate Monolayers and Multilayer Assemblies.* Langmuir, 1993. **9**(8): p. 2156-2160.

38. Yang, H.C., K. Aoki, H.G. Hong, D.D. Sackett, M.F. Arendt, S.L. Yau, C.M. Bell, and T.E. Mallouk, *Growth and Characterization of Metal(Ii) Alkanebisphosphonate Multilayer Thin-Films on Gold Surfaces*, in *Journal of the American Chemical Society*. 1993. p. 11855-11862.

39. Zeppenfeld, A.C., S.L. Fiddler, W.K. Ham, B.J. Klopfenstein, and C.J. Page, *Variation of Layer Spacing in Self-Assembled Hafnium-1,10-Decandiylbis(phosphonate) Multilayers As Determined by Ellipsometry and Grazing Angle X-ray Diffraction.* J. Am. Chem. Soc., 1994. **116**: p. 9158-9165.

40. Byrd, H., J.K. Pike, and D.R. Talham, *Inorganic Monolayers Formed at an Organic Template - a Langmuir-Blodgett Route to Monolayer and Multilayer Films of Zirconium Octadecylphosphonate.* Chemistry of Materials, 1993. **5**(5): p. 709-715.

41. Byrd, H., S. Whipps, J.K. Pike, J.F. Ma, S.E. Nagler, and D.R. Talham, *Role of the Template Layer in Organizing Self-Assembled Films - Zirconium Phosphonate Monolayers and Multilayers at a Langmuir-Blodgett Template.* Journal of the American Chemical Society, 1994. **116**(1): p. 295-301.

42. Fanucci, G.E. and D.R. Talham, *Langmuir-Blodgett films based on known layered solids: Lanthanide(III) octadecylphosphonate LB films.* Langmuir, 1999. **15**(9): p. 3289-3295.

43. Bakiamoh, S.B. and G.J. Blanchard, *Characterizing metal phosphonate surface coverage using surface second harmonic generation. Evidence for the coexistence of ordered and disordered domains*, in *Langmuir*. 2002. p. 6246-6253.

44. Zwahlen, M., S. Tosatti, M. Textor, and G. Hahner, *Orientation in methyl- and hydroxyl-terminated self-assembled alkanephosphate monolayers on titanium oxide surfaces investigated with soft X-ray absorption*, in *Langmuir*. 2002. p. 3957-3962.

45. Williams, M.E. and J.T. Hupp, *Scanning electrochemical microscopy assessment of rates of molecular transport through mesoporous thin-films of porphyrinic "Molecular squares".* Journal of Physical Chemistry B, 2001. **105**(37): p. 8944-8950.

46. Czaplewski, K.F., J.T. Hupp, and R.Q. Snurr, *Molecular squares as molecular sieves: Size-selective transport through porous-membrane-supported thin-film materials.* Advanced Materials, 2001. **13**(24): p. 1895-+.

47. Zhang, J.L., M.E. Williams, M.H. Keefe, G.A. Morris, S.T. Nguyen, and J.T. Hupp, *Molecular sieving and thin film transport by molecular materials featuring large component cavities.* Electrochemical and Solid State Letters, 2002. **5**(5): p. E25-E28.

48. Merlau, M.L., M.D.P. Mejia, S.T. Nguyen, and J.T. Hupp, *Artificial enzymes formed through directed assembly of molecular square encapsulated epoxidation catalysts.* Angewandte Chemie-International Edition, 2001. **40**(22): p. 4239-4242.

49. Mines, G.A., B.C. Tzeng, K.J. Stevenson, J.L. Li, and J.T. Hupp, *Microporous supramolecular coordination compounds as chemosensory photonic lattices.* Angewandte Chemie-International Edition, 2002. **41**(1): p. 154-157.

50. Keefe, M.H., K.D. Benkstein, and J.T. Hupp, *Luminescent sensor molecules based on coordinated metals: a review of recent developments.* Coordination Chemistry Reviews, 2000. **205**: p. 201-228.

51. Yan, S.G., J.S. Prieskorn, Y.J. Kim, and J.T. Hupp, *In search of the inverted region: Chromophore-based driving force dependence of interfacial electron transfer reactivity at the nanocrystalline titanium dioxide semiconductor/solution interface.* Journal of Physical Chemistry B, 2000. **104**(46): p. 10871-10877.

52. Clearfield, A. and Z.K. Wang, *Organically pillared microporous zirconium phosphonates.* Journal of the Chemical Society-Dalton Transactions, 2002(15): p. 2937-2947.

53. Milic, T., J.C. Garno, J.D. Batteas, G. Smeureanu, and C.M. Drain, *Self-organization of self-assembled tetrameric porphyrin arrays on surfaces.* Langmuir, 2004. **20**(10): p. 3974-3983.

54. Horne, J.C. and G.J. Blanchard, *The Role of Substrate Identity in Determining Monolayer Motional Relaxation Dynamics.* J. Am. Chem. Soc., 1998. **120**: p. 6336-6344.

55. Gurney, R.W., A.M. Massar, J.A. Libera, C.P. Schwartz, P. Paoprasert, R.C. Bailey, H. Jin, K.F. Morris, M.D. Wightman, M.J. Bedzyk, S.T. Nguyen, and J.T. Hupp, *Directed-Assembly of Nanoporous, Porphyrin-Based, Molecular-Square Thin-Films.* Submitted to: JACS.

56. Massari, A.M., R.W. Gurney, M.D. Wightman, C.H.K. Huang, S.B.T. Nguyen, and J.T. Hupp, *Ultrathin micropatterned porphyrin films assembled via zirconium phosphonate chemistry*, in *Polyhedron*. 2003. p. 3065-3072.

57. Massari, A.M., R.W. Gurney, C.P. Schwartz, S.T. Nguyen, and J.T. Hupp, in *Langmuir*. 2004.

58. Wang, J., M.J. Bedzyk, and M. Caffrey, *Resonance-Enhanced X-Rays in Thin-Films - a Structure Probe for Membranes and Surface-Layers.* Science, 1992. **258**(5083): p. 775-778.

59. Libera, J.A., R.W. Gurney, S.T. Nguyen, J.T. Hupp, C. Liu, R. Conley, and M.J. Bedzyk, *X-ray Nanoscale Profiling of Layer-by-Layer Assembled Metal/Organo-Phosphonate Films*, in *Langmuir*. 2004.

60. Zhuravlev, L.T., *Concentration of hydroxyl groups on the surface of amorphous silicas*, in *Langmuir*. 1987. p. 316-318.

61. Cao, G., H.G. Hong, and T.E. Mallouk, *Layered metal phosphates and phosphonates: from crystals to monolayers*, in *Accounts of Chemical Research*. 1992. p. 420-427.

62. Nam, J.M., C.S. Thaxton, and C.A. Mirkin, *Nanoparticle-based bio-bar codes for the ultrasensitive detection of proteins.* Science, 2003. **301**(5641): p. 1884-1886.

63. Bustamante, C., Z. Bryant, and S.B. Smith, *Ten years of tension: single-molecule DNA mechanics.* Nature, 2003. **421**(6921): p. 423-427.

64. Levene, M.J., J. Korlach, S.W. Turner, M. Foquet, H.G. Craighead, and W.W. Webb, *Zero-mode waveguides for single-molecule analysis at high concentrations.* Science, 2003. **299**(5607): p. 682-686.

65. Raspaud, E., M. Olvera de la Cruz, J.L. Sikorav, and F. Livolant, *Precipitation of DNA by polyamines: A polyelectrolyte behavior.* Biophysical Journal, 1998. **74**(1): p. 381-393.

66. Olvera de la Cruz, M., L. Belloni, M. Delsanti, Dalbiez, J.P., O. Spalla, and M. Drifford, *Precipitation of highly charged polyelectrlyte solutions in the presence of multivalent salts.* J. Chem. Phys., 1995. **103**(13): p. p.5781-5791.

67. Netz, R.R. and J.F. Joanny, *Adsorption of semiflexible polyelectrolytes on charged planar surfaces: Charge compensation, charge reversal, and multilayer formation.* Macromolecules, 1999. **32**(26): p. 9013-9025.

68. Sens, P. and J.F. Joanny, *Counterion release and electrostatic adsorption.* Physical Review Letters, 2000. **84**(21): p. 4862-4865.

69. Dobrynin, A.V., A. Deshkovski, and M. Rubinstein, *Adsorption of polyelectrolytes at oppositely charged surfaces.* Macromolecules, 2001. **34**: p. 3421-3436.

70. Czajkowsky, D.M., J. Mou, Y.Y. Zhang, and Z. Shao, *DNA on cationic lipid bilayers for AFM imaging in solution: Resolution of the double helix.* Biophysical Journal, 1996. **70**(2): p. WAMG8-WAMG8.

71. Fang, Y. and J.H. Hoh, *Surface-directed DNA condensation in the absence of soluble multivalent cations.* Nucleic Acids Research, 1998. **26**(2): p. 588-593.

72. Fang, Y. and J. Yang, *Two-dimensional condensation of DNA molecules on cationic lipid membranes.* J. Phys. Chem. B, 1997. **101**(3): p. 441-449.

73. Fang, Y. and J. Yang, *Effect of cationic strength and species on 2-D condensation of DNA.* J. Phys. Chem. B, 1997. **101**(18): p. 3453-3456.

74. Hansma, H.G. and D.E. Laney, *DNA binding to mica correlates with cationic radius: assay by atomic force microscopy.* Biophysical Journal, 1996. **70**(April): p. 1933-1939.

75. Pastre, D., O. Pietrement, P. Fusil, F. Landousy, J. Jeusset, M.O. David, C. Hamon, E. Le Cam, and A. Zozime, *Adsorption of DNA to mica mediated by divalent counterions: A theoretical and experimental study.* Biophysical Journal, 2003. **85**(4): p. 2507-2518.

76. Behrens, S.H. and D.G. Grier, *The charge of glass and silica surfaces.* Journal of Chemical Physics, 2001. **115**(14): p. 6716-6721.

77. Hiemstra, T., J.C.M. Dewit, and W.H. Vanriemsdijk, *Multisite Proton Adsorption Modeling at the Solid-Solution Interface of (Hydr)Oxides - a New Approach .2. Application to Various Important (Hydr)Oxides.* Journal of Colloid and Interface Science, 1989. **133**(1): p. 105-117.

78. Dale, R.M.K., E. Martin, D.C. Livingston, and D.C. Ward, *Direct Covalent Mercuration of Nucleotides and Polynucleotides.* Biochemistry, 1975. **14**(11): p. 2447-2457.

79. Zhuravlev, L.T., *Concentration of hydroxyl groups on the surface of amorphous silicas.* Langmuir, 1987. **3**: p. 316-318.

80. Stumm, W., H. Hohl, and F. Dalang, Croat. Chem. Acta., 1976. **48**: p. 491.

Appendix A: Documentation of MATLAB Programs

A.1 Introduction

This Appendix provides documentation for the XSW analysis MATLAB functions developed for this thesis. In this Appendix, all MATLAB functions or variable names are indicated in *blue italic text* with functions denoted with a ".m" extension. The main computer programs that were developed are adaptations of the predecessor computer programs XSWAN and SUGO written in FORTRAN code for the MAC computer platform. The Fortran XSWAN program was transcribed to the MATLAB program *xswan2b.m*, preserving only the functionality that calculates the XSW E-field intensity, amplitude and phase and the X-ray reflectivity and transmissivity. The SUGO program was replaced by the MATLAB graphical user interface program *SUGOM.m* which combines the peak fitting functionality of SUGO and normalization array arithmetic previously done using the SWAN program. Numerous additional functions were developed for the creation of LSM model files, least squares fitting of reflectivity and yield, and the computation of index of refraction data. The general analytical method is outlined below followed by specific documentation for the individual functions and a user guide for the *SUGOM.m* GUI. For the purpose of this Appendix, all the functions listed here were archived on a CD in a folder named Matlab/JAL_Thesis_10_04/. These MATLAB files are current to this Appendix and contain comments providing further detailed documentation.

XSW Analytical Computer Tools:

1. Determine the LSM model that best fits measured reflectivity:

   We measure the X-ray reflectivity of flat substrates using a θ-2θ scan. At low angles of incidence, Paratt's recursion formulation is used to theoretically predict the measured reflectivity. A layered model is constructed by defining a series of slabs or layers where each layer in the model contains: (a) index of refraction ($n = 1-\delta-i\beta$), (b) thickness and (c) roughness for the interface between the present layer and the one above it. The layered model is first constructed using an assumed or previously known layer structure with parameters that are optimized against the measured reflectivity using least squares fitting techniques. The final result of this step is an LSM that correctly predicts the observed X-ray reflectivity from the sample. The LSM model is then held fixed for the next steps. MATLAB functions: *xswan2b_SP.m*, *Reflect_LSM.m*, *Ref_Vec.m*, *LSM05.m*, *LSM05_X.m*, *LSM_plot.m*, *leasqrpf.m*, *dfdppf.m*.

2. Compute the E-field intensity from the LSM:

   Paratt's recursion formula is used to calculate the E-field intensity over the θ-z range over which it is desired to predict an observed X-ray fluorescence yield. This computation is performed over a 2-d θ-z grid and is stored in the MATLAB array *EFI_array*. For example, in the analysis of the Chapter 4 metal phosphonate samples, the EFI_array is a 600 x 603 size array of floating

point precision numbers whose stored file size is 3 Mbytes. The computation of this array takes about 1 hour to perform on a 2 GHz PC computer. For this reason, the calculation is performed once and then stored in a MATLAB variable file with a .MAT extension and later read in for yield calculations. MATLAB functions: *xswan2b_SP.m*, *rgG1_EFI_array.m*, *EFI_th_smooth.m*, *EFI_plot.m*, *EFI_th_var_smooth.m*.

3. Calculation of the X-ray fluorescence yield:

Once the *EFI_array* calculation is complete, the modeling of unknown atomic distributions can be performed by model calculations to the observed X-ray fluorescence yield. The yield is calculated from a model atomic distribution $\rho(z)$ by evaluating the integral:

$$Yield(\theta) = \int \rho(z)\, I(\theta_i, z_j)\, dz$$

Where $I(\theta_i, z_j)$ = *EFI_array*. The parameters of the model $\rho(z_j)$ are optimized to provide the best fit to the observed X-ray fluorescence. MATLAB functions: *YFIT_ObjF_5.m*, *leasqrpf.m*, *dfdppf.m*, *EFI_convolve.m*, *gauss.m*, *flat_decay.m*, *gauss_random.m*, *step_random.m*, *SStep_random.m*, *abStep_random.m*.

4. Utility functions:

The definition of LSM files is greatly simplified by the ability to determine the index of refraction using a MATLAB function. The alternative is to look up the

data from tables or a website. The MATLAB function *IOR.m* was written for this purpose.

XSW Experimental Computer Tools:

1. Beamline data acquisition:

Several methods of acquiring XSW data are available. The SPEC macros used for single crystal XSW such as xsw.mac, thtth.mac, or xswdxp.mac. These tools provide control of the θ and 2θ motors as well as the acquisition of X-ray detector spectra. An alternative method is to use a simpler SPEC macro (mcamac.mac) which sets up the X-ray detector as though it was a simple counter and where the mca output is placed inline with the standard SPEC scan output. Each of these two cases produces its own output file format. In this thesis, the SPEC macro thtth.mac was used to collect XSW data at the X15A beamline while the in-line method was used to collect the XSW data at ESRF. Each method produces the same data in different formats and must include the following information at each angle step: (a) angle position, (b) reflectivity detector counts, (c) incident beam monitor counts, (d) mca spectra and (e) all necessary fluorescence detector channels necessary to compute the live-time fraction correction for the fluorescence detector. The details of (e) depend on the particular X-ray fluorescence detector system.

2. Peak Fitting and Normalized Yield Calculaton:

Once an XSW scan is complete, the normalized yield is calculated using the MATLAB GUI *SUGOM.m*. This user-friendly program reads in the SPEC output file ands parses it into a standard XSW data structure named *yield_array*. The user then performs the peak fitting using the GUI and the normalized results are written into yield_array which can be output in its entirety as an EXCEL spreadsheet. Additional XSW analysis corrections such as footprint corrections, X-ray detector efficiency and attenuation corrections are done in the EXCEL spreadsheet or elsewhere. Viewing the SUGOM.m out EXCEL spreadsheet provides a detailed view of the function performed by the SUGOM program and has all the raw data variables as well as the final normalized yield so that manual checks can be performed if desired. Each data variable is provided with its standard deviation.

xswan2b.m User Guide:

The *xswan2b.m* program is a general Paratts recursion formula implementation which can calculate the XSW E-field and X-ray reflectivity. To be general it calculates at only one value of θ and z. Examples of how to calculate reflectivity and E-field intensity are given in MATLAB programs rgG1_Rfit2.m and rgG1_EFI_array.m, respectively. The program rgG1_Rfit2.m calculates X-ray reflectivity with the option of invoking least squares fitting on any or all of the input parameters. This program is just an example of one way to use the xswan2b.m function which is actually called in the function Reflect_LSM.m in this case. The comments in the program listing provide an explanation of this function.

SUGOM.m User Guide:

The SUGOM.m program is launched by typing SUGOM and the MATLAB command prompt which launches the GUI as depicted in Figure 3.2. Since the SUGOM.m program was used only for the work of this thesis, some features are not generalized and probably cannot be, requiring future users to provide the required customization for each beamline SPEC and detector setup encountered. The details provided in this Appendix will make it possible for others to perform the beamline specific customization required. As an example, the customization required about 4 hours of MATLAB programming during the ESRF experiments in July, 2003 and were done at the beamline. For the remainder of this section, it will be assumed that the necessary customizations have been completed. This guide will use an ESRF XSW scan as an example. The ESRF data was taken with the mac data in-line with the SPEC scan output file. For this reason, a filename and SPEC scan number are required to load the XSW scan. The SPEC file rgI8_18_5_01 is used as an example and contains the XSW scan for sample I8 of this thesis. Follow the steps below to analyze the Hf La, Hf Lb1, HLb2, Zn/Re and Zr X-ray peaks. Text in bold red refers to SUGOM GUI interface data entry boxes or controls:

SUGMO.m Tutorial:

1. Launch MATLAB. Launch *SUGOM.m* by typing SUGOM in the MATLAB command line.

2. Enter 60,600 in the **refl_STB** data entry box. Enter 53,800 in the **mon_STB** data entry box. These values must be entered before loading the SPEC scan because it is during the loading process that normalized reflectivity is calculated.

3. Enter “5” in the **Spec Scan** data entry box. Click on the **Load ESRF File** button and navigate the file dialog to open the SPEC file rgI8_18_5_01. The 5th SPEC scan loads and the angle totalized mca spectrum is displayed.

4. Familiarize yourself with the *SUGOM.m* display controls. Adjust the values in the **Upper Ch**, **Lower Ch**, **Upper Step**, and **Lower Step** controls to select any range of mca channels or steps to display. Toggle between a log or linear counts axis using the **Log** and **Linear** control buttons.

5. Set the **Lower Ch**=20, **Upper Ch**=1280, **Lower Step**=1 and **Upper Step**=1280. Click on the **Ouptut MCA Spectrum** button to create a two column text output file of the currently displayed mca spectrum. This can be used at the beamline to perform EXCEL or Kaleidagraph X-ray calibration.

6. Click on the down arrow in the list box directly below the Compute Yields control button and note that the list has the entries “no lines” and “pulser”. Next click on the **Load Line List** button and navigate to and open the file *ESRF1_Line_List.m.* Click on the down arrow in the list box again and note the new list entries. These labels were created knowing which lines were going to be found in the mca spectrum. The user can also create his own list of labels as required. This file is a simple text list of X-ray line labels which are used to identify X-ray peaks during peak fitting. Open the file *ESRF1_Line_List.m* in the MATLAB editor to see the simple format of this file. Up to 10 text labels an be made. These labels will appear as column headers in the yield_array output file.

7. Set the **Lower Ch**=950, **Upper Ch**=1070. Enter “1” in the **# of Peaks** data entry box. Click on the **Show Peaks** control button. Use on the Peak Number control to select **Baseline** or peak **1**. Select peak **1**. Select **ZrKa** from the drop-down

list below the **Compute Yields** control button. Note that this label now appears in the box below the **Peak Number** control indicating that peak **1** will be associated with the ZrKa label.

8. With peak **1** selected, click anywhere on the mca graph to preposition a Gaussian peak on the Zr peak. Use the **Peak Position**, **Peak FWHM** and **Peak Height** slider controls or data entry boxes to adjust your guess. Select **Baseline** from the **Peak Number** selector and adjust the baseline as appropriate. Use the Log display to accentuate the display for the baseline. Set the display scale to **Linear**. Click on the **Prefit Spectrum** control button to execute a fit of your guess to the spectrum. Add or remove peaks as necessary. In this case one peak is sufficient. Click on the Compute Yields button to compute the peak areas of all peaks for each angle step. This can be observed step by step on the display.

9. Select **ZrKa** from the **Yield Array** drop-down list. Click on the **Plot Yield Array Ch** button to produce a plot of ZrKa and R.

10. Now repeat the peak fitting for the Hf and Zn/Re peaks. Set the **Lower Ch**=463, **Upper Ch**=632. Enter “5” in the **# of Peaks** data entry box. Using the peak editing tools described above make the following peak label associations: peak **1** = **HfLa**, peak **2** = **Zn/Re**, peak **3** = **HfLb1**, peak **4** = **HfLb2**, peak **5** = **no line**. Construct a guess using these 5 peaks with the order of peaks from left to right being in the order **1** to **5**. Click on **Prefit Spectrum** and then **Compute Yields**.

11. Select from the **Yield Array** drop-down list and click on the **Plot Yield Array Ch** button to produce a plot of various peaks just fit. Click on **Output Normalized Yields** to save the yield array to column text file. View the file with MS Excel.

This Tutorial provides a simple demonstration of the features and use of SUGOM.m. The more difficult part of customization of SUGOM requires a good knowledge of MATALB programming. A guide to the necessary steps for customization are given below:

SUGMO.m Customization Guide:

SUGOM.m is a MATLAB program file containing a large number of functions which control the GUI, load data and save output data. The GUI requires a figure file which is *SUGOM.fig*. One MATLAB function needs to be altered or rewritten when the format of the SPEC data files are different than those currently implemeted in the *SUGOM.m* program. For the example used in the tutorial, this function is *Load_ESRF_File_Callback.m*. This function is called when the user clicks on the **Load ESRF File** button. This function performs the SPEC file loading, parsing and initial definition of the *yield_array* variable. The best way to understand this function is to examine first the MATLAB code that defines *yield_array*. To understand the parser section at the beginning of this function, work through the SPEC file and the code together to see how this is done. Apply similar techniques for a different SPEC file formats. Understanding this function is probably the most difficult aspect of *SUGOM.m* and several days may be required to get good at it.

MATLAB major variable documentation:

LSM(i,j)

This array stores all information of the layered model used in Paratts recursion formula and is defined below. The first row (LSM(1,j) is for general parameters. The

first layer starts in the 2nd row. Two vacuum layers (2nd and 3rd rows) are required in the present implementation. The first material layer is the 3rd layer which is in the 4th row. The Nth or final layer is in the N+1 row:

LSM(1,1)=0; *LSM(1,2)*=0; *LSM(1,3)*=incident X-ray energy in keV; *LSM(1,4)*=0;

LSM(2,1)=0; *LSM(2,2)*=0; *LSM(2,3)*=2000; *LSM(2,4)*=0;

LSM(3,1)=0; *LSM(3,2)*=0; *LSM(3,3)*=2000; *LSM(3,4)*=surface roughness

LSM(4,1)=delta; LSM(4,2)=beta; *LSM(4,3)*=thickness; *LSM(4,4)*=roughness

LSM(i,1)=delta(i); *LSM(i,2)*=beta(i); *LSM(i,3)*=thickness(i); *LSM(i,4)*=roughness(i)

LSM(N+1)=delta(N+1); *LSM(N+1,2)*=beta(N+1); *LSM(N+1,3)*=thickness(N+1);

LSM(N+1,4)=roughness(N+1).

EFI_array(i,j)

This array stores the E-field intensity for a 2-d q-z grid. In addition, the reflectivity is also calculated and stored for convenience. The definitions of the *EFI_array* MATLAB array variable are as follows:

EFI_array (i=1:M,j=1:N)

M = numbers of θ points + 2

N = number of z points +1

EFI_array(M, i=1:N-2) = z_i

EFI_array(i=1:M-1, j=1:N-2) = EFI(i,j)

EFI_array(i=1:M-1,N) = θ_i;

EFI_array(i=1:M-1,N-1) = R_i;

EFI_array(M,zcount) = z;

All EFI_array file s are made by MATLAB program such as *rgG1_EFI_array.m* as an example. The variable name is *EFI_array* is preserved in each stored file so that any MATLAB program that loads an *EFI_array* file uses this name. See for example *EFI_plot.m* for an example of how to load the *EFI_array* from a particular file and then produce a surface plot.

MATLAB function documentation:

---

xswan2b_SP.m

[EFI,ref,phase] = xswan2b_SP((ang,layer_no,z,LSM)

This function computes the XSW E-field intensity, reflectivity and XSW phase. The inputs to the function are:

ang = incident X-ray angle in mrad

layer_no = the layer in the model. The reflectivity is calculated for the interface between this layer and the one above it. Note: this is not the LSM variable row number; the LSM array row=*layer_no* +1.

z = position measured from the top of the layer in angstroms.

LSM = the array defining the layered model (defined above)

Notes: This function computes a single θ,z point. This function can be improved by globally storing the Fresnel coefficients when repeated calls are made in which only *z* is varied while θ is held fixed.

EFI_plot .m

EFI_plot(EFI_fname,az,el)

This function generates a surface plot of the E-field intensity as a function of θ and *z*.

EFI_fname = name of the file in which the EFI_array is stored.

az = azimuthal angle (surface plot parameter)

el = elevation angle (surface plot parameter)

Reflect_LSM .m

[Ref_data]=Reflect_LSM(LSM,plot,th_i,th_f,M_th,av_pts)

This function calculates the X-ray reflectivity from the top surface of a layered model by making calls to the function *xswan2b_SP.m* where layer 2 is specified. The angle range is specified along with the number of points to calculate in that range.

Ref_data(mrad,R) = output vector of reflectivity as a function of angle.

LSM = the array defining the layered model (defined above)

plot = flag to cause a plot to be generated. 0=no plot 1=plot.

th_i = start angle in mrad

th_f = end angle in mrad

M_th = number of angle points

av_pts = boxcar average points. 0=no angle averaging.

Notes: The boxcars averaging recalculates R at each point using a boxcar average with the points i-*av_pts*:i+*av_pts* for the i^{th} point.

Ref_Vec.m

[Ref_data]=Ref_Vec(LSM,AngVect)

This function is similar to *Reflect_LSM.m* except that it takes an input vector for the angle values or which to calculate the reflectivity. This function is used in fitting routines where the reflectivity needs to be calculated at the experimental angles.

Ref_data = output vector of reflectivity as a function of angle.

LSM = the array defining the layered model (defined above)

AngVect = a vector of angles in mrad.

LSM05.m

[LSM] = LSM05(V)

This function is a typical example of a program generated model LSM array. The program contains all the information to specify the number and properties of each layer. This function creates an LSM model for Si/Mo multilayer LSM substrates. Nevot-Croce graded interfaces are used to model the interfaces between the Si and Mo layers. The exact structure of the model is best understood by examining the MATLAB function line by line.

V = vector of model parameters (see function listing for a detailed description of each parameter.

LSM = the array defining the layered model (defined above)

LSM05_X.m

[R]=LSM05_X(x_data,V)

This function is an intermediate function used in least squares fitting routines. Its purpose is to provide a function that returns a vector of calculated reflectivity values for a given input parameter vector *V*. It is possible in this function for an x-shift parameter to be used. For example, specifying *V(k)* = x_shift and then setting x_data=x_data+x_shift will effectively allow the optimization of the angle alignment zero error. Normally in least squares fitting, the independent variables cannot be changed but this intermediate function permits this to be done. The least squares optimization function calls this function where it varies the input parameter vector *V* seeking to minimize the error between measured values and the calculated values *R*.

[R] = calculated reflectivity

X_data = input angle vector (mrad)

V = vector of model parameters (see function listing for a detailed description of each parameter.

LSM_plot.m

[LSM_plotdata]=LSM_plot(LSM,layer_i,layer_f)

This function calculates a 2-d vector which describes a layered LSM model. The output is a series of line segments for each layer in the specified range of layers. The real part of the index of refraction is calculated as a function of z.

[LSM_plotdata] = (z,delta)

LSM = the array defining the layered model (defined above)

layer_i = start layer (z=0)

layer_f = end layer

Notes: A typical LSM has two vacuum layers (layers 1 and 2) and a final substrate layer (layer N) that is very thick. To plot the material layers choose from layers 3 to N-1.